Pollution dispersion from highways

Enhancing particulate matter capture using aerodynamics

Laboratory for Aero and Hydrodynamics
Process & Energy Department
P&E Report number 2837

Amitosh Dash

Technische Universiteit Delft

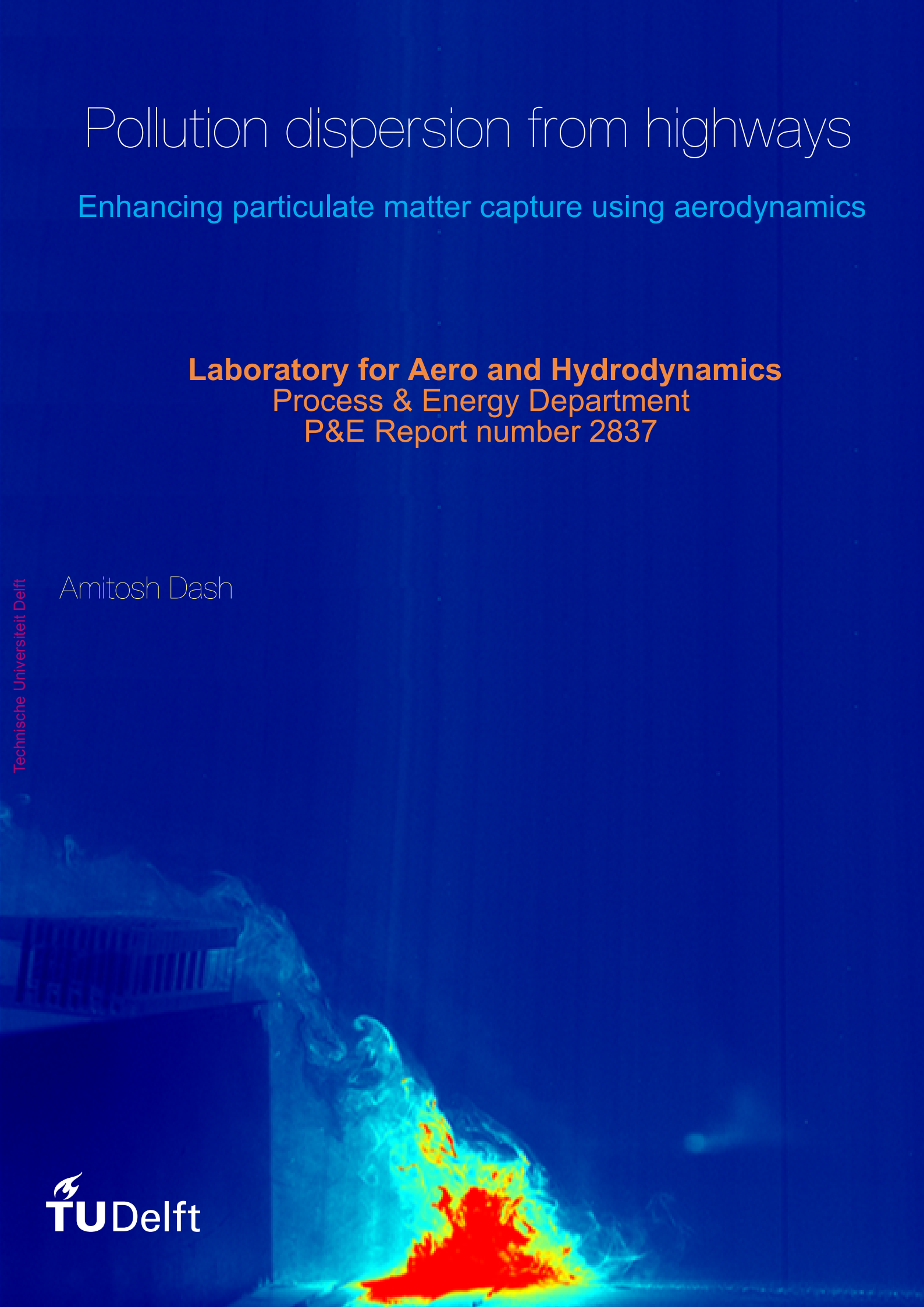

TU Delft

Pollution dispersion from highways

Enhancing particulate matter capture using aerodynamics

by

Amitosh Dash

to obtain the degree of Master of Science
at the Delft University of Technology,
to be defended on Thursday August 31, 2017 at 02:00 PM.

Student number:	4463978	
Project duration:	November 9, 2016 – August 31, 2017	
Thesis committee:	Dr. ir. Gerrit Elsinga,	TU Delft, supervisor
	Dr. ir. Mathieu Pourquie,	TU Delft
	Dr. Sasa Kenjeres, Dipl.-Ing.	TU Delft
	Dr. ir. Ferry Schrijer,	TU Delft
	Ir. George Bitter,	Antea group

An electronic version of this thesis is available at https://repository.tudelft.nl/.

TU Delft

Preface

This thesis is a short study looking into the aerodynamics of pollutant dispersion from highways towards the adjacent sound barriers, through scaled down experiments. The work presented is mainly in the framework of installing the 'Open Air Line ESP', an innovative product intended to capture particulate matter that might otherwise afflict the people living close to the highways. However, the conclusions of this work may also be extended to other pollutant capturing devices meant to be installed by highways, on top of sound barriers. The results presented here can be used as a starting point for small-scale field tests on understanding the performance of this ESP.

Readers who are particularly interested in the results of this study are directed to Section 5.4, which also includes a discussion on how the results of the scaled down experiments can be interpreted for real-scale installation. On the other end of the spectrum, scaling down (pollution dispersion) experiments involve several assumptions and simplifications, which have been summarized in Chapter 2. Any future experimentalist who might want to perform similar experiments may find Chapter 4 and Appendix B useful, where the practical aspects concerning the different measurement techniques used, are dealt with.

This thesis has been proofread with care, but mistakes, typographical or logical, may still have crept in. If the reader encounters any, I would be glad to be notified of the same. The image on the cover is a raw image belonging to a planar laser induced fluorescence dataset, which shows the dispersion of the passive scalar dye towards the model sound barrier and an electrostatic precipitator model placed on top, at a slight angle.

Amitosh Dash
Delft, August 2017

Acknowledgments

I would like to thank several people whose patience and expertise has supported the work presented in this thesis. Firstly, I would like to acknowledge the support I received from the technical staff at the laboratory, whose vast knowledge and experience came in really 'handy' (since the author has 'twee linkerhanden'). *Edwin Overmars*: Thanks for guiding me in the setup of my experiments as well as ensuring the good quality of the PIV+PLIF experiments. I learned a lot about the practical aspects of performing experiments from you and I am sure it will help me in the future as well. *Jasper Ruijgrok*: Thanks for the several times you assisted me with the little things in my setup and also for constructing the ESP model. *Jan Graafland*: Thanks for assisting me with the pitot tube measurements and introducing me to the 'electrical' aspect of the setup. In addition, *Mike van Meerkerk*: Thanks for promptly helping me in the earlier stages of my experimental setup and helping me get acquainted with the laboratory. A thesis is incomplete without the defence, so *Caroline Legierse*: Thanks for looking after the administrative tasks related to setting up my thesis defence.

This project was built on the ideas and work of a few predecessors, so *George Bitter*, *Bob Smulders* and *Michiel Hennink*: Thanks for making this project available and sharing a lot of practical knowledge regarding your ESP. The possibility of the results from this project having practical implications was a major incentive for me to select this project in the first place. I am indeed also very grateful to the predecessor of the 'pollution dispersion' experiments at my host laboratory, *Dr. Jerke Eisma*: Thanks for leaving behind a wonderful thesis and experimental setup. In addition, thanks for sharing your post-processing codes with me, which accelerated my progress.

I have also had the opportunity to present this work to *Prof. Doris Vollmer*, *Prof. Detlef Lohse*, *Dr. Jonas Allegrini*, *Dr. Karen Mulleners* and *their respective group members*: Thanks for being audience to my presentations. The questions asked and feedback received were extremely helpful in shaping the content of this thesis, as well as warming me up for the defence. The thesis committee also includes *Dr. Mathieu Pourquie*, *Dr. Sasa Kenjeres* and *Dr. Ferry Schrijer*: Thanks for agreeing to be on my thesis committee which will (hopefully) allow me to graduate in my targeted time limit. I look forward to our discussions and your feedback, during the defence.

The perk of working in this laboratory was the large number of peers, so *everyone in the Masters students room*: Thanks for all the conversations, theses related or otherwise. I would also like to thank *all the other members of my host laboratory*: Thanks for creating a pleasant and vibrant work atmosphere. I enjoyed visiting all the lunch talks/seminars and learning more about your respective topics of research. In addition, I must acknowledge the helping hand of *Pratik Nayak*: Thanks for voluntarily reading my thesis and providing additional feedback. A book is often judged by its cover, so *Digvijay Rawat*: Thanks for the tips which greatly improved the quality of the cover of my thesis. Of course, I am also grateful to *my parents* for financing my stay at Delft.

Lastly, and most importantly, I would like to thank my supervisor, *Dr. Gerrit Elsinga*: Thank you very much for your patience in dealing with me and being extremely approachable. I learned a lot from our many discussions and your depth of knowledge in this field was awe-inspiring. Your guidance allowed me to streamline the workflow and complete a passable thesis in time. Thanks also for proofreading this thesis and providing regular critical feedback on my progress. I really hope I will have a chance to collaborate with you again in the future.

Amitosh Dash
Delft, August 2017

Contents

List of Figures

List of Tables

Summary

People living or working close to the highways are at risk to higher exposure levels of different air pollutants, one of which is particulate matter. These ultrafine particles can easily infiltrate into ones respiratory system and increase the possibility of associated health issues. Air pollutants are often correlated with reduced lifespans, even in first world countries like The Netherlands.

Under the Dutch Air Quality Innovation Program, the addition of sound barriers to separate highways from adjoining urban areas was proposed. These sound barriers have shown to alleviate the peak concentrations of particulate matter in their downwind sections, by increasing their dispersion. However, the pollutants still remain in the atmosphere.

The Antea group has recently proposed the addition of Electrostatic Precipitators (or ESPs) on the top of these sound barriers, in order to capture the particulate matter and safely discard them. This is an attractive, but expensive, supplement, which makes it necessary to understand its performance, prior to their large-scale installation.

While estimates of the collection efficiency (i.e. what percentage of particulate matter mass entering the ESP is collected by the device) are known, the aerodynamic efficiency of the ESP (i.e. what percentage of pollutants reach the ESP entrance as compared to the mass emitted) is yet to be determined. The net efficiency of the ESP will be the product of the above two efficiencies, making it necessary to study the latter.

Scaled down experiments have been a common way to understand pollution dispersion for many decades, and has been selected as the diagnostic tool for the current study to understand the aerodynamic performance of the ESP. Of course, this entails certain assumptions and simplifications. These include restrictions on geometric scaling (i.e maintaining ratios of physical objects), flow similarity (i.e. the model satisfying the minimum threshold for a Reynolds number independent flow regime was given utmost importance) and the aerodynamic performance of the model ESP through the drag coefficient (i.e. the model ESP should affect the flow in a similar manner as the actual prototype would). Additional simplifications include the disregarding of influential factors existent in reality, such as thermal stratification in the atmosphere, presence of moving vehicles and the spatial and temporal variability in wind characteristics, among others.

The final model is rather simplified. A sound barrier model is installed in the test facility with a line source installed upstream of it and an ESP model suspended on top of the barrier. The line source is a model for the highway, from which fluorescent dye, which mimics the passive pollutants, is released into the incoming flow. The incoming flow has a velocity profile typical of a neutral atmospheric boundary layer. It was ensured that the scaled down ESP model demonstrated a drag coefficient, in the same order of magnitude as would be expected theoretically.

The experiments were performed in a water channel housed in the Laboratory for Aero and Hydrodynamics at the Delft University of technology. Simultaneous measurements of the flow velocities and dye intensities in the symmetry-plane of the channel were made through planar Particle Image Velocimetry (PIV) and Planar Laser Induced Fluorescence (PLIF).

The simultaneous implementation of the above two techniques helps in determining the instantaneous intensity based flux of the fluorescent dye (product of the velocity and dye intensity) in the flow. This enables defining the aerodynamic efficiency of the ESP as the ratio between the flux of the dye entering the ESP as compared to the flux of the dye leaving the entire region above the sound barrier. Following this, a few flow configurations were studied by varying certain parameters.

The first parameter was the height of the sound barrier. Installing an ESP (with fixed dimensions) on top of a shorter barrier was found to be more effective (64% efficiency) than on a taller one (27% efficiency). This is attributed to the formation of a larger separation bubble in the latter case which causes a larger vertical dispersion of the dye and leads to reduced efficiencies. These trends agree well with the expectations based on experiments without any ESP suspended in the flow.

The second parameter investigated was the vertical displacement of the ESP on top of the barrier.

It was found that slightly raising the ESP improved the aerodynamic performance (an increment in efficiencies of 9-11%). The slight elevation leads to the horizontal velocity component increasing twofold, assisted by a better alignment of the velocity vector angles to the ESP entrance, by nearly 10°. One possible reason for this improvement is the attenuation of the drag force acting against the flow in the streamwise direction, in the gap formed between the ESP and the sound barrier, but this needs to be verified. On the other hand, lifting the ESP too much would result in a huge gap allowing for a larger proportion of the dye to escape between the ESP and the sound barrier.

The third case was the highway canyon, which is formed by adding a second sound barrier model upstream of the line source. The parameter varied here was the canyon aspect ratio (ratio between the canyon width and height). Previous literature on urban/street canyons had indicated the presence of different flow regimes based on the canyon aspect ratio. The subtle difference in these experiments is the upstream sound barrier being the first roughness element which leads to much stronger variations in the flow regimes. For low canyon aspect ratios, a 'reverse skimming flow regime' was observed, which led to backflow through the ESP, rendering it completely ineffective. The ESP displayed non-zero aerodynamic efficiencies for canyons with higher aspect ratios (16-35% efficiency) and when the ESP was elevated above the shear layer (formed by the upstream sound barrier) in canyons with lower aspect ratios (39% efficiency). For intermediate canyon aspect ratios, a complete change in the flow regime was observed by the addition of an ESP, which formed a step-up canyon. Without any ESP, the aforementioned 'reverse skimming flow regime' was present, with backward flow in the region directly above the sound barrier.

In conclusion, it can be asserted that, first order estimates on the aerodynamic efficiencies of the ESP were determined. This was accompanied by the identification of ESP performance trends that should serve as a guideline for the initial testing of the ESPs at full scale. The guidelines include the physical location and entrance orientation of the ESP. Of course, the scaled down experiments, and thus the results, were not without their simplifications and this would be reflected in the results obtained via full-scale implementation. In addition, it is known that the collection efficiency of the ESP is a function of the incoming flow velocity. It is recommended that the entrance flow velocities reported here be used as an input for calculating the associated particle collection efficiency. A preliminary, but fruitless, effort to identify events that maximize the aerodynamic efficiency of the ESP was also made.

Together, the collection and aerodynamic efficiencies can be used to estimate the overall efficiency of the ESP. If the overall efficiency satisfies a minimum desirable threshold, the field experiments yield promising results, the device clears safety requirements, and the benefits outweigh the costs, the 'Open Air Line ESP' can be installed along the highways en masse in the future.

1

Improving air quality in rural-urban fringes using Electrostatic Precipitators (ESPs)

The Antea group in the Netherlands has recently developed an Electrostatic Precipitator (ESP), called the “Open Air Line ESP”. This device will be employed to capture Particulate Matter (PM) arising from vehicular traffic and improve air quality, especially in urban regions close to highways. Before its large-scale installation, it is necessary to understand its aerodynamic impact and maximize its pollutant capturing efficiency.

The positive impact of installing Sound Barriers (SBs) along highways on air quality is first explored in Section 1.1. The terms SB and fence are used interchangeably in this report. Next, the influential factors affecting the performance of the ESP are looked into in Section 1.2. Then, the main research questions concerning the performance of this product, along with the applied investigation approach is presented in Section 1.3. This is followed by a brief overview of the structure of this thesis in Section 1.4.

1.1. Sound barriers to reduce air pollution

According to a 2006 study by the World Health Organization (WHO) [2], people in the European Union, on an average, live approximately 9 months shorter due to health problems caused by PM, which is an air pollutant consisting of a mixture of solid and liquid particles suspended in air. Among the several ways to classify PM, the most frequently used parameter is the aerodynamic diameter of the particle (the size of a unit-density sphere with the same aerodynamic characteristics). The term PM_x refers to all particles with an aerodynamic diameter $\leq$x µm.

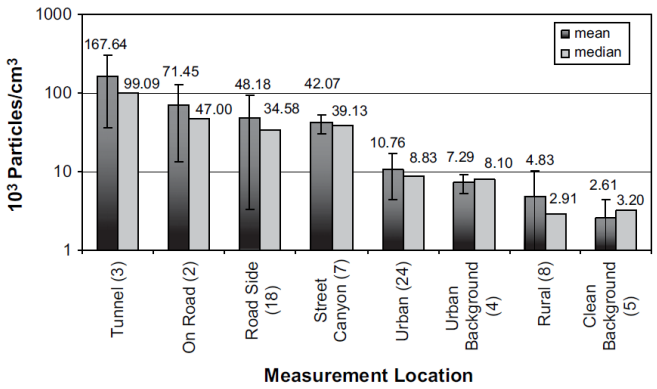

Figure 1.1: Mean and Median particle number concentrations in different environments as reported by Morawska et al. [1]. The numbers in the brackets indicate the count of sites for each environment.

The term Ultrafine Particles (UFPs) is used to denote particles with an aerodynamic diameter $\leq$0.1 µm (or $PM_{0.1}$). These are usually released into the atmosphere via vehicular emissions and are capable of remaining airborne in the atmosphere for hours while traveling up to tens of kilometers. Figure 1.1 shows the distribution of particle concentrations in different topographies. It is observed that the concentration

of particles increases upon moving closer to the traffic. Similar observations were made by Keuken et al. [3] based on measurements of PM concentration in the Rotterdam area. Thus, the maximum concentration of the UFPs is expected to be nearer to the sources, i.e. the vehicles.

Urbanization in the Netherlands has led to the rise of large-scale constructions in the rural-urban fringes which is defined, by Hamers et al. [4], as a transitional area between the city and the countryside. The constructions at these fringes include large-scale and small-scale residential areas, commercial zones, office parks and recreational areas. A number of motorways pass through these fringes, as shown in Figure 1.2, and thus, the inhabitants of these regions tend to have higher exposure to the pollutants (including UFPs).

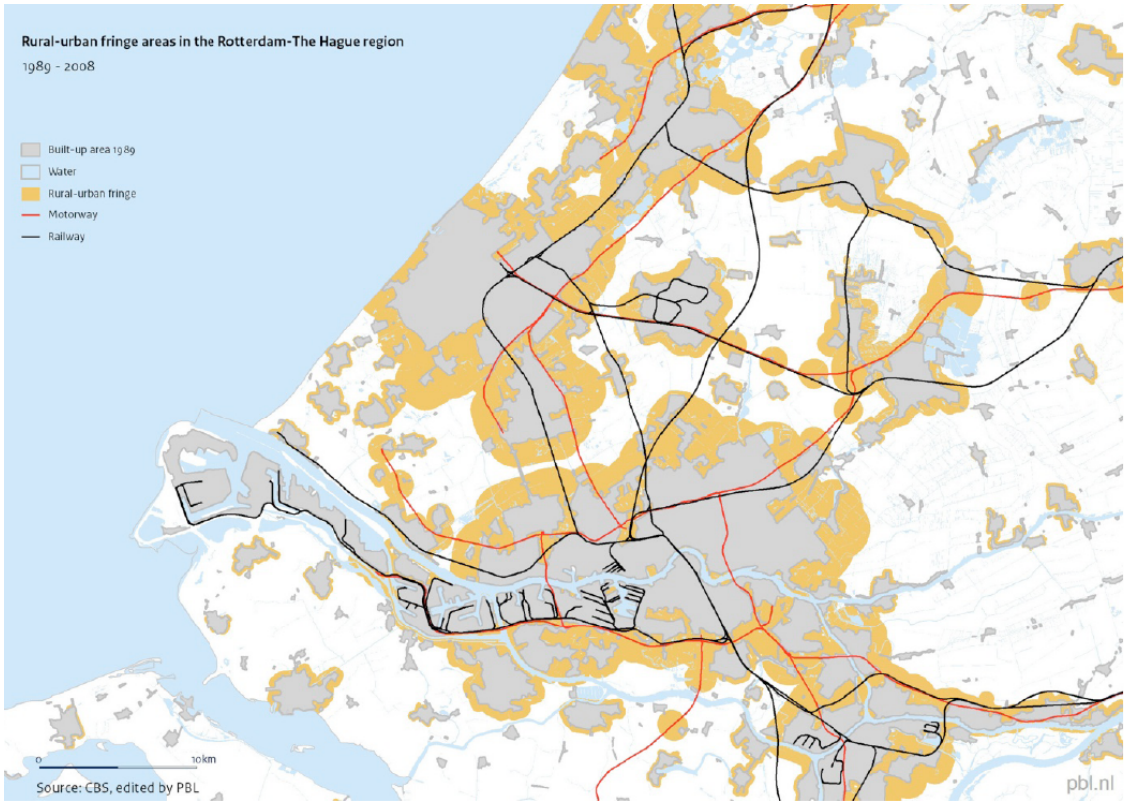

Figure 1.2: Rural-urban fringe areas (yellow patches) with the motorways (solid red lines) passing through, in the Rotterdam-The Hague region. Figure reproduced from Nabielek et al. [5].

Air quality standards were set by the WHO [6] in 2005 to provide guidelines to policy makers on reducing the repercussions of air pollution on health. The Dutch Air Quality Innovation Programme or *Innovatieprogramma Luchtkwaliteit (IPL)* was then established in 2005 to propose extensively feasible, innovative solutions for improving the air quality alongside motorways in the Netherlands. The main findings of this program over a five year period have been communicated in the IPL report [7].

Under the IPL, six independent, innovative solutions were proposed and tested over a five year period: (i) Roadside SBs (ii) Cleaning of road surfaces (iii) Catalytic coatings (iv) Motorway canopies (v) Roadside vegetation, and (vi) Dynamic Traffic Management.

Out of these proposed solutions, the first is of most interest within the scope of the current project. Motorway canopies can be considered as an extreme extension of roadside SBs. However, based on the IPL report [7], it was concluded that constructing such canopies could lead to impractical, astronomical costs, to the tune of over 15 million euros per kilometer of a 2×3-lane highway.

While the main objective of a SB is to reduce noise levels from traffic by blocking or deflecting the sound waves, they also aid pollutant dispersion. The improvement of near-road air quality upon installation of SBs, via field measurements, was previously demonstrated by Baldauf et al. [9].

Under the IPL, the impact of nine different SBs on the air quality along arterial roads were tested. The test site was located along the A28 at Strandnulde. Details regarding the tested SBs and the

measurement techniques have been reported by Hooghwerff et al. [8] and also in another report by the IPL [10]. A 4 m high SB reduced PM_{10} by about 34%, 10 m behind the SB, while a 7 m high SB showed a reduction of approximately 44%. A section of the standard 7 m SB (one of the nine tested SBs) can be seen in Figure 1.3.

Figure 1.3: A 7 m tall sound barrier being tested at Strandnulde. Photo reproduced from Hooghwerff et al. [8].

The Antea group (erstwhile Oranjewoud) in the Netherlands recently developed a solution to further reduce PM concentrations in the urban areas near highways. The solution involves installing an "Open Air Line ESP" on top of the SBs along the highways. This device captures the UFPs by a combined effect of electrostatic fields and turbulent flow inside the ESP. Alfonsi et al. [11] have provided a very comprehensive summary on all aspects of the performance of the ESP, for the interested reader. For a quicker understanding of its working mechanism, one can watch a short video created by the developers [12]. Further information of the product is also provided in Appendix A.

This ESP is capable of capturing around 75 to 80 percent of the UFPs passing through. While this number is impressive, it only represents a part of the picture. Quantitative estimates of the proportion of the emitted PM passing through the ESP duct are not yet available. This ratio is the other major part of the ESP efficiency that must be known in order to grade the performance of the product.

Cost estimates for the operation of ESPs (albeit, for industrial sized ones) were made by Turner et al. [13]. The "Open Air Line ESP", however, is much smaller than the typical industrial ESPs. It is capable of being powered by solar energy and is supposedly low maintenance. Even then, ballpark estimates of the capital investment along with associated annual costs, would amount to thousands of euros per ESP. Taking into account that the product is intended to be installed on a large-scale, the overall investment would be enormous. Thus, it is vital to understand and maximize the aerodynamic performance of the ESP to make the most of the investment.

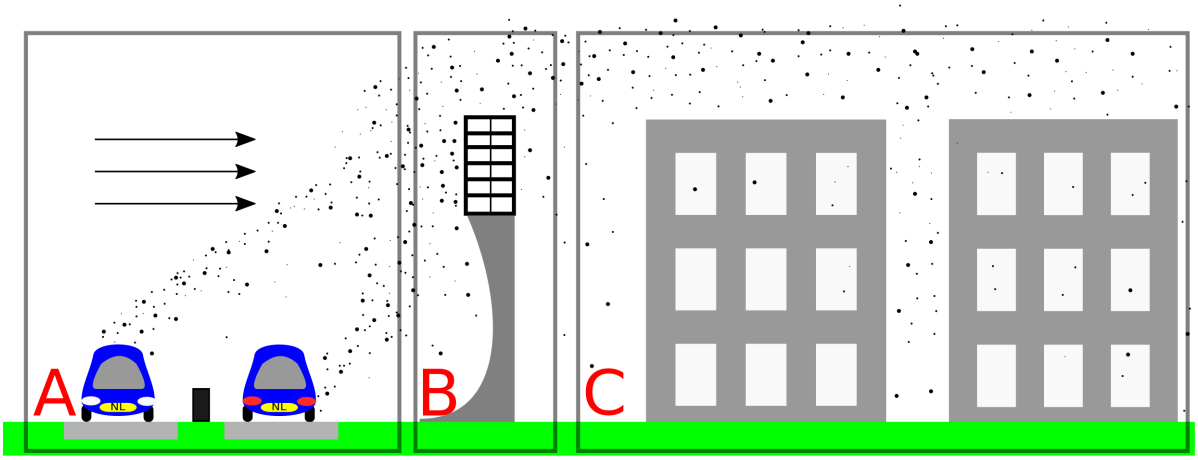

Figure 1.4: Phenomenon of pollutant dispersion in the typical Dutch rural-urban transition. Regions A, B and C correspond to the freeway, urban-freeway boundary and the urban region respectively.

1.2. Factors influencing the performance of the Open Air Line ESP

The problem statement of this project can be understood better from the illustration in Figure 1.4. The reader is advised not to make any inferences about the flow physics from this figure as it meant for

representational purposes only.

Three different topographies are considered in this case. Region A, in this figure, is the freeway with the vehicles being the source of the pollution in the form of particulate matter (denoted by black dots of different radii) and the flow at this level can be characterized by an incoming boundary layer profile. Region B is the focus of this project, which consists of an ESP mounted on top of a sound barrier. Finally, Region C is the urban area consisting of buildings and street canyons where the PM concentration is intended to be kept to a minimum. The section upstream of Region A could either be a rural area (typical of the Dutch highways) or even an urban area. However, the characteristics of the upstream fetch could have significant implications on the incoming turbulent boundary layer profiles, which will also be discussed later in Section 2.1.

The ESP is positioned right on top of the SB to capture the maximum PM. This is based on the findings of Eisma [14] and Tomas [15], wherein maximum concentration of the pollutants are found in a narrow band just above the SB. This is illustrated in Figure 1.5. Of course, the addition of the ESP would provide an additional resistance to the flow, thus affecting the pollution dispersion.

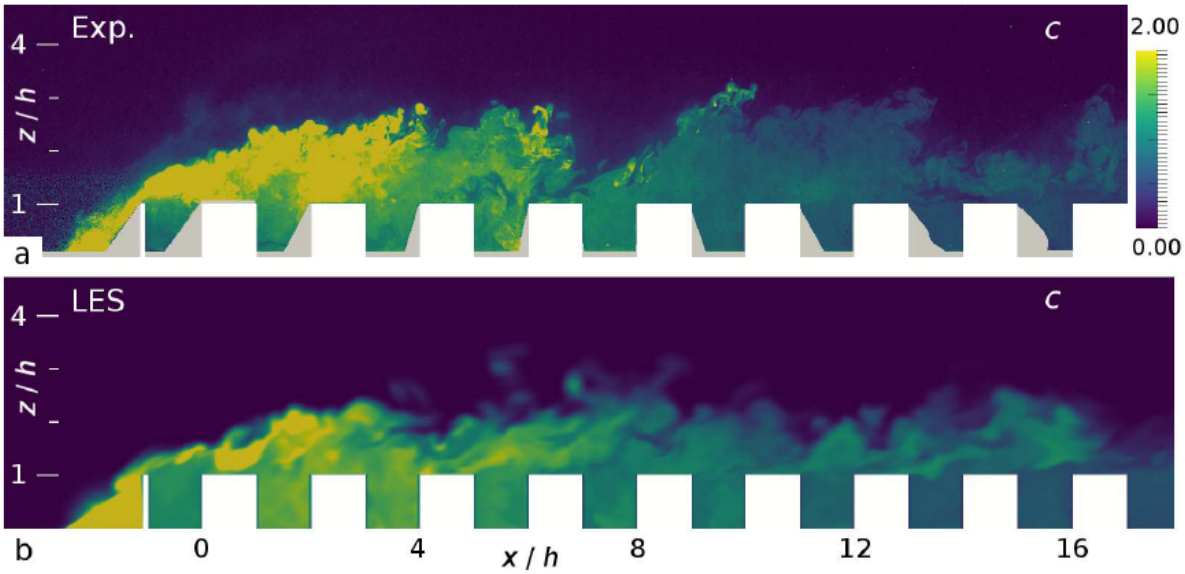

Figure 1.5: Contours of instantaneous concentration of released pollutants. (a) Scaled experiments and (b) Large Eddy Simulations. Figure reproduced from Eisma [14] and Tomas [15].

As justified in the previous section, it is important to make the most out of a single ESP. There are primarily two kinds of efficiencies, that can be defined for this case.

The first efficiency (aerodynamic efficiency), at a mesoscale, is associated with the ratio between the net PM emitted along the highway and the amount of PM entering inlet of the ESP. This quantity would be dependent on the topology and flow pattern upstream of the fence (i.e. corresponding to region A and even further upstream of region A in Figure 1.4).

The second efficiency (collection efficiency), at a microscale, is related to the flow inside the ESP itself (i.e. corresponding to region B). It can be quantified as the ratio between the mass of PM collected by the ESP and the mass entering the inlet of the ESP. This quantity would be dependent on the electrohydrodynamics occurring inside the device. The interested reader can refer to numerical studies investigating the coupling between turbulence and the electrostatic fields performed by Yamamoto [16], Choi and Fletcher [17] and Soldati [18]. Kallio and Stock [19] performed flow visualization experiments inside an ESP, while Mizeraczyk et al. [20] and Niewulis et al. [21] have performed Particle Image Velocimetry (PIV) measurements inside ESPs.

The overall efficiency of the ESP can be approximated as a product of the two efficiencies defined above. While estimates of the second efficiency (about 75-80%) are known to the product designers, estimates about the first efficiency (henceforth, simply referred to as the aerodynamic efficiency) are not known.

The following parameters are expected to have an effect on the performance efficiency of the ESP: (a) Size and structure of the SB (b) Presence of upstream objects (for example, an additional SB or buildings) (c) Incoming wind characteristics (such as, speed and angle of attack) (d) Concentration and relative buoyancy of the PM (e) Thermal stratification in the Atmospheric Boundary Layer (ABL) (f) Positioning, shape and alignment of the ESP (g) Roadway configuration (for example, flat, raised or sunken roadways) (h) Presence of vegetation (i) Traffic induced turbulence (j) Mechanical ventilation by the roadways (for example, fans).

Several of these parameters, albeit without an ESP model, have been studied by Gazzolo [22] qualitatively using flow visualization as well as quantitatively using a combination of planar PIV and Fiber Optic Assisted Laser Induced Fluorescence. Nevertheless, the above list cannot be considered complete and there could be other factors that would affect the near-field pollution dispersion as well.

1.3. Aims of the current project and the utilized approach

The investigation in this project will be limited to the the following parameters[†]:

- The position of the ESP relative to that of the sound barrier
- Shape of the fence (straight/curved) as well as its size
- Orientation of the ESP (tilt of the ESP with respect to the direction normal to the road)
- Incoming flow velocity
- Addition of an upstream SB to form a highway canyon
- Changing the specific gravity (buoyancy) of the pollutant

In the current project, the aforementioned questions will be answered by replicating the real-life scenario at a smaller scale. Experiments will be performed in the water tunnel at the Laboratory for Aero and Hydrodynamics at the Delft University of Technology (TU Delft). A scaled model of the highway (the line source), the SBs and the ESP are constructed, while the incoming flow is typical of the ABL. If promising results are observed, investment can indeed be made to facilitate small-scale field measurements to assess the real-time performance in the future.

A fluorescent dye will be released into the water tunnel to simulate vehicular PM emissions. The two employed measurement techniques are planar Particle Image Velocimetry (PIV) and Planar Laser Induced Fluoroscence (PLIF), the former providing velocity fields, while the latter returning dye concentration fields, over a planar region of interest. Results from the two techniques can be combined to obtain the concentration fluxes of the passive scalar, which is the fluorescent dye. With a combination of these techniques, the aerodynamic performance of the ESP can be evaluated.

The performance of the ESP can be judged by answering the following questions:

- Is there a clear, discernible effect on the flow passing through the ESP upon varying only one of the above design parameters?
- What is the aerodynamic efficiency of the ESP, in terms of the dye passing through the ESP as a fraction of the dye released from the line source?
- What is the optimal position/orientation of the ESP relative to the fence to maximize the above efficiency?
- What is the incoming flow velocity at the ESP inlet when placed under different configurations?

The above questions can be answered in several ways, one of which would include installing life-size ESPs along the freeways and making field measurements in the real atmosphere where it would eventually be utilized. While results from such full-scale measurements would give a very realistic impression of the performance, it would also be impractical for the following reasons:

[†]While experiments for all these parameters have been performed, the discussion in the thesis only includes the cases of SB height, vertical displacement of the ESP and highway canyons.

- The measurements would correspond to a specific site geometry and meteorological conditions.
- Some of the parameters whose effects wish to be investigated, such as the characteristics of the incoming flow, would not be controllable, and thus not repeatable.
- The amount of PM emitted cannot be controlled or determined accurately either.
- Only point measurements would be possible, thus limiting the resolution of the results.
- The costs and time involved in setting up and performing experiments at full-scale would far exceed that required in laboratory-scale experiments.

Performing scaled experiments will pose certain restrictions as follows:

- Maintaining geometric similarity between all the combinations of the ABL, the sound barrier and the ESP is not possible simultaneously. This shall also be looked into in Section 3.2.
- The hydraulic resistance posed by the ESP leads to a pressure drop across its ends. This phenomenon will be captured in the scaled model, by replicating the coefficient of drag (c_D), while considering only the internal structure (and ignoring the outer casing). There is no electrostatic component in the scaled ESP model.
- The ABL is simulated in the water tunnel by installing the same setup used by Eisma [14]. Scaling an ABL too requires satisfaction of several similarities, and only the ABL height shall be given consideration.
- Since it is impossible to maintain all the non-dimensional numbers (such as those discussed later in Section 2.3.2) as desired, only the Reynolds number will be considered. Furthermore, since it is not possible to have the model Reynolds number equal to that in reality, it is ensured that the two Reynolds numbers correspond to the same flow regime.
- While thermal stratification (and several other factors discussed later in Section 2.2) significantly influences the flow and pollutant dispersion, only neutral conditions can be investigated with the present water tunnel.
- Owing to time constraints, only a few design parameters are investigated using simultaneous PIV and PLIF.

1.4. A guide to this thesis

In the current chapter, an introduction to the problem of PM dispersion from highways was put forth. One of the PM mitigation strategies involves the installation of ESPs atop SBs. The research question, targets, limitations and techniques for the current project were also defined. The remainder of this thesis is structured as follows.

The physics of the pollution dispersion around a highway SB, based on previous studies, is discussed in Chapter 2. This chapter also presents a discussion on the complexity involved with satisfying multiple similarity criteria simultaneously and justifications for a few of the simplifications.

In Chapter 3, the development of the scaled model of the ESP is discussed in detail. The validity of the scaling too is justified. The functioning of the ESP is discussed at, both, a local as well an aerodynamic level while results of previous investigations on the aerodynamic aspect are also presented.

Following this, a brief overview of the experimental setup is given in Chapter 4. This includes the water channel in which the experiments are performed as well as the different boundary layers generated in the facility. Following this, the application of flow measurement techniques like the pitot-static tubes, PIV and PLIF are discussed in the framework of the current experiments.

The results of the experiments performed are then elaborated in Chapter 5. This includes the characterization of the model ESP and the incoming turbulent ABL profile. After defining the aerodynamic efficiency of the ESP, the aerodynamic performance of the ESP under different configurations is investigated. This is followed by a critical discussion on how the results of the scaled down experiments can be translated back to reality. A short exploration on the existence of events maximizing the aerodynamic efficiency of the ESP closes the chapter.

Lastly, the major conclusions of this project are summarized in Chapter 6. This chapter also includes a few suggestions on how to build up on the work and findings presented in this thesis.

2

Flow over a fence in an Atmospheric Boundary Layer

In Chapter 1, it was asserted that scaled experiments of a SB immersed in a simulated ABL need to be performed. Before proceeding to this step, it is interesting to learn more about the characteristics of the ABL and the flow around a fence submerged in one. These two matters are addressed in Section 2.1 and Section 2.2 respectively. Lastly, a short discourse on simplifying similarity, one of the biggest drawbacks of performing scaled experiments, is given in Section 2.3.

2.1. Structure of the Atmospheric Boundary Layer

The ABL is defined as the portion of the atmosphere most affected by the boundary (the Earth's surface). While the effect of thermal stratification on pollution dispersion near a SB will be discussed later in Section 2.2.3, it is interesting to learn more about the ABL, where the pollution dispersion occurs. A detailed review on the ABL is given in Stull [23] and Stull [24], wherefrom the majority of the content in this section is borrowed.

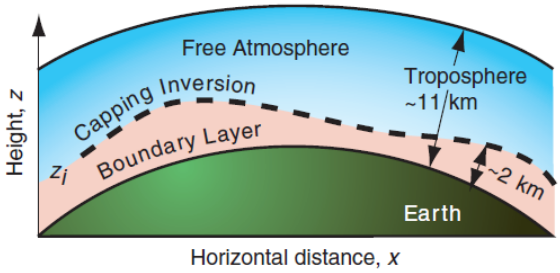

Figure 2.1: Vertical cross section of the Earth and troposphere. Figure reproduced from Stull [23].

A strong stable layer, called the capping inversion, is sandwiched between the ABL and the troposphere above (the free atmosphere). This is illustrated in Figure 2.1. It plays a major role in trapping the dispersed pollutants within the ABL causing us to "stew in our own waste" in the words of Stull [23].

The height of the ABL varies with space and time and can range from less than a hundred meters to a few thousand meters depending on the orography (topography of mountains), surface cover, season, daytime and weather, as noted by Hennemuth and Lammert [25].

The boundary layer evolution in time is sketched in Figure 2.2. Unstable boundary layers (during sunny days) are characterized by vigorous turbulence which causes mixing. Thus, the bottom part of the ABL becomes homogenized and is characterized by a near uniform potential temperature. In such a scenario, the ABL is also referred to as the mixed layer. The bottom part (20 to 200 m) of the mixed layer is called the surface layer where the frictional drag, heat conduction and evaporation from the surface cause substantial variations of wind speed, temperature and humidity with height. Since turbulent fluxes vary uniformly with the altitude in the surface layer, it is also called the constant flux layer.

At night, a (relatively shallower) statically stable boundary layer is formed underneath a statically neutral residual layer. This residual layer contains pollutants and moisture from the previous mixed

layer, but is not very turbulent.

The free atmosphere is separated from the mixed layer by a strongly stable entrainment zone of intermittent turbulence. However at night, the entrainment zone becomes non-turbulent and the layer is now called the capping inversion, which too is strongly stable.

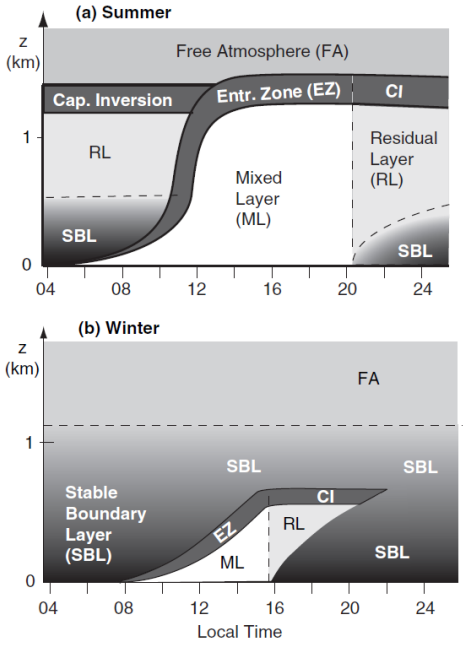

Figure 2.2: Daily evolution of boundary layer structure by season, for fair weather over land. (a) Summer (b) Winter. Shading indicates static stability: white = unstable, light grey = neutral (the shade used for RL), dark grey = strong static stability. Figure reproduced from Stull [24].

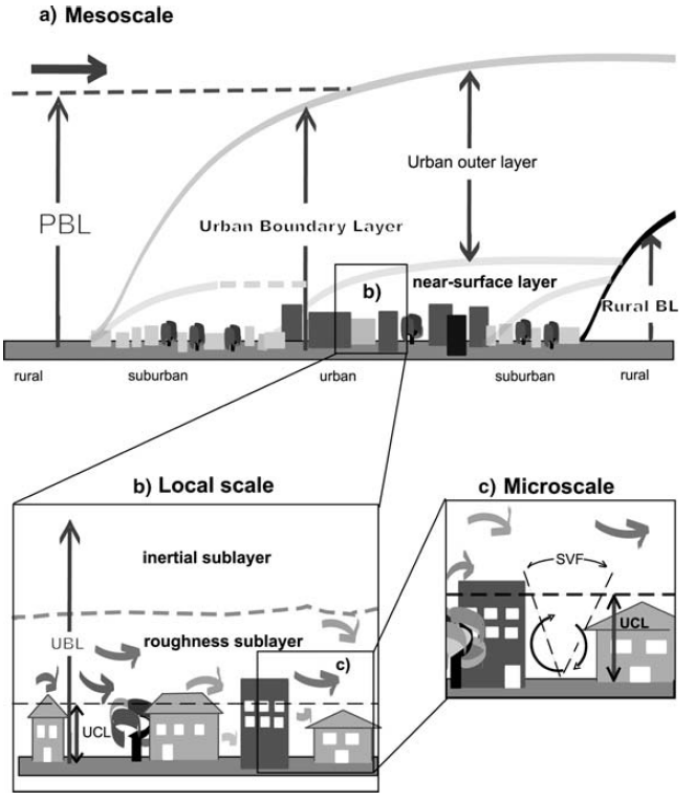

Figure 2.3: Sketch of the urban boundary layer and its various sublayers. Figure reproduced from Piringer et al. [26].

The already complicated structure of the ABL is further complicated by the presence of roughness elements (for example, urban regions, forest canopies, mountains etc). An example of the (complex) urban boundary layer is illustrated in Figure 2.3. The rural boundary layer can thus be expected to have different characteristics as compared to the urban boundary layer.

The effective roughness length for the Netherlands, accounting for the orography and small-scale obstacles (such as tree lines and dikes) is 0.334 m, as reported by de Jong et al. [27]. Charts of the dominant landuse and effective roughness length for the Netherlands (in the year 1997) are shown in Figure 2.4.

2.2. Flow around a sound barrier

Pollution dispersion around a SB is highly dependent on the nature of the flow around the SB. Thus, it is necessary to have a basic understanding of the dynamics governing the flow in this region. While most investigations in literature focus on the section downstream of the SB, the focus of the current project is more towards the section upstream of the SB. The flow characteristics around a single or a pair of sound barriers as well as select factors that can affect pollution dispersion from a highway are looked into in the subsequent subsections.

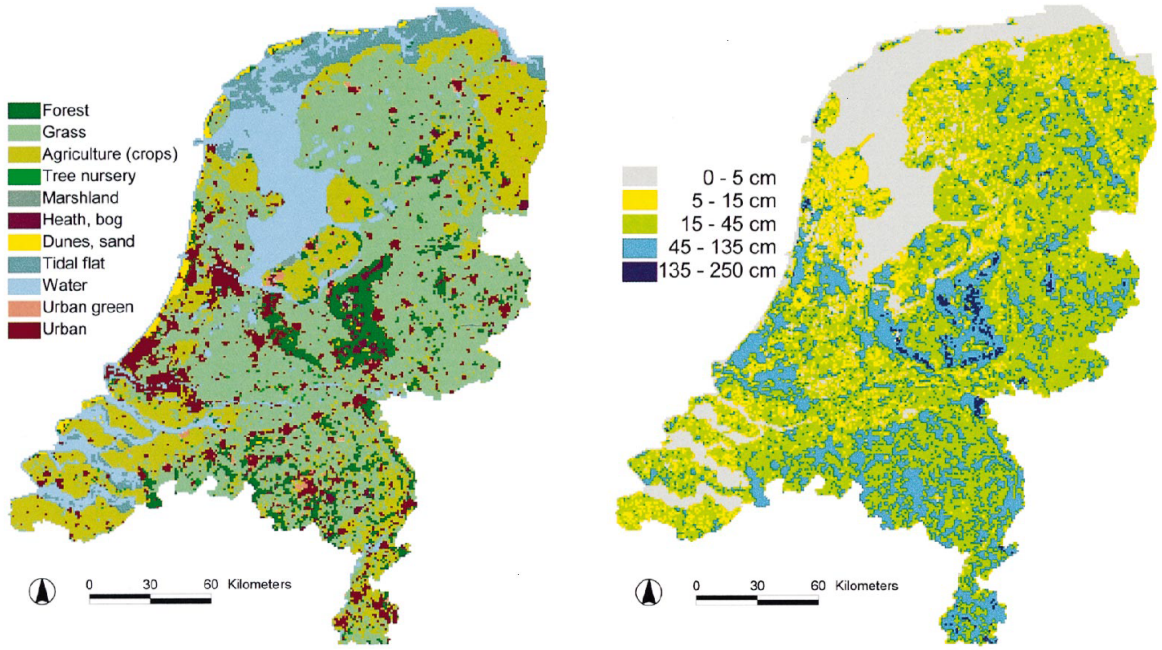

(a) Dominant landuse.

(b) Effective roughness length.

Figure 2.4: Characteristics of the Dutch land usage. Figure reproduced from de Jong et al. [27].

2.2.1. Flow around a single sound barrier

Streamlines representing the flow around a solid windbreak (structure similar to a SB) are shown in Figure 2.5. The presence of a barrier or fence-like obstacle exerts a drag force on the approaching wind flow, which is deflected upwards and separates at the top of the obstacle. A shear layer develops from the separation point, which then steeply impinges onto the ground, creating the reattachment region on the leeward side. A recirculation bubble is also created in front of the fence, as can be seen from the streamlines separating from the ground and moving above the fence.

For the current study, it is assumed that SBs located by the highways are impermeable. If the SB is semi-permeable, there will also be a 'bleed flow' through it, and a weaker upward displacement, upstream of the SB will be visible, as demonstrated by Raine and Stevenson [28]. This could strongly affect the dispersion of the pollutants. For the purpose of this project, the SB is also considered as a two-dimensional object with an infinite width. This eliminates any edge effects, and also eliminates any pressure gradient in the lateral direction.

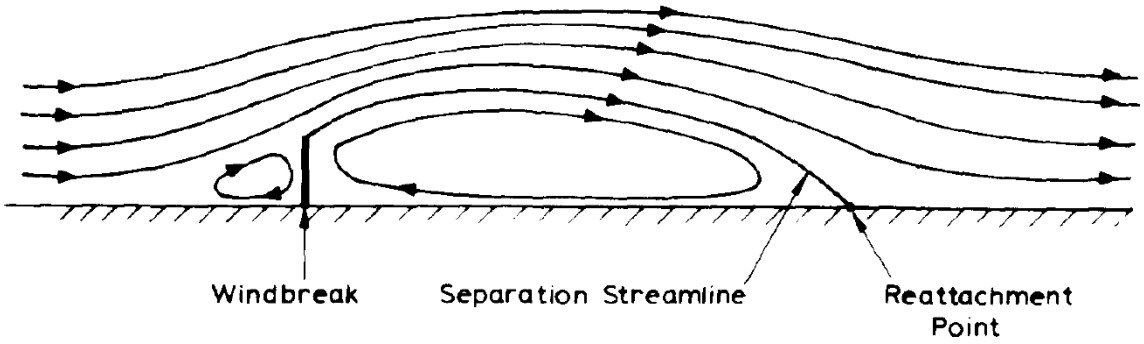

Figure 2.5: Streamlines of the flow around a solid windbreak. Figure reproduced from Raine and Stevenson [28].

Kim and Lee [29] suggest that the flow separation in front of a fence is induced by an adverse pressure gradient rather than by geometry. For geometry induced flow separation, one edge of the separation bubble is fixed. However, in the case of a fence, both the trailing and leading edges of the bubble are free to move. Siller and Fernholz [30] showed that static pressure rises in the streamwise direction and normal to the streamlines. It was also shown that right above and immediately downstream of the fence, the static pressure is reduced due to the sudden contraction of the flow. Vortices are shed from the edge of the fence, which can be attributed to two factors according to Sigurdson [31]: shedding from the fence edge and from the Kelvin-Helmholtz instabilities arising from the shear layer.

For a flow around a fence in a turbulent boundary layer, the flow is mainly influenced by the object height, boundary layer thickness, the boundary layer turbulence, and the friction velocity. On top of that, the friction velocity hardly varies over a large range of velocities, in a turbulent boundary layer. A commonly used justification in scaling down problems is based on the findings of Castro [32]. It was found that for a flow around a sharp-edged obstacle in an incoming turbulent boundary layer flow, the effect of Reynolds number (based on obstacle height and freestream velocity) was negligible between the range of 0.5×10^4 and 2×10^4.

Roadside SBs affect the initial dispersion of vehicular emissions as investigated by Bowker et al. [33] and Schulte et al. [34]. Firstly, the emissions are lifted over the SB. Secondly, they also increase the vertical dispersion through additional turbulence generated in the wake of the SB. Thirdly, vertical mixing occurs in the cavity on the lee side of the SB, resulting in reduced concentrations. Results from the semi-empirical model developed by Schulte et al. [34] also demonstrate the significant reduction of pollutant concentrations in the near field of the SB as compared to the case without one.

2.2.2. Flow over two sound barriers

Features of the flow over two SBs, forming the so called ‘highway canyon’, were investigated by Alfonsi et al. [11], and streamlines for such a case are shown in Figure 2.6. The geometry formed by the SBs represented the k-type of roughness. A ‘street canyon flow’ was observed wherein flow along the bottom of the canyon moved upstream and vice versa. The vortices shed from the upwind SB mix air from the polluted highway with the clean upwind air, while moving downstream. The concentration flux over the downstream SB is largely influenced by the shear layer shed from the upstream SB.

Durst et al. [35] too investigated flow over two fences, albeit in a closed channel, resulting in relatively high blockage ratios. It was found that the size of the recirculation zones upstream of each fence was not strongly influenced by the Reynolds number, with the recirculation zone of the second fence found to be always smaller. Also, for certain ranges of Reynolds numbers, the separation zone upstream of the second fence merged with the separation zone downstream of the first one.

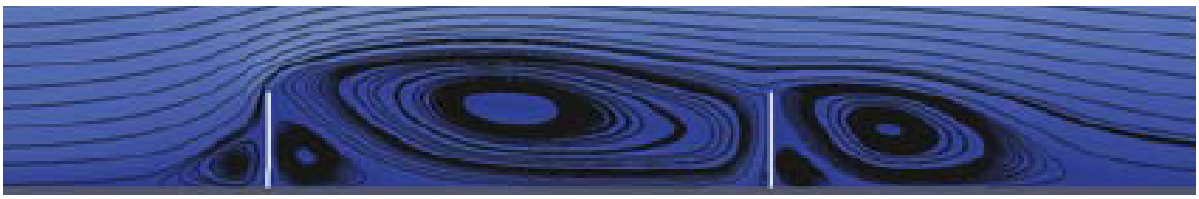

Figure 2.6: Streamlines for flow over two sound barriers. Figure adapted from Alfonsi et al. [11].

There are several studies regarding urban canyons where spacing between (cubical) buildings form streets. Pollution dispersion from such canyons have been studied extensively. However, it is unclear to the author whether inferences from such studies can be applied in a one-to-one manner to flow over thin fences, where the breadth of the obstacle is treated as negligible compared to the obstacle height.

The general pollutant dispersion in a street canyon is shown in Figure 2.7, whereas the effect of aspect ratio on the flow regimes is shown in Figure 2.8. There are three different flow regimes based on the spacing between the buildings, as explained by Oke [36]. When the buildings are far apart, there is no interaction between the flow artefacts around each building, leading to a flow regime known as the ‘isolated roughness’. When the spacing between the buildings is reduced a bit, the downstream

separation bubble of the windward building interacts with the upstream separation bubble of the leeward building, in a regime called the 'wake interference' flow regime. If the buildings are brought further closer, a single stable vortex is established in the canyon, in what is known as the 'skimming flow'. In the latter case, the free stream flow is unable to penetrate into the canyon. The transition between regimes is not only dependent on the height of the buildings but also on the length of the building normal to the flow.

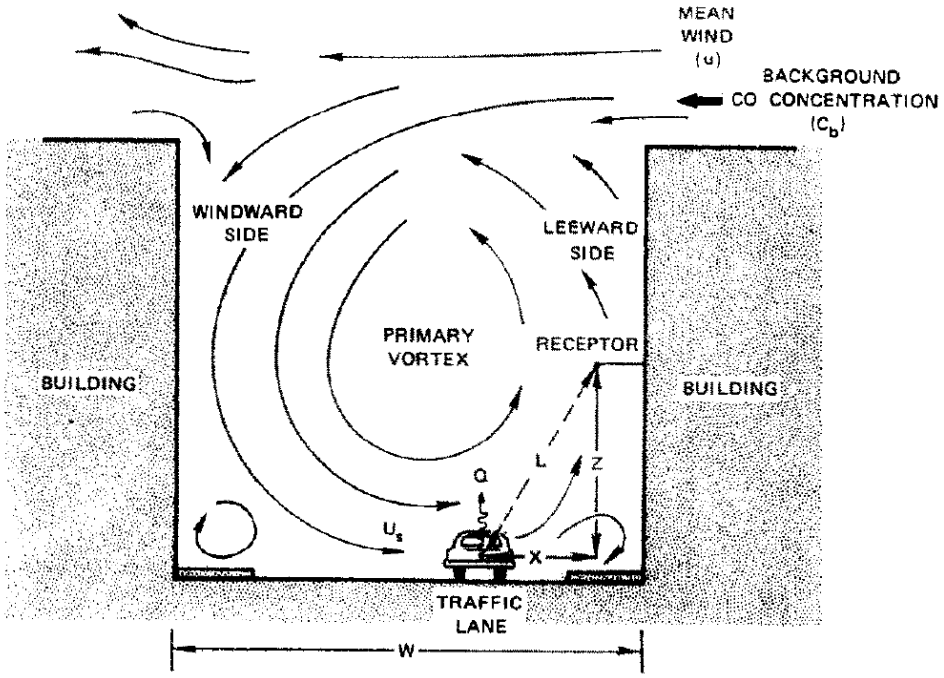

Figure 2.7: Pollution dispersion in a regular street canyon. Figure reproduced from Dabberdt et al. [37].

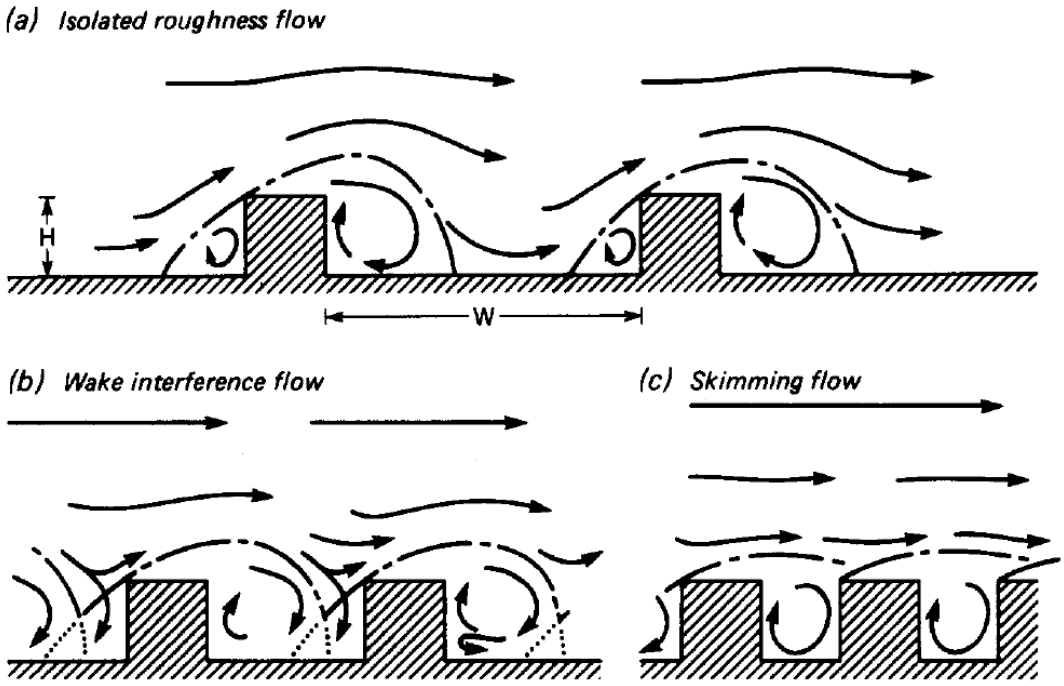

Figure 2.8: Flow regimes for different aspect ratios of street canyons. Figure reproduced from Oke [36].

2.2.3. Effect of atmospheric thermal stratification

Thermal stratification also has an important role in atmospheric flows. On a warm, sunny day, the ground is heated up, causing the lighter air to rise up through buoyancy. This is a case of an unstable ABL, while a stable ABL may be observed under cool, nocturnal conditions. Neutral conditions are present during bad weather (i.e. moderate to strong winds, overcast conditions). The Richardson number is often used to characterize the stability of the thermal stratification in the atmosphere. A positive Richardson number indicates a stable atmosphere while a negative Richardson number indicates an unstable atmosphere.

Thermal stability in the atmosphere also controls the shape of the turbulent eddies as illustrated in Figure 2.9. Under unstable conditions, anisotropy, with excess turbulent energy in the vertical direction, would be expected. This would make a plume loop up and down more in the vertical direction as compared to in the horizontal direction. Under neutral conditions, the turbulence can be considered to be more isotropic and pollutants would disperse via coning, where the vertical and horizontal spreads are equal. Finally, under stable atmospheric conditions, anisotropy is observed again with little energy in the vertical direction (due to buoyant consumption) leading the pollutants to fan out horizontally. An example of the effect of thermal stability on the flow characteristics around a fence is shown in Figure 2.10 while typical velocity profiles for differently stratified ABLs are shown in Figure 2.11.

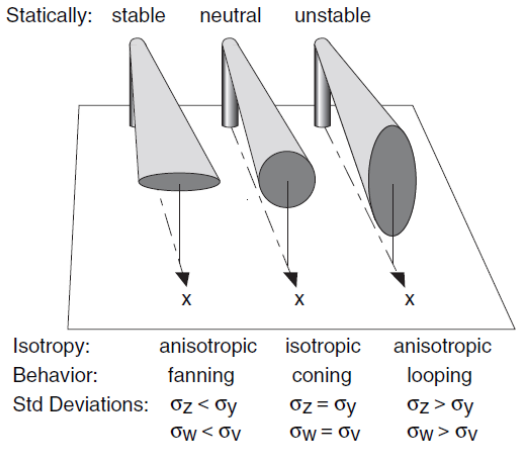

Figure 2.9: Isotropic and anisotropic dispersion of smoke plumes under different thermally stratified atmospheric boundary layers. Figure reproduced from Stull [38].

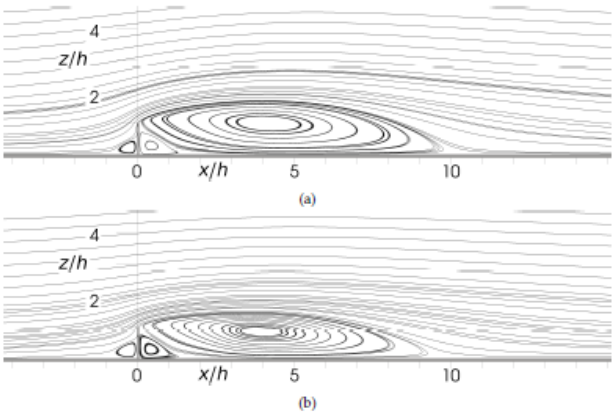

Figure 2.10: Effect of thermal stratification on the downstream recirculation zone. Scenarios: (a) Richardson number = 0 (neutral) and (b) Richardson number = 0.147 (stable). Figure reproduced from Tomas [15].

Field measurements by Jacobs [39] in the Netherlands, demonstrated that the speed of recovery (recovery of the mean velocity profiles behind a fence back to that of the incoming flow) decreases in the following order: unstable, stable, and neutral boundary layers. This too implies that the velocity profiles and thus, the dispersion of pollutants, would depend on the thermal stratification in the atmosphere.

More recently, Tomas [15] investigated the flow and dispersion of pollutants around a two dimensional fence for three different stably stratified ABLs. The upstream recirculation region had a height equal to 2/3rd of the fence height while its length was equal to the fence height. It was found that only the height of the recirculation zone behind the fence is influenced by the stratification. In Figure 2.10, it can be seen that under stable conditions, there is considerable suppression of the downstream recirculation bubble in the vertical direction as compared to the case with neutral conditions. The recirculation region height is 1.7 and 1.45 times the fence height for the neutral and stable cases, respectively.

While Tomas [15] asserts that there is a weak effect of the Richardson number on the length of the downstream recirculation zone, this conclusion contradicts the findings of Ogawa and Diosey [40] as well as of Trifonopoulos and Bergeles [41]. Results obtained by Ogawa and Diosey [40] show that the cavity wake length decreases drastically with increasing Richardson numbers, while the wake length decreases slightly as the flow becomes more unstable. Both, Ogawa and Diosey [40] as well as Trifonopoulos and Bergeles [41], attribute their observations to the stable ABL which inhibits the influence

of the fence.

Schulte et al. [34] showed that a SB has greatest impact in reducing pollutant concentrations during stable atmospheric conditions (i.e. early morning, late evening and nighttime) which may correspond to the rush hours, depending on the season.

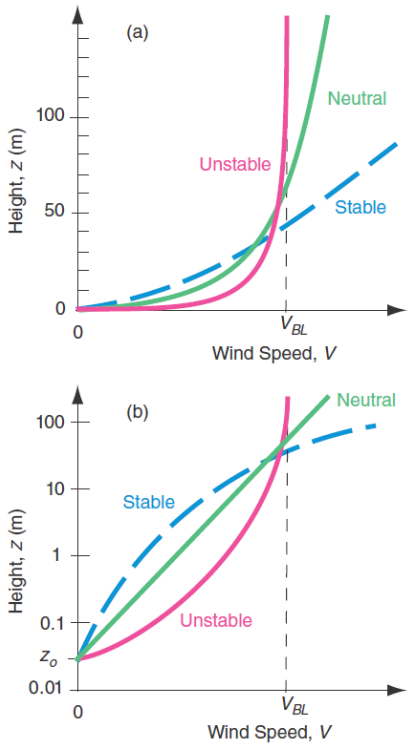

Figure 2.11: Typical variation of wind speeds with height in the surface layer for different static stabilities. (a) Linear plot (b) Semi-log plot. Figure reproduced from Stull [23].

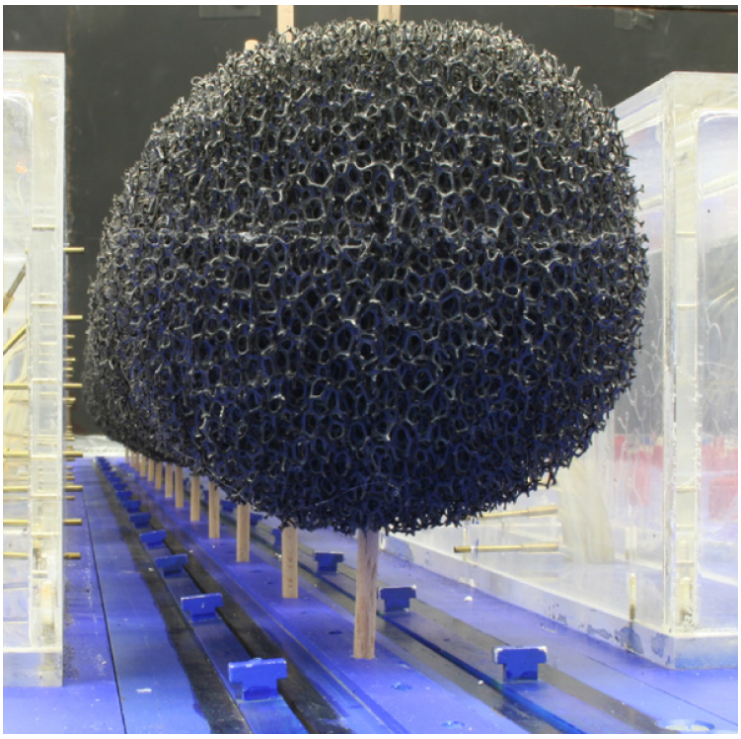

Figure 2.12: A scaled model for simulating vegetation and traffic induced turbulence. Figure reproduced from Gromke and Ruck [42].

2.2.4. Effect of vegetation

Presence of vegetation by the highway can impact the pollutant dispersion by not only affecting the aerodynamics, but also by collecting/absorbing the pollutants. Several studies, including field measurements, are available on this subject.

The effect of additional trees at the center of a canyon, on the highway pollution emissions, was analyzed by Gromke and Ruck [42] through scaled experiments. An image of the modeled trees can be seen in Figure 2.12. The parameters varied included the diameter of the tree crowns, total tree height and the lateral spacing between the trees. It was found that a single row of trees led to higher concentrations on the windward wall and lower concentrations on the leeward wall. From the perspective of ventilation, three recommendations were put forth: the tree crowns should not occupy large canyon volumes in order to aid the ventilating canyon vortex system; the total tree height should not exceed the roof top level, which may lead to substantial reduction of entrained air; and a broader tree spacing ensured better ventilation of the canyon by allowing easier intrusion of the atmospheric overflow.

Janhäll [43] too investigated the effect of vegetation on urban air quality. Some of the vegetation design considerations put forth included: vegetation should be low enough to allow dilution of emissions with clean air from aloft; vegetation should be closer to the source to allow for increased deposition of pollutants; and vegetation barriers should be high and porous enough to let the polluted air through but solid enough to let air pass close to the surface. It was also found that the deposition of coarse particles is more efficient at high wind speeds and the opposite holds for UFPs. Deposition can be improved by

having hairier leaves and having a large but penetrable leaf area index (amount of vegetation surface per m^2 of ground area).

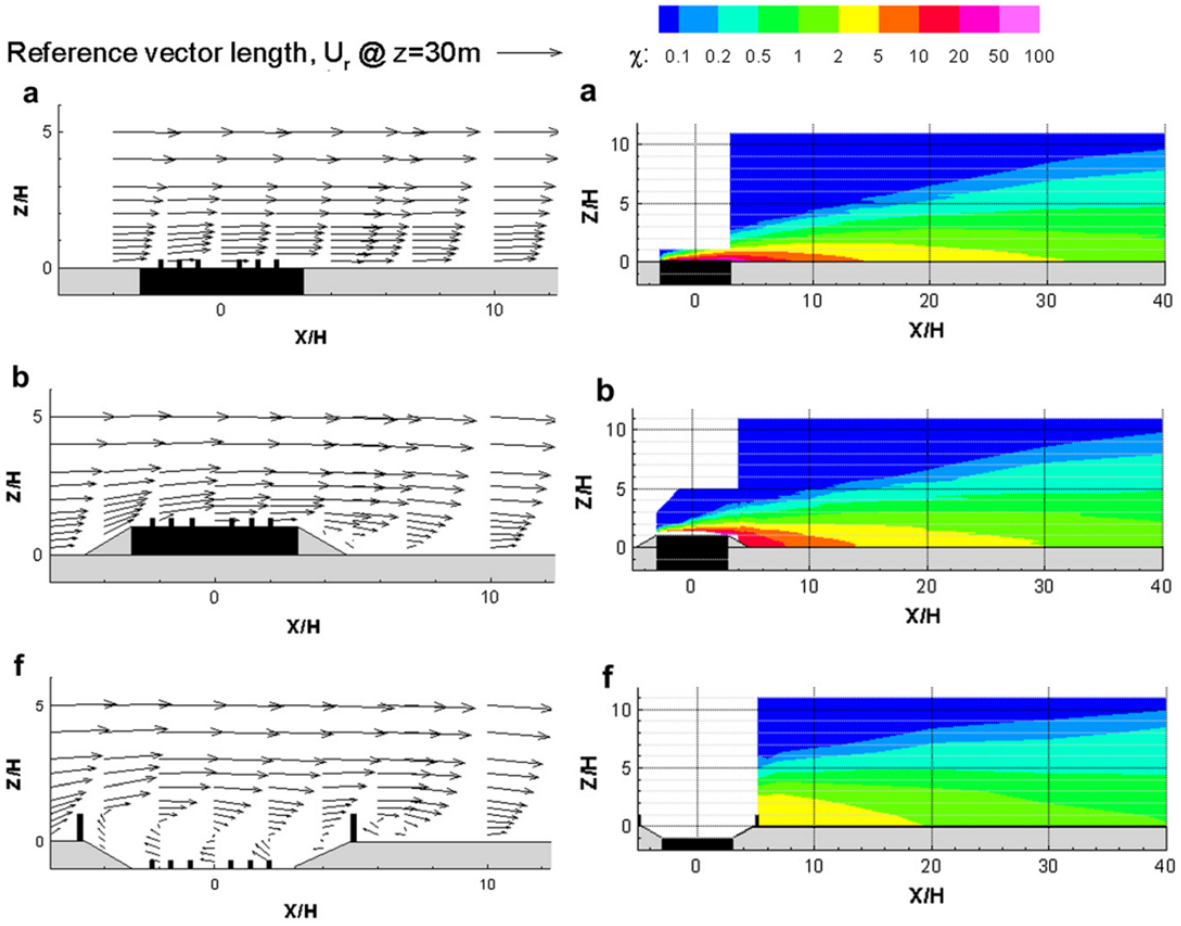

Figure 2.13: Effect of elevated and depressed roadways on pollution dispersion. (a) Baseline case with flat terrain and no sound barriers, (b) Elevated roadway with no sound barriers inclined at 30° and (f) Depressed roadway inclined at 30°. The images in the left column depict the velocity profiles whereas the images on the right display the non-dimensionalized concentrations. Figure adapted from Heist et al. [44].

2.2.5. Effect of roadway geometry

Roadway geometry includes the geometry of the roadway as well as the geometry and placement of the SB relative to the pollutant source. Schulte et al. [34] discovered that the SB height has the most influence on concentrations near the SB and the vertical plume spread is expected to be directly proportional to the SB height as observed by Pournazeri and Princevac [45].

Heist et al. [44] performed wind tunnel measurements for several roadway configurations (for example, elevated roadways, sunken roadways with varying depths and gradient to at-grade elevation, addition of SBs in upwind and/or downwind directions of varying heights and streamwise position). An elevated roadway (without SBs) was shown to have the least impact on reducing ground-level pollutant concentrations downwind of the roadway as compared to the flat terrain without SBs. The greatest improvement was observed for the case of a depressed roadway with SBs on either side. The streamwise position of the SB was shown not to have any significant impact on the ground-level concentrations. Select results from this study are shown in Figure 2.13.

Pournazeri and Princevac [45] drew similar conclusions regarding the positive downwind impact of depressed roadways with SBs. The dispersion of pollutants placed between different SB configurations (upwind or downwind or both), as shown in Figure 2.14, were also visualized. For the downwind

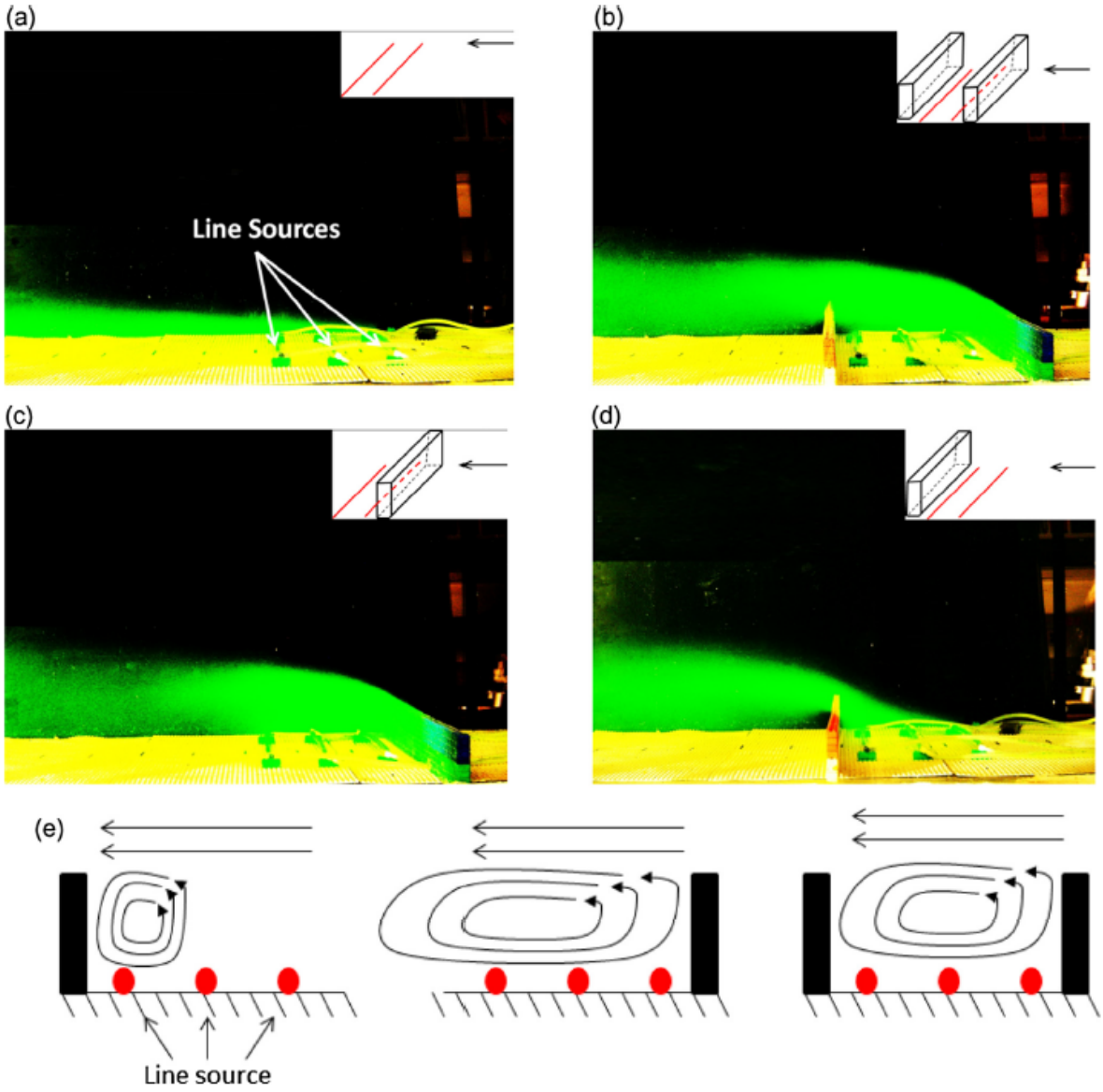

Figure 2.14: Plume visualization for different sound barrier configurations. Scenarios: (a) None, (b) Two sound barriers, (c) Upwind only, and (d) Downwind only. (e) Change in size of the recirculation flow under different configurations. Arrows in the schematic represent the flow direction. Figure reproduced from Pournazeri and Princevac [45].

configuration, the size of the recirculating zone is constrained by the SB height rather than the width of the roadway. Thus, the pollutants on the highway will be impacted by only a smaller region of high turbulence leading to higher on-road concentrations for the downwind only case. It was also found that the upwind SB was more effective in lifting the plume due to the strong recirculation in its wake.

The cases of step-up/down canyons were also investigated by Pournazeri and Princevac [45]. These refer to the cases where there is asymmetry in the SB heights on either side of the roadway. It was shown that the upwind SB was more effective in lifting the plume due to the recirculation in the wake. While increasing the height of the downwind SB did not have a significant effect in lifting the plume, it reduced concentrations in a larger area downwind of the downwind SB. This case has been illustrated in Figure 2.15.

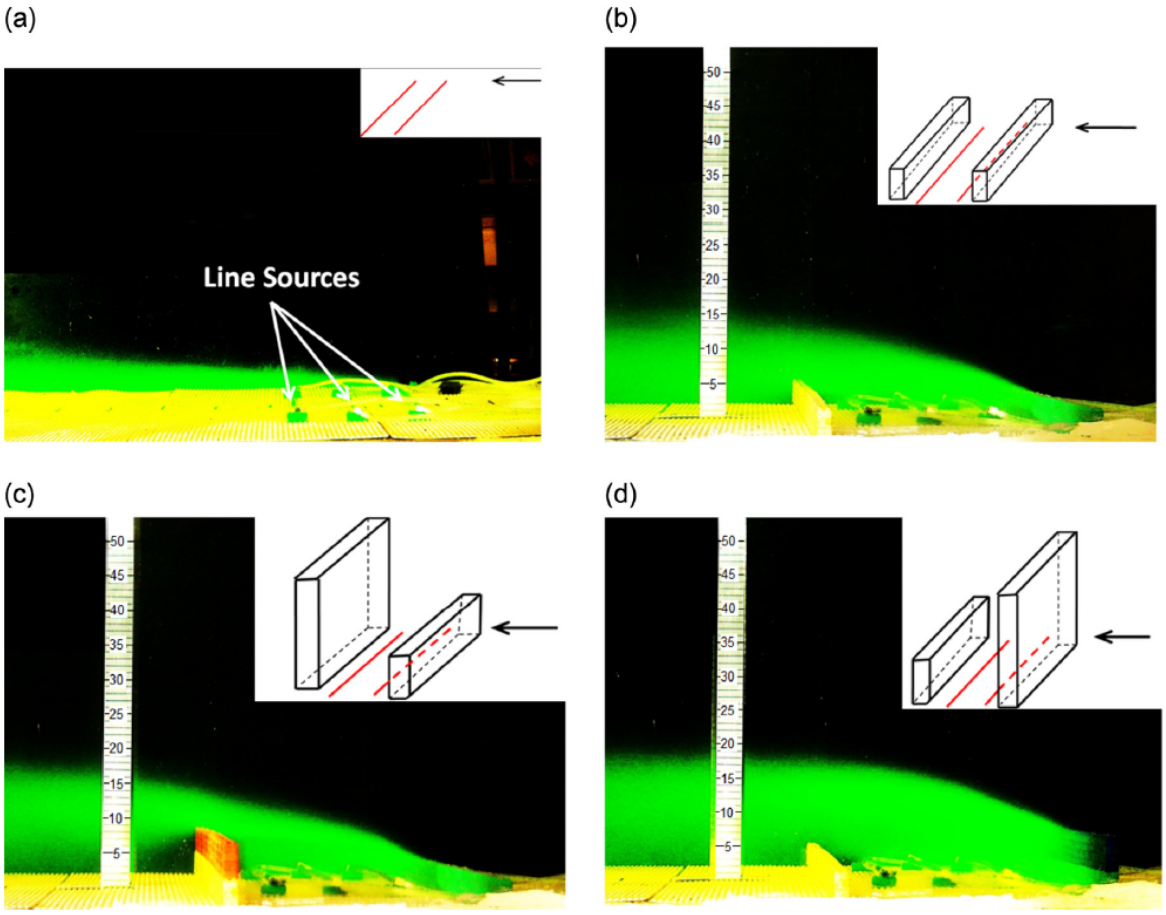

Figure 2.15: Plume visualization for step up and step down canyons. Scenarios: (a) No fence, (b) Fences of equal height, (c) Double height for downwind fence, and (d) Double height for upwind fence. Figure reproduced from Pournazeri and Princevac [45].

2.2.6. Effect of incoming wind characteristics

Flow towards a sound barrier is characterized by an incoming speed and angle of incidence. In reality, the wind velocity (both magnitude and direction) varies with the altitude. A few studies have looked into the effect of these parameters on the pollution dispersion process.

Steffens et al. [46] tested the effect of wind speed (doubling and halving) on the flow characteristics as well as (non-dimensional) pollutant concentrations. It was found that decreasing the wind speed increased the concentrations, by decreasing the rate at which the tracers could be transported away and vice versa. It would be expected that the non-dimensional concentrations are independent of the flow speed (for reasonably high Reynolds numbers). However, the discrepancies were attributed to a possible imperfect simulation of the neutrally stratified ABL and additional edge effects, which causes secondary recirculations. Similar minor discrepancies were observed by Steffens et al. [47], which were attributed to static on-road turbulence introduced in their numerical model by adding stationary blocks to simulate vehicle induced turbulence.

As the incident flow angle increases, the dispersion of pollution is dominated by flow channeling rather than flow recirculation resulting in larger on-road concentrations, as observed by Steffens et al. [46] and Pournazeri and Princevac [45]. The effect of the wind angle of attack on velocity contours and plume dispersion is illustrated in Figure 2.16 and Figure 2.17 respectively.

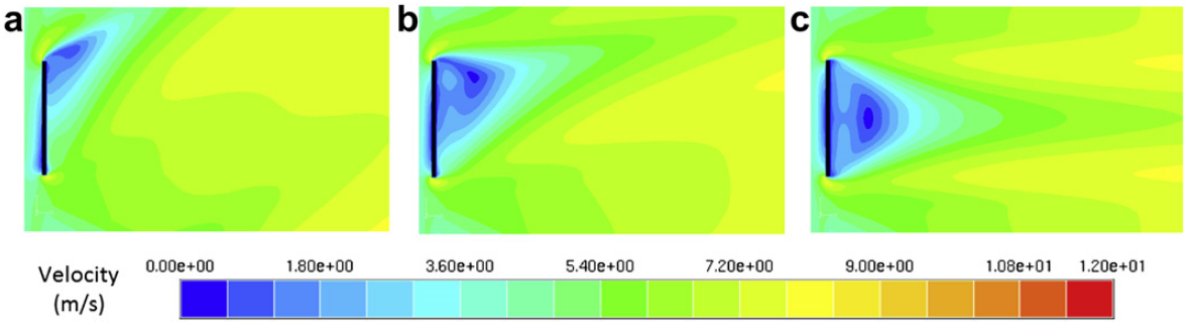

Figure 2.16: Velocity contours for different incoming flow angles. Scenarios: (a) 30°, (b) 14° and (c) 0°. Figure reproduced from Steffens et al. [46].

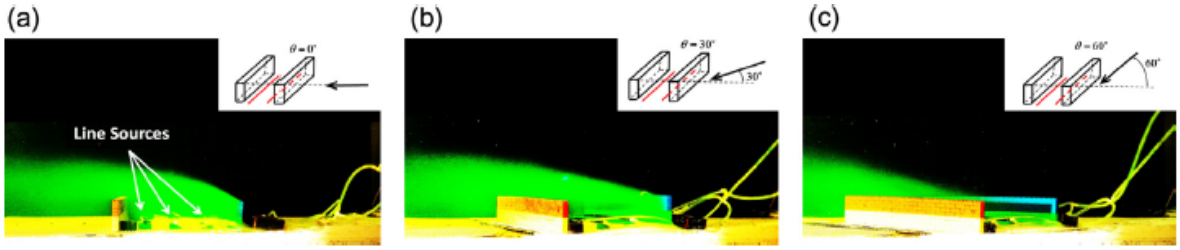

Figure 2.17: Plume visualization for different wind angles. Scenarios: (a) 0°, (b) 30° and (c) 60°. Figure reproduced from Pournazeri and Princevac [45].

2.2.7. Effect of traffic induced turbulence

For the interested reader, a comprehensive review on the effect of traffic induced turbulence is given by Ahmad et al. [48]. Scaling down of traffic induced turbulence is often performed by maintaining the ratio between energy production due to traffic and energy production by the wind. This is based on the similarity criterion proposed by Plate [49]. Traffic induced turbulence is often modeled by mounting small blocks or plates on a rotating belt as shown in Figure 2.12.

Eskridge and Rao [50] found that local wind flows inside street canyons are greatly affected by moving vehicles i.e. traffic induced turbulence. Under 'calm' wind conditions (<1 m/s), the vehicle induced turbulence would also contribute significantly to the pollution dispersion. Exhaust buoyancy is expected to be an important factor too, but in street canyons, its effect becomes negligible due to the vehicle induced turbulence, as postulated by Isyumov [51]. For modeling purposes, according to Isyumov and Ramsay [52], the source strength can also be exaggerated without altering the flow environment or the mixing process.

Kastner-Klein et al. [53] demonstrated the effect of traffic induced turbulence under different traffic arrangements on the pollutant concentrations. This is illustrated in Figure 2.18. For the cases with no traffic and two-way traffic, a symmetric distribution of concentrations with a maximum at the centerplane were observed. The decay towards the canyon edges is due to the ventilation at the outlets. The slightly lower concentrations for the two-way traffic is due to the additional diffusion of the pollutants due to traffic induced turbulence. For the one-way traffic configuration, the vehicle induced motion plays a dominant role in creating a skewed concentration field through a strong piston effect.

Kastner-Klein et al. [53] also reported the additional effect of turbulence induced by different traffic configurations on the mean velocity and velocity fluctuations. The one-way traffic is shown to have a significant effect on the lateral mean velocity component, which is the driving factor for the aforementioned piston effect. Other factors, including increasing traffic velocity and increasing traffic density, showed a reduction in on-road pollution, as reported by Kastner-Klein et al. [54].

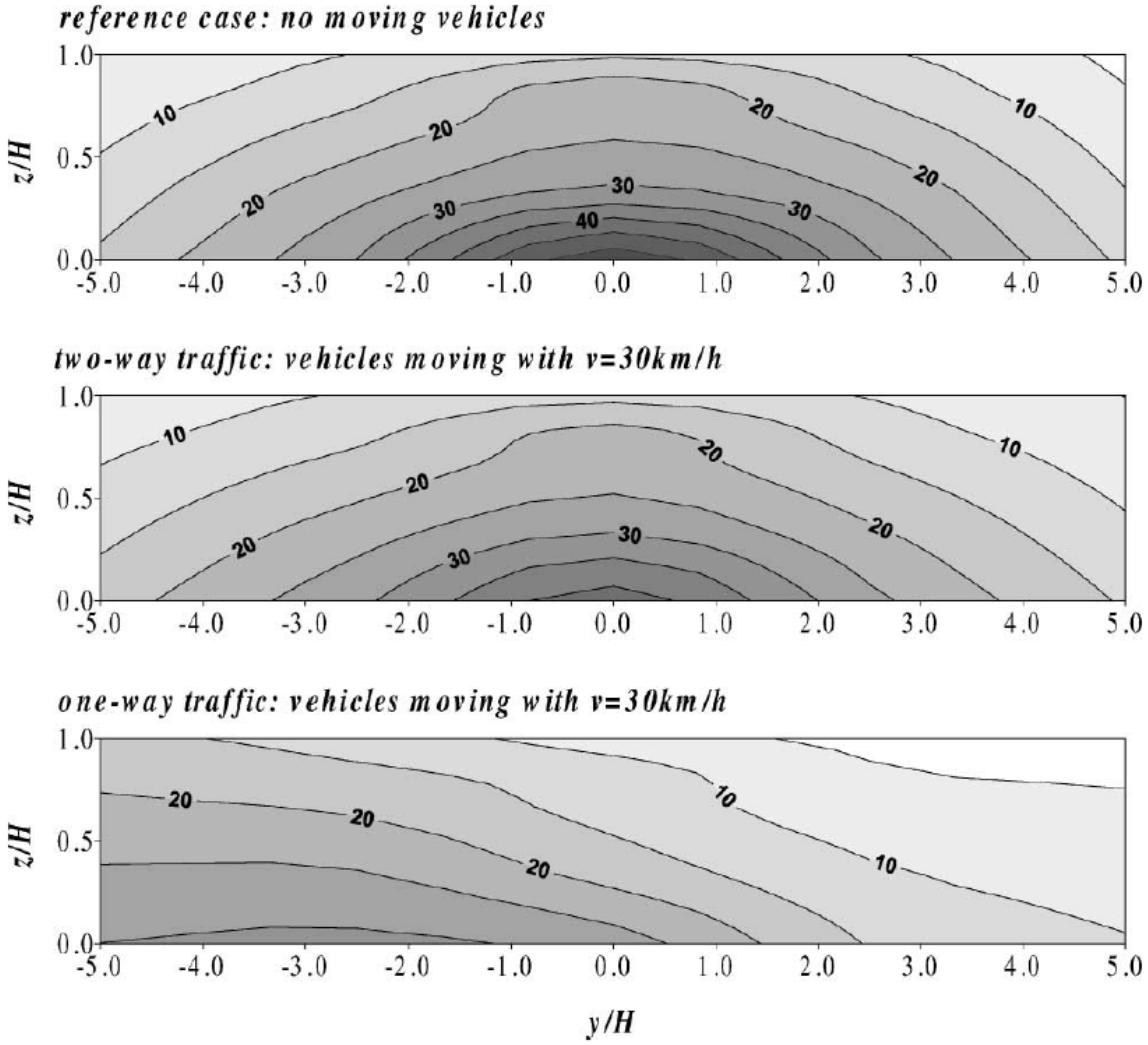

Figure 2.18: Effect of different traffic configurations on pollution dispersion in a street canyon. Contours of normalized concentrations are shown in the spanwise-wall-normal plane at the leeward wall of the street canyon. Figure reproduced from Kastner-Klein et al. [53].

2.3. Similarity satisfaction

Using non-dimensional numbers is a widespread practice in the field of Fluid Mechanics. It helps to understand the contribution of a certain physical quantity relative to another. Two flow fields are considered similar if all the relevant non-dimensional numbers are equal. In order to avoid the complexity of performing expensive real-scale measurements, selection of scaled (down) experiments to study a certain phenomenon is a commonly used approach as discussed previously in Section 1.3.

Scarano [55] gives a brief overview on flow similarity and three levels of flow field similarity can be distinguished. The first is geometric similarity, wherein every ratio of geometric lengths in the model and prototype is the same. The second is kinematic similarity wherein similarity for time-related quantities such as velocities and accelerations need to be maintained as well. The third consideration is dynamic similarity where the flow mass distribution must be similar, which involves forces. In the framework of the current project, a fourth requirement is the similarity satisfaction between the concentration of the passive scalar, the fluorescent dye, and the actual amount of emitted PM in reality.

Besides these, certain (non-dimensional) boundary conditions need to be considered too. The different boundary conditions mentioned by Meroney [56] include surface boundary conditions (for example, similarity of roughness distributions, surface temperature distributions etc.), approach-flow

characteristics and similar conditions aloft (for example, location of the upper streamline).

2.3.1. Atmospheric Boundary Layer

The atmospheric flow close to the ground is often modeled by a turbulent boundary layer flow over a flat plate. The major difference between the two, as noted by Armitt and Counihan [57], include the variation in wind direction as well as temperature with changing altitude, both of which can have major implications in the process of pollution dispersion. In most experimental studies, the study is often restricted to neutral ABLs.

The flow in the ABL can be characterized by the following: (a) Mean velocity distribution as a function of altitude (b) Turbulence intensities as a function of altitude (c) Integral scales of turbulence (d) Micro-scales of turbulence (energy dissipation scale) (e) Reynolds stress components and (f) Spectra of turbulence.

Hunt and Fernholz [58] summarize the various techniques utilized to simulate ABLs (with and without thermal stratification) in a wind tunnel. Snyder [59] hints that the first two moments of velocity, temperature distributions and the boundary layer heights must correspond reasonably well with the geometrical scale ratio, for a good model.

2.3.2. Pollution dispersion in the atmosphere

The current project is associated with modeling the phenomenon of air pollution dispersion. A comprehensive review on the similarity criteria for this application has been given by Snyder [59] which is the source for large portions of the content in this subsection.

Snyder [59] identifies the Rossby (ratio of inertial to Coriolis forces), Froude (ratio of fluid inertial forces to external force field, such as gravity or reduced gravity for buoyancy driven flows), Reynolds (ratio of fluid inertial to viscous forces), heat transfer and mass transfer Peclet numbers (ratio between transfer by advection to transfer by diffusion) as decisive factors for the dispersion of a passive contaminant. Other important non-dimensional numbers noted by Meroney [56] include the Euler (ratio between pressure and flow inertial forces), Richardson (ratio between buoyancy and flow shear terms), Prandtl (ratio between viscous diffusion rate and thermal diffusion rate), Schmidt (ratio between viscous and molecular diffusion rate) and Eckert (ratio between flow kinetic energy and boundary layer enthalpy difference) numbers. Not all of these numbers are independent of each other, as it will be seen later in this subsection.

It is impossible to simultaneously satisfy all the non-dimensional numbers and models must satisfy similarity partially or at least, approximately. The relevant non-dimensional numbers are selected based on the application.

The effect of Rossby number is negligible for cases simulating terrains with length scales smaller than 5 km as postulated by Snyder [59]. The Euler number can be easily simulated when air is used as the working fluid. The effect of Richardson number can be neglected when neglecting atmospheric thermal stratification. Eckert number effects can also be considered negligible as its value is small compared to unity for subsonic flows.

Prandtl and Schmidt numbers are fluid, not flow, properties, and are automatically satisfied when using air as a working fluid. The Prandtl number criterion can be easily satisfied with air since this quantity does not vary strongly with temperature. However, with water, the Prandtl number is already about ten times larger than with air, and it varies rather greatly with temperature. Similarly, the Schmidt number can be easily modeled with air as a medium. The Schmidt number for most gases in air is one while for salts/dyes in water it can be in the order of hundreds or thousands. Thus, strict similarity for Prandtl and Schmidt numbers will be difficult to satisfy using water.

The heat and mass transfer Peclet numbers are the product of Reynolds number with the Prandtl and Schmidt numbers respectively. The problem with matching these Peclet number stems not much from the Prandtl and Schmidt numbers, but from Reynolds number.

Heat and mass are considered as passive scalar contaminants. For flows with sufficiently high Reynolds numbers, the main structure of the turbulence will be responsible for the transport of these

scalars. Since turbulent diffusion dominates over molecular diffusion, the urge for matching the Peclet numbers, the Prandtl number and the Schmidt number is unnecessary. Thus, both air and water can be used as working media from the modeling perspective.

The Reynolds number is the most abused criterion in models of atmospheric flows, as noted by Snyder [59]. Scale reductions usually result in model Reynolds numbers a few orders of magnitude smaller than in the atmosphere. If Reynolds similarity were to be set as a strict requirement, almost no atmospheric flow could be modeled.

One of the most regularly used justification for the goodness of scaled down experiments is the Reynolds number independence criterion (when ignoring thermal and Coriolis effects). This hypothesis put forth by Townsend [60] stated "geometrically similar flows are similar at all sufficiently high Reynolds number". This alleviates the burden of having equal Reynolds number. Based on results from grid-generated turbulence, Snyder [59] states that "integral scales reduce with the first power of the geometrical scale ratio (as desired), whereas Kolmogoroff microscales reduce with only the one-fourth power of the geometrical scale ratio". Majority of the pollutant dispersion would be governed by the larger scales and less by the microscales, at least for long and intermediate travel times.

Based on results obtained by Castro [32], the commonly used threshold for the Reynolds number independence is 5000. Here, the Reynolds number is based on the surface-mounted object height and the freestream velocity. This number is based on results for cubes oriented normally to the incoming turbulent boundary layer flow and the pollutant source located at the ground level near the obstacle.

The Froude number represents the ratio between inertial and buoyancy forces. A large Froude number indicates negligible buoyancy forces and thermal effects become important when this number approaches unity. The Froude number can be considered as the inverse square root of a Richardson number as shown by Batchelor [61]. It is also related to the Monin-Obukhov length (the height at which turbulence generated by buoyancy equals that generated by wind shear) defined by Monin and Obukhov [62].

Tominaga and Stathopoulos [63] state that it is difficult to satisfy the Froude and Reynolds number criterion simultaneously. In case of buoyant emissions, the Froude number gets the priority. The parameters to be satisfied while modeling buoyant emissions include, as noted by Tominaga and Stathopoulos [63], the pollutant emitting area, the Froude number of the emission gases, the density ratio of the gases and the emission speed ratio.

Jensen [64] also recommends scaling the roughness length, if it can be estimated for the prototype. All elements smaller than the roughness length have very little effect on the overall flow and need not be modeled. The above criterion, Jensen's criterion, can be abandoned for large scale reductions, as justified by Snyder [59].

The flow near a wall is dominated by the viscous stresses in a thin viscous sublayer and is dependent on the Reynolds number. If the surface has irregularities, larger than the viscous sublayer that would have existed on an otherwise smooth surface, the viscous stresses become negligible. This happens because the irregularities behave as bluff bodies and the resistance is dominated by the pressure difference across the irregularities instead of viscous stresses. Such a surface is called aerodynamically rough and the flow over it is independent of the Reynolds number. Sutton [65] prescribes that the Reynolds number based on the friction velocity and roughness length be more than 2.5 for the surface to be aerodynamically rough. Most atmospheric flows are almost always aerodynamically rough.

Finally, it can also be concluded that, both, air and water can be used as working fluids. Each has its pros and cons. One of the advantages of using water is that for the same Reynolds number and characteristic length scales, the velocities are scaled down by a factor of almost 15, which is useful. In addition, water is more suitable for studying buoyant emissions. Finally, performing PLIF measurements is more convenient in a water facility. Performing PLIF in air would add the complication of dealing with and safely discarding tracer gases (such as Sulphur hexafloride, SF_6) which may be harmful if inhaled in excess.

3

Scaling down the Open Air Line ESP

As explained in Chapter 1, a scaled simulation of the pollutant dispersion will be performed in a water channel. Most of the experimental components in the current investigation are either borrowed or slightly modified from those used by Eisma [14]. New to this setup is the addition of the scaled model of the ESP and the associated traverse mechanism.

The working of a typical ESP is briefly introduced first in Section 3.1. Next, the procedure to design the scaled model of the ESP is presented in Section 3.2.

3.1. The chronicles of the Open Air Line ESP

Before proceeding to the scaling of the ESP model, it is interesting to learn more about the device as well as associated investigations in the past. The majority of the content in this section is borrowed from the article by Alfonsi et al. [11]. This article is a result of the work initiated by the erstwhile Oranjewoud (presently, the Antea group) on reducing UFPs with ESPs.

The etymology of the device name “Open Air Line ESP” can be explained as follows. The “Line” comes from the fact that the ESPs are meant to be installed in a line on top of SBs next to highways. Typically, ESPs are utilized in industries placed in conduits subject to a forced flow of air. In contrast, when installed along highways, i.e. in “Open Air”, this setting does not exist and hence, the ESP must be designed differently.

3.1.1. Working principle of a typical industrial ESP

A typical ESP design utilized in the industry is the so called wire-plate ESP, illustrated in Figure 3.1. This is generally composed of grounded parallel plates forming a duct through which the polluted air flows. Between these plates lie thin wires that are highly charged, usually with a negative voltage (50 kV is a ballpark value).

The high voltage in the wire causes nearby gas molecules to lose an electron and transform into a positive ion. This phenomenon is known as the Corona discharge. These electrons follow the electric field lines between the wire and the grounded plates. Upon encountering a dust particle in its path, the free electron gets attached to it, making it negatively charged. These charged dust particles too are accelerated by the electric field and obtain a steady state velocity, known as the drift velocity. An example of the path lines followed by the dust particles is shown in Figure 3.2. Finally, these charged dust particles get attached to the grounded plates via Van der Waals force and this way, the incoming air is cleaned off the pollutants.

The collection efficiency of the ESP is defined as the ratio between the particle mass collected to that entering the ESP. It is strongly dependent on the particle diameter and the electric fields strength.

Two forces act on these charged dust particles within the ESP duct, far away from the wires. The first is the electric force which is directly proportional to the charge of the dust and the electric field

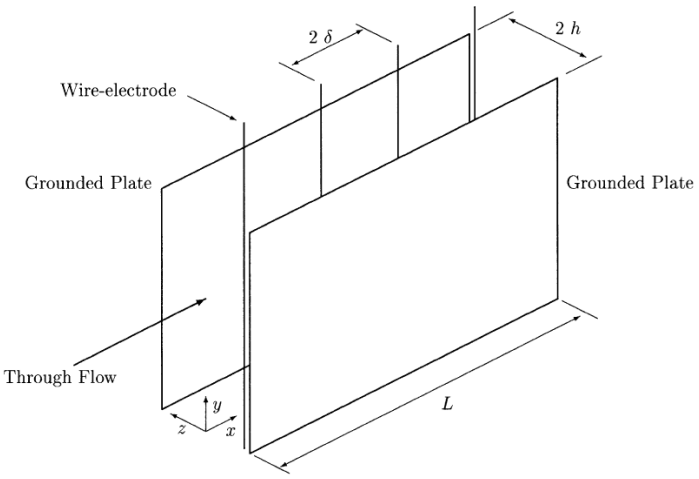

Figure 3.1: Schematic of a wire-plate electrostatic precipitator. L is the duct length, $2h$ is the duct width and 2δ is the wire to wire spacing. Image reproduced from Soldati [18].

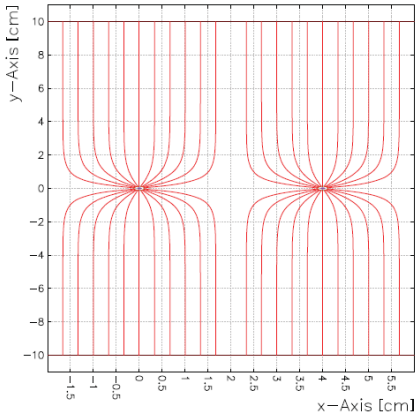

Figure 3.2: Sketch of a single stage ESP. The red lines show the path of the positive ions produced in the high field region towards the collection plates. The wires possess a positive voltage. Figure reproduced from Alfonsi et al. [11].

strength. The second is the effective drag force experienced by particles moving through a viscous fluid, and can be evaluated using Stokes' law.

The charged particles then attain the so called migration velocity which is the steady-state velocity component perpendicular to the plate surface. The largest particles experience a larger electric force charge while the smallest particles experience very little drag and these particles will attain a relatively high migration velocity. In contrast, particles whose diameters are of the order of the mean free path of the gas ions experience a drop in the migration velocity.

3.1.2. The Open Air ESP

Industrial ESPs are subjected to forced flow of air, allowing for a construction providing relatively high flow resistance. In comparison, the Open Air ESP to be installed along highways must provide as little flow resistance as possible in order to maximize the flow rate of the UFPs through it. An optimization for the open air installation is to have wires installed in square grids in place of parallel plates.

The design parameters of these grids include the wire diameter, the wire pitch and the porosity of the mesh. For minimizing the flow resistance, the mesh needs to have maximal porosity and minimal wire diameter. However, such changes would reduce the collection efficiency of the ESP, thus necessitating a compromise.

According to Alfonsi et al. [11], the pressure drop over a conventional industrial ESP with plates of dimensions 1×1 m^2, separated by 0.5 m, is estimated to be 3 N/m^2. On top of this, accounting for the external casing and components such as supporting beams, the total flow resistance of such an ESP is approximately 4 N/m^2. The pressure drop over a wire screen with a wire diameter of 1 mm and a pitch of 2 cm, the pressure drop is estimated as 1.7 N/m^2. Assuming a supporting structure similar to that of an industrial ESP, the total pressure drop is approximately 2.7 N/m^2. This represents a theoretical improvement of 32% with respect to the conventional ESP model.

3.1.3. Previous aerodynamic investigations on the presence of an ESP

Results of preliminary experiments and simulations on the aerodynamics around ESPs have been presented by Alfonsi et al. [11]. These ESPs are installed atop SBs which form a highway canyon. The Reynolds number based on the free stream velocity and the SB height was maintained above 5000, for the experiments, while the sound barriers formed a k-type roughness. In a k-type roughness, eddy

shedding from the cavity to the freestream flow is present in contrast with the d-type roughness. This is illustrated in Figure 3.3. This is similar to the different flow regimes in street canyons illustrated in Figure 2.8. The channel width to height ratio is set as 5 for these studies.

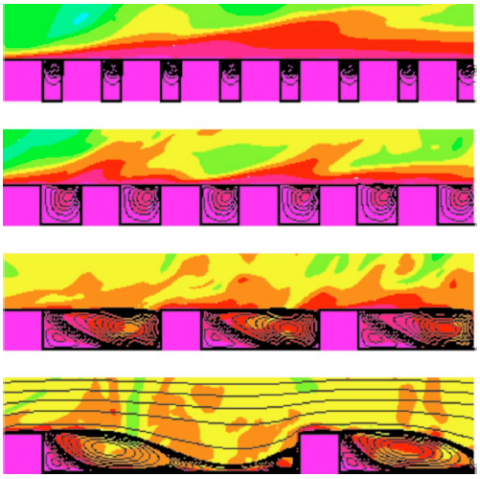

Figure 3.3: Flow profiles for different surface roughness patterns. Instantaneous passive scalar contours are superimposed on mean streamlines. Different roughness pitch to height ratios from top to bottom: 0.5, 1, 3, 7. Figure reproduced from Leonardi et al. [66].

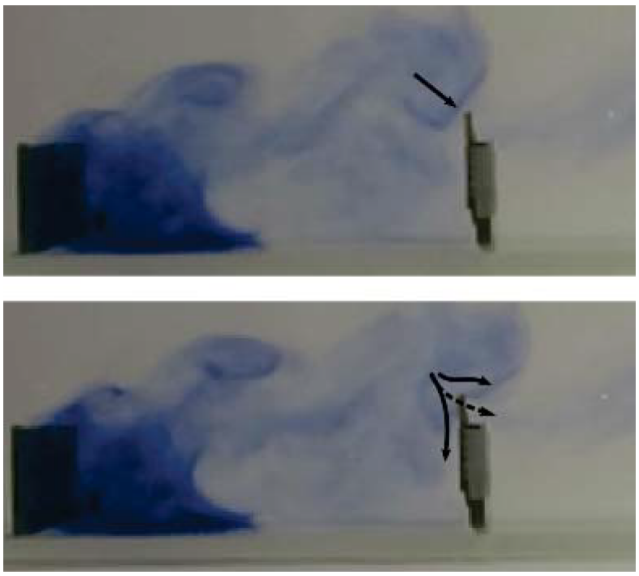

Figure 3.4: Flow visualization investigating the effect of an ESP installed on top of the downwind sound barrier. Figure reproduced from Alfonsi et al. [11].

Flow visualization experiments

Three different cases were studied through flow visualization experiments: No ESP on the SBs, a vertical ESP on one SB and a larger sloping ESP on the SB. The experiments were performed in a flow tunnel with the SB modeled by a 2 cm high obstruction and the ESP with a coarse grid. Ink was injected by a dropper at relevant positions to model the diffusion of pollutants.

With plain barriers, the “street canyon flow”, described in Section 2.2, is observed. The ESP was modeled with a messing grid with a wire diameter of 0.75 mm and wire spacing of 2 mm. The porosity of such a grid is larger than that of a well-designed ESP. This semi-permeable structure was then mounted on top of the impermeable SB. The effect of the ESP is shown in two consecutive recorded image frames in Figure 3.4. A filament of ink approaches the ESP with only a small fraction of it passing through. This happens despite the relatively high porosity of the grid, illustrating the importance of low flow resistance. In other words, the addition of an ESP providing higher flow resistance, creates a canyon with a higher effective height.

Figure 3.5: Flow visualization investigating the effect of overhanging ESPs installed on top of the sound barriers. Figure reproduced from Alfonsi et al. [11].

The final set of experiments were performed with overhanging ESPs. It is expected to provide a few benefits. Firstly, it reduces the region where mixing between the clean and the polluted air takes place. Secondly, the sloping ESP helps contain the pollutants to the highway as it escapes from the

downwind ESP. Lastly, the larger effective frontal area of the ESP also improves the efficiency. This is illustrated in Figure 3.5 where a large portion of the pollutant travels through the downstream ESP.

Large Eddy Simulations

In addition to experiments, numerical simulations using DALES-urban, which solves Large-Eddy equations for incompressible fluids, were performed by Alfonsi et al. [11]. Neutral thermal stratification was assumed and the effect of traffic induced turbulence was neglected. The fine dust was modeled as a passive tracer (neutrally buoyant, advects with the flow and no chemical reactions). Two line sources of constant mass flux were added to the domain to simulate emission from the traffic. The Reynolds number based on the SB height and the mean free-stream velocity was 3300.

Simulations for flow over two SBs, as illustrated in Figure 2.6, show the presence of a large recirculation area between the two SBs, which suggests that mounting an ESP close to the upwind SB might be an effective measure to capture the UFPs.

To investigate this further, simulations were also performed with a "pollutant capture" sink in the domain which captures pollutants whenever they passed through this small volume, while not influencing the flow. The results in Figure 3.6 show a visible decrease in concentration levels in the downstream direction. This capture volume has a length of 0.42*h* and height of 0.33*h*, where *h* is the SB height. This sink improves air quality by 27% and 13%, for the upstream and downstream source respectively, at the location of the downstream SB.

Table 3.1: Maximum efficiency of pollutant capture for an ESP mounted on the downstream sound barrier. *h* is the height of the sound barrier. η_{sL} and η_{sR} are the percentage of emitted concentrations captured from the upstream and downstream source respectively. Data obtained from Alfonsi et al. [11].

ESP Height	η_{sL}	η_{sR}
0.25*h*	11%	12%
0.50*h*	26%	28%
0.75*h*	41%	43%
1.00*h*	60%	62%

The maximum efficiency of mounting an additional ESP on the downstream SB was also computed. Different ESP heights were considered and the results are tabulated in Table 3.1.

Increasing the Reynolds number fourfold, was found not to affect the large scale structures. In contrast, the mass flux through the sink near the upstream SB doubles, improving the efficiency to 47% and 28% for the upstream and downstream source respectively. However, the efficiency of capturing the UFPs at the downstream SB is unaffected and the efficiency is expected to be just as the data in Table 3.1.

3.2. Design of the scaled down ESP

While designing the scaled model of the ESP, several similarities must be respected. The ESP has two major partitions, the outer casing and the inner structure. The outer casing is designed mainly with the geometric similarity and flow regime in mind, while the internal structure is designed so as to replicate the drag coefficient expected for the actual Open Air Line ESP.

3.2.1. Outer Casing

Model dimensions of a prototype of the Open Air Line ESP are available in the technical drawings provided by the Antea group [67]. While scaling down the prototype, the aspect ratio of the lengths should be maintained.

The height of the ESP model in the wall-normal direction is chosen as 10 mm. This value is selected on the basis of Figure 1.5. The plume width at the location of the SB is approximately 25% of the SB heights. The SB heights to be used for the current investigation range from 10 mm to 50 mm. This results in an plume width of 2.5 mm - 12.5 mm, which the ESP should capture. Thus, the height of the ESP model is chosen as 10 mm, which is comparable to the plume width. The length of the model in the streamwise direction, while maintaining an aspect ratio of length:height of 1.16, is chosen as 11.6

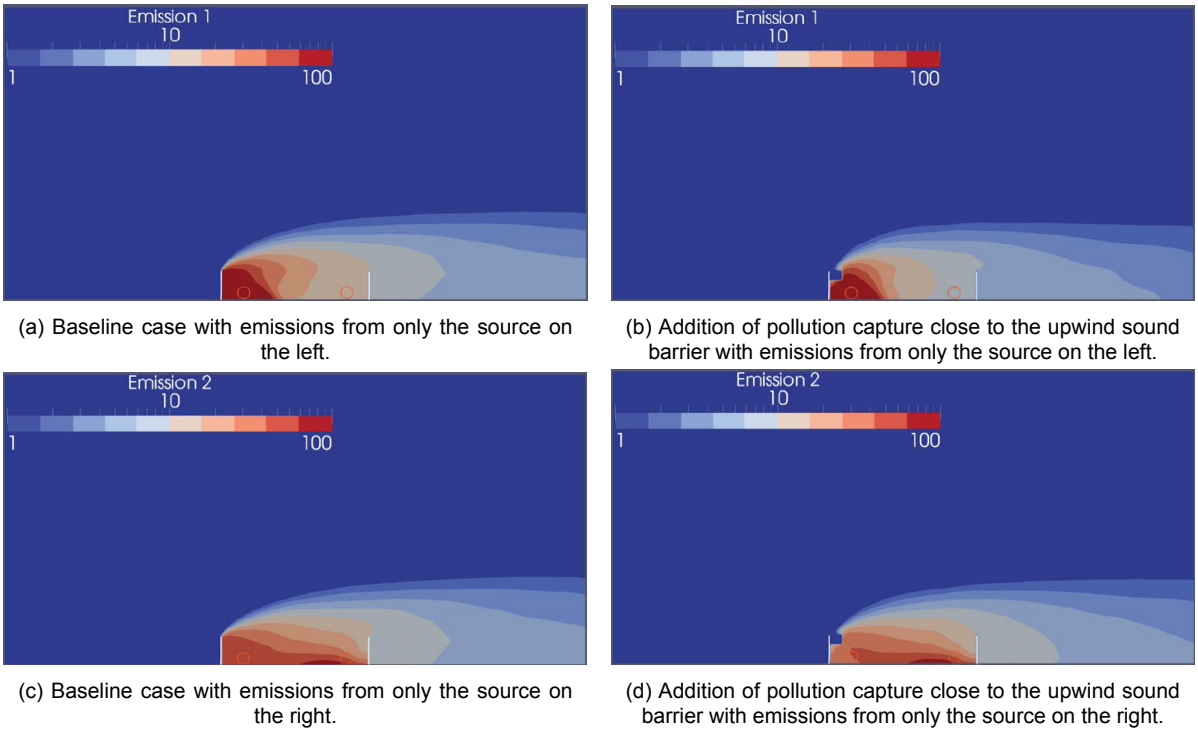

(a) Baseline case with emissions from only the source on the left.

(b) Addition of pollution capture close to the upwind sound barrier with emissions from only the source on the left.

(c) Baseline case with emissions from only the source on the right.

(d) Addition of pollution capture close to the upwind sound barrier with emissions from only the source on the right.

Figure 3.6: Large Eddy Simulation results investigating the impact of the presence of a pollutant catcher near the upwind sound barrier. The orange circles represent source locations. Figure reproduced from Alfonsi et al. [11].

mm. The width of a single model ESP, while maintaining the aspect ratio between width and height of 2.74, would be 27.4 mm. But, in reality, an isolated ESP would not be installed along the highways, hence the width of the model ESP along the spanwise direction is chosen as 191.8 mm (as if 7 ESPs are kept adjacent to each other in a single line).

Geometric similarity

Besides the ESP, the other characteristic lengths involved in the flow are that of the model SB and the simulated ABL. These length scales need to be as realistic as possible.

The height of the urban ABL varies between 100 and 1000 m, as reported by Davies et al. [68] for the ABL height at an airfield located close to a suburban area with two-storey buildings. This might be representative of the rural-urban fringes which are being targeted in the current study. The expected ABL height in the water tunnel is approximately 20 cm, based on the study by Eisma [14].

Heights of actual SBs installed by the Dutch highways have typical heights ranging from 4-7 m, while model Aluminum fences used by Eisma [14] ranged from 1-3 cm in height.

Table 3.2: Geometric similarity between the SB and the ABL. h_{SB} is the height of the SB, while h_{ABL} is the height of the ABL.

Real/Model	h_{SB} [m]	h_{ABL} [m]	$\frac{h_{SB}}{h_{ABL}}$
Real	4	100-1000	0.004-0.04
	7	100-1000	0.007-0.07
Model	0.01	0.2	0.05
	0.03	0.2	0.15
	0.05	0.2	0.25

Table 3.3: Geometric similarity between the ESP and the ABL. h_{ESP} is the height of the ESP, while h_{ABL} is the height of the ABL.

Real/Model	h_{ESP} [m]	h_{ABL} [m]	$\frac{h_{ESP}}{h_{ABL}}$
Real	0.74	100-1000	0.00074-0.0074
Model	0.01	0.2	0.05

Table 3.4: Geometric similarity between the ESP and the SB. h_{ESP} is the height of the ESP, while h_{SB} is the height of the SB.

Real/Model	h_{ESP} [m]	h_{SB} [m]	$\frac{h_{ESP}}{h_{SB}}$
Real	0.74	4	0.185
	0.74	7	0.106
Model	0.01	0.01	1
	0.01	0.03	0.333
	0.01	0.05	0.2

The conditions for geometric similarity between various combinations of the SB, ABL and the ESP are summarized in Tables 3.2 to 3.4. The ABL is intermittent in nature and it is preferable to have the SB and the ESP within the turbulent region of the ABL. A good criterion would be for the SB and ESP to lie within 40% of the ABL height.

From Table 3.2, it is observed that all model SBs would lie within 40% of the ABL height, but the SB of 1 cm would come closest in satisfying the geometric similarity criterion. Similarly, from Table 3.3, it is seen that the ESP model will also lie within 40% of the ABL height, regardless of which model SB is deployed. Lastly, from Table 3.4, it is concluded that the model SB of height 5 cm will come closest to satisfying the ESP-SB similarity, especially when compared to the real SB of 4 m.

Reynolds number similarity

Another criterion to be satisfied is that the Reynolds number for the model ESP should correspond to the same flow regime as for the Reynolds number for the actual ESP. The Reynolds number for the actual ESP, based on its height and mean wind velocity, is approximately 1.5×10^5, assuming a wind velocity of 3 m/s in the atmosphere, while the Reynolds number for the model ESP in the water tunnel is approximately 7500, assuming the free stream velocity to be 0.75 m/s. Both these numbers would rise upon considering the height of the SB it is mounted upon. Since both these cases lie in the the regime where Reynolds number ($\geq$5000) effects on the flow over sharp-edged obstacles are considerably small, as per Castro [32], the Reynolds number criterion can be considered satisfied.

3.2.2. Pressure drop estimation

In order to replicate the performance of the actual ESP, the internal structure of the model ESP must be such that the drag coefficients of the two are nearly identical. In order to simplify the calculation of the drag on the ESP, it is assumed that, at the inlet, there is a uniform velocity profile along the surface perpendicular to the flow. This way, the drag coefficient becomes equal to the pressure drop coefficient, as shown later in Section 5.1.1, which simplifies the estimation. However, information about the pressure drop across the Open Air Line ESP must be known. Since this data was unavailable at the time of designing the actual ESP, an estimate of the pressure drop was made.

The Open Air Line ESP is composed of several components, including 15 square meshes, separated from each other by 120 mm, constructed from cylindrical wires with a diameter of 4 mm. These meshes are aligned in a manner such that one set of 19 vertical cylindrical wires lie in the cross-flow configuration

while the other orthogonal set of 18 cylindrical wires lie in the longitudinal flow configuration. These meshes are symmetric with a pitch of 40 mm. For a first order estimation of the pressure drop, other components such as the side plates, support pillars and other wires (96 wires with 0.5 mm diameter) are neglected.

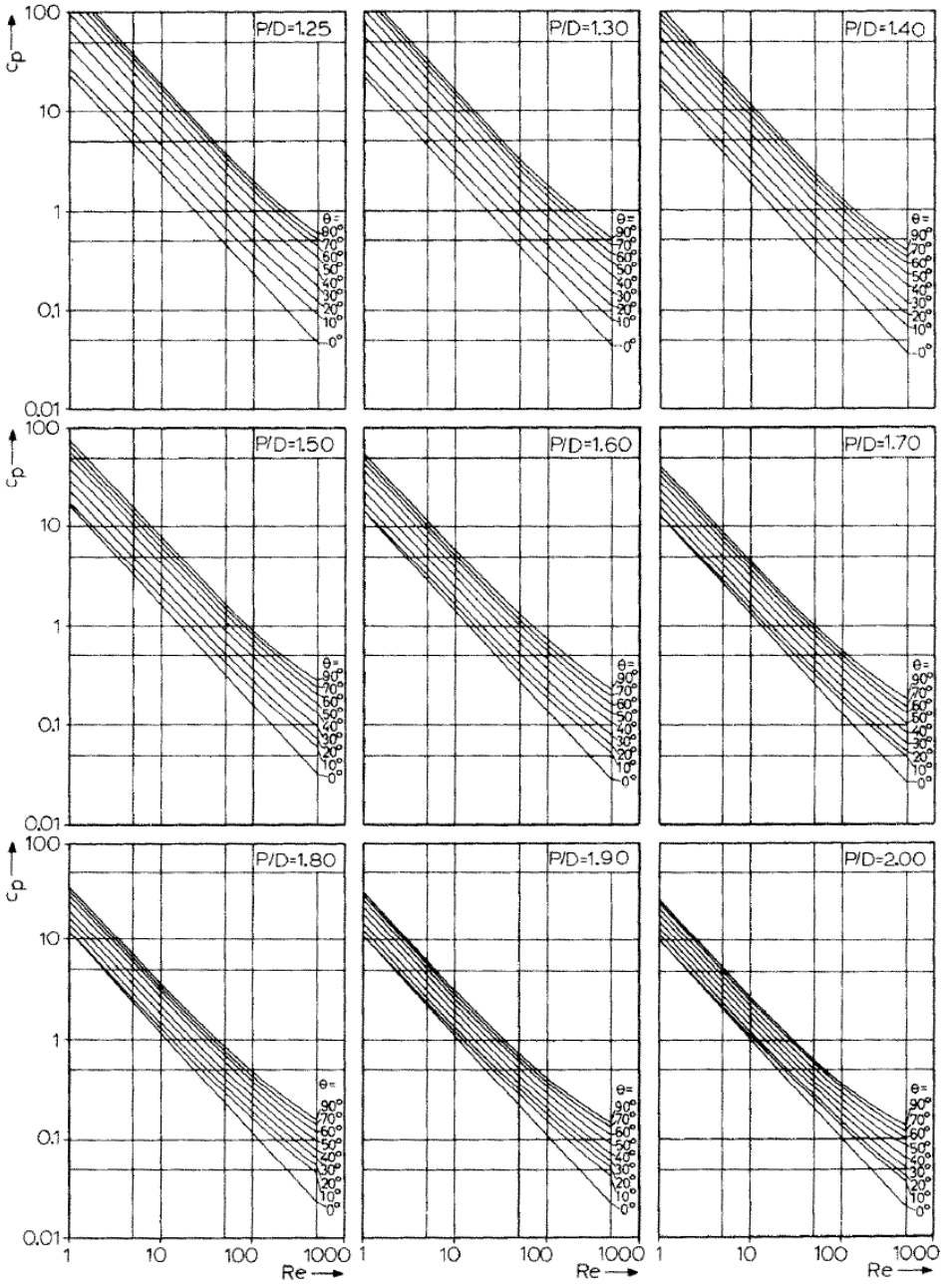

Figure 3.7: Pressure drop coefficient (c_P) vs Reynolds number (Re) with the inclination angle θ as a parameter for laminar, oblique, fully-developed flow through in-line square assemblies of tubes with pitch-to-diameter ratio P/D = 1.25-2.00. $\theta = 90°$ corresponds to the cross-flow configuration while $\theta = 0°$ corresponds to the longitudinal flow configuration. Figure reproduced from Antonopoulos [69].

Roach [70] formulated empirical correlations between pressure drops and mesh design parameters, for meshes lying in a plane normal to the flow direction, which is not applicable to the current case. To the best of the authors knowledge, no data on pressure drop across a mesh for a flow configuration akin to the current case is available.

A first assumption to simplify the analysis is to neglect those cylindrical wires lying in the longitudinal flow configuration. This is a reasonable assumption based on the results obtained by Antonopoulos [69], for oblique flow through in-line tube assemblies. The pressure drop coefficients for longitudinal flow configurations are up to an order of magnitude lower than for the cross-flow configurations as illustrated in Figure 3.7. This could be attributed to frictional drag dominating the pressure drag for the former case.

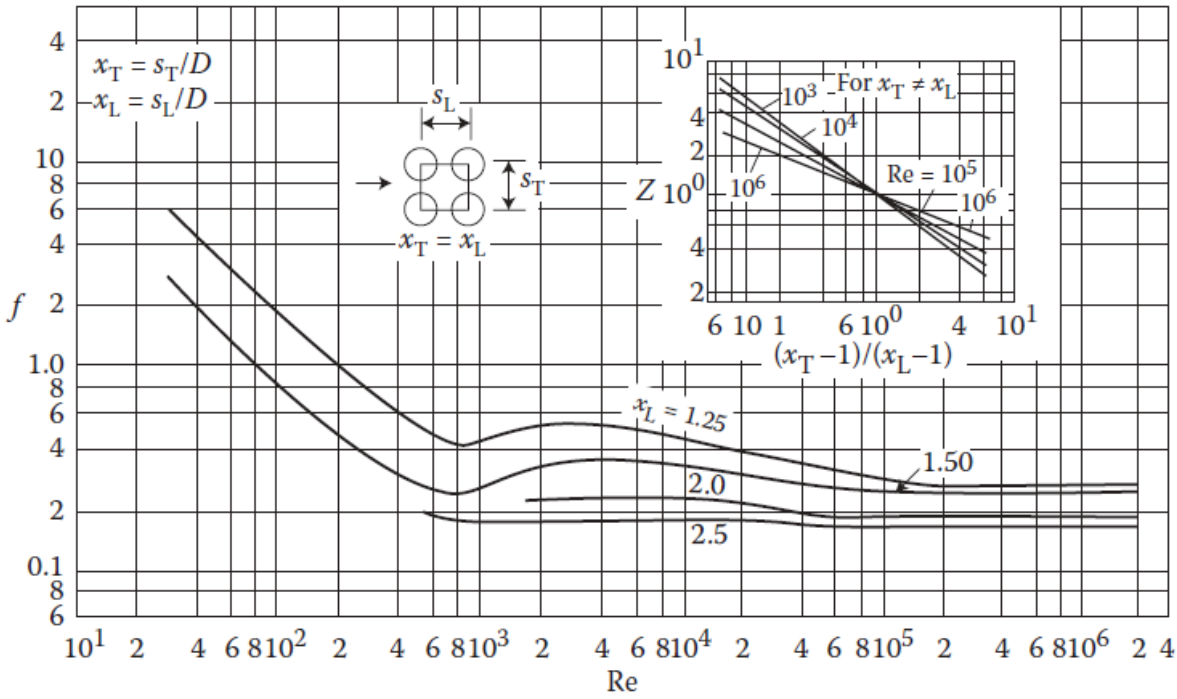

Figure 3.8: Friction factor (f) and the array design associated correction factor (Z) as a function of Reynolds number (Re) and array symmetry ((x_T-1)/(x_L-1)) for use in Equation (3.1) for an in-line tube arrangement. s_T and s_L are the transverse and longitudinal pitches respectively while D is the diameter of the tubes in the bank. Figure reproduced from Todreas and Kazimi [71].

One approach to determine the pressure drop across the mesh (after neglecting the wires in the longitudinal flow configuration) would be to use the pressure drop correlations proposed by Žukauskas [72] for in-line tube bundle arrangements.

The chart in Figure 3.8 provides correlations for the friction factor (f) and the array structure associated correction factor (Z) as a function of the Reynolds number (Re) and the array symmetry. For N rows of tubes/wires in the flow direction and a maximum mass flux of $G_{\max}$, for a fluid with density ρ, the pressure drop (Δp) can be estimated by:

$$\Delta p = f \frac{N G_{\max}^2}{2\rho} Z \tag{3.1}$$

The design parameters are the wire/rod diameter (D) as well as the pitches, in the transverse (s_T) and longitudinal (s_L) direction. Furthermore, x_T is the wire diameter normalized transverse pitch, while x_L is the wire diameter normalized longitudinal pitch. The Reynolds number is defined as $Re = G_{\max} D/\mu$, where μ is the dynamic viscosity of the fluid.

For the wire arrangement in the Open Air Line ESP, D is 4 mm, s_T is 120 mm, while s_L is 40 mm. This results in a value for x_L of 10. Thus, the charts in Figure 3.8 are inapplicable to the current case since the correlations for x_L are available only till a maximum of 2.5. It is not possible to extrapolate from the curves either, necessitating a different approach.

The next approach to simplifying the pressure drop estimation is isolating and analyzing independently each row of cylindrical wires located in a plane whose normal is aligned in the streamwise direction.

This is a reasonable assumption since x_L is 10 which means that the longitudinal pitch is relatively much larger than the wire diameter. This implies that the wires do not lie in the wake of the adjacent upstream cylindrical wires.

This situation is better illustrated in Figure 3.9. For the case with the longitudinal pitch of $6D$, the flow characteristics of the second cylinder seem independent of that of the first cylinder, while this is not so for arrangements with longitudinal pitches of $3D$ and $1.6D$.

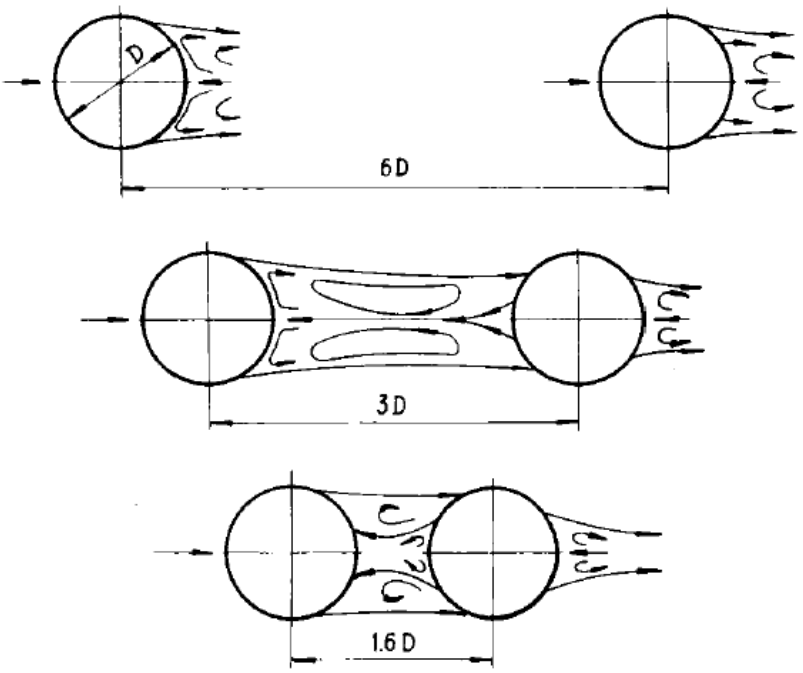

Figure 3.9: Flow past a tube in a longitudinal row. Figure reproduced from Žukauskas [72].

Roach [70] proposed a correlation for pressure drop Δp across a grid of parallel rods in incompressible flow with the correlation given in Equation (3.2).

$$\frac{\Delta p}{q} = A\left(\frac{1}{\beta^2} - 1\right)^B \tag{3.2}$$

Here, q is the upstream dynamic pressure and β is the grid porosity. The grid porosity for an arrangement of parallel rods (like in Figure 3.10a) can be defined as $\beta = 1 - d/M$, where d is the rod diameter, while M is the mesh pitch. A and B are functions of Reynolds number, Mach number and grid geometry. The pressure loss factor A, for a grid of parallel circular rods, was found to be dependent on the Reynolds number as shown in Figure 3.10b. The curve fit is expressed as: $A = 14/Re$ for $Re < 10$; $A = 0.52 + 66/Re^{4/3}$ for $40 < Re < 10^5$. For such a setup, B is 1.

For a single row of wires in the cross-flow configuration in the Open Air Line ESP, d is 4 mm and M is 120 mm. The Reynolds number, Re, for the flow of air past a single wire of 4 mm diameter, assuming a mean velocity of 3 m/s, is approximately 800. The net pressure drop, based on Equation (3.2), accounting equally for all 19 rows in the longitudinal direction, is estimated to be 1.89 Pa. An upstream dynamic pressure of 5.5 Pa implies a drag coefficient of 0.343.

In the above analysis, the cross-sectional area is based on the frontal area occupied by the cylindrical wires. Upon accounting for the entire cross-sectional area of the ESP, the corrected drag coefficient of the Open Air Line ESP, in a mean velocity of 3 m/s, is estimated to be 0.244.

To validate the above drag coefficient, a third approach is also used. Since, both, the transverse and longitudinal pitches are significantly larger than the wire diameter, an estimate of the drag coefficient of the entire ESP can be made by isolating a single cylinder.

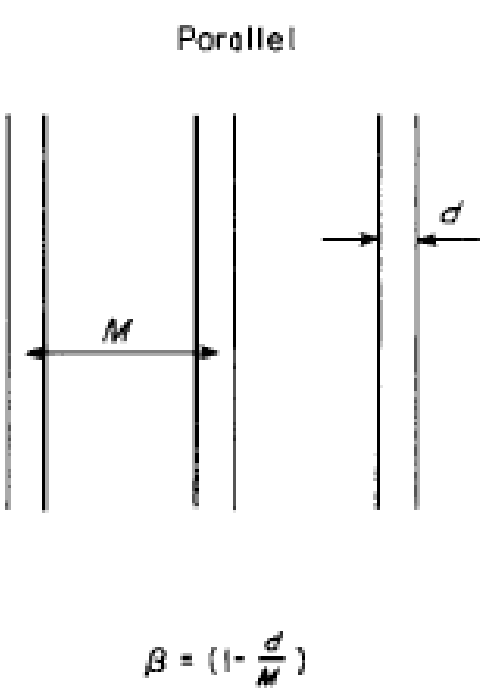

(a) Schematic of a grid of parallel rods. d is the rod diameter. M is the grid pitch. β is the grid porosity.

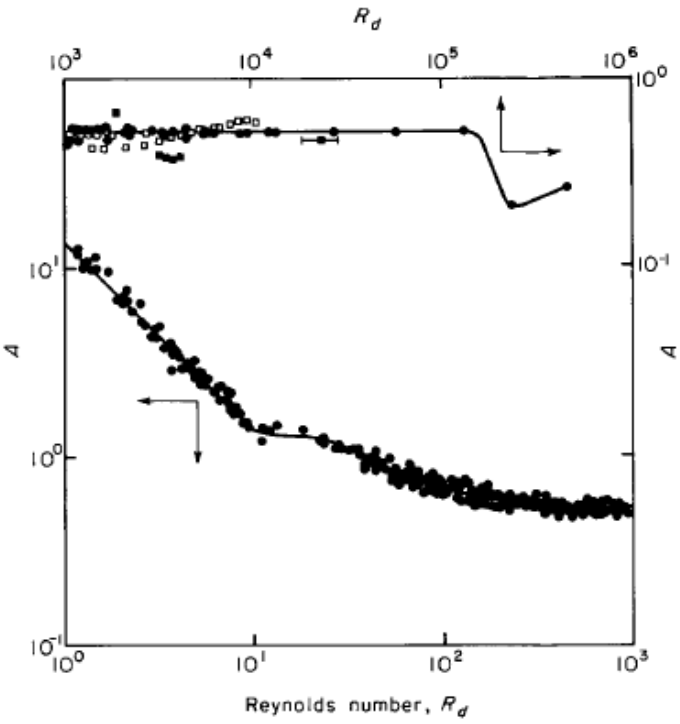

(b) Reynolds number (R_d) dependence of pressure loss factor A in Equation (3.2) for a grid of parallel rods.

Figure 3.10: Pressure drop in a grid of parallel rods. Figure reproduced from Roach [70].

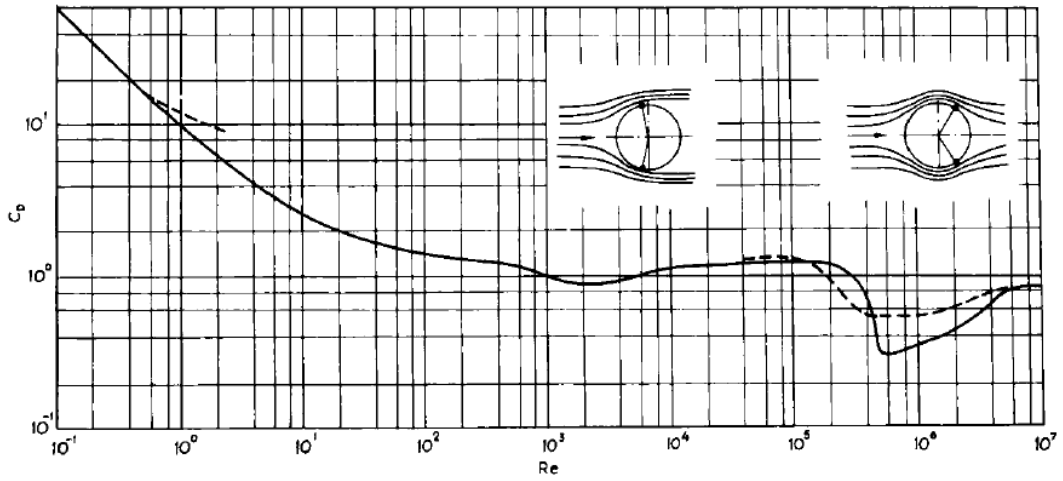

Figure 3.11: Drag coefficient of a tube as a function of Reynolds number. Figure reproduced from Žukauskas [72].

The drag coefficient of a single, circular, infinite cylinder based on Figure 3.11, is approximately 1 at a Reynolds number of 800. If this value is corrected to account for the entire ESP frontal area as compared to only the cylinder frontal area, the value now becomes 0.711. This value lies in the same order of magnitude as the previously calculated drag coefficient. It also represents an upper limit on the drag coefficient for the ESP since it neglects the presence of the neighboring cylinders.

In fact, the aforementioned drag coefficient of 0.244 might also be an overestimation. This is because the final rows of cylinders will experience a lower drag since there has already been a drop in the pressure due to the upstream row of cylinders. On top of this, the presence of an external casing

is expected to increase the drag coefficient. Nonetheless, the objective of the above calculations was to get a ballpark estimate of the pressure drop coefficient for the ESP, which has been achieved.

3.2.3. Inner Structure

The internal area of the model ESP is composed of an array of in-line cylindrical wires. These are arranged in a manner to generate pressure drop to replicate the previously estimated drag coefficient of 0.244.

While it is not extremely important, it is preferable for the wires in the model ESP to lie in a flow regime similar to the mesh wires in the actual ESP. The mesh wire associated Reynolds number was calculated as 800, where the wake is turbulent/transitional in nature. Thus, the wire diameter in the model ESP to operate in the water tunnel is selected as 1 mm to have a Reynolds number of approximately 800 (assuming a velocity of 0.75 m/s).

One more consideration is the alignment of the cylinders with respect to the coordinate system. The cylinders can be aligned either in the spanwise direction or in the wall-normal direction. In the former configuration, the spacing between the cylinders and the walls would become an additional design constraint. This is not the case for the latter. In addition, the latter is also more suitable for structural reasons, and is hence selected.

Following this, the structure of the wire packing needs to be determined. This can be done by either utilizing the correlations in Figure 3.8 in combination with Equation (3.1) or through Equation (3.2).

In the first approach, a value of x_L must be selected from the available options in Figure 3.8. The drag coefficient is a product of the friction factor (f), the array symmetry associated correction factor (Z) and the number of rows of cylinders in the flow direction (N). f and Z can be selected from the charts in Figure 3.8. N can then be chosen accordingly while bearing in mind that the upper limit on N is determined by the longitudinal pitch (s_L) and the length of the model ESP in the streamwise direction.

The second approach utilizes Equation (3.2) while also maintaining a relatively large x_L of at least 6. This ascertains that a row of cylinders does not lie in the wake of the upstream one and then each row of cylinders can be treated independently with Equation (3.2).

Table 3.5: Details of the internal structure of the proposed ESP model designs illustrated in Figure 3.12. N_L and N_T are the number of rows of wires in the longitudinal and transverse directions, respectively. c_D is the estimated drag coefficient.

Design	x_L	x_T	N_L	N_T	c_D
1	2.5	10	5	19	0.25
2	2.5	8.5	4	23	0.24
3	1.5	4	4	48	0.24
4	6	10.2	2	19	0.244

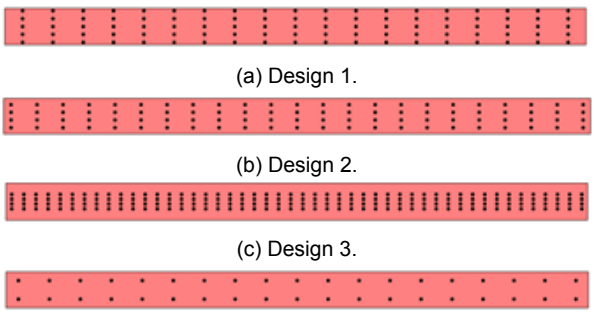

(a) Design 1.

(b) Design 2.

(c) Design 3.

(d) Design 4.

Figure 3.12: Top views of the internal structure of the model ESP. Details of the designs are in Table 3.5. The black circles are the cylindrical wires and flow is in the vertical direction.

Four designs were proposed for the internal structure of the model ESP based on these two methods. Top views of the designs are illustrated in Figure 3.12, while details of the geometry and estimated drag coefficient are presented in Table 3.5.

Designs 1 through 3 are based on the first approach while design 4 is based on the second one. Designs 1 and 4 have a very similar structure in the transverse direction, but the number of wires in the longitudinal direction are 5 and 2 respectively. Despite this, both are expected to perform similarly in terms of the drag coefficient. This can be justified by the use of different approaches in computing the

drag coefficient.

Design 1 is selected for ease of manufacturing and subsequent experimentation. Practicality is an important aspect to consider while choosing a design, which rules out Design 3 due to the thick density of 1 mm thin diameter wires. Designs 1 and 2 are quite similar in construct. In case the drag coefficient of the model ESP with Design 1 is overmuch, a row of wires can be eliminated. It is easier to destroy than to create!

3.2.4. The actual scaled prototype

In the previous subsections, the design of the scaled model was discussed from a theoretical perspective. The dimensions of the actual developed model is slightly different from the proposed theoretical model. The outer casing is built using plexiglass while the cylindrical wires of 1 mm are made of stainless steel. The plexiglass casing has a thickness of 3 mm. In addition, 20 rows of cylinders are present in the transverse direction instead of 19. The overall dimensions of the scaled model is 17.54×200.0×11.71 mm^3. Various views of the model are shown in Figures 3.13a to 3.13d.

In addition to the ESP model, a traverse, shown in Figure 3.13e, was also constructed. This traverse is mounted atop the water tunnel and is intended to provide one translational and two rotational degrees of freedom. The traverse beam holding the ESP model is approximately 1.2 cm thick, is located approximately 5.0 cm on one side of the center, while the cylindrical rod is approximately 6.0 cm behind the trailing edge of the ESP.

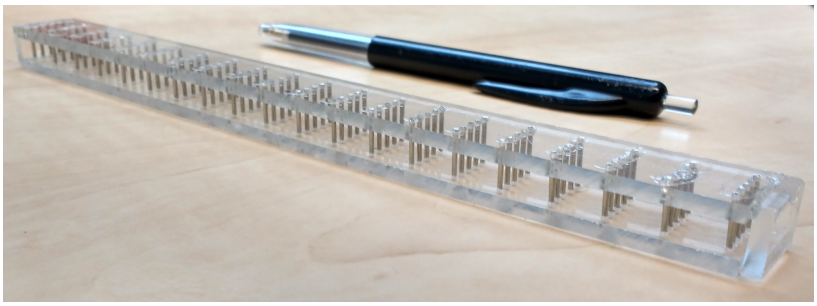

(a) Isometric view.

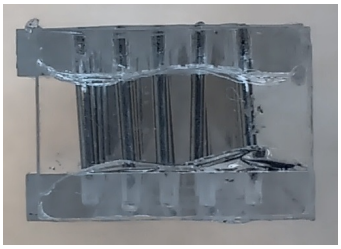

(b) Side View.

(c) Top view.

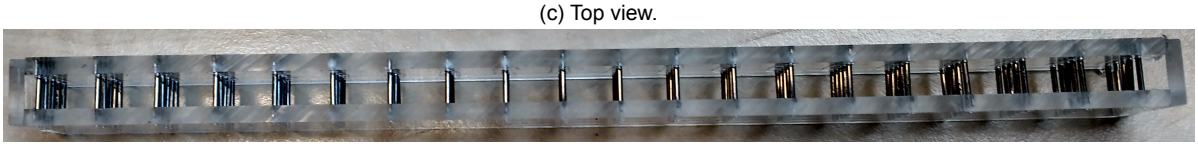

(d) Front View.

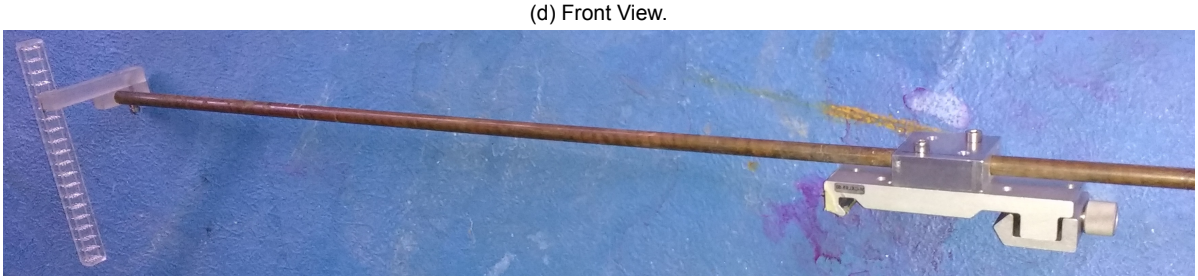

(e) Traverse for the model ESP.

Figure 3.13: The scaled ESP model used for the experiments.

4

Anatomy of the experimental setup

The different components of the experimental techniques utilized are described in this chapter. Firstly, a short description of the water channel is provided in Section 4.1. This is followed by a brief description of the boundary layers along the walls of the water tunnel in Section 4.2. Finally, the working mechanisms and the several components of different measurement techniques utilized in this project, i.e. pitot-static tube, PIV, PLIF are provided in Section 4.3, Section 4.4 and Section 4.5 respectively. The reader interested in the practical application of these measurement techniques may refer to Appendix B.

4.1. The water tunnel

The flow facility utilized for the study was a recirculating, closed-loop water tunnel at the Laboratory for Aero- and Hydrodynamics. It is bounded by plexiglass panes allowing for optical diagnostic applications. It was constructed by Engineering Laboratory Design and was commissioned in 2004. The water tunnel can be seen in Figure 4.1.

The test section has a cross-sectional area of 60 $\times$ 60 cm^2 and a length of 500 cm. The inlet is preceded by a set of honey-comb meshes, wired screens, perforated plates (all arranged in a decreasing order of coarseness) and a contraction of 6:1 to ensure a homogeneous flow with low turbulence intensities enters the test section. The maximum flow speed at the inlet is 1 m/s with turbulence intensities of less than 1%. The total volume of water that can be contained is 11 m^3 and the water is pumped with a pump running at 22.4 kW.

The rotational frequency of the pump motor can be controlled by a manual keypad, which indirectly determines the flow speed in the water tunnel. The frequency ranges from 0-55 Hz. The water tunnel is also equipped with a flow meter, which displays the volumetric flow rate averaged over the last 3 seconds. The volumetric flow rate ($\dot{Q}$ in m^3/h) is a function of the pump rotational frequency (f in Hz) and voltage (V in V) according to:

$$\dot{Q} = 22.88f - 6.22 \qquad \dot{Q} = 327.14V - 325.56 \tag{4.1}$$

For all the experiments, the water level was set at approximately 63.0 cm from the bottom of the channel. Decreasing or increasing the water level too much from this level, might lead to the generation of relatively large waves, which are undesirable. In the former scenario, the incoming flow being detached from the walls may be a source for the waves. In the latter, a large recirculation region is formed just above and downstream of the inlet, which acts as a source for the waves.

Since the water tunnel is relatively long, it is comprised of two separate sections, which are welded together. This welded area is often problematic and may be subject to leaks, especially on cold, wintry days. This is because the low temperatures leads to the welded area to contract, and subsequently leak. Thus, it is recommended that not only a water collection facility (for example, a large tub) be kept at hand, but also the room temperature be kept high.

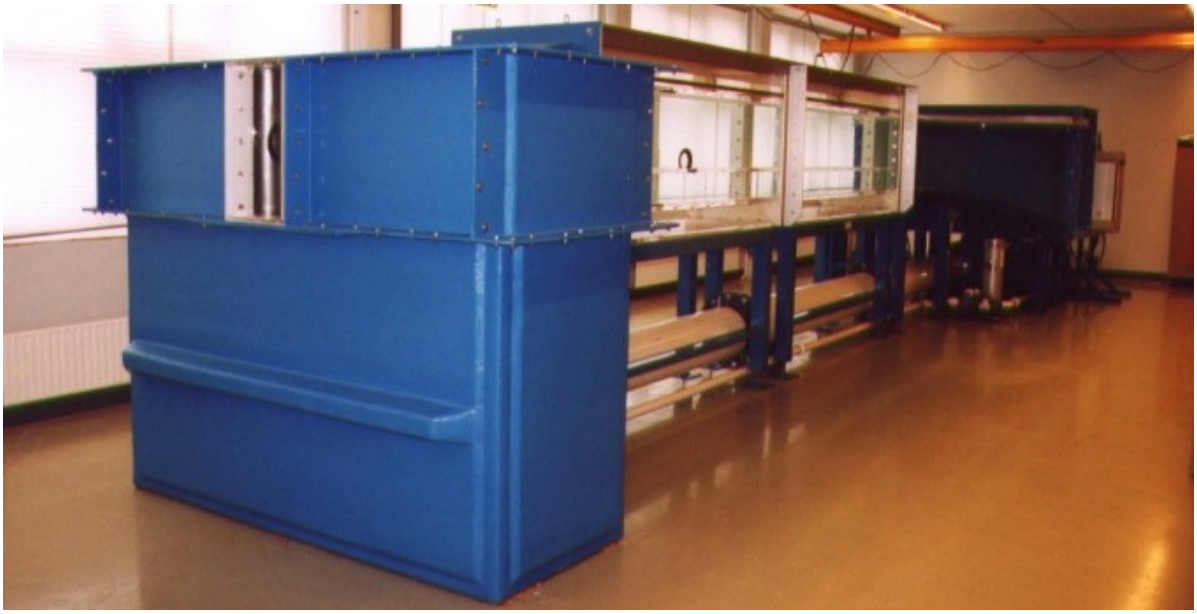

Figure 4.1: The water tunnel facility. Image reproduced from the website of Engineering Laboratory Design Inc [73].

4.2. Boundary layer development in the water tunnel

The current experimental setup includes components that affect the development of a boundary layer along the walls of the water tunnel. In Section 4.2.1, the boundary layer development along the side walls is discussed followed by the method used to simulate a scaled ABL along the bottom walls in Section 4.2.2.

4.2.1. Side Walls

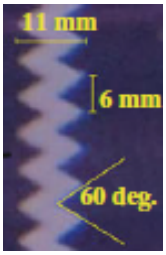

Figure 4.2: Details of the zigzag trip on the side walls of the water tunnel. Image reproduced from Elsinga and Westerweel [74].

Table 4.1: Summary of the boundary layer properties 3.5 m downstream of the zigzag trip. Data reproduced from Eisma [14].

Free-stream velocity (U_∞)	0.73 m/s
Boundary layer thickness (δ_{99})	74 mm
Displacement thickness (δ^*)	11.3 mm
Momentum thickness (θ)	8.7 mm
Friction velocity (u_τ)	26.5 mm/s
Momentum thickness based Reynolds number (Re_θ)	6578
Friction velocity based Reynolds number (Re_τ)	2053
Shape factor ($H = \delta^*/\theta$)	1.31
Skin friction coefficient (c_f)	2.7×10^{-3}

The side walls of the water tunnel are equipped with zigzag shaped boundary layer trips glued approximately 24 cm downstream of the water channel inlet. Boundary layer trips force the flow from a laminar to turbulent state. As noted by Elsinga and Westerweel [74], this is performed to fix the point of transition, to prevent laminar separation bubbles from appearing and to reduce the drag of bluff bodies at certain Reynolds numbers. Tripping of the boundary layer can be performed by attaching a passive roughness element to the wall, among other techniques. In this category, the zigzag strip is the most efficient and has a much smaller height in comparison with other forms of roughness elements.

The zigzag boundary layer trip, along with its important dimensions, is shown in Figure 4.2. Results of boundary layer measurements performed by Eisma [14], approximately 3.5 m downstream of this boundary layer trip, at a free stream velocity of 0.73 m/s, are summarized in Table 4.1. By forming a boundary layer along all walls, including the side walls, the effective velocity along the centerline of the water channel is raised. The growth of the boundary layers along the walls also introduces a pressure gradient. Furthermore, the side wall boundary layers also reduce the region of spanwise uniform flow.

4.2.2. Bottom Wall

In order to simulate a scaled ABL in the water channel, the setup developed by Eisma [14] was utilized. A false floor, with dimensions 4.5×0.6 m^2, is mounted 0.17 cm above the bottom of the water channel. Since the false bottom is much closer to the central plane of the contraction outlet, the incoming flow can be expected to be more homogeneous and contain fewer disturbances. In addition, installations (by drilling holes) can be made without causing any permanent damage to the water channel.

Of the several techniques available to generate the scaled ABL (such as active grids, spires or through surface mounted roughness), the combination of a fence and triangular spires is used. The design of the triangular spires is based on the recommendations of Irwin [75] to develop a ABL with a thickness (δ_{99}) of 20 cm and an exponent of the power-law velocity profile (α) of 0.1 in accordance with Equation (4.2).

$$\frac{U}{U_\infty} = \left(\frac{z}{\delta_{99}}\right)^{\alpha} \tag{4.2}$$

The spires are installed approximately 42 cm downstream of the sharp leading edge of the ground plate. An additional fence with a height of 2 cm is placed approximately 12 cm upstream of the spires which generate an additional momentum deficit at the start of the boundary layer. A schematic of the spires and the setup generating the scaled ABL can be seen in Figure 4.3 and Figure 4.4 respectively.

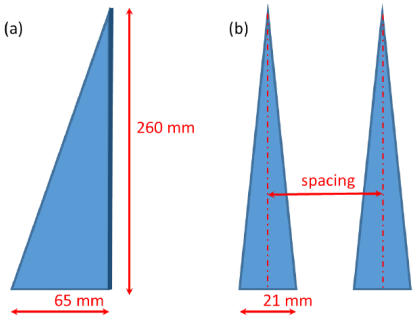

Figure 4.3: Schematic of the installed spires. (a) Side view (b) Front view. Figure reproduced from Eisma [14].

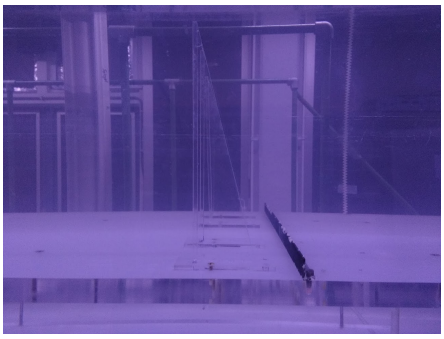

Figure 4.4: Setup of the triangular spires and fence in the upstream section of the water channel to develop the scaled ABL.

The characteristics of the incoming scaled ABL are described later in Section 5.2. The spanwise layout, in mm, between the four spires used in the current study was 65-130-190-120-110. The first and last numbers represent the distance between the spires next to the wall and the wall itself. This layout is different compared to the one used by Eisma [14] (105-110-170-110-105). While the spanwise variation in the mean velocity has not been investigated in the current study, Eisma [14] observed a spanwise inhomogeneity of 7.5%.

4.3. Pitot Tube - setup and specifications

Pitot-static tubes have been utilized to measure the pressure drop across the model ESP. A brief overview about its working principle and practical guidelines concerning this measurement technique,

in the context of the current project, is presented in this section. The working principle of the pitot-static tube is first described in Section 4.3.1. Information about the different components in the setup is provided in Section 4.3.2.

4.3.1. Working principle of a Pitot-static tube

The pitot-static tube is a commonly used device to measure the velocity of a flow. Klopfenstein Jr [76] has provided a basic description of the working principle of the pitot tube. The pitot tube is used in conjunction with a differential pressure measurement device (usually a pressure transducer, which is an electromechanical device) which returns the dynamic pressure, i.e. the difference between the total pressure and the static pressure.

The basic pitot tube is L-shaped with two pressure ports located on the top, as shown in Figure 4.5a, which are eventually connected to the pressure transducer. The bottom consists of the sensing tip, which is aligned in the flow direction. These sensing tips can have several designs as illustrated in Figure 4.5b. The different tip designs are attempts at reducing the errors in the static pressure readings caused by the flow moving over the tube.

Also seen in Figure 4.5b is the coaxial tubing present in the pitot tube. The inner tubing transmits information from the sensing tip to the total pressure port, while the outer tubing connects the static pressure taps to the static pressure port.

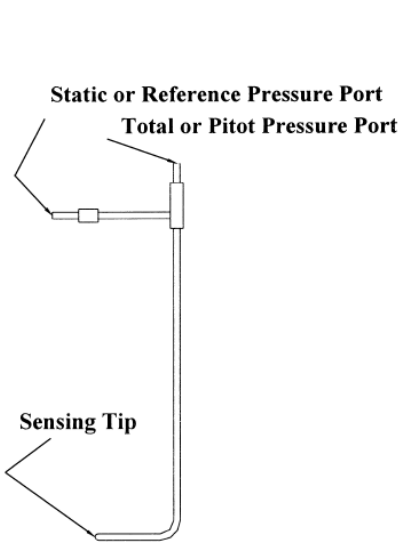

(a) Construction of a pitot tube.

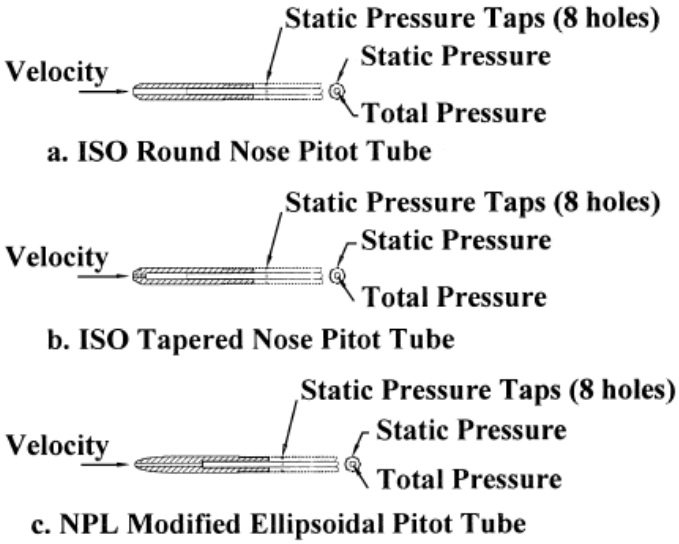

(b) Sensing tip designs of a pitot tube.

Figure 4.5: Schematic of a pitot tube. Figures reproduced from Klopfenstein Jr [76].

The velocity of the flow is computed using a simple correlation between the dynamic pressure and the local velocity. The total pressure (p_t) is the sum of the static pressure (p_s) and the dynamic pressure ($\frac{1}{2}\rho V^2$). For a fluid with density ρ, the velocity is given by $V = \sqrt{\frac{2(p_t - p_s)}{\rho}}$.

4.3.2. Components of the Pitot tube measurement system

As stated in Section 4.3.1, the central components of the pitot tube measurement system include the pitot tube itself and the pressure transducer. Other components include the signal conditioner, which feeds the signal into the computer via a data acquisition system for further processing. A custom LabVIEW program has been developed, which can not only be used for recording the flow velocity by the pitot tube, but also the flow rate in the water tunnel and temperature of the water.

Figure 4.6: The pitot-static tube in the water tunnel.

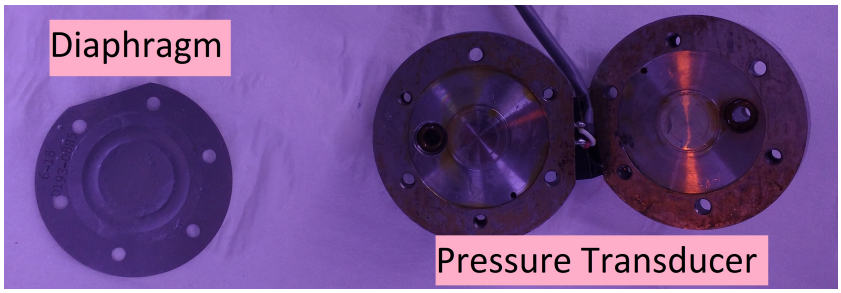

Figure 4.7: The differential pressure transducer and the diaphragm.

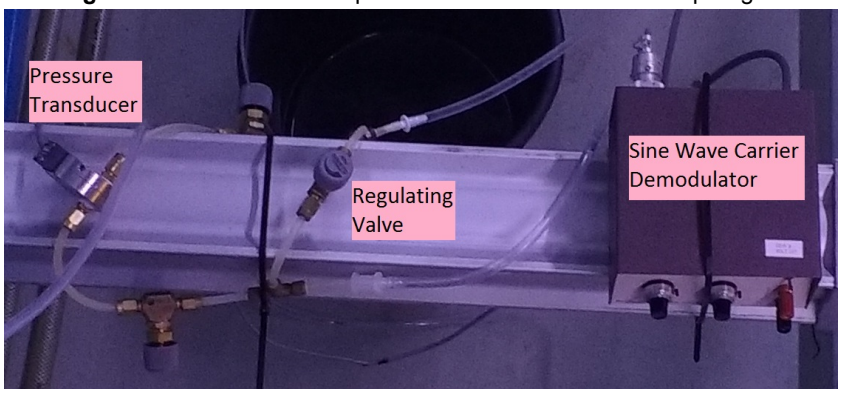

Figure 4.8: The differential pressure transducer and the signal conditioner.

The pitot tube used in the current project has a nose diameter of approximately 10 mm with a sensing tip length of approximately 42 mm. The static pressure taps are 18.5 mm downstream from the total pressure tap. The pitot tube and the associated traverse is shown in Figure 4.6.

The pressure ports are connected to the ends of a differential pressure transducer, via transparent tubing. The Validyne DP45 very low differential pressure transducer is utilized for this purpose. The pressure transducer is used in tandem with a diaphragm that senses the differential pressure across its sides. These are shown in Figure 4.7. Since it is known that the maximum operating speed of the water tunnel is 1 m/s, corresponding to a dynamic pressure of approximately 500 Pa (or 5.10 cm H_2O), the diaphragm -18 was selected, which has a pressure range of upto 5.6 cm H_2O. The ends of the pressure transducer are then connected to a CD15 Sine Wave Carrier Demodulator, which acts as a signal conditioner. The pressure transducer and the diaphragm are shown in Figure 4.8.

Data acquisition is performed via a National Instruments USB-6008, shown in Figure 4.9, which is compatible with LabVIEW. Besides the voltage difference across the pressure transducer, volumetric flow rate in the water channel as well as the water temperature is acquired via a flow meter and a thermocouple respectively. Thermocouple type K6, made of Nickel-Chromium/Nickel-Aluminium (NiCr/NiAl) is used for this purpose. It was calibrated so as to have linear variation of 0.1 V/°C between 0-100°C Readings from the thermocouple are extremely sensitive to nearby electrical disturbances and the signal is hence, low pass filtered. Data acquisition for further analysis can be controlled via a custom-made LabVIEW program. The sampling rate can be controlled via this program and 100 Hz is selected for current measurements.

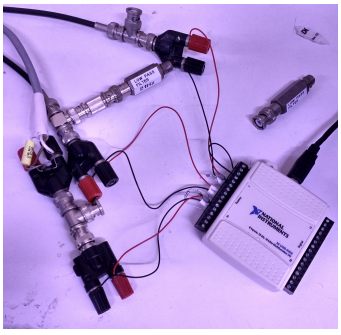

Figure 4.9: The data acquisition system.

4.4. Particle Image Velocimetry (PIV) - setup and specifications

Planar PIV has been utilized to measure the velocity of the flow around the SB and the ESP. A brief overview about its working principle and the specifications of its various components are presented in this section. In Section 4.4.1, a brief overview of the working principle of the measurement technique is provided. The different components of the PIV setup are listed in Section 4.4.2.

4.4.1. Working principle of Particle Image Velocimetry

PIV is a popular measurement technique whose popularity has been on the rise over the past few decades. Compared to Hot Wire Anemometry and Laser Doppler Anemometry, PIV provides the advantage of being a whole field method, wherein instantaneous qualitative and quantitative information can be obtained over planar or volumetric domains. In addition, unlike pressure probes or hot wires, it is (almost completely) non-intrusive. On the flipside, PIV is relatively more complex to setup and requires experience and expertise from the user.

PIV has been reviewed extensively in literature and is also the subject of books by Raffel et al. [77] as well as Adrian and Westerweel [78]. For a more concise introduction, the interested reader can refer to a course reader by Scarano [55]. Thus, the working principle of this measurement technique will not be described in detail in this report.

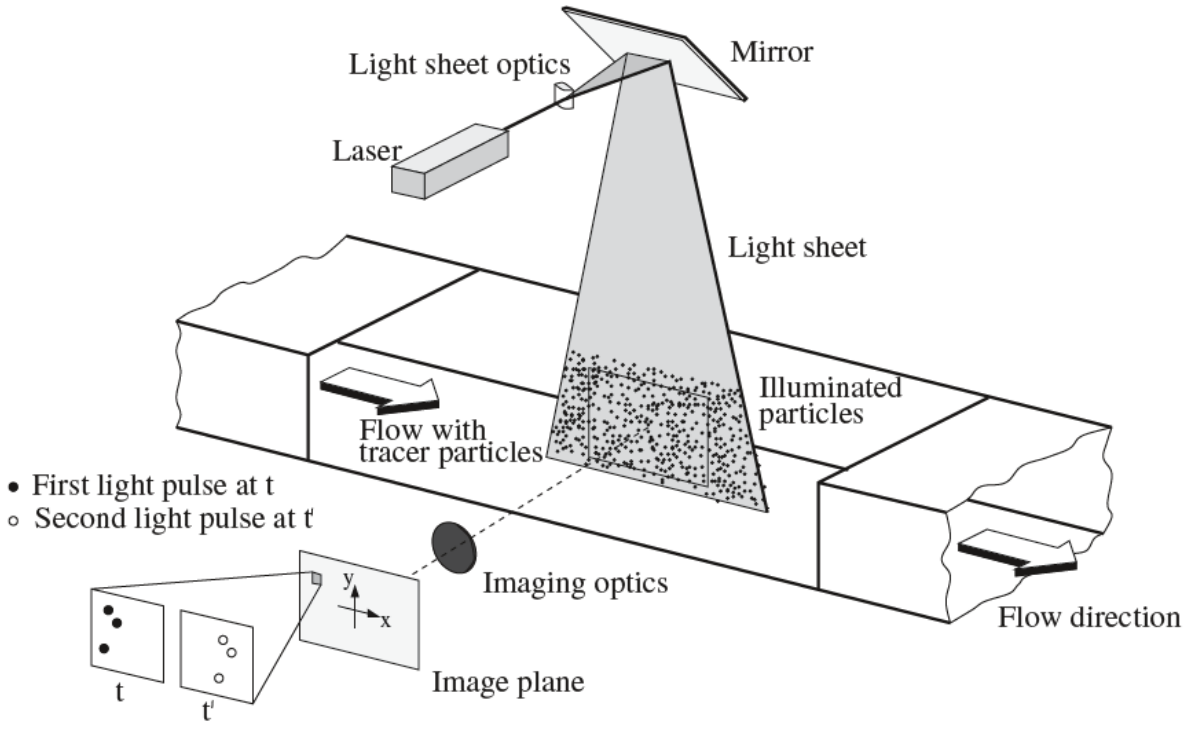

Figure 4.10: Typical arrangement for a planar PIV experiment. Figure reproduced from Raffel et al. [77].

A schematic of a typical setup for a planar PIV experiment, including the major components, is shown in Figure 4.10. Velocity measurement in PIV is done indirectly by measuring the displacement of small tracer particles moving with the flow over a short time interval. It is assumed that these tracer particles follow the flow faithfully and do not affect the flow characteristics. In order to obtain the displacement, the particles need to be illuminated at least twice in an extremely short period, which is often performed with a pulsed laser. The laser beam is manipulated into a light sheet with the aid of light sheet optics, which includes a combination of mirrors and lenses. The light scattered by the tracer particles is captured on two separate frames by a digital imaging device.

The recorded images are then evaluated by dividing it into several smaller areas, called “interrogation regions”. It is assumed that the particles in a single interrogation region have moved homogeneously between the two illuminations. Cross-correlation analysis between the two images returns a displacement, which upon combination with the image magnification and the time delay between the two illuminations, returns the velocity field.

4.4.2. Components of the PIV setup

The different components used in the present PIV experiment setup are shown in Figure 4.11. For this planar PIV experiment, the flow was seeded with 10 µm neutrally-buoyant tracer particles (Sphericell). The seeding density in the image was around 0.04 particles per pixel. A plane along the center-line of the water tunnel was illuminated using a twin-cavity double pulsed Nd:YAG laser (Spectra-Physics Quanta Ray), capable of firing at 15 Hz. The field of view was approximately 15 $\times$ 10 cm^2. To facilitate a stable and flexible mounting of components like optics and cameras, an extensive support structure was built using X95 structural optical rails and carriers. The optics involved in manipulating the laser beam into a laser sheet included mirrors, a spherical lens with a focal length of 500 mm and a cylindrical lens with a focal length of -25 mm. A Flowmaster Imager Intense camera, as seen in Figure 4.11e, capable of capturing images at frame rates upto 10 Hz, with a resolution of 1376 $\times$ 1040 pixels, pixel size of 6.45 µm and 12 bits dynamic range were used. It was equipped with Nikkor F35 mm lenses via optomechanical components as well as a green color filter to minimize the influence of the fluorescent signal from the dye. The lens was operated at an aperture number $f_\#$ of 5.6. It was mounted atop a Scheimpflug adapter to allow focusing, especially when the lens plane is not parallel to the laser sheet. The camera looked into the field of view with a small angle of approximately 4 ° and also a small vertical inclination. A programmable timing unit by LaVision, as seen in Figure 4.11i, coordinated the triggers between the double-pulse laser and the cameras. Data acquisition was performed using the commercial software package DaVis 8.4.0, which was also used to calibrate and process the PIV data. The raw PIV images were stored on a remote server which too can process the PIV data. Images are processed using a multi-pass interrogation technique, where the final windows had a size of 16 $\times$ 16 pixels, with 50% overlap between the neighboring windows. This corresponds to a spatial resolution of 0.8 mm (or h_{ESP}/14.6, where h_{ESP} is the height of the ESP, or η/61.3, where η is an estimate for the associated Kolmogorov length scale) for the velocity measurements. Images were acquired at a rate of 5 Hz, allowing for consecutive measurements to be statistically uncorrelated. The time separation between image pairs was maintained at 2.5 ms, which corresponds to a particle displacement of 12 pixels between frames, which is less than one fourth of the initial correlation window size of 64 $\times$ 64 pixels.

4.5. Planar Laser Induced Fluorescence (PLIF) - setup and specifications

PLIF is a commonly used non-intrusive technique used for measuring scalar quantities (for example, concentration and temperature). A comprehensive summary on the application of PLIF to aqueous flows is given by Crimaldi [80], whereas a more concise summary relevant to the current project is given by Eisma [14]. The working principle of this measurement technique is briefly discussed in Section 4.5.1 followed by a description of the components used in the current setup in Section 4.5.2.

4.5.1. Working principle of Laser Induced Fluorescence

The basic process involved in PLIF, as described by Vanderwel and Tavoularis [81], is the introduction of an aqueous solution of a fluorescent dye into the water flow, illuminating a thin layer of the water with a laser sheet and recording its image. As a final step, the intensity maps from the recorded images can be converted to planar maps of scalar quantities (for example, concentration or temperature) though a calibration process.

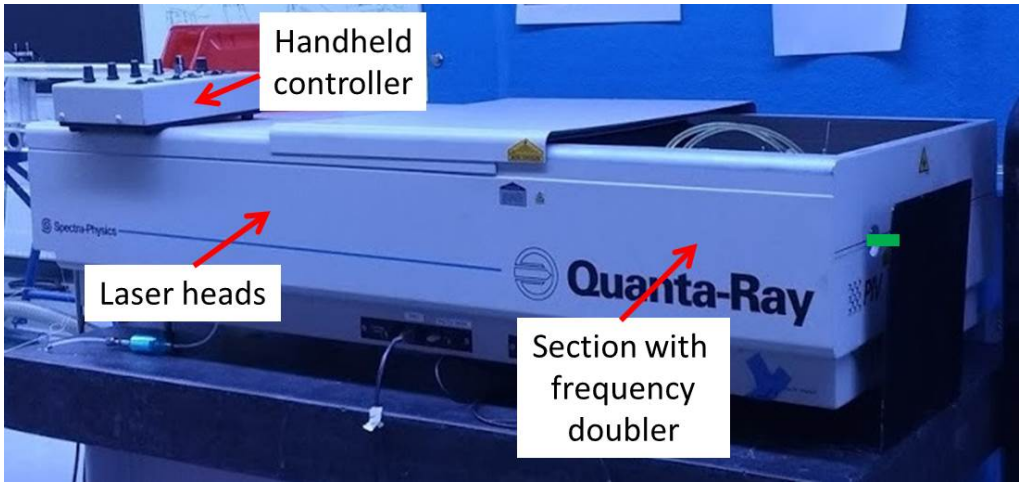

(a) The laser head of the double pulsed Nd:YAG laser utilized for the experiments.

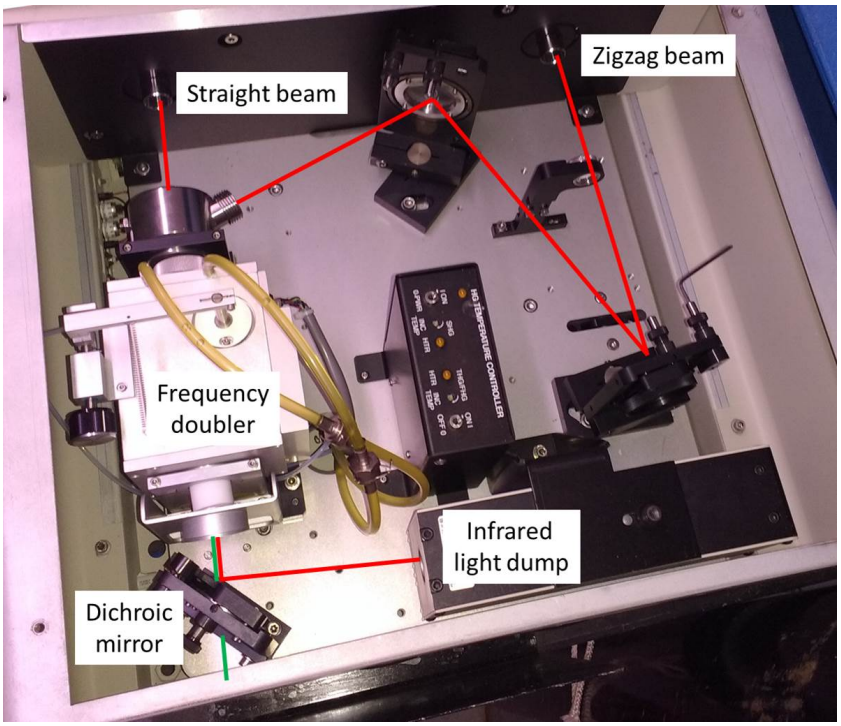

(b) The internal section of the laser associated with the beam propagation. The paths of the original infrared and final green beams have been shown in red and green respectively.

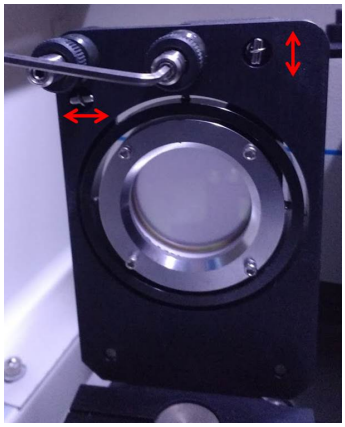

(c) The mirror in the laser used to adjust the beam overlap. The arrows indicate the direction in which the outgoing beam profile is shifted.

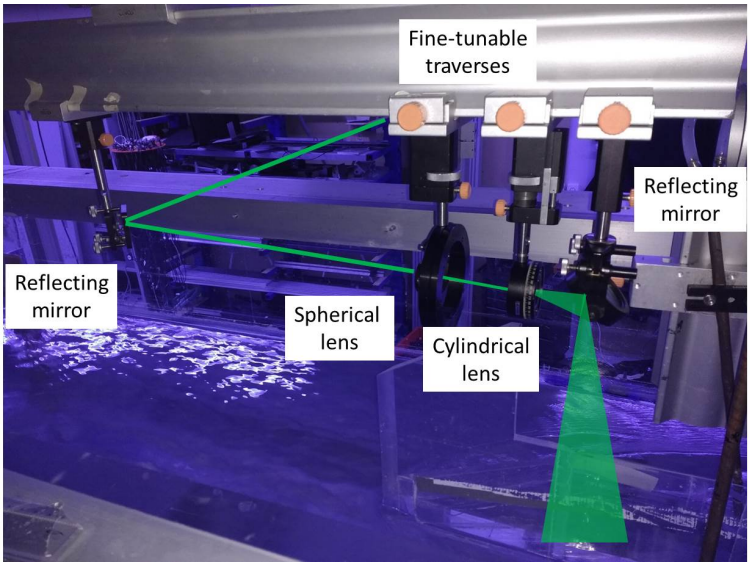

(d) A portion of the optics used to shape the laser sheet.

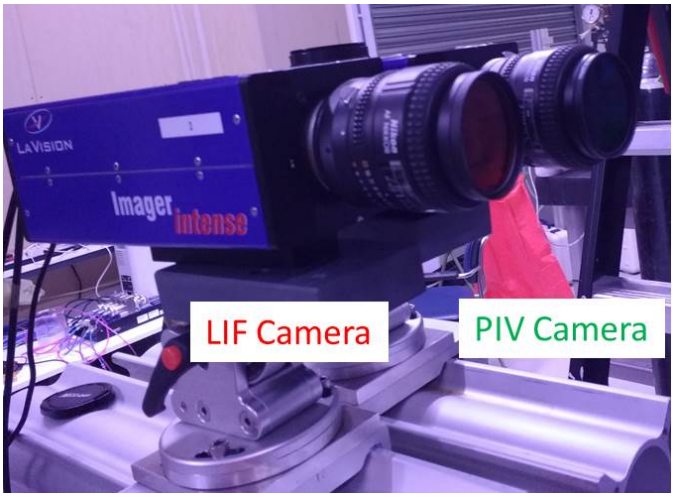

(e) The cameras along with the associated color filters used in the experiments.

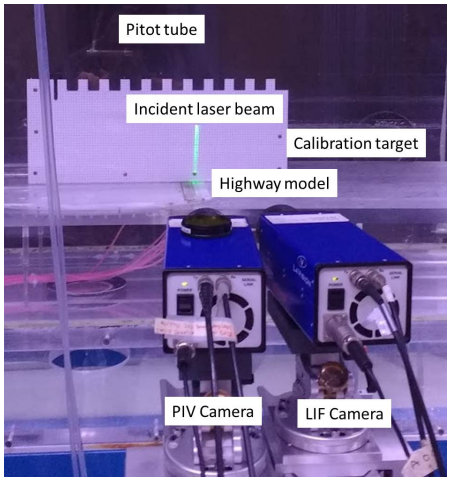

(f) The custom-made calibration target used for field of view adjustment, PIV calibration as well as laser sheet alignment.

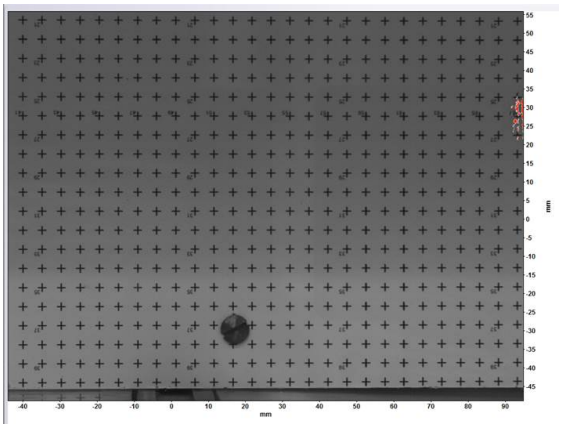

(g) Adjusting the field of view for the PIV camera.

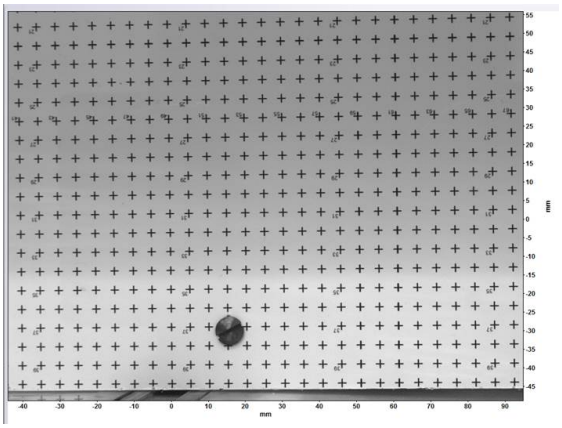

(h) Adjusting the field of view for the PLIF camera.

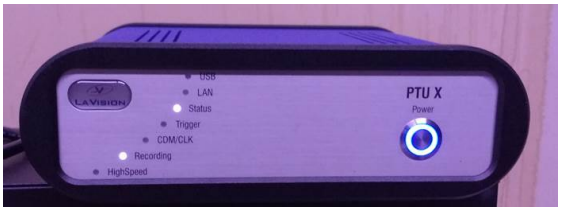

(i) The programmable timing unit responsible for controlling triggers to the laser and the cameras.

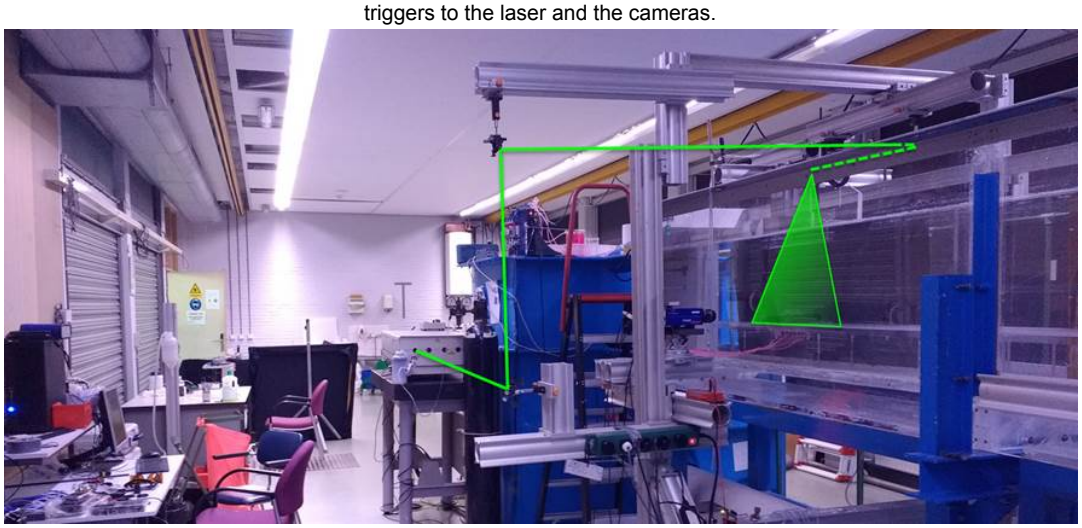

(j) A portion of the setup located outside the water channel.

Figure 4.11: The different components involved in the current planar PIV setup.

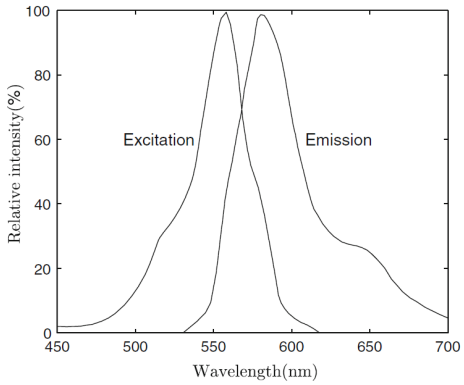

(a) The absorption and emission spectra of Rhodamine-WT. Figure reproduced from Pedocchi et al. [79].

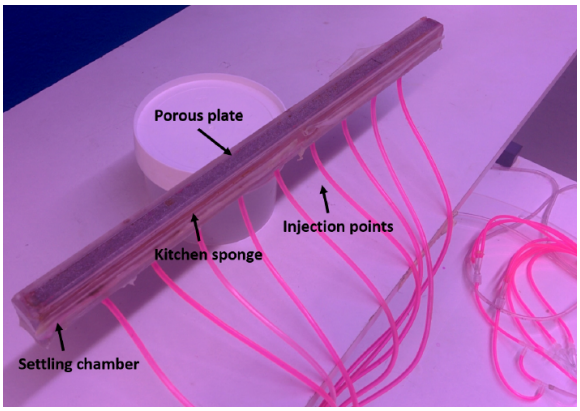

(b) The line source labeled with the different components. Picture reproduced from Eisma [14].

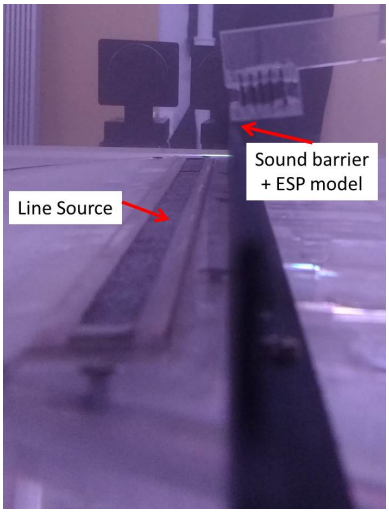

(c) The line source embedded into the turntable which in turn is screwed into the false bottom.

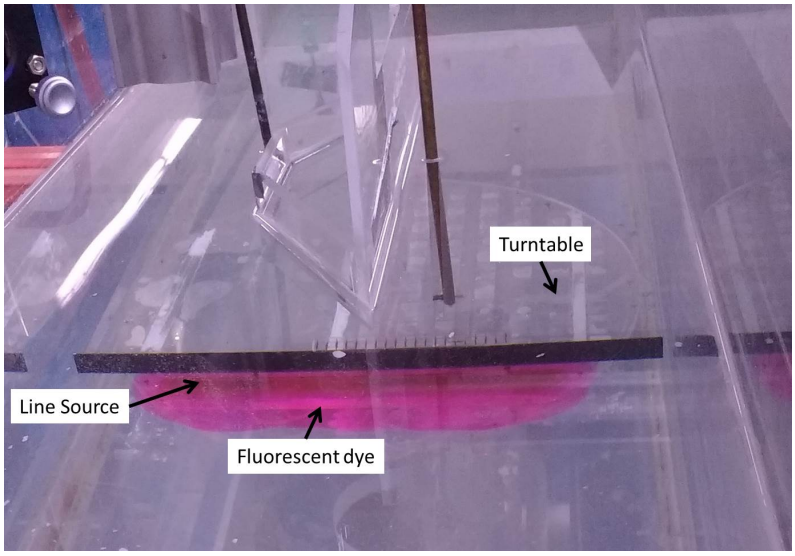

(d) Release of dye from the line source.

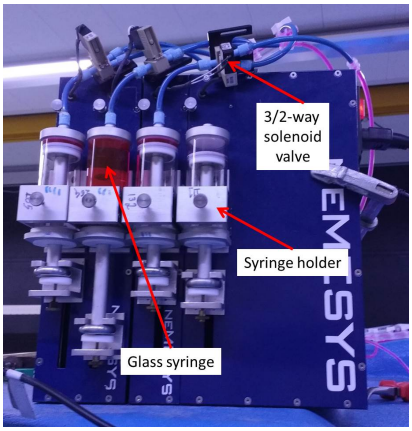

(e) The syringe pump utilized for modulating the dye flow to the line source.

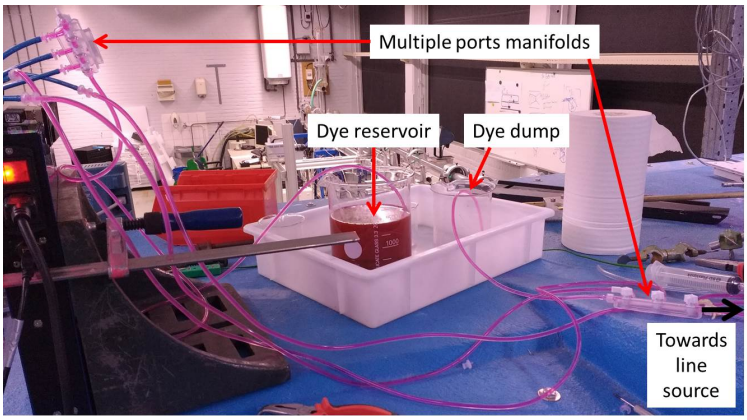

(f) Intermediate fluidic connections between the syringe pump and the line source.

(g) The neMESYS user interface used to control the syringes.

Figure 4.12: The different components involved in the current PLIF setup.

One major simplification in the PLIF analysis involves considering the system as 'optically thin'. According to the Beer-Lambert law, a light ray with intensity I passing through a medium with thickness dr, extinction coefficient ϵ and concentration c experiences and intensity change dI as given in Equation (4.3).

$$\frac{dI}{I} = -\epsilon c dr \tag{4.3}$$

For a light ray traveling between $z = z_0$ and $z = z_1$ through a medium with spatially varying concentration $c(x, z)$, the above equation can then be integrated to obtain:

$$I(x, z) = I_0(x, z) e^{-\epsilon \int_{z_0}^{z_1} c(x,z) dz} \tag{4.4}$$

Here, $I_0(x, z)$ refers to the local excitation intensity (for example, that of the laser). If the exponent on the right hand side of the above equation satisfies $\epsilon \int_{z_0}^{z_1} c(x, z) dz << 1$, then the attenuation of the laser sheet due to the presence of dye can be neglected and $I(z_1) \approx I(z_0)$. This approximation allows the system to be considered as optically thin.

Finally, under optically thin conditions, the imaged fluorescence intensity ($I_F(i, j)$) where (i, j) refers to the pixel location, can be related to the local concentration by Equation (4.5).

$$I_F(i, j) = \alpha(i, j) I_0(x, z) c(x, z) \tag{4.5}$$

A calibration procedure, as prescribed by Eisma [14], can be performed by placing a container with known uniform concentrations in the field of view. The value of the calibration coefficient $\alpha(i, j) I_0(x, z)$ can be evaluated at each individual pixel by performing a linear least squares fit. However, this has not been performed in the current project. Inferences on the dye concentration were drawn from the image intensities itself. While this affects the accuracy of the measurements, it is shown in Section 5.3 that the lack of calibration might not be a major issue in the context of the current project.

4.5.2. Components of the PLIF setup

Since PLIF is employed in tandem with planar PIV, a large number of components, including the laser and the laser sheet forming optics are common. Some of the components and processes associated with the PLIF setup are shown in Figure 4.12. The laser must be combined with an appropriate fluorescent dye i.e. the absorption spectrum of the dye must be compatible with the laser excitation (532 nm). In addition, other desirable features as noted by Crimaldi [80] include a large separation between the absorption and emission spectra, and high quantum efficiency to maximize signal strength. The dye utilized in the current experiments is Rhodamine-WT whose spectral characteristics, shown in Figure 4.12a, are compatible with the laser. A dilute solution of the dye (≈20 mg/L) is used for the experiments. This solution of the fluorescent dye is slowly diffused into the flow by a uniform line source constructed by Eisma [14], shown in Figure 4.12b, which also acts as a model for the highway emitting pollutants. The flow to the line source is controlled by a 4-axle syringe pump system (neMESYS, Cetoni GmbH), shown in Figure 4.12e, via the neMESYS user interface, shown in Figure 4.12g. A continuous volumetric flow rate of 4.5 ml/s is used for the experiments which results in an average vertical injection velocity of 1.1 mm/s through the line source. Reasonably uniform dye release from the line source, along the spanwise direction was observed through visual inspection, as seen in Figure 4.12d. Images were captured using a second Flowmaster Imager Intense camera (same as the camera used for the PIV recordings) with a red color filter in front. This camera too looked at the field of view at an angle of approximately 6° and had a slight vertical inclination. It too was operated at an aperture number $f_\#$ of 5.6. Image recording was performed simultaneously with the PIV camera using DaVis 8.4.0. The fluorescent dye intensity information was available at each pixel which roughly corresponds to a spacing of 0.1 mm.

5

What influences the aerodynamic performance of the ESP? How and why?

Results from different experiments are presented in this chapter. The characterization of the ESP and the incoming ABL are discussed in Section 5.1 and Section 5.2 respectively. Following a short discussion on data post-processing and the aerodynamic efficiency definition in Section 5.3, the effect of a few parameters are investigated in Section 5.4. Lastly, the existence of aerodynamic efficiency maximizing events is explored in Section 5.5.

5.1. Characterization of the model ESP

Flow over a fence or a SB has been the topic of several studies, as discussed in Chapters 1 to 3. The major addition in the current investigation is the model ESP, whose design was discussed in detail in Section 3.2. Characteristics of the drag force it exerts on the flow are discussed in this section.

5.1.1. Desired quantities

Since the current investigation involves scaling down the problem by a few orders of magnitude, it is necessary to maintain similarity. Among the different similarity constraints, one of the desired constants for the model ESP is the drag coefficient (c_D), as discussed in Section 3.2.

A control volume analysis to estimate the drag coefficient for the ESP from the experiments, along with the associated assumptions are discussed first. The control volume along with the relevant control surfaces are shown in Figure 5.1. The selection of the control volume is in accordance with the measurement points selected, which are discussed later in Section 5.1.2. An introduction to control volume analysis is given in the book by Kundu et al. [82].

The desired quantity here is the drag coefficient due to the drag force, F_d, experienced by the ESP, with a height h, per unit spanwise length, placed in the flow, which is defined in Equation (5.1). The fluid has a density of ρ and the flow approaching the ESP has a streamwise velocity component of U_W.

$$c_D = \frac{F_d}{h \cdot \frac{1}{2}\rho U_W^2} \tag{5.1}$$

The drag force is the sum of pressure drag and frictional drag. In the current case, the rectangular cylinder shaped ESP acts as a blunt body and the pressure drag is dominant. Thus, the drag force per unit spanwise length is simplified into the product of the static pressure drop (ΔP) and the ESP height, according to Equation (5.2). Using these two equations, the drag coefficient can be simplified into the pressure drop coefficient per Equation (5.3). The pressure drop coefficient obtained through

the theoretical analysis in Section 3.2 can thus be compared to the drag coefficient calculated later. However, this assumes a uniform pressure drop profile across the ESP height.

$$F_d = \Delta P \cdot h \tag{5.2}$$

$$c_D = c_P = \frac{\Delta P}{\frac{1}{2}\rho U_W^2} \tag{5.3}$$

U and W are used to denote the streamwise and wall-normal velocity components, respectively, at a given location. There are several simplifications and assumptions involved with the current analysis, as given below. While these are quite strong assumptions, the purpose of this exercise is to obtain a ballpark estimate of the ESP drag coefficient.

- There is a uniform velocity (both components) and pressure profile along all the control surfaces. While this is reasonable for the windward surface, it is less appropriate for the remaining surfaces, especially since they are located in the direct vicinity of the ESP.
- A uniform static pressure is present throughout the control volume. However, it is likely that the pressure will vary upon approaching the ESP.
- The surfaces of B and T are free from any shear stresses and have a uniform streamwise velocity component of U_W.
- There is no vertical velocity component along the leeward control surface. However, this is unlikely since the flow is expected to be highly turbulent just behind the ESP.
- The effect of gravity is neglected.

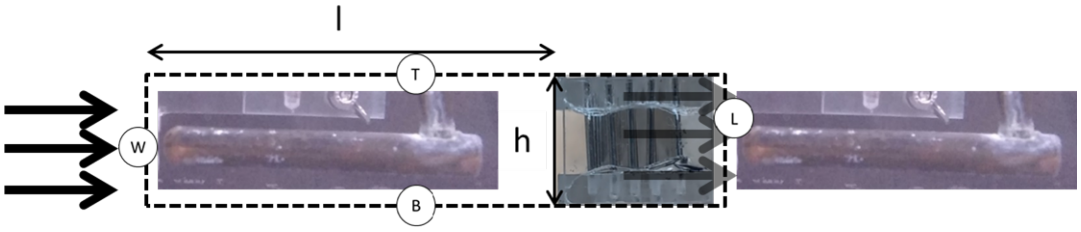

Figure 5.1: Control volume and control surfaces used for estimating the ESP drag coefficient. W, B, T and L are used to denote the windward, bottom, top, and leeward control surfaces respectively. l is the permeable length of the control surfaces B and T while h is the height of the control surfaces W and L. The surfaces are always denoted by subscripts. Images are not to scale.

When the conservation of mass is imposed upon the control volume, Equation (5.4) is obtained which can be rearranged to yield Equation (5.5).

$$U_W h = W_T l - W_B l + U_L h \tag{5.4}$$

$$(W_T - W_B) l = (U_W - U_L) h \tag{5.5}$$

Similarly, the conservation of momentum in the streamwise direction, per unit spanwise length, yields Equation (5.6). By applying Equation (5.5) to Equation (5.6), the pressure drop across the ESP can be determined through Equation (5.7). Static pressure terms have not been considered in accordance with the assumption of constant static pressure in the control volume. Finally, using Equation (5.7) in tandem with Equation (5.3), the drag coefficient can be simplified to Equation (5.8).

$$\rho U_W^2 h = \rho U_W W_T l - \rho U_W W_B l + \rho U_L^2 h + F_d \tag{5.6}$$

$$F_d = \rho U_L (U_W - U_L) h \tag{5.7}$$

$$c_D = \frac{\rho U_L (U_W - U_L)}{\frac{1}{2}\rho U_W^2} = 2\frac{U_L}{U_W}\left(1 - \frac{U_L}{U_W}\right) \tag{5.8}$$

The drag force exerted by the ESP is measured through separate pitot tube measurements, whose technique was previously described in Section 4.3. The pitot tube has been used to separately measure the dynamic pressure ($= \frac{1}{2}\rho U_{W,L}^2$) in the windward and leeward side of the ESP, from which the individual velocities can be extracted.

The semi-permeable model ESP experiences a drag force not only because of the external flow over the outer casing that behaves as a (finite length rectangular cylinder shaped) bluff body, but also due to the flow through the internal structure of the systematically arranged rows of cylinders. Together, these are expected to influence the drag coefficient as the flow Reynolds number changes.

5.1.2. Specific details of the experimental setup

The model ESP was hung approximately 409 cm downstream of the water channel inlet and about 23 cm from the bottom of the false floor. The center of the ESP was aligned with the centerline of the water channel cross-section. The blockage ratio based on the separation between the false floor and the maximum water level is a negligible 2.6%.

The spires and the fence setup, described previously in Section 4.2.2, were installed at the time of these measurements, but it can be expected that the ESP is located close to the freestream flow and not exposed to the shear flow of the ABL. However, it might still be exposed to the turbulent fluctuations in the range of 3-5% of the freestream velocity. While the characteristic length of turbulence structures is unknown, turbulence intensities are known to have an effect on flow past rectangular cylinders, at least in the range of 6-10%, as investigated by Nakamura and Ohya [83].

The pitot tube measurements were made approximately 0.6 cm (or 0.06 l_{ESP}, where l_{ESP} is the half spanwise length of the ESP) away from the centerline of the ESP in the spanwise direction. This reduces the effect of the edges on the flow near the measurement points.

For the measurements in the windward side of the ESP, the front end of the pitot tube was approximately 8.1 cm (or $6.9h_{\mathrm{ESP}}$, where h_{ESP} is the height of the ESP) in front, while it was approximately 0.6 cm (or $0.5h_{\mathrm{ESP}}$) behind the trailing edge of the ESP for the leeward velocity measurements. It was also necessary to have repeatable experiments. The pitot tube was positioned within $\pm$ 0.3 cm (or $0.25h_{\mathrm{ESP}}$), in the streamwise and spanwise directions, between the nine different measurement runs.

Data was acquired at 100 Hz for one minute. Resonance-esque vibrations of the pitot tube as well as the model ESP were also observed at the flow settings corresponding to the higher Reynolds number (> 10000).

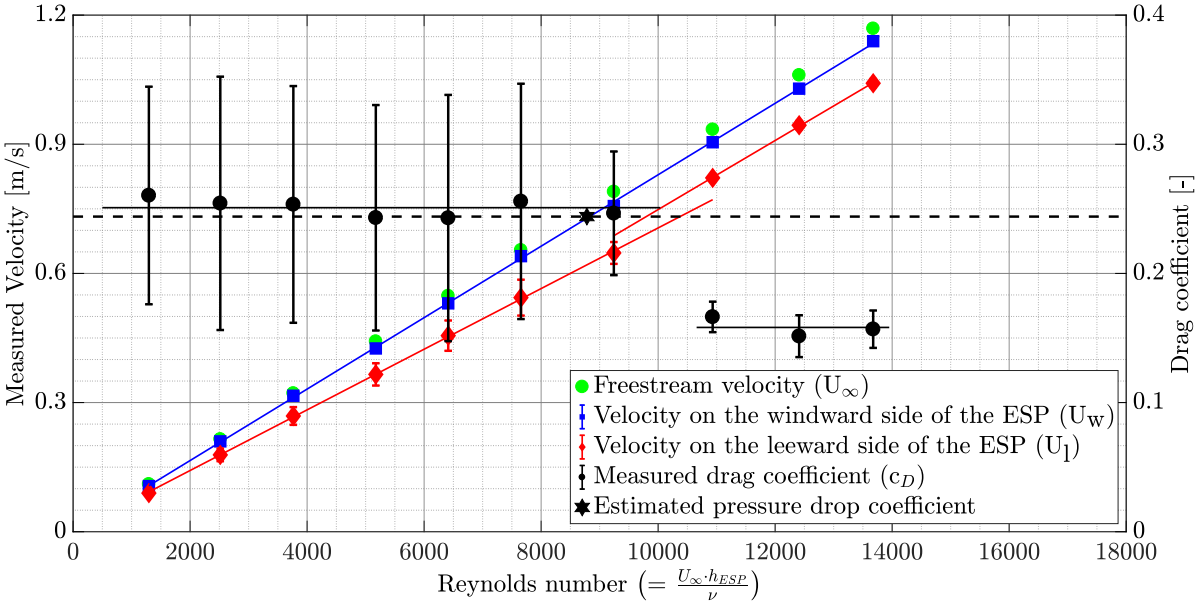

Figure 5.2: Velocity measurements in the windward and leeward side of the ESP and the corresponding drag coefficients, as a function of the Reynolds number. The vertical bars represent the standard deviation. The theoretical pressure drop coefficient was previously estimated in Section 3.2.2.

5.1.3. Two regimes of the ESP

The results of these experiments are presented in Figure 5.2. The Reynolds number is based on the freestream velocity measured in the absence of the ESP model. As can be seen, these values are only slightly higher than the velocities measured on the windward side of the ESP. Despite the sensitive end of the pitot tube being approximately $6.9h_{\mathrm{ESP}}$ in front of the leading edge of the ESP, its presence probably leads to a slight flow deceleration upstream by generating an adverse pressure gradient.

There is an evident linear rise in the windward velocity measurements with increasing Reynolds number throughout the entire measurement range. In comparison, two clearly distinguishable regimes are observed for the leeward velocity profiles and, thus, the drag coefficients. The first regime is observed at relatively lower Reynolds numbers (< 10000) characterized with relatively high drag coefficients, while the second regime is observed at higher Reynolds number (> 10000) which experiences a sudden drop in the drag coefficient.

The ratio between the slope of the linear fit for the leeward velocities in the first regime to the slope of the linear fit for the windward velocity profile is 0.84. For the second regime, this value is 0.96. Consequently, the mean drag coefficients for the first and second regimes are approximately 0.251 and 0.158 respectively. The measured drag coefficient in the first regime agrees reasonably well with the theoretically estimated value of 0.244, and the flow setting corresponding to the Reynolds number of approximately 9200 is selected for the current experiments.

Another striking feature separating the two regimes is the larger magnitude of uncertainties in the first regime as compared to the negligible ones in the second regime. The uncertainties are based upon the standard deviation of results from the nine measurement runs. As mentioned previously, not all measurements were perfectly repeatable from the perspective of the placement of the pitot tube relative to the ESP as well as the large size of the pitot tube in comparison with the ESP model. In the first regime, the location of the transition point to turbulent flow might be variable between the runs leading to larger fluctuations in the drag coefficients. In the second regime, this transition point may be fixed allowing for better repetition. However, the above reasoning is purely speculative and requires verification through future measurements.

5.1.4. Possible reasons for a regime transition

Looking back at Figure 3.8, the friction factor for an in-line arrangement of cylinders is almost constant throughout the entire range of Reynolds number of the current experiments. This rules out the possibility of any change in flow regimes due to the internal structure of the model ESP.

The next possible source for this observation, could be on the basis of the bluff body behavior of the (finite length rectangle-cylinder shaped) ESP model. This trend seems to resemble the observations of Achenbach and Heinecke [85] concerning a sharp drop in the drag coefficient for a single circular cylinder, at a critical Reynolds number, corresponding to the 'drag crisis' regime and is attributed to a sudden downstream shift of the separation point. Such a trend was also seen previously in Figure 3.11.

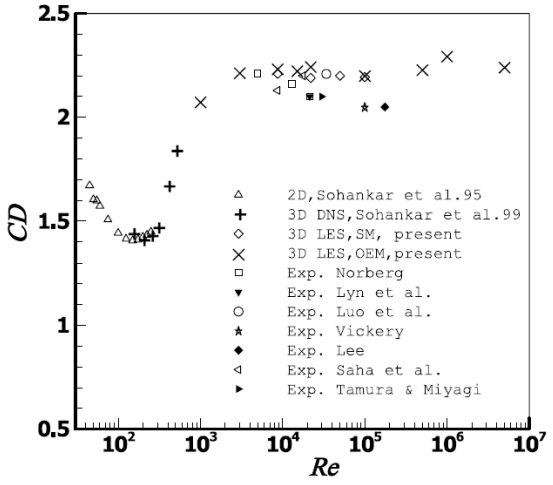

Figure 5.3: Drag coefficient as a function of Reynolds number for a square cylinder. Figure reproduced from Sohankar [84].

In contrast, no such trend is clear for the case of a square cylinder as seen in Figure 5.3 and also for bodies with sharp corners in Figure 5.4. Tamura et al. [86] observed a drag crisis like behavior for square cylinder, albeit with rounded corners. However, the current model has sharp corners. Sohankar et al. [87] also notes that above the critical Reynolds number of 175, the flow always separates at the upstream corner. Tomonari [88] found that for a transverse galloping square cylinder, as

the Reynolds number was raised from 10^3 to 10^4, the transition point from laminar to turbulent flow moved forward beyond the rear edge of the cylinder. If such a transition occurs in the current case, it could lead to a compressed wake region and thus, lower drag coefficients. However, this would need to be confirmed through additional experiments.

One other possibility for this trend might be the aforementioned observation of vigorous vibrations of the ESP along the flow direction, under high speed flows. This may result in additional turbulence in the near field of the ESP, leading to relatively more uniform velocities around it and thus, a reduced drag force.

However, in order to arrive at a concrete conclusion, it is recommended that some PIV measurements be made around the model ESP at the different Reynolds numbers including a higher resolution between 9000 and 11000, to verify the presence of a transition region.

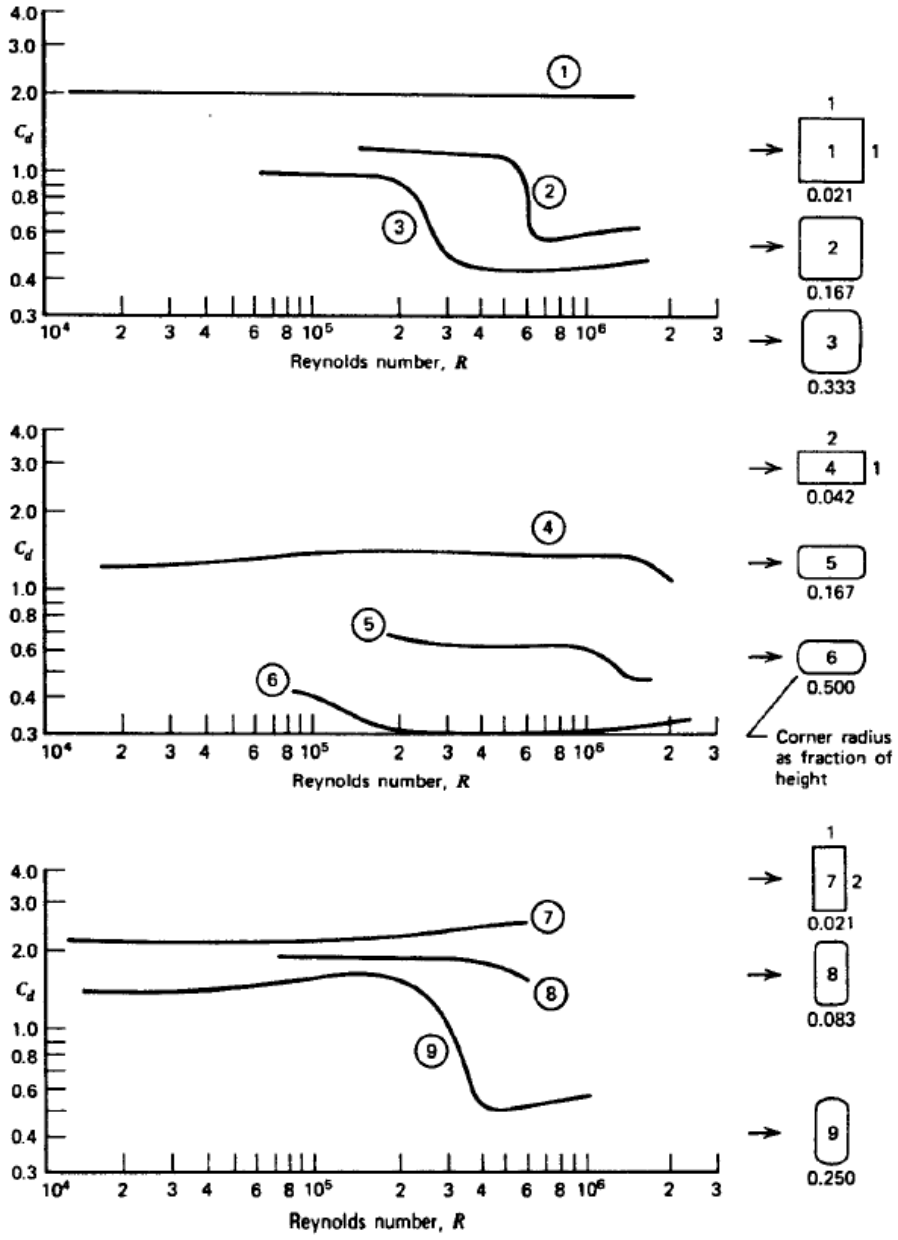

Figure 5.4: Drag coefficients for various rectangular cylinder shapes as a function of Reynolds number. Shape 4 comes closest to resembling the cross-section of the model ESP. Figure reproduced from Buresti [89].

5.1.5. Improvements for future experiments

Several simplifications were utilized in the control volume analysis done in Section 5.1.1. One way around this is by having an extremely large control volume in height and length, i.e. the surfaces B and T should be located far enough that they are subject to a streamwise velocity component equal to U_W. Having these surfaces at a farther distance will also alleviate the assumption on the constant static pressure throughout all the surfaces. The only downside would be that numerous point measurements would be needed along the surface L, which would be a function of the wall-normal coordinate. On the plus side, any wall-normal velocity components will be absent along L. This analysis can be better done through a planar PIV experiment with a much larger field of view around the ESP.

While estimating the theoretical value of the pressure drop coefficient of the ESP prototype, the effect of the external casing as a bluff body was ignored. Thus, it is imaginable that the expected theoretical pressure drop coefficient would be higher than what was predicted. It is recommended that pressure drop measurements be made around the prototype ESP for developing a more representative model.

On the contrary, the drag force measurements using the pitot tube were not without their flaws. The windward velocity was measured rather upstream from the leading edge of the ESP, which is not ideal. In addition, the velocity profile in the downwind wake of the ESP is expected to be rather three-dimensional. The total pressure port of the pitot tube is only capable of detecting the streamwise velocity component, while the static pressure ports might be influenced by the additional turbulent fluctuations. Furthermore, there is a streamwise separation between the total and static pressure ports, i.e. the dynamic pressure is not obtained at a single point.

Despite these shortcomings, the performance of the model ESP is in the same order of magnitude as the prototype and can thus be considered representative of the real case.

5.2. Characterization of the incoming boundary layer

The setup for the simulated incoming ABL was previously discussed in Section 4.2.2. The characterization of the ABL was performed approximately 3.4 m downstream of the spires. Since the ABL generation mechanism was nearly identical to that originally used by Eisma [14], a comparison between the results of the current study and the preceding work has been performed. The results are illustrated in Figure 5.5.

The cases compared include the cases where the spires and barrier (shown in Figure 4.4) were installed upstream to accelerate the boundary layer development and also the case where they were absent. These are compared to data extracted from the results of Eisma [14]. In Figure 5.5a and Figure 5.5d, 'Eisma outer scaling' refer to data extracted from plots presented in the outer scaling while 'Eisma inner scaling' refer to those plotted in the inner scaling (wall units) form. The minor discrepancies between the two may be attributed to the error made while extracting information out of the plots. Since the calibration target has a height of 30 cm, results above this height must be treated with caution. The spatial resolution between two consecutive vectors for these measurements is approximately 2.4 mm.

The variation of the mean streamwise velocity component is plotted in Figure 5.5a. These are compared to the theoretically expected power-law velocity profile from Equation (4.2), which is an appropriate estimate for velocity values not too close to the ground. It is observed that the velocity profiles of Eisma [14] agree better with this theoretical estimate. However, measurements by Eisma [14] were made a further 0.5 m downstream than in the current measurements, allowing for a longer length for the ABL development. Ironically, the boundary layer development without spires (i.e. boundary layer development over a smooth flat plate) seems to resemble the theoretical power law better. However, from Figure 5.5b and Figure 5.5c, it is evident that the ABL formed without spires is not turbulent enough.

A comparison between the mean streamwise velocity profile (in wall units) can be performed as shown in Figure 5.5d. Reasonably good agreement between the theoretical log-law fit and the velocity profiles are obtained for a large range of z^+ values: between 300 and 3000 with spires, 600 and 9000 without spires and between 150 and 3000 for results obtained by Eisma [14]. The low spatial resolution in the current experiment did not allow visualization in the viscous sublayer or the buffer layer. However, the log-law is expected to be valid from z^+ values of 30, which is not the case here. This

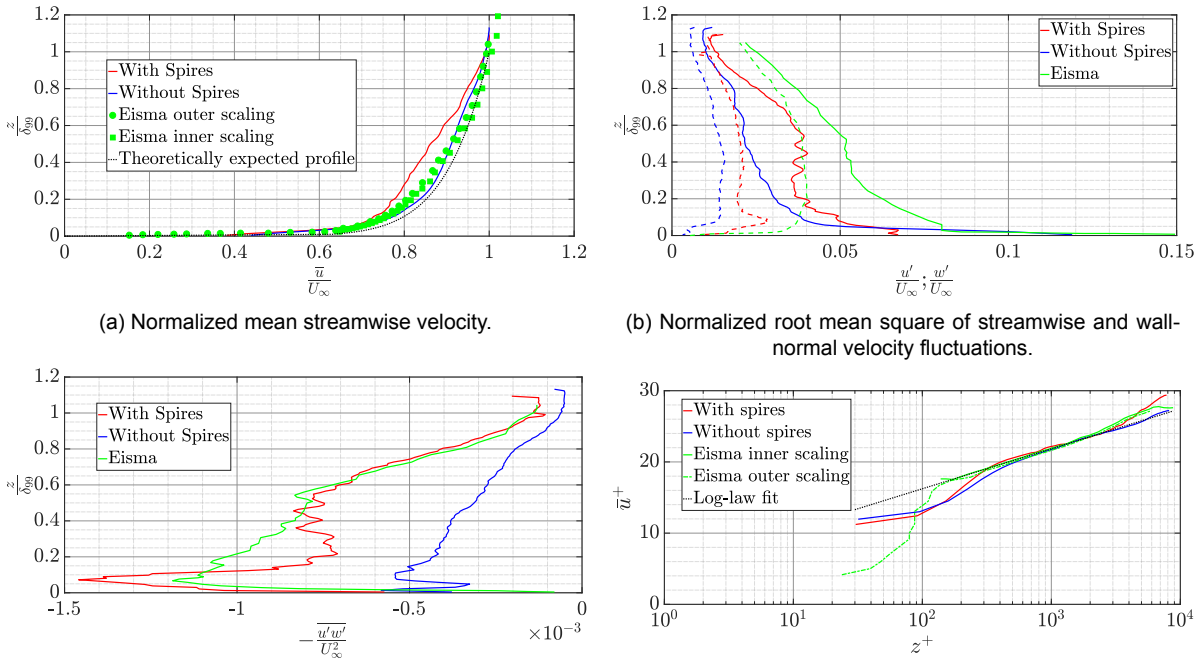

(a) Normalized mean streamwise velocity.

(b) Normalized root mean square of streamwise and wall-normal velocity fluctuations.

(c) Normalized Reynolds shear stress.

(d) Log-law fit.

Figure 5.5: Comparison of the current boundary layer characteristics with previous studies, specifically Eisma [14]. 'Eisma outer scaling' refer to the data from plots in the outer scaling while 'Eisma inner scaling' refer to those plotted in the inner scaling form. Data from Eisma [14] (specifically 'Exp. 3') is used here. The streamwise and wall-normal fluctuations in (b) are denoted by the solid and dashed lines respectively.

might mean that the simulated ABL is not perfectly neutral. Another possibility is that due to the limited spatial resolution of the camera, velocities near the wall are not resolved very well. The region near the wall is subject to a higher shear rate and this might not be captured well in a single correlation window.

Another way to judge the relevance of the turbulence intensity profiles is by comparing the ratio between the different components of the turbulent fluctuations and the wall friction velocity, near the ground. According to Teunissen [90], these ratios for the root mean square velocity fluctuations in the longitudinal, lateral and vertical (or streamwise (u'), spanwise (v') and wall-normal (w') in the laboratory frame) directions are approximately 2.5, 2.0 and 1.3 respectively. In the current study, the ratio between w' and u' for the entire height is approximately 0.5960 $\pm$ 0.1467, while a value of around 0.52 would be expected theoretically. Root mean square velocities of approximately 8.5% and 4.4% (for the streamwise and wall-normal components respectively) of the freestream velocity would be expected near the ground (or floor). For the case with spires, these values are 6.5% and 3% respectively, while Eisma [14] attains values of 9% and 4% respectively. The ABL in the current case is not as turbulent as ideally desired. One of the possible sources for the turbulence deficiency could be the incorrect alignment of the spires to the incoming flow. According to Irwin [75], the splitter plate on the spire should lie on the downwind side of the triangular face, which was not the case in the current setup. The appropriate alignment of the spire with respect to the incoming flow is illustrated in Figure 5.6.

A litmus test to determine the goodness of the measured wall-bounded turbulent flow has been proposed by Alfredsson and Örlü [91]. This is known as the 'diagnostic plot' where the normalized velocity fluctuations is plotted against the normalized mean velocity. Both these quantities are normalized by the freestream velocity. This method does not require knowledge of the wall position or the friction velocity. An example is shown in Figure 5.7, where data from current experiments are plotted against data from Eisma [14] and Alfredsson and Örlü [91]. However, the mean velocity data for Eisma [14] is based on the power law in shown previously in Figure 5.5a. The data of Eisma [14] agrees better with the data of Alfredsson and Örlü [91] in the outer region $\left(\frac{\overline{u}}{U_\infty} > 0.70\right)$.

The profile from the current case qualitatively resembles the expected profile, albeit with suppressed

turbulent intensities. The turbulence intensities in the current study might be underestimated due to the limit posed by the spatial resolution of the PIV measurement. A single correlation window is approximately 186 times the Kolmogorov length scale (approximately 13 μm). Lavoie et al. [92] have previously shown that a finite spatial resolution in PIV experiments leads to suppressed velocity statistics, which might be the case here. The measurements of Eisma [14] had a much higher spatial resolution. Another possible explanation for suppressed turbulence intensities is the selection of a rather long averaging streamwise length whose effect is discussed in Appendix C. However, it is also noteworthy that while the ABL in the water channel may be subject to a slight favorable pressure gradient (due to the growing boundary layer on the side walls of the channel with a constant cross-sectional area), the 'diagnostic plot' is valid only for zero pressure gradient boundary layers as noted by Cierpka et al. [93].

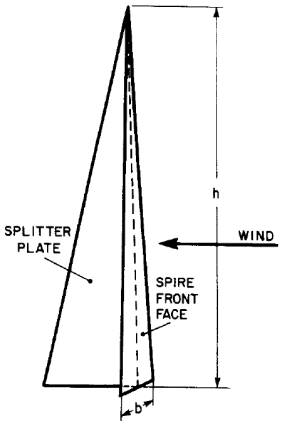

Figure 5.6: Correct alignment of a triangular spire. Figure reproduced from Irwin [75].

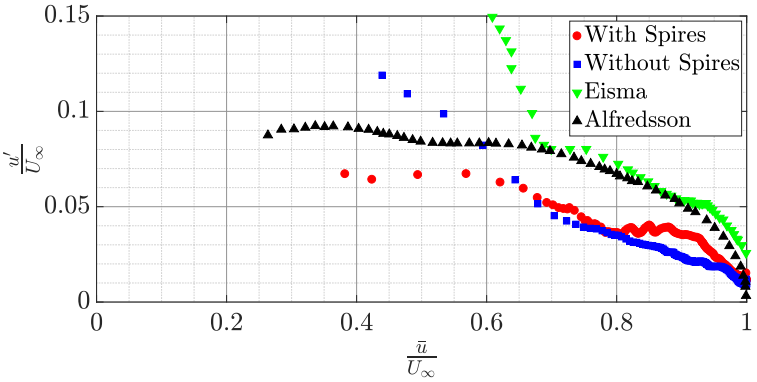

Figure 5.7: Diagnostic plot comparing the mean and fluctuating velocity components. Data from Eisma [14] (specifically 'Exp. 3') and Alfredsson and Örlü [91] (specifically 'Re_θ = 18700') is used here. In comparison, the Re_θ for the case with spires is approximately 18250 and 15750 for the data of Eisma [14].

Another commonly used technique to characterize boundary layers, is by evaluating other properties as listed below, and also summarized by Paterna [94]. These properties are summarized in Table 5.1 and compared with values obtained by Eisma [14].

- The boundary layer thickness (δ_{99}) is arbitrarily defined as the height at which the mean streamwise velocity attains 99% of the free-stream velocity (U_∞). In the current case, U_∞ is determined as the maximum measured streamwise velocity. The δ_{99} value is also compared to the value of 1.1×δ_{90} (δ_{90} is the height at which the streamwise velocity attains 90% of the freestream velocity).
- The displacement thickness (δ^*) is the height by which the surface must be displaced in the wall-normal direction for a frictionless fluid to reach the same flow rate as in the actual flow. Mathematically, it is expressed as $\delta^* = \int_0^{\delta_{99}} \left(1 - \frac{\bar{u}}{U_\infty}\right) dz$.
- The momentum thickness (θ) is the integral of the momentum deficit normalized by the freestream velocity squared, across the ABL. Mathematically, it is expressed as $\theta = \int_0^{\delta_{99}} \left(\frac{\bar{u}}{U_\infty}\right)\left(1 - \frac{\bar{u}}{U_\infty}\right) dz$.
- The shape factor (H) is the ratio between δ^* and θ, often used to monitor flow separation. Mathematically, $H = \frac{\delta^*}{\theta}$.
- The friction velocity (u_*) is a commonly used quantity to non-dimensionalize quantities close to the wall. It is mathematically defined as $u_* = \left(\sqrt{\frac{\tau_s}{\rho}}\right)$, where τ_s is the shear stress on the wall, while ρ is the density of the fluid. There are two ways to evaluate this quantity. The first is by optimizing the u_* values until the difference between the law of the wall ($\overline{u}^+ = \frac{1}{\kappa} \ln z^+ + B$, where κ is the von Kàrmàn constant 0.41 while B is 5.0) and the velocity profile in the inner scaling is minimized. The other way is by evaluating the shear stresses in the logarithmic layer $\left(u_* = \sqrt{|\overline{u'w'}|}\right)$. The former has been utilized in the current analysis.

Table 5.1: Comparison of the boundary layer characteristics. Data from Eisma [14] is also used for comparison. δ_{99}, $1.1\delta_{90}$, δ^* and θ are reported in cm while u_τ and U_∞ are reported in m/s. H is dimensionless.

Case	δ_{99}	$1.1\delta_{90}$	δ^*	θ	H	u_τ	U_∞
Spires	27.55	18.44	3.08	2.47	1.29	0.025	0.739
NoSpires	28.53	13.49	4.20	3.24	1.25	0.026	0.717
Eisma	19.18	11.11	2.70	1.92	1.41	0.030	0.82

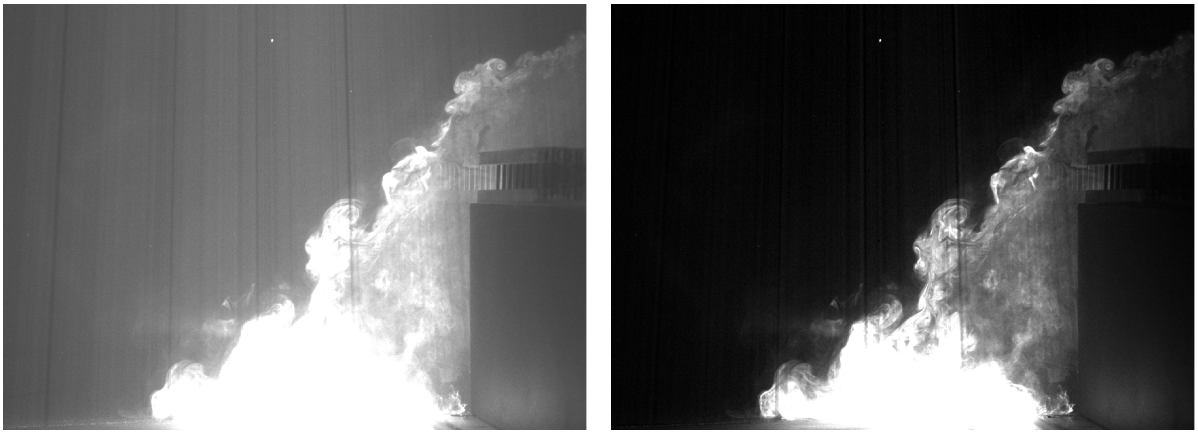

(a) Raw PLIF image with background fluorescence.

(b) PLIF image after subtracting background.

Figure 5.8: Subtraction of background from raw PLIF images to remove background noise. Incoming flow is directed from the left to right. While a scale is not shown, intensity counts vary from 0 to 256.

5.3. Post-processing of the PIV+PLIF experiments

Before proceeding to the analysis of the results from the various parametric studies (the parameters were previously defined in Section 1.3), it is interesting to learn about the post-processing involved with the raw PIV and PLIF data. To be able to read raw PIV and PLIF data into Matlab R2017a, readimx version 2.1 from LaVision GmbH was used.

With respect to the PIV data, a set of vector fields are available and the only modification involves mapping the vector fields from the coarse PIV grid on to the much finer PLIF grid. The interpolation is performed using the cubic spline method, whereas extrapolation is performed using the nearest neighbour technique.

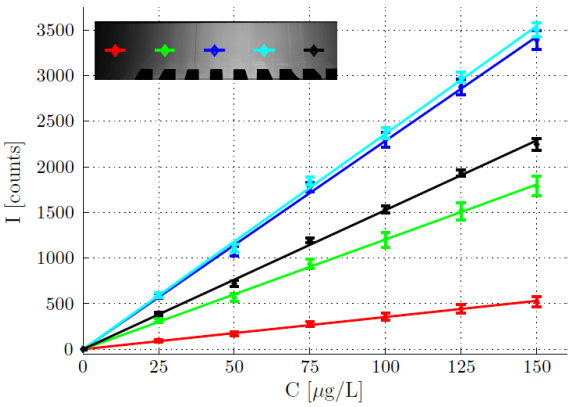

Figure 5.9: Typical calibration curves from a PLIF experiment. Figure reproduced from Eisma [14]. The inset shows the plexiglass container and the locations at which the displayed calibration curves are taken.

The raw PLIF data, I_{raw}, is an array of intensity counts at all pixels across the entire image. The values of these intensity counts range from 0 to 4096 (= 2^{12} for a 12 bit camera). One minor modification is needed, namely, background subtraction. After a few experiments, a noticeable amount of fluorescent dye is present in the water channel. This shows up in the raw PLIF images as background noise, for example in Figure 5.8a. This is taken care of by taking 50 background images before and after an experiment. If the mean of these background images are denoted by BG_{before} and BG_{after} respectively, for an experiment with n images, the intensity map of the i^{th} image ($I(i)$) can be modified to $I_{\text{corrected}}$ through the following expression in Equation (5.9). The aforementioned PLIF image would then be transformed to Figure 5.8b. The

intensity maps can be modified into concentration maps via calibration, but this has not been used in the current experiments for reasons explained later. However, typical calibration curves are shown in Figure 5.9.

$$I_{\text{corrected}}(i) = I_{\text{raw}}(i) - \left(\frac{i-1}{n-1} BG_{\text{after}} + \frac{n-i}{n-1} BG_{\text{before}} \right) \tag{5.9}$$

Once, both, the velocities ($\vec{U}$) and corrected intensities (I) are available, further processing can be performed with respect to evaluating the performance of the ESP. The intensity based flux of the fluorescent dye ($I\vec{U} \cdot \vec{n}$) is the product of the dye intensity and the velocity. $\vec{n}$ is the normal on a surface of a control volume of interest.

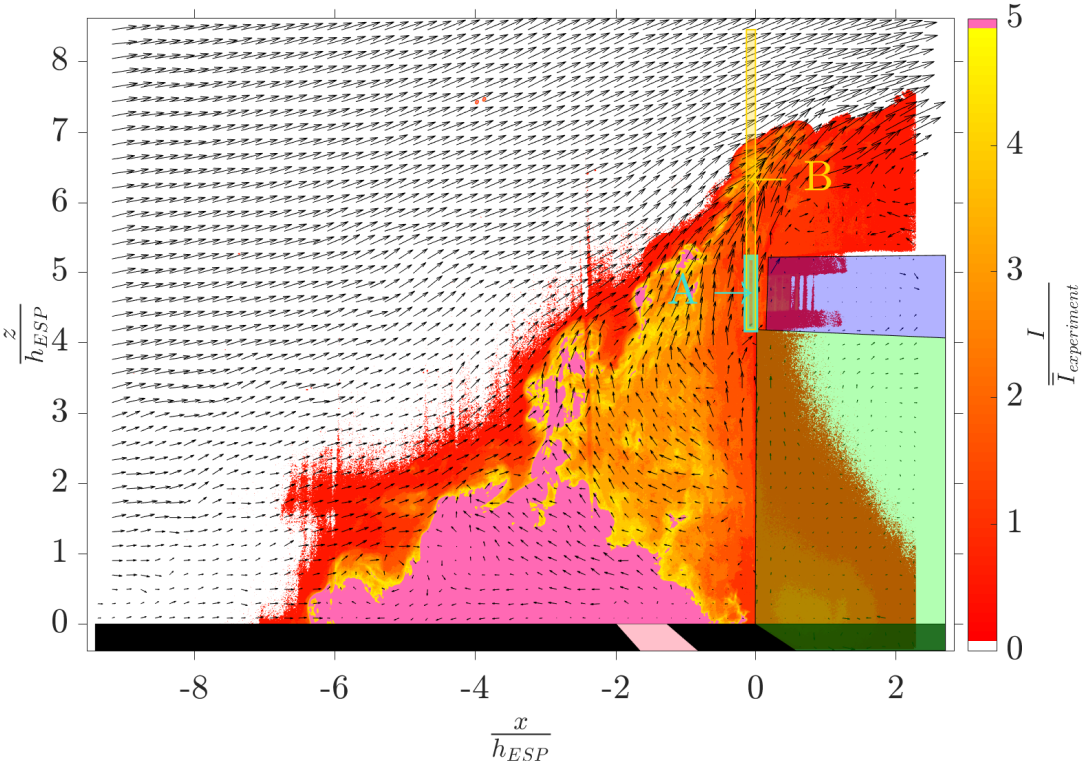

Figure 5.10: Definition of the aerodynamic efficiency of the ESP. Shown in this figure are the instantaneous velocity vectors as well as contours of the recorded instantaneous dye intensity. Every third velocity vector (in each direction) is shown. The ground is depicted in black with the location of the line source in pink. The area in light green is the fence while the area in light blue is the ESP. Velocity vectors in the light green and light blue patches are the vectors corresponding to those downstream of the fence and the ESP respectively. Shown also are the rectangular areas, A and B (in turquoise and gold respectively), used to evaluate the efficiency. This image is taken from Run 1 of the experiment with a 3 cm high SB (h_{SB} = 2.56h_{ESP}).

Figure 5.10 aids understanding the scenario better. The physical coordinates are normalized by the height of the ESP (h_{ESP}) with the origin located at the intersection between the ground and the SB. The intensities are normalized by the spatio-temporal average of the intensities ($\bar{I}_{experiment}$) for the experiment an image belongs to. The effect of intangible parameters such as size of the efficiency evaluation domain and experiment acquisition time is the topic of Appendix D.

In the bigger picture, the quantity of interest is the aerodynamic efficiency of the ESP. All of the dye released from the line source is expected to leave from the cross-section B (shown in gold) in Figure 5.10, with a fraction of it entering the cross-section in front of the ESP (shown in turquoise). The aerodynamic efficiency (η_{ESP}) is defined as the percentage of intensity flux entering the ESP (section

A in Figure 5.10) in comparison to that leaving the entire cross-section (section B in Figure 5.10). This is mathematically expressed according to Equation (5.10).

The efficiency obtained would be even more accurate if actual concentration fluxes were used instead of the intensity counts based fluxes. With the aid of Equation (4.5), Equation (5.10) can be modified into the form of Equation (5.11). A typical image for calibration curves is shown in Figure 5.9. It can be seen that for areas with near uniform laser intensity, I_0, the calibration curves are nearly alike. The current experiments involve a much smaller field of view than that employed by Eisma [14]. This leads to the laser intensity profiles being much more uniform across the aforementioned cross section B (and thus, cross section A), as also evident from Figure 5.8a. It can be expected that the calibration coefficients ($\alpha_{A,B}$) are nearly alike and their effect may be neglected in Equation (5.11), which results in Equation (5.10). However, verification is needed to understand the impact of the calibration coefficients.

$$\eta_{ESP} = \frac{(I\vec{U} \cdot \vec{n})_A}{(I\vec{U} \cdot \vec{n})_B} \tag{5.10}$$

$$\eta_{ESP} = \frac{(I\vec{U} \cdot \vec{n})_A}{(I\vec{U} \cdot \vec{n})_B} \times \frac{(I_0\alpha)_B}{(I_0\alpha)_A} \tag{5.11}$$

In Figure 5.10, results from a single instantaneous image is shown. Since multiple images are captured in a single experiment, statistics from all the images can be used for further analysis. Time-averaged quantities across the cross-section B from Figure 5.10 can be plotted. For such plots, the zero of the z_{SB} coordinate is located on top of the respective SB.

One such example is shown in Figure 5.11. In this plot, the mean horizontal velocity, dye intensity, the intensity based flux and the potential ESP efficiency at a certain height are shown. A boundary layer like horizontal velocity profile is visible. On the other hand, the dye intensity decreases with increasing height. The product of these two quantities returns the intensity based flux. The latter quantity, a potential efficiency of the ESP at a certain height (since there is no ESP at each wall-normal coordinate), is defined according to Equation (5.12). The potential efficiency at a given height, $\eta_{potential}(z_{SB})$, is the amount of pollutant flux passing through a hypothetical ESP centered at that location as a fraction of the pollutant flux leaving the height of the entire cross-section above the fence (h_B). Due to this averaging, the ESP efficiency curve strongly correlates with the profile of the intensity based flux, but is much smoother.

Finally, a histogram of instantaneous efficiencies can be plotted, along with a fitted probability distribution function. A kernel distribution is used to fit the probability density function curve through the histogram. An example is shown in Figure 5.12.

$$\eta_{potential}(z_{SB}) = \frac{\sum_{z_{SB}-0.5*h_{ESP}}^{z_{SB}+0.5*h_{ESP}} (I\overline{u})}{\sum_{0}^{h_B} (I\overline{u})} \tag{5.12}$$

5.4. Factors affecting the aerodynamic efficiency of the ESP

In this section, a few factors affecting the aerodynamic performance of the ESP shall be looked into. At first, the pollutant dispersion over fences with different heights, without any ESP, is discussed in Section 5.4.1. This is followed by a discussion on the influence of an additional ESP on top of the SB in Section 5.4.2. The effect of installing the ESP at a location higher than the SB top is looked into in Section 5.4.3. Finally, the performance of the ESP in the 'highway canyons' formed by two SBs is looked into in Section 5.4.4. The different cases considered here are illustrated in Figure 5.13.

The repeatability of the experiments is looked into for a couple of cases in Appendix E. The results shown in this section in visual forms are also tabulated in Appendix F. Lastly, typical flow statistics around a SB with an ESP atop is shown in Appendix G.

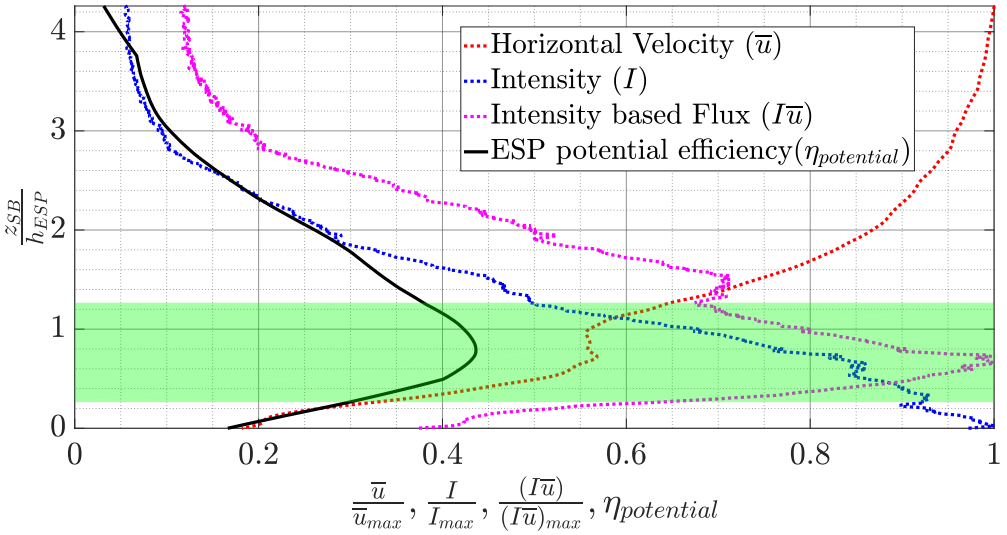

Figure 5.11: Profiles of various quantities above the sound barrier. z_{SB} is the coordinate axis in the wall-normal direction with the zero located at the top of the fence. The light green patch represents the area equal to the ESP entrance through which the maximum flux of pollutants pass through i.e. maximum potential efficiency. The data shown here corresponds to the experiment considered in Figure 5.10.

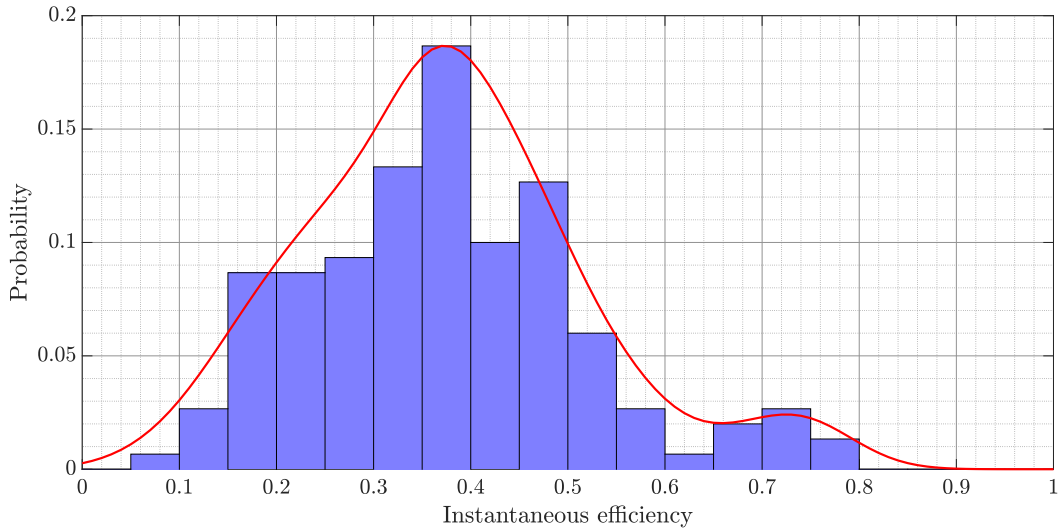

Figure 5.12: A histogram of instantaneous efficiencies at the ESP entrance, along with a kernel distribution fitted probability distribution function, from a single experiment. The data shown here corresponds to the experiment considered in Figure 5.10.

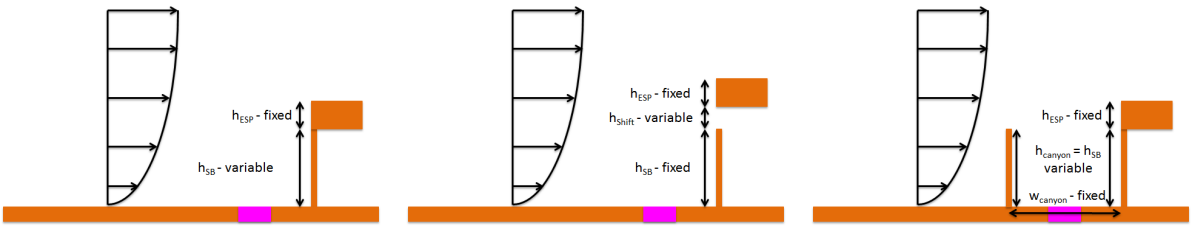

(a) Varying fence height with the ESP on top. Corresponding discussion in Section 5.4.2.

(b) Vertically displacing the ESP with a fixed fence. Corresponding discussion in Section 5.4.3.

(c) Changing fence height in a canyon with a fixed width and an ESP on top of the downstream fence. Corresponding discussion in Section 5.4.4.

Figure 5.13: Schematics of the different cases considered.

5.4.1. Shorter fences seem ideal for ESP installation

It is known that the SB height has a major influence in the vertical dispersion of pollutants released from a freeway. A taller SB will result in a higher vertical dispersion of the pollutant leading to reduced peak concentrations downstream of the SB. The effect of the SB height on the pollutant dispersion can be qualitatively observed in Figure 5.14. As the SB height increases, the mean separation bubble height increases as well, which creates an impenetrable region for the incoming flow. As the size of this impenetrable region increases, the angle at which the flow separates increases too, leading to a higher vertical dispersion of the pollutants.

The above explanation can also be observed in the plots shown in Figure 5.15a. While the velocity profiles are similar in nature, especially in the outer region, a strong variation in the intensity profiles is visible. For example, for the case of the tallest SB ($h_{SB} = 4.27h_{ESP}$), the normalized intensity profile decays to 20% of the maximum value at a height nearly four times more than the case of the shortest fence ($h_{SB} = 0.85h_{ESP}$). This also explains the larger vertical spread and the upward shift in the peaks of the intensity based flux curve as well as the potential efficiency curve in the wall-normal direction, also shown in Figure 5.15a.

Shown in Figure 5.15b are probability distribution functions of several quantities at the entrance of a hypothetical ESP located flush on top of the SB. There is a clear indication that installing a ESP of a fixed design is more effective on a shorter fence than on a taller one. While there is no discernible effect of the fence height on the normalized incoming flow velocity, according to Figure 5.15b, this could help determining the wind speed at the ESP inlet for real atmospheric conditions. This wind velocity could then be used for evaluating the collection efficiency. However, as anticipated from the velocity vectors in Figure 5.14, the angle of the flow in front of the hypothetical ESP reduces with the fence height contributing to the increased efficiency of the product.

The important statistics concerning the performance of a hypothetical ESP are summarized in Figure 5.15c. These too, like the probability distribution functions, suggest that, upon increasing the size of the SB, the aerodynamic performance of the ESP would decrease, with the flow angle becoming less horizontal, leading to the pollutants grazing past the ESP.

5.4.2. Shorter fences are indeed more effective for ESP installation

In Section 5.4.1, it was observed that the addition of an ESP would be most effective on top of a shorter ESP. To validate this hypothesis, the aerodynamic performance of the ESP was observed by installing the model ESP on top of the model SBs. The effect of addition of the ESP on top of the fence on the flow field and dye dispersion is shown in Figure 5.16. A similar trend in the increase of the mean upstream separation bubble size is observed upon increasing the size of the SB. It is expected that the addition of the ESP would act as a de facto increase in the SB height, and thus lead to an increase in the separation bubble size. It should be noted that all the results for the 3 cm and 5 cm high SB (h_{SB} = $2.56h_{ESP}$ and h_{SB} = $4.27h_{ESP}$) are ensemble averages of the five runs, shown in Appendix E.

From the line plots for the horizontal velocity component, shown in Figure 5.17a, higher velocities at the location of the ESP are observed for the shorter SBs, which was not the case when the ESP was absent. This is also visible in the probability distribution functions in Figure 5.17b. This could be attributed to the increased resistance to the flow approaching at a rather large angle. Another visible aspect from the time-averaged dye intensity profiles above the SB is the faster decay observed for shorter SBs. Like the case without an ESP, a clear flattening of the velocity vectors is observable upon decreasing the SB height. There are also instances with negative horizontal velocities which correspond to instances with flow angles larger than 90°, or the ESP behaving as an impenetrable obstacle. The above factors combine to improve the aerodynamic efficiency of the ESP on top of the shorter fences.

The addition of the ESP is expected to act as an additional resistance to the flow. This is visible as lower horizontal velocities and larger flow angles in front of the ESP as compared to the case without the ESP. These two have countering effects. The higher angles would lead to an increased vertical dispersion of the pollutants, i.e. inhibit aerodynamic efficiency, while the reduced velocities could enhance the collection efficiency of the ESP. Another aspect that could play a role is the placement of the line source relative to the SB (fixed at $1.7h_{ESP}$ upstream of the SB). If the line source were to placed

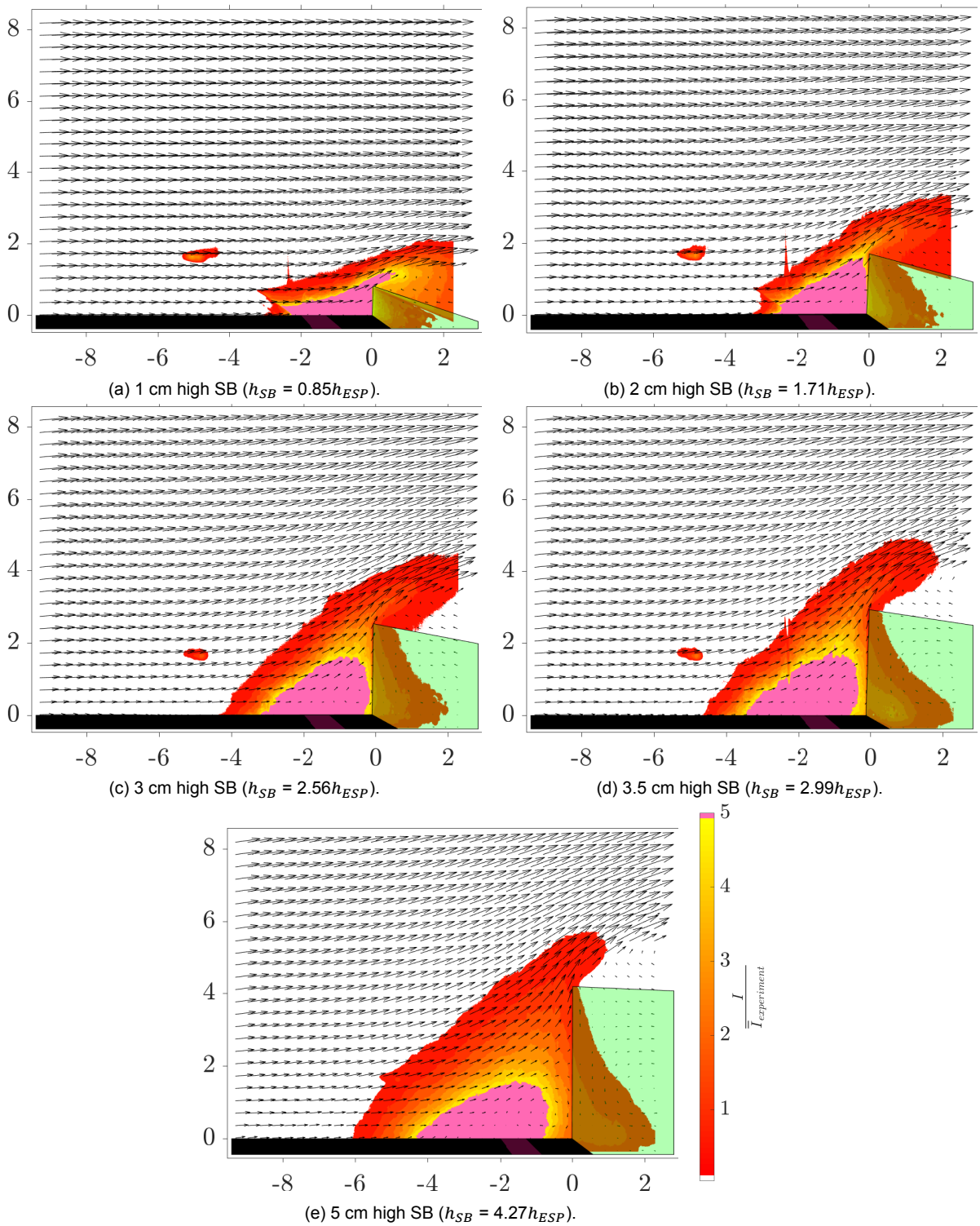

(a) 1 cm high SB (h_{SB} = 0.85h_{ESP}).

(b) 2 cm high SB (h_{SB} = 1.71h_{ESP}).

(c) 3 cm high SB (h_{SB} = 2.56h_{ESP}).

(d) 3.5 cm high SB (h_{SB} = 2.99h_{ESP}).

(e) 5 cm high SB (h_{SB} = 4.27h_{ESP}).

Figure 5.14: Pollution dispersion around sound barriers of different heights. Contours of the mean dye intensity and mean velocity vectors are shown. Every fifth vector, in each direction, is displayed. The x and y axes in these plots represent $\frac{x}{h_{ESP}}$ and $\frac{z}{h_{ESP}}$ respectively.

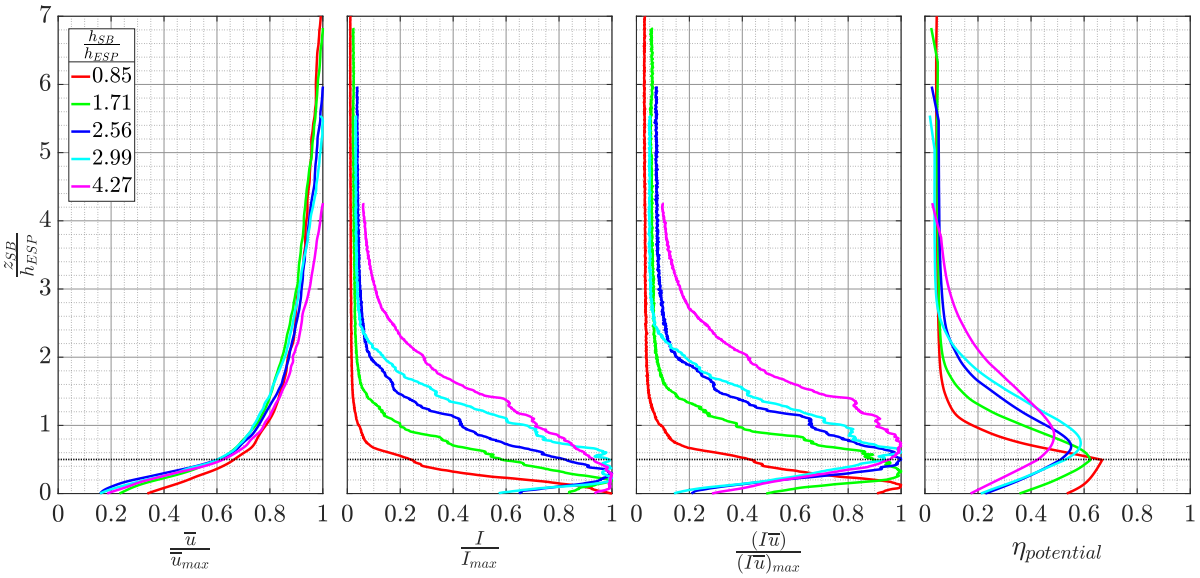

(a) Profiles of various normalized quantities. The black dotted line represents the location of centerline of the hypothetical ESP.

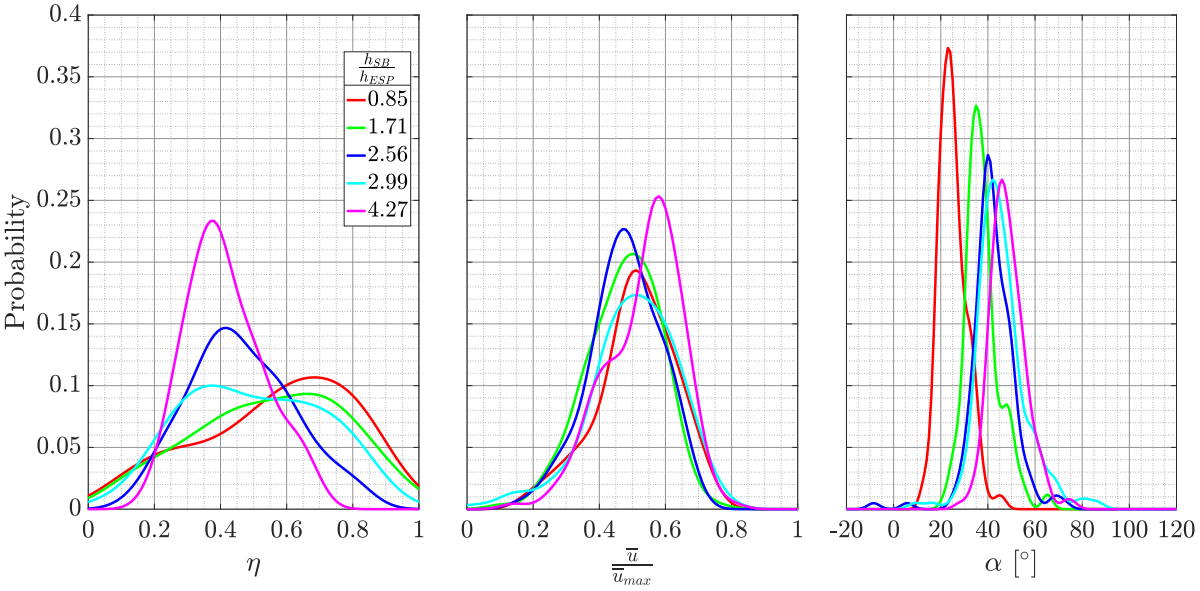

(b) Probability Distribution Functions of various quantities in front of the entrance of a hypothetical ESP placed just on top of the SB.

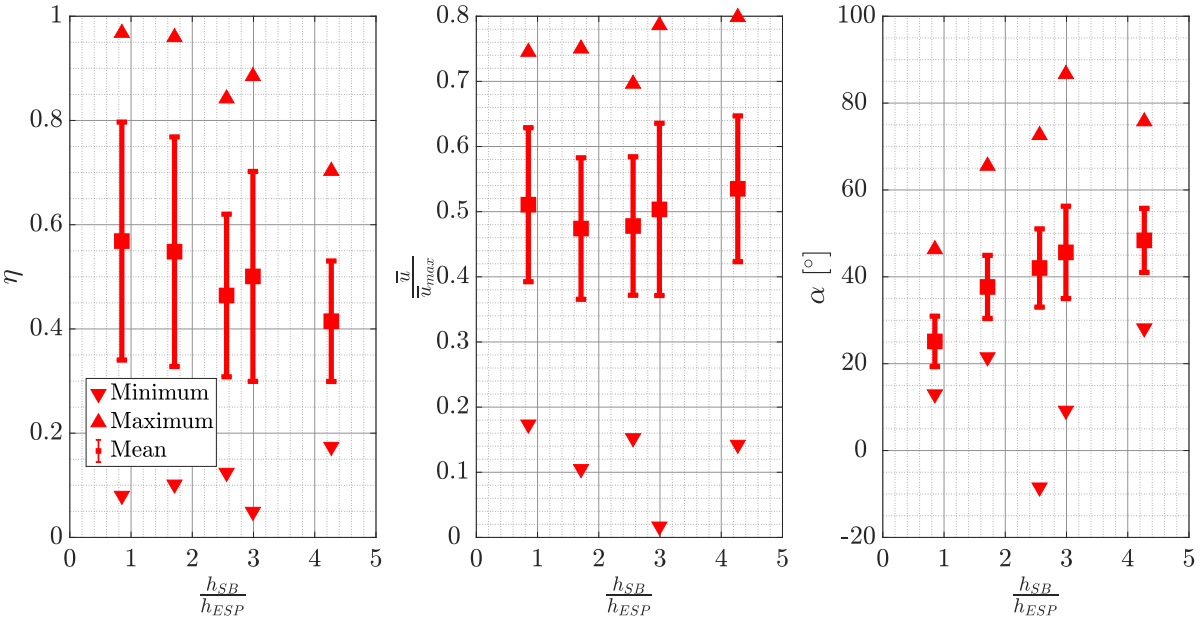

(c) Statistics on the inflow characteristics and performance of the hypothetical ESP. Errorbars indicate standard deviation.

Figure 5.15: Pollution dispersion characteristics for different sound barriers and no ESP atop.

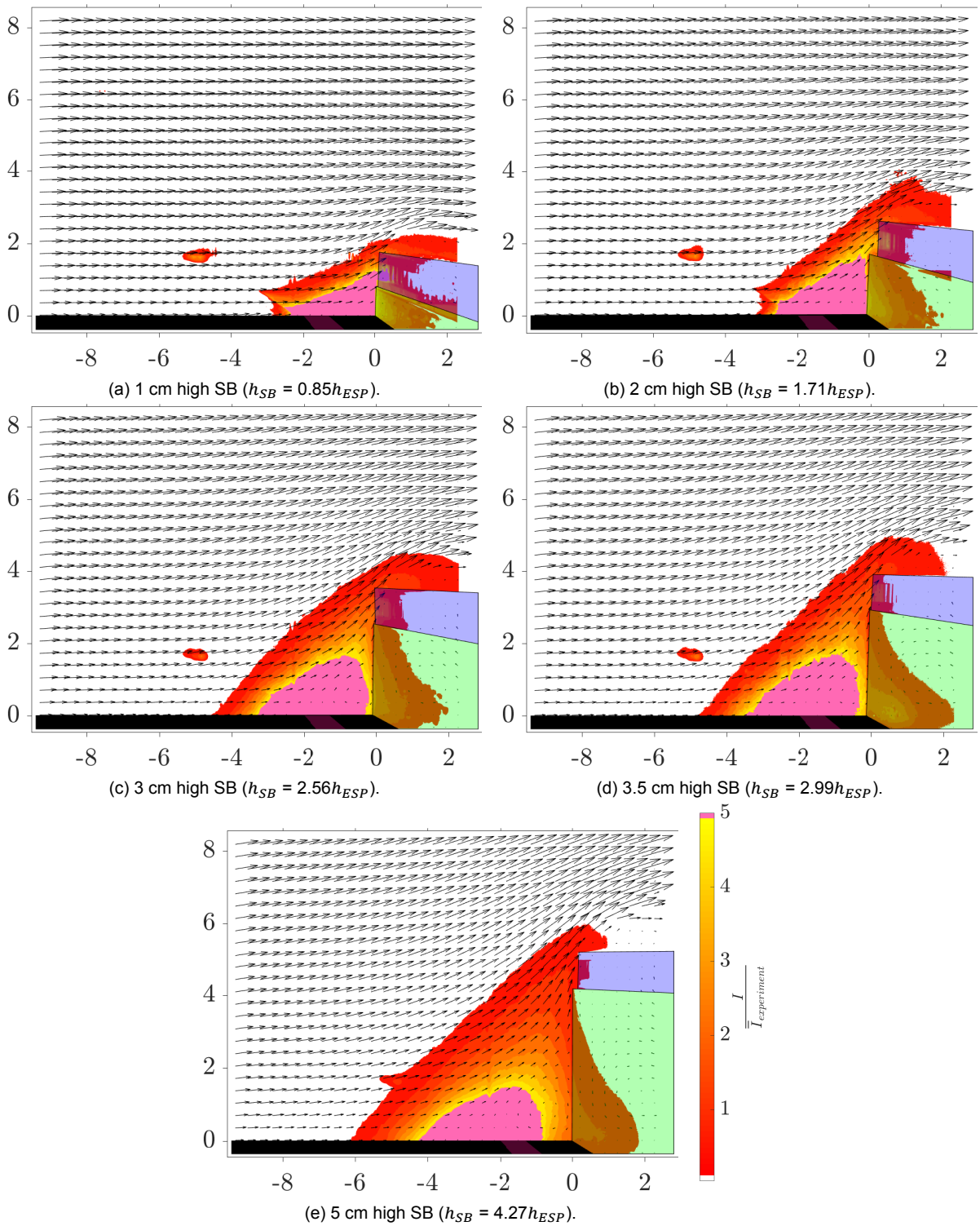

(a) 1 cm high SB (h_{SB} = 0.85h_{ESP}).

(b) 2 cm high SB (h_{SB} = 1.71h_{ESP}).

(c) 3 cm high SB (h_{SB} = 2.56h_{ESP}).

(d) 3.5 cm high SB (h_{SB} = 2.99h_{ESP}).

(e) 5 cm high SB (h_{SB} = 4.27h_{ESP}).

Figure 5.16: Pollution dispersion around sound barriers of different heights and an ESP atop. Contours of the mean dye intensity and mean velocity vectors are shown. Every fifth vector, in each direction, is displayed. The x and y axes in these plots represent $\frac{x}{h_{ESP}}$ and $\frac{z}{h_{ESP}}$ respectively.

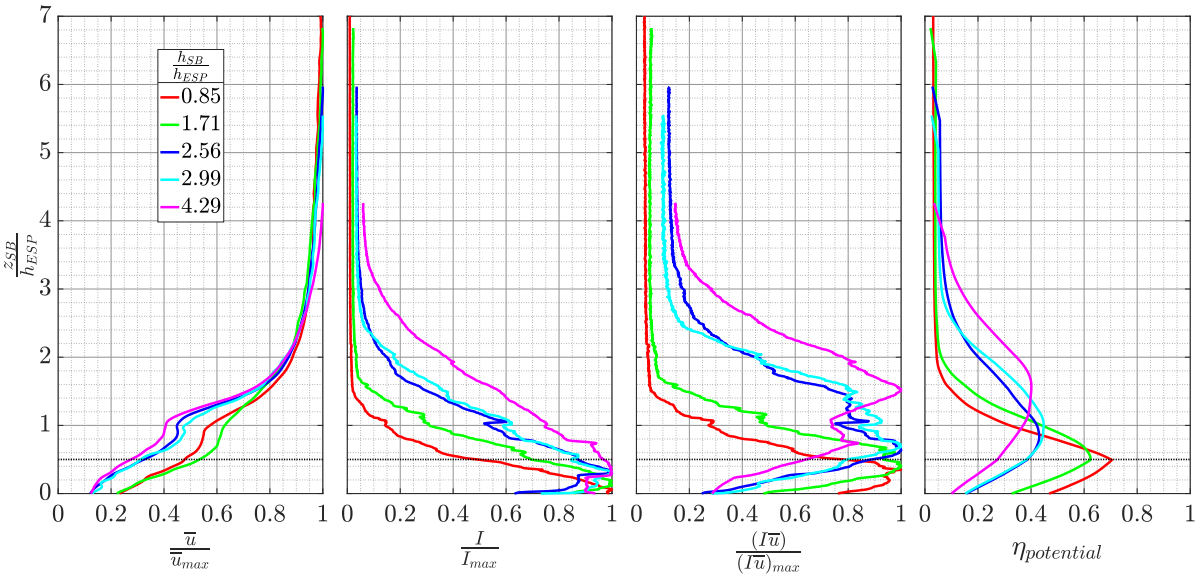

(a) Profiles of various normalized quantities. The black dotted line represents the location of the centerline of the ESP.

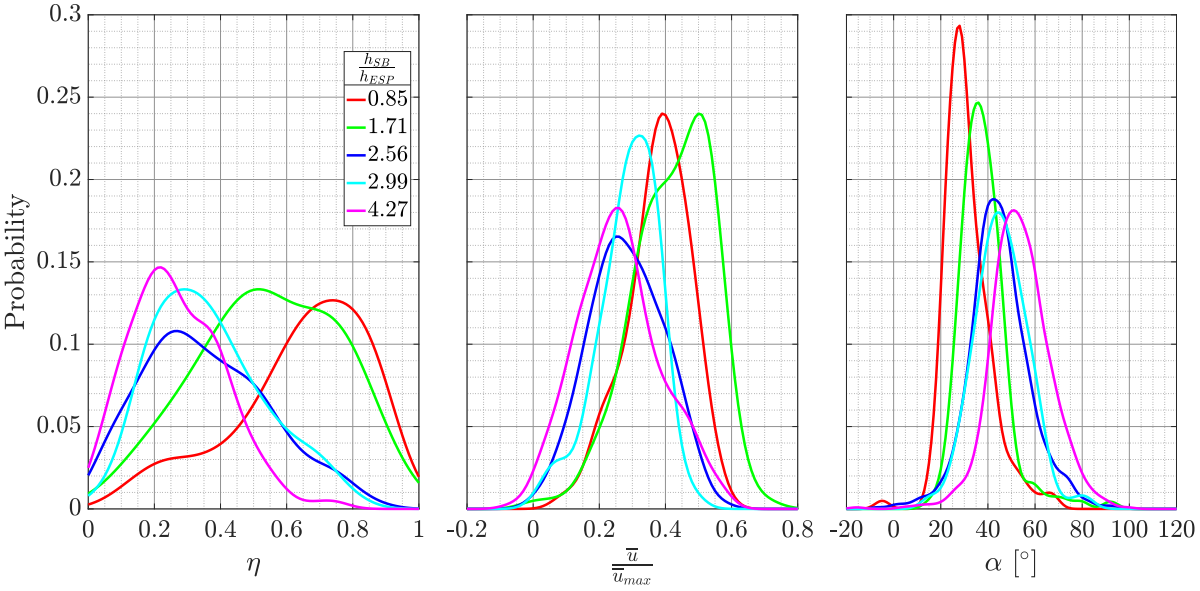

(b) Probability Distribution Functions of various quantities in front of the entrance of an ESP placed on top of the SB.

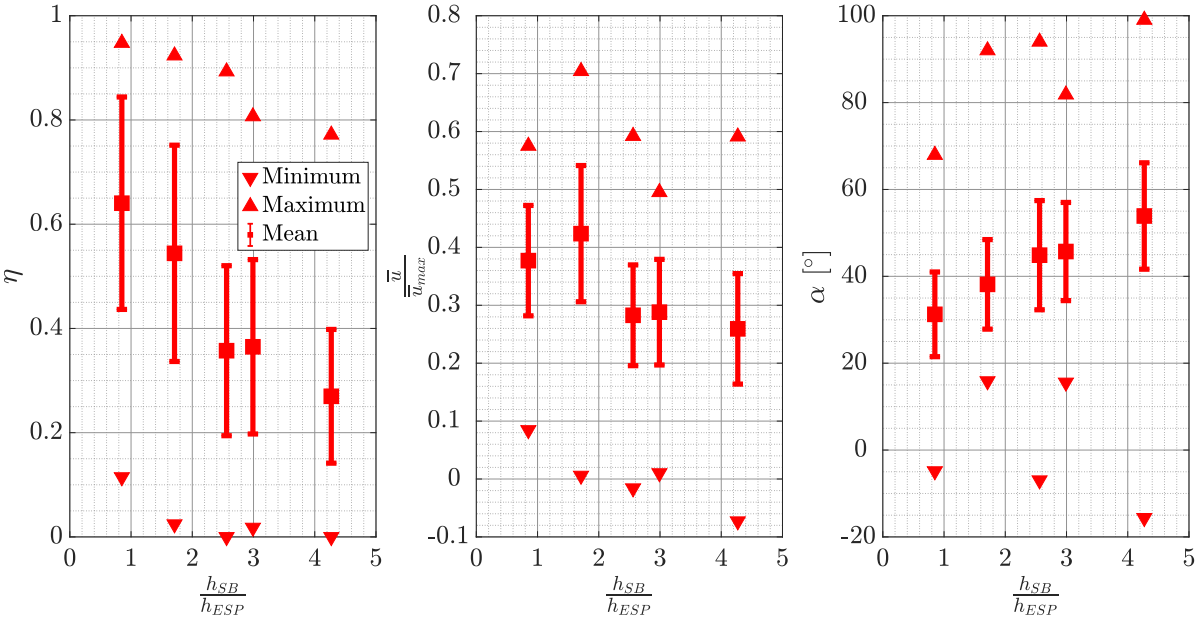

(c) Statistics on the inflow characteristics and performance of the ESP.

Figure 5.17: Pollution dispersion characteristics just in front and above the sound barrier for different barrier heights and an ESP atop.

outside the limits of the time-averaged separation bubble, it could be expected that the dye would be less subject to the turbulence of the bubble which would decrease the intermittency at which the dye escapes the freeway. An instantaneous separation bubble larger than the mean separation bubble would result in an upstream burst of dye and lead to a higher vertical dispersion of the dye, leading to an expected decrease in instantaneous aerodynamic efficiency.

Lastly, the major aspects of the ESP aerodynamic performance are summarized in Figure 5.17c. A sharper drop in the mean efficiency (65% - 25%) is observed with the ESP as compared to the previous case with the hypothetical ESP (55% to 40%) which could be attributed to the indented horizontal velocity profiles in front of the ESP (due to the resistance provided by it).

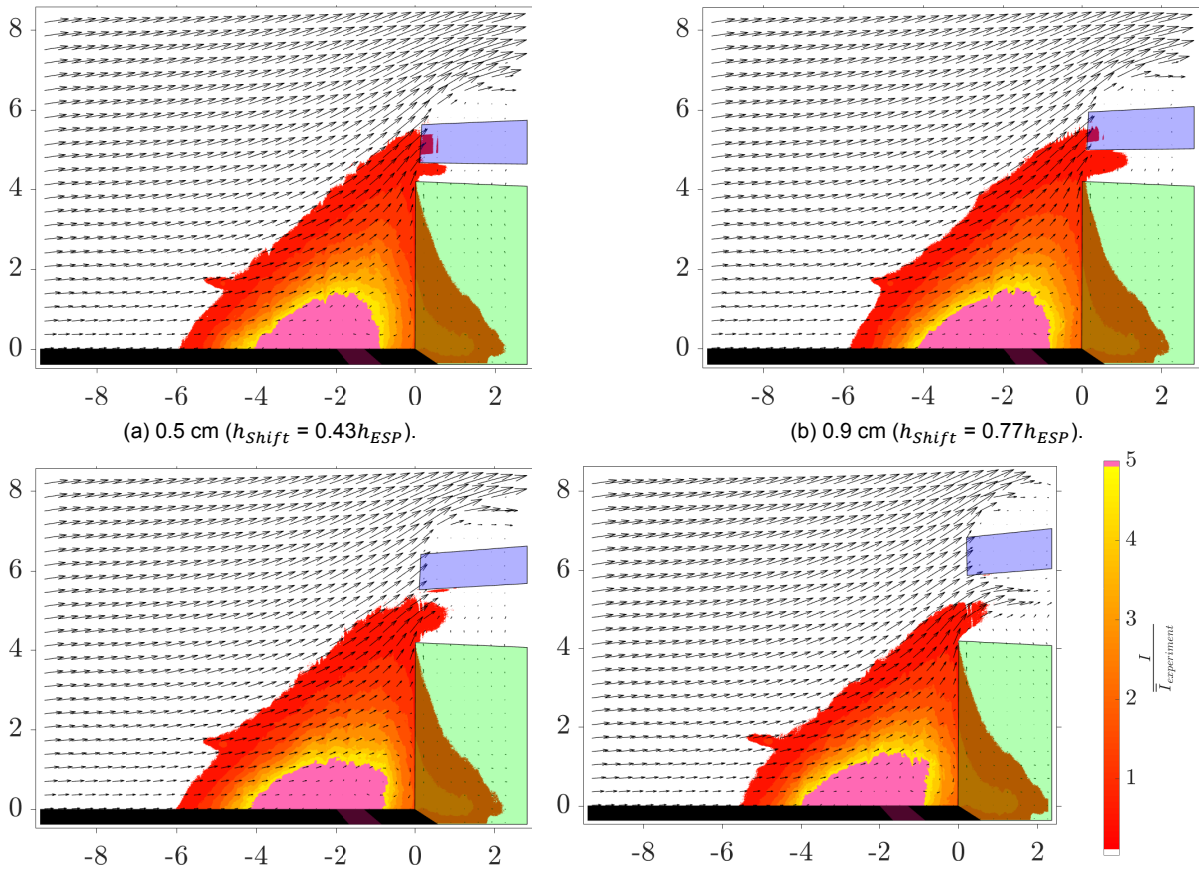

(a) 0.5 cm (h_{Shift} = 0.43h_{ESP}).

(b) 0.9 cm (h_{Shift} = 0.77h_{ESP}).

(c) 1.5 cm (h_{Shift} = 1.28h_{ESP}).

(d) 2.0 cm (h_{Shift} = 1.71h_{ESP}).

Figure 5.18: Pollution dispersion for different cases of vertical displacement of the ESP on top of a 5 cm high SB (h_{SB} = 4.27h_{ESP}). Contours of the mean dye intensity and mean velocity vectors are shown. Every fifth vector, in each direction, is displayed. The x and y axes in these plots represent $\frac{x}{h_{ESP}}$ and $\frac{z}{h_{ESP}}$ respectively.

5.4.3. Slightly raising the ESP improves aerodynamic performance (at least for relatively taller sound barriers)

As a next parameter, the effect of raising the ESP relative to the top of the SB is considered. The height of the SB is fixed while the ESP is moved around. h_{Shift} is used to denote the vertical displacement of the ESP with respect to the top of the SB. This was tested for two different SB heights (h_{SB} = 4.27h_{ESP} and h_{SB} = 2.56h_{ESP}). All results with zero shift are ensemble averages of the five runs shown in Appendix E.

The case with the 5 cm high SB (h_{SB} = 4.27h_{ESP}) is considered first. The dye intensity contour plots combined with the velocity vectors for this case are shown in Figure 5.18, for different (non-zero) vertical shifts of the ESP. At the very least, it can be concluded that displacing the ESP too much would

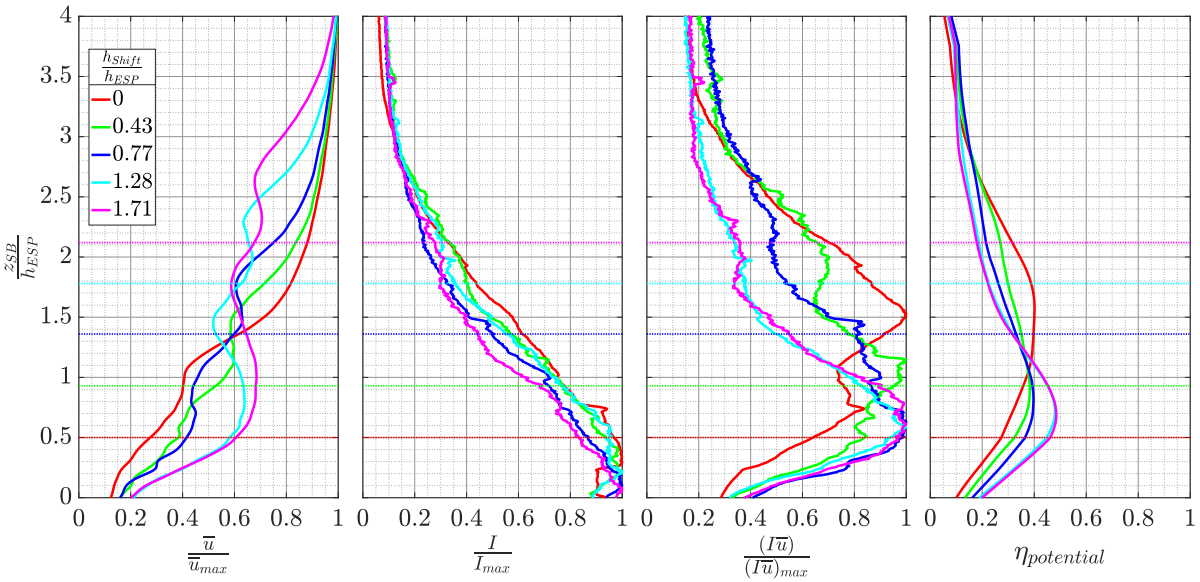

(a) Profiles of various normalized quantities. The horizontal dotted lines denote the location of the ESP centerline location corresponding to its respective color.

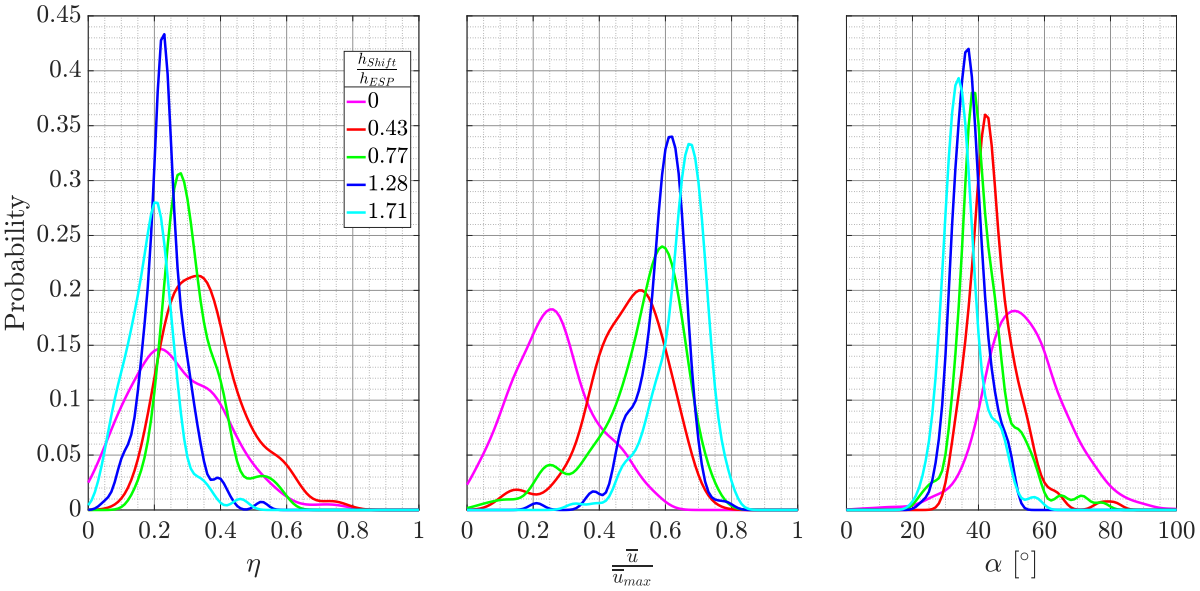

(b) Probability Distribution Functions of various quantities in front of the entrance of the ESP.

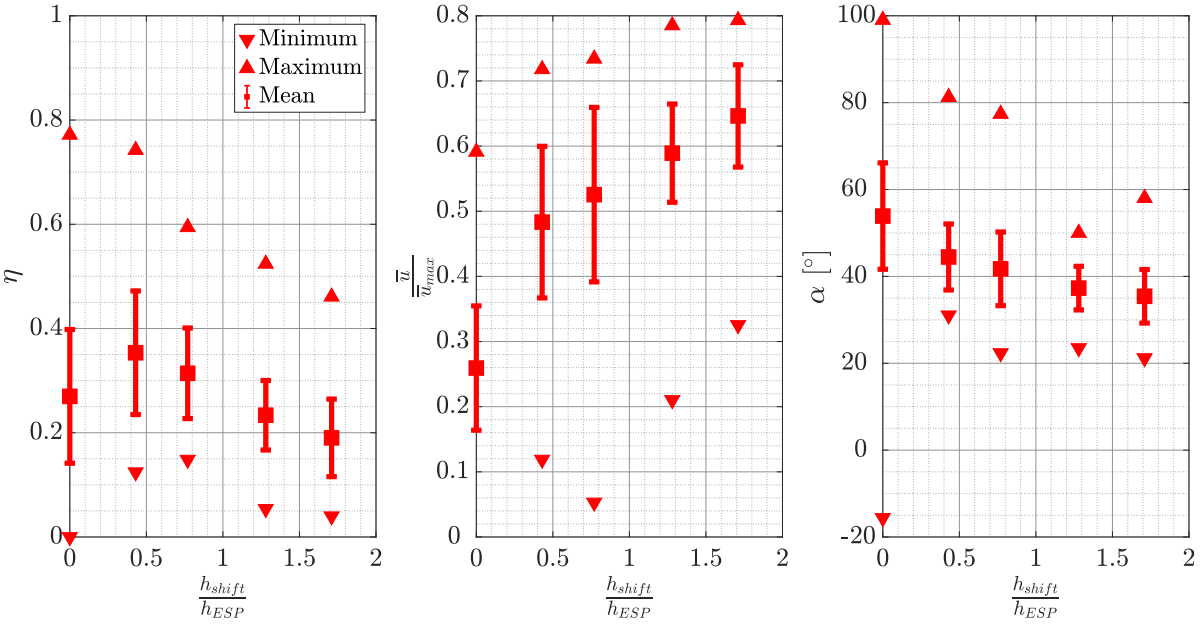

(c) Statistics on the inflow characteristics and performance of the ESP.

Figure 5.19: Pollution dispersion characteristics just in front and above the sound barrier for different vertical displacements of the ESP on top of a 5 cm high fence (h_{SB} = 4.27h_{ESP}).

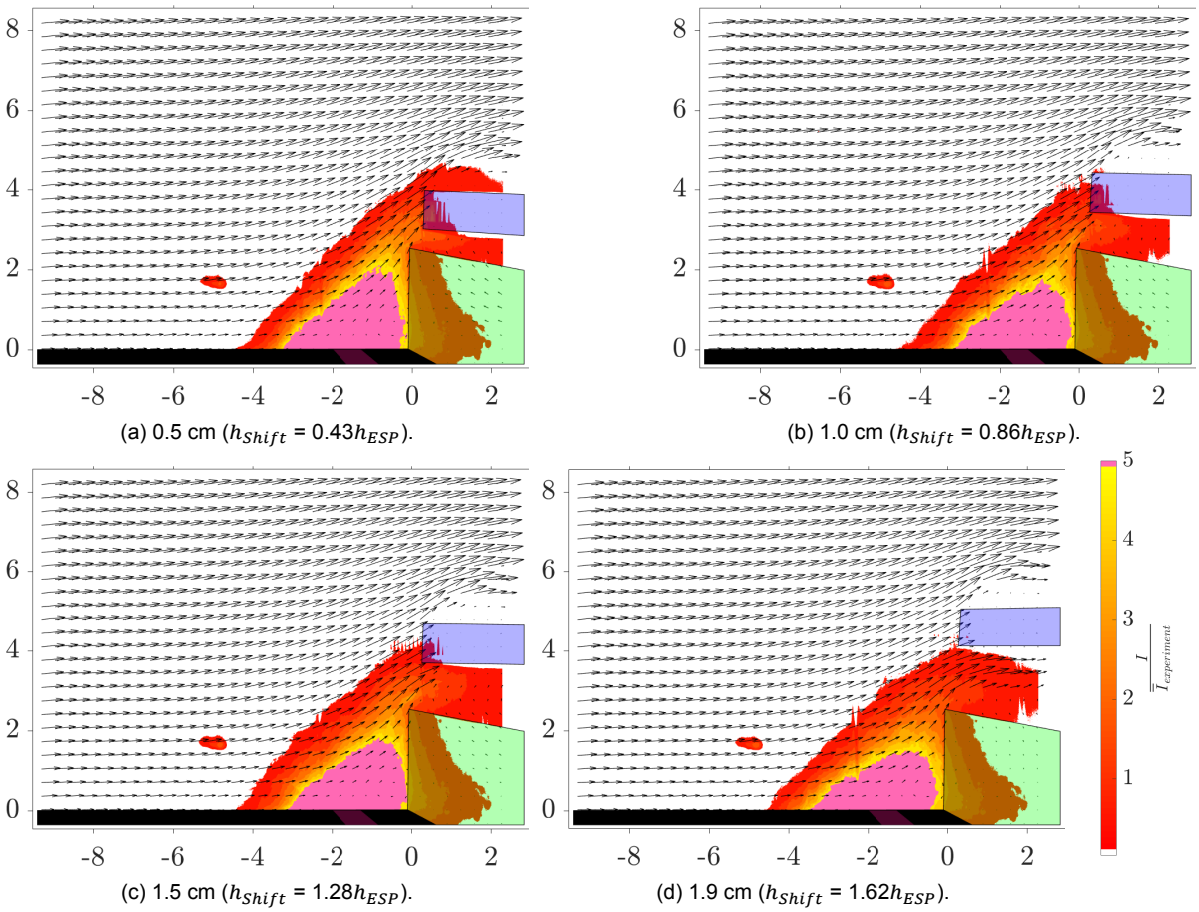

(a) 0.5 cm (h_{Shift} = 0.43h_{ESP}). (b) 1.0 cm (h_{Shift} = 0.86h_{ESP}).

(c) 1.5 cm (h_{Shift} = 1.28h_{ESP}). (d) 1.9 cm (h_{Shift} = 1.62h_{ESP}).

Figure 5.20: Pollution dispersion for different cases of vertical displacement of the ESP on top of a 3 cm high SB (h_{SB} = 2.56h_{ESP}). Contours of the mean dye intensity and mean velocity vectors are shown. Every fifth vector, in each direction, is displayed. The x and y axes in these plots represent $\frac{x}{h_{ESP}}$ and $\frac{z}{h_{ESP}}$ respectively.

result in an escape of a larger proportion of the dye from the gap between the ESP and the top of the SB, resulting in an expected reduction in the aerodynamic efficiency.

The shifting of the ESP in the vertical direction disturbs the smoothness of the boundary layer like velocity profile that is obtained without any displacement of the ESP (h_{Shift} = 0h_{ESP}). The velocity values increase along the wall-normal direction with sharp drops at the edges of the impenetrable outer casing of the ESP, as seen in Figure 5.19a. As the vertical displacement of the ESP is increased, the amount of dye present in front of the ESP entrance drops. However, from the time-averaged efficiency profiles along the wall-normal, it is evident that the ESP location is closer to the peaks of theses curves for the vertical displacements of 0.5 cm and 0.9 cm (h_{Shift} = 0.43h_{ESP} and h_{Shift} = 0.77h_{ESP} respectively).

The increased efficiencies for the cases h_{Shift} = 0.43h_{ESP} and h_{Shift} = 0.77h_{ESP}, are also visible in the efficiency probability distribution function plots in Figure 5.19b. Another striking observation is the near twofold increase in the horizontal velocity component aided by a reduction of the flow angle by 10° (a contribution of a factor of 1.4) by only slightly raising the ESP. These two factors can lead to an increase in the aerodynamic performance of the ESP. However, the increased incoming velocities may result in reduced collection efficiencies. The slight upward displacement of the ESP creates a small gap between the ESP and the SB, which reduces the streamwise resistance to the dye flow. However, due to the relative small size of this gap along with the high angle of the velocity vectors in front of this gap, only a small fraction of the dye is able to escape this region. Nevertheless, this small gap helps in flattening out the velocity vectors and increasing the horizontal velocity components. On the other end, if the ESP is displaced too much, the gap created is rather large allowing for a generous amount of the dye to escape which diminishes the aerodynamic effectiveness of the ESP. The important statistics

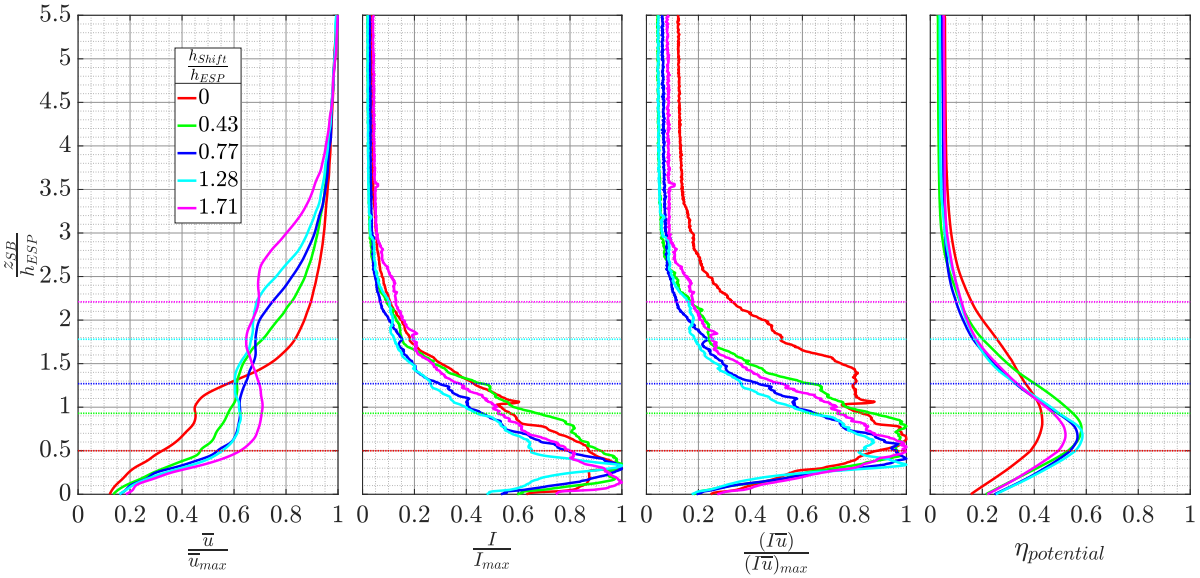

(a) Profiles of various normalized quantities. The horizontal dotted lines denote the location of the ESP centerline location corresponding to its respective color.

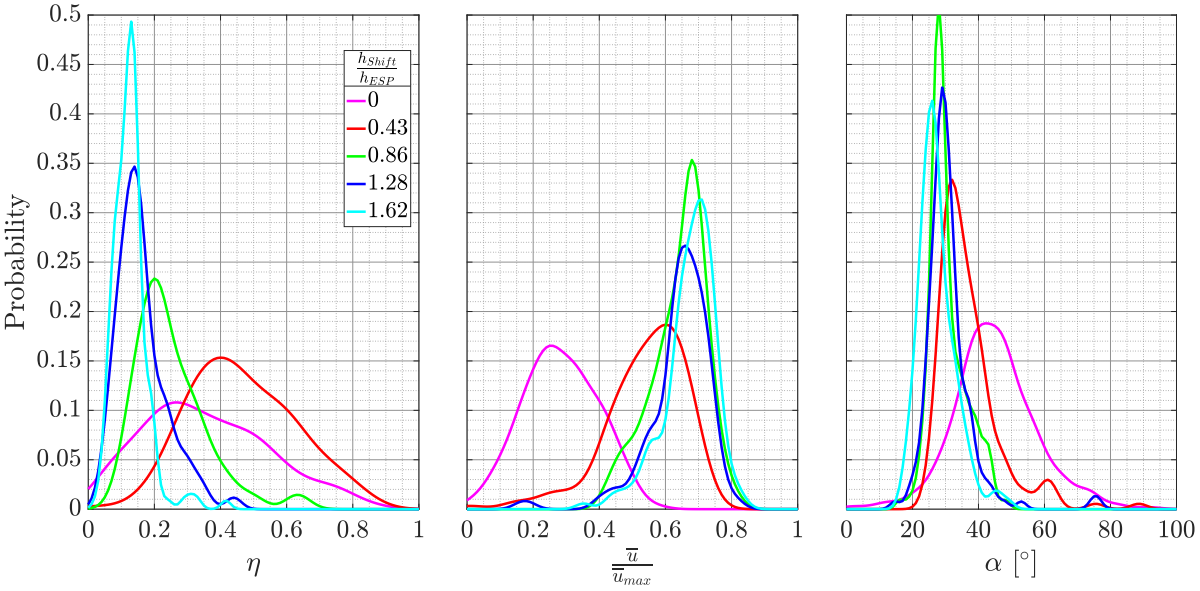

(b) Probability Distribution Functions of various quantities in front of the entrance of the ESP.

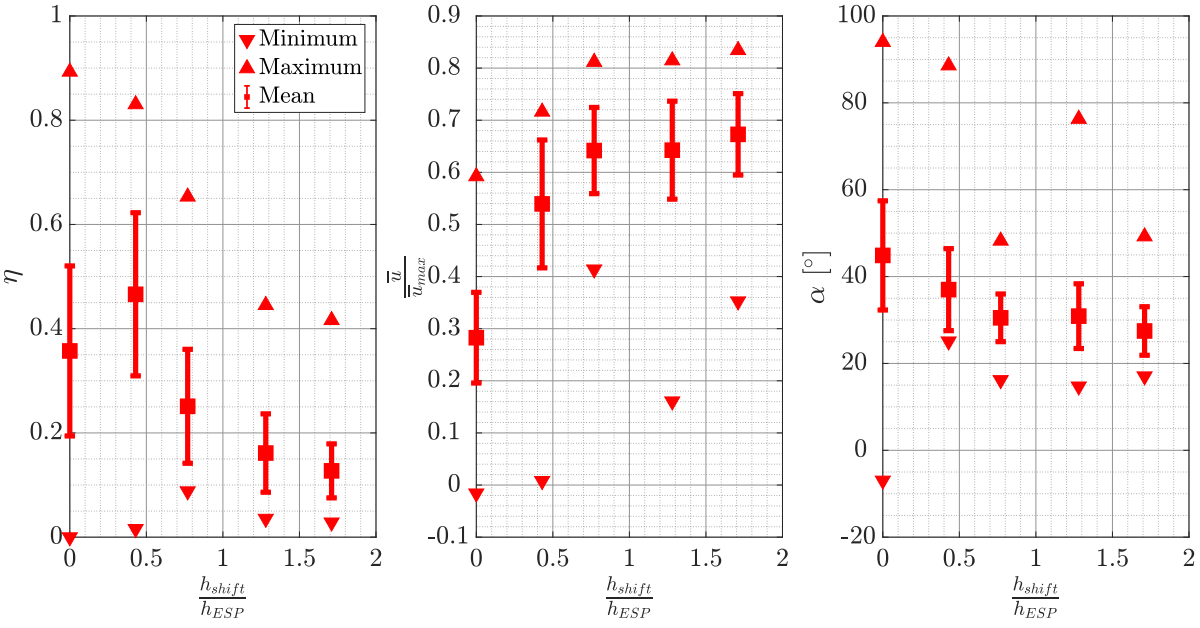

(c) Statistics on the inflow characteristics and performance of the ESP.

Figure 5.21: Pollution dispersion characteristics just in front and above the sound barrier for different vertical displacements of the ESP on top of a 3 cm high fence (h_{SB} = 2.56h_{ESP}).

concerning the ESP aerodynamic performance are summarized in Figure 5.19c.

The corresponding results for the 3 cm high SB (h_{SB} = 2.56h_{ESP}) are shown in Figures 5.20 and 5.21. The conclusion for this case is the same as for the previous one, where slightly raising the ESP improves the aerodynamic performance of the ESP. However, it is doubtful whether this 'rule of thumb' of slightly raising the ESP is applicable to the cases of the shortest fences. In these cases, the maximum quantity of the dye is already reaching the entrance of the ESP as seen from the results in Section 5.4.2. Raising the ESP, even slightly, might allow for the escape of the dye from this gap, rather than assist in lifting them towards the ESP.

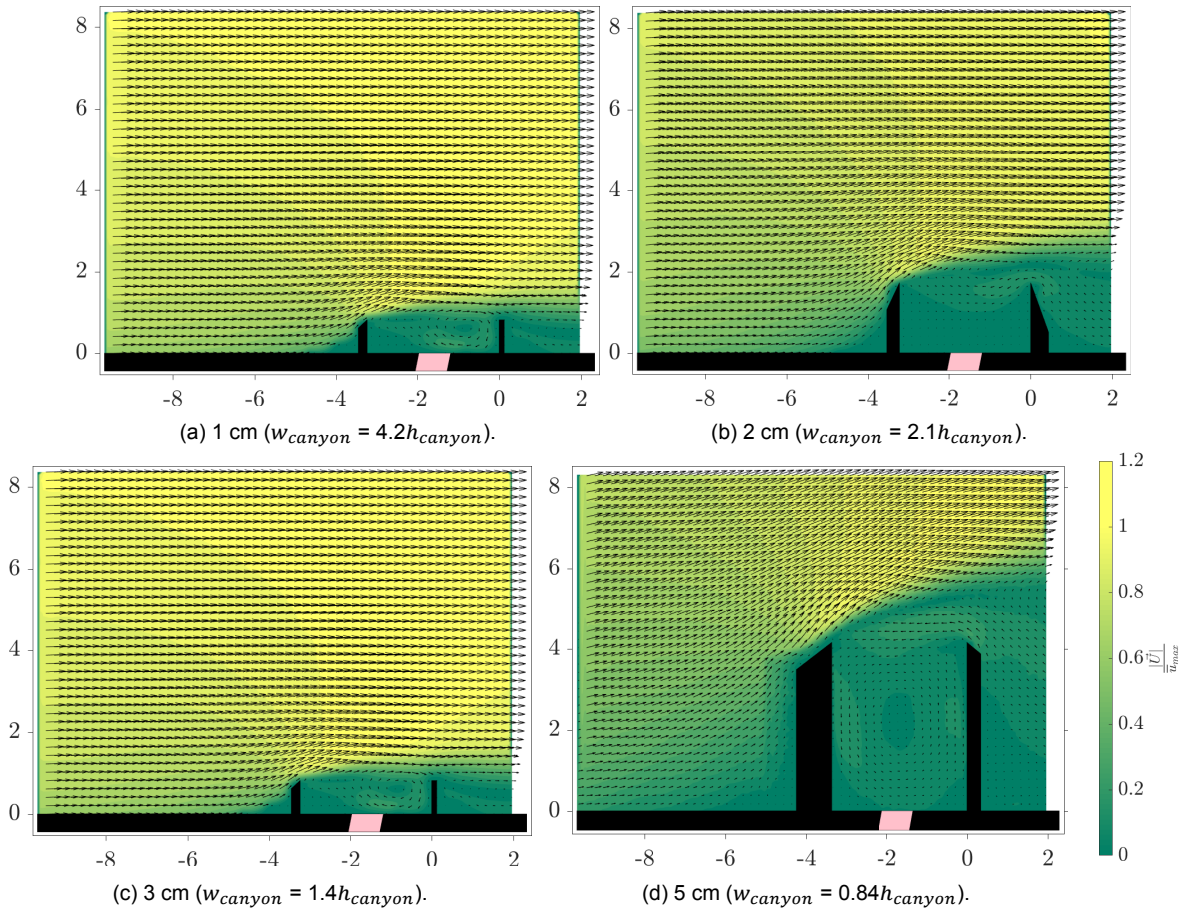

(a) 1 cm (w_{canyon} = 4.2h_{canyon}). (b) 2 cm (w_{canyon} = 2.1h_{canyon}).

(c) 3 cm (w_{canyon} = 1.4h_{canyon}). (d) 5 cm (w_{canyon} = 0.84h_{canyon}).

Figure 5.22: Flow regimes observed for different aspect ratios of the highway canyons. Contours of the velocity magnitude and velocity vectors are shown. Every third vector, in each direction, is displayed. Results with the 5 cm fence are based on 200 images whereas the others are based on 1000. The x and y axes in these plots represent $\frac{x}{h_{ESP}}$ and $\frac{z}{h_{ESP}}$ respectively.

5.4.4. ESP in a highway canyon: Chaotic flow regimes

As a next complication, a SB was installed upstream of the line source as well, in a symmetric manner. It was expected that different 'highway canyon' aspect ratios would lead to different flow regimes, based on previous findings of Oke [36] and shown in Figure 2.8. The velocity maps and vectors for different canyon aspect ratios are shown in Figure 5.22. One major difference between the current case and the typical urban/street canyons is that the SB in the current case is the first roughness element. This is expected to have an effect on the transition between different regimes. For typical urban/street canyons, the flow has already encountered several roughness elements and developed accordingly. All of the present highway canyon cases have in common a shear layer detaching from the upstream SB and reattaching downstream, in most cases further downstream of the downstream SB (which is not visible in the field of view). The canyon aspect ratio is defined as the ratio between the canyon

width (w_{canyon}) and the canyon height (h_{canyon} = h_{SB}).

As shown in Figure 5.22a, for the canyon with 1 cm high SBs (w_{canyon} = 4.2h_{canyon}), the shear layer from the upstream SB is unable to go over the downstream SB and a strong clockwise (mean) separation bubble is formed upstream of the downstream SB while a weak, tiny counter-clockwise separation bubble is formed downstream of the upstream SB. In comparison, for the rest of the canyon aspect ratios (w_{canyon} = 2.1h_{canyon}, 1.4h_{canyon} and 0.84h_{canyon}), the detached shear layer from the upstream SB reattaches in a manner that leads to a region of backward flow over the top of the downstream SB and then interacts with the aforementioned shear layer, as seen in Figures 5.22b to 5.22d. It would be interesting to understand this process, which requires future experiments with a wider field of view. This backward flow over the canyon top induces a counterclockwise circulation bubble in the canyon. Another noticeable aspect is that with increasing SB height, the height of the section with backward flow over the downstream SB increases as well, both of which will increase the effective blockage in the water channel. The former regime can be treated as an 'isolated roughness flow' while the latter regimes can be treated as 'reverse skimming flows'.

Looking at these flow patterns, it is expected that all the cases where the canyon (width:height) ratio exceeds unity, installing an ESP atop the downstream SB, at least in the region with backward flow would be pointless. However, the addition of an ESP (on the downstream SB) may also alter the flow. Thus, the next set of experiments were dedicated towards that. The flow regimes for different canyon aspect ratios with an additional ESP are shown in Figures 5.23a to 5.23d. An extra case on the effect of raising the ESP above the shear layer of the upstream SB is shown in Figure 5.23e.

For the lower canyon aspect ratios (w_{canyon} = 0.84h_{canyon} and w_{canyon} = 1.4h_{canyon}), shown in Figures 5.23c and 5.23d, there is no change in the flow regime observed. This would mean that the ESP tends to clean the region behind the freeway rather than the freeway itself, rendering it useless in such configurations. This is in line with the expectations from the results in Figures 5.22c and 5.22d. While this is not visible, this backward flow induces an extremely weak counterclockwise circulation region in the canyons, in both cases. This weakness can be attributed to the reduced magnitudes of the reverse flow through the semi-permeable ESP. This would also imply that the pollutants reside in the canyon (or at the pedestrian level) for longer periods. However, if there are fast moving vehicles or thermal convective flows, the pollutant removal process from the canyon can be expedited. An experiment in the 'reverse skimming flow', but with the ESP raised well above the shear layer of the upstream SB (h_{Shift} = 1.28h_{ESP}) was also performed. There were no major changes in the flow regime and as expected or desired, the tendency of the pollutants to reach the entrance of the ESP increased dramatically. The flow circulation strength in the canyon however seems stronger, which could alleviate the pollutant levels at the pedestrian level.

The flow regime for the highest canyon aspect ratio (w_{canyon} = 4.2h_{canyon}) does not change either, with similar flow features present as without any ESP, as seen in Figure 5.23a. The ESP is expected to have a nonzero effectiveness in this case. The remaining case (w_{canyon} = 1.4h_{canyon}) shows an unexpected change in the flow regime upon the addition of an ESP, as shown in Figure 5.23b. Without an ESP, backward flow was observed over the top of the downstream SB, seen in Figure 5.22b. However, the addition of the ESP creates a step-up canyon like scenario with an effective step-up ratio (ratio between $h_{SB,downstream}$ and $h_{SB,upstream}$) of about 1.58. The shear layer leaving the upstream SB encounters the ESP instead of hurdling over. This reduces the possibility of reverse flow through the ESP and causes a strong mean clockwise circulation in the canyon. This would have a stronger effect in driving the pollutants towards the mouth of the ESP.

The corresponding profiles of different (normalized) quantities just in front of and above the downstream SB are shown in Figure 5.24a. The horizontal velocity profiles closer to the freestream region are nearly the same for different configurations. One telling feature is the presence of reverse flow for the taller SBs, even when the ESP is raised. However, when the ESP is raised above this region of backward flow, the ESP is exposed to flow entering from the freeway. The velocity profile for the SB with h_{SB} = 1.71h_{ESP} displays the lowest velocity deficit which contributes to the increased efficiency. The intensity profiles decay quicker with decreasing SB height, in accordance with previous results concerning a single SB. The raised ESP is however fed with a lot of dye. From the potential efficiency curves, it can be concluded that for taller SBs, the taller the fence, the higher is the optimal vertical location of the ESP.

From the probability distribution functions, it can be seen that for the taller SBs, there is very high

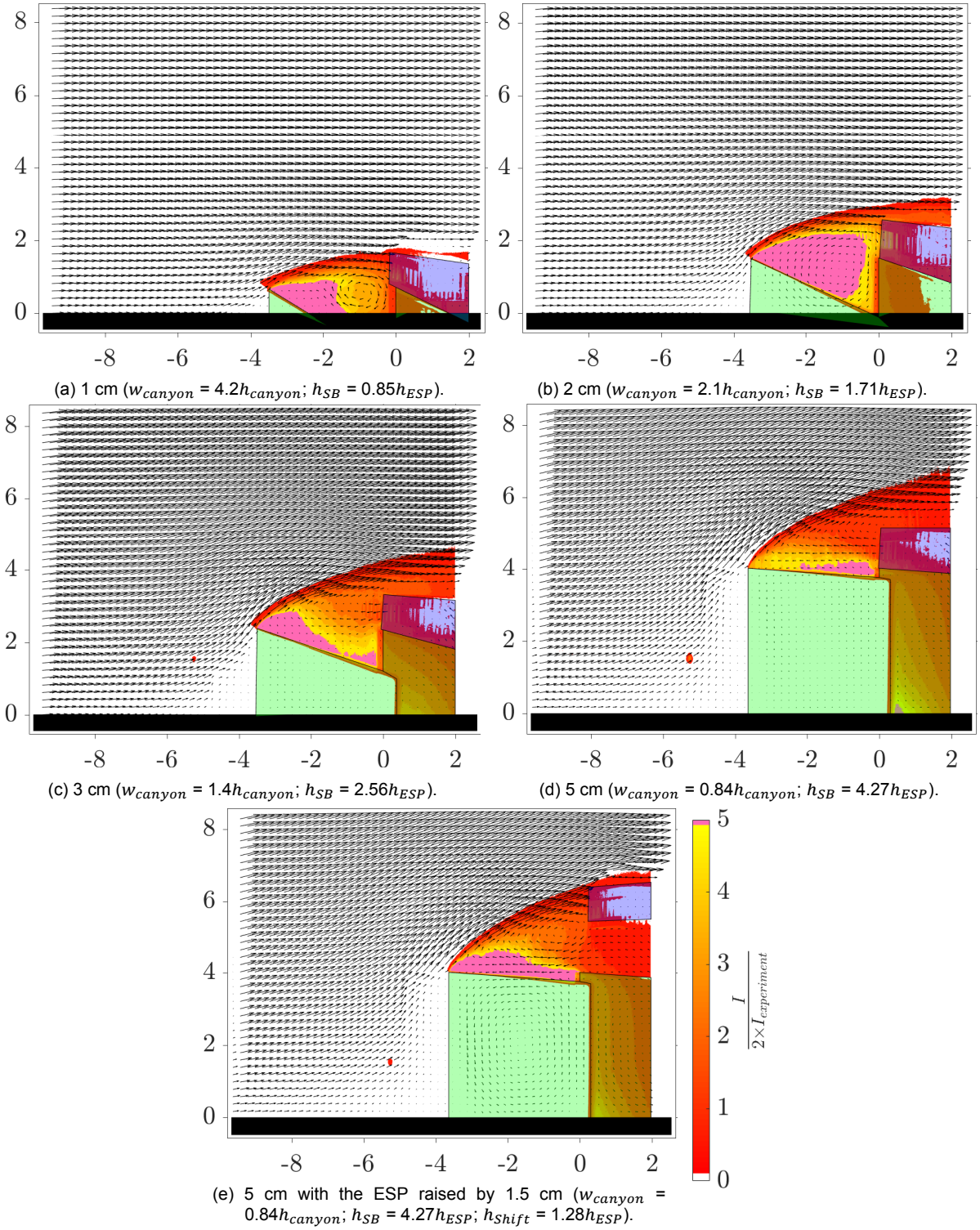

(a) 1 cm (w_{canyon} = 4.2h_{canyon}; h_{SB} = 0.85h_{ESP}).

(b) 2 cm (w_{canyon} = 2.1h_{canyon}; h_{SB} = 1.71h_{ESP}).

(c) 3 cm (w_{canyon} = 1.4h_{canyon}; h_{SB} = 2.56h_{ESP}).

(d) 5 cm (w_{canyon} = 0.84h_{canyon}; h_{SB} = 4.27h_{ESP}).

(e) 5 cm with the ESP raised by 1.5 cm (w_{canyon} = 0.84h_{canyon}; h_{SB} = 4.27h_{ESP}; h_{Shift} = 1.28h_{ESP}).

Figure 5.23: Pollution dispersion for different aspect ratios of highway canyons with an ESP installed over the downstream SB. Contours of the dye intensity and velocity vectors are shown. Every fifth vector, in each direction, is displayed. The vectors in (c)-(e) are scaled up by a factor of 1.5 compared to all the other plots in this report. The x and y axes in these plots represent $\frac{x}{h_{ESP}}$ and $\frac{z}{h_{ESP}}$ respectively.

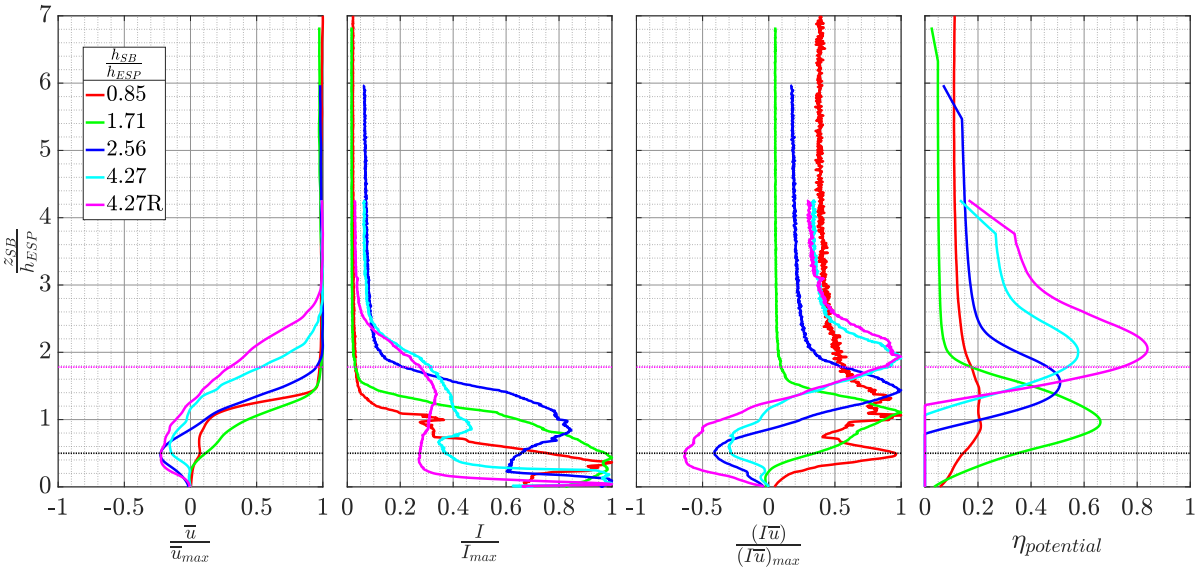

(a) Profiles of various normalized quantities. The horizontal dotted magenta line is used to denote the location of the ESP centerline location corresponding to the case with the raised ESP while the horizontal dotted black line is used for the rest of the cases.

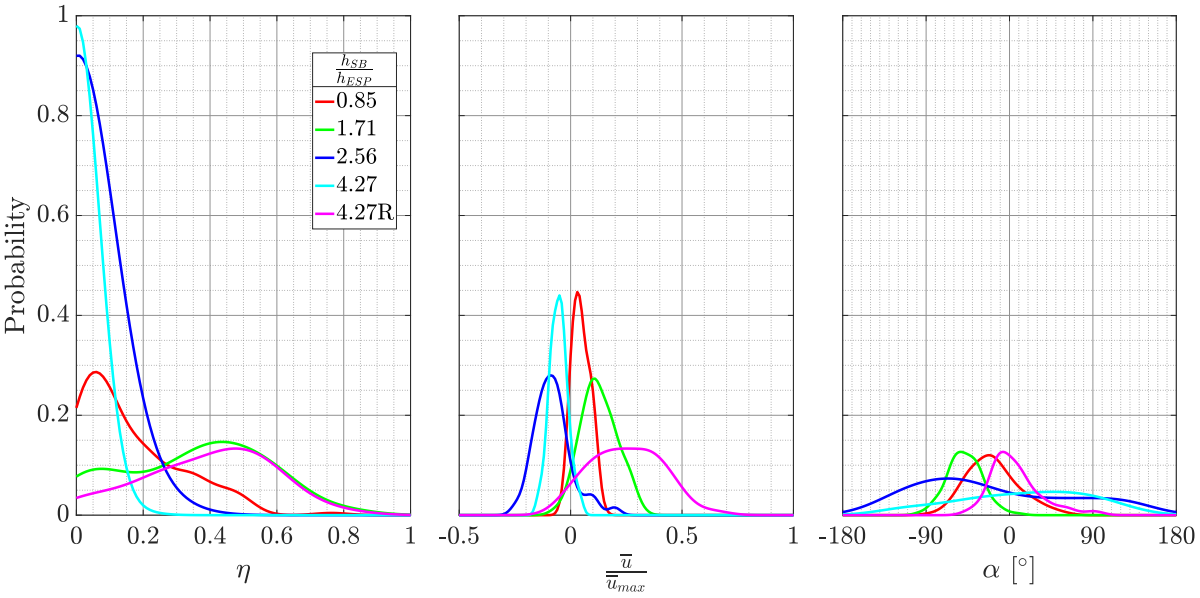

(b) Probability Distribution Functions of various quantities in front of the entrance of the ESP.

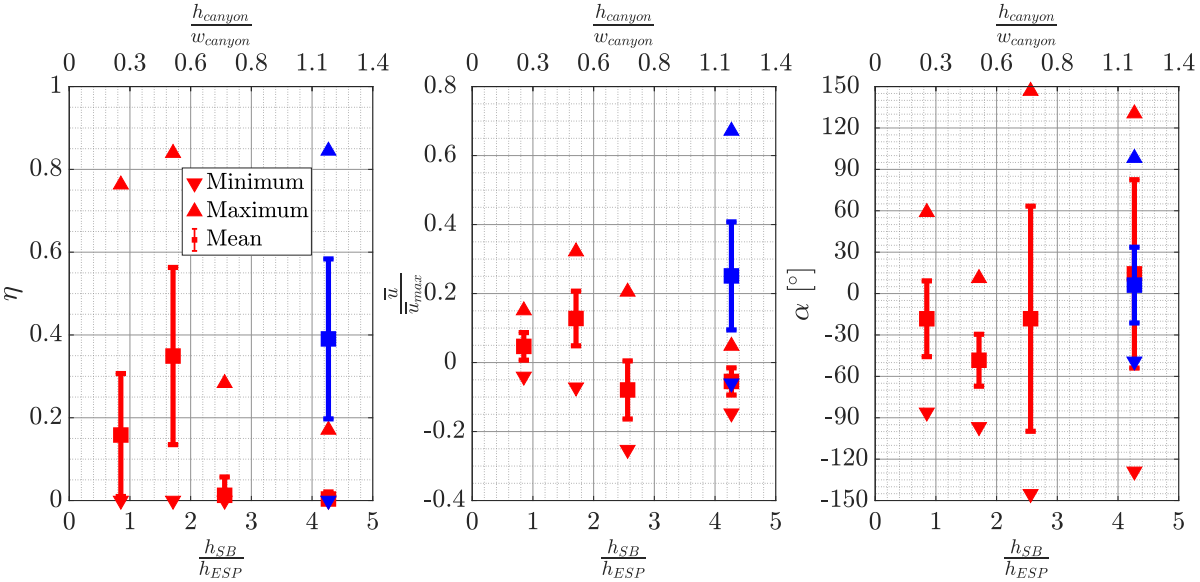

(c) Statistics on the inflow characteristics and performance of the ESP. Blue symbols correspond to the case with the ESP raised.

Figure 5.24: Pollution dispersion characteristics just in front and above the downstream sound barrier for different aspect ratios of highway canyons. 'R' in the legend refers to the case where the ESP is raised.

probability for the pollutants not to enter the ESP, which also correlates with higher probabilities of negative incoming velocities and the magnitude of the incoming angles being higher than 90°. For the remaining cases, the pronounced peaks are nonzero, which correspond to positive incoming angles and the magnitude of the flow angles being under 90°. While all conclusions are being drawn based on the advective fluxes, the role of the turbulent fluxes become evident from the efficiency probability distribution function. There are instances, albeit very few, where the dye does enter the ESP (for the tall SBs) owing to the turbulent nature of the flow, which is not insinuated in the mean flow patterns.

A summary of the ESP aerodynamic performance under different configurations is summarized in Figure 5.24c. No concrete conclusions can be drawn from the mean values of the angles for the taller SBs (h_{SB} = 2.56h_{ESP} and h_{SB} = 4.27h_{ESP}). For example, instances of 115° and -105°, none of which are desirable, will give a mean of 5° which is highly desirable, but misleading. Regardless, it is fruitless to install an ESP in these configurations. For the other cases (h_{SB} = 0.85h_{ESP} and h_{SB} = 1.71h_{ESP}), the mean angles are negative, implying that the optimal placement of the ESP would be with the entrance facing the sky rather than the ground. The reason behind the reduced aerodynamic performance for the shortest SB (h_{SB} = 0.85h_{ESP}) is unclear. From a physical viewpoint, the presence of the weak counterclockwise circulation region just downstream of the the upstream SB might take the dye away from the ESP. Another possibility is due to the noisy intensity based flux (and thus potential efficiency) profile in Figure 5.24a.

Changing the height of the SB in the canyon configuration affects two parameters: the canyon aspect ratio as well as the ratio between the heights of the SB and ESP. Based on the regimes observed in Figure 5.22, without any ESP, and Figure 5.23, with an ESP, the flow regime is affected by the presence of the ESP only for the SB with h_{SB} = 1.71h_{ESP}. Thus, the canyon aspect ratio is expected to predominantly determine the flow regime, while the addition of an ESP could modify the scenario to a step-up canyon in a limited range of aspect ratios, where the shear layer of the upstream SB clears the downstream SB at the planned location of the ESP.

5.4.5. Extrapolating the results of the model: A reality check

In Sections 5.4.2 to 5.4.4, the aerodynamic performance of the ESP in different configurations was looked into. However, it is necessary to understand how the results from the scaled down experiments might translate into reality, which has its own set of complications. This aspect can be appreciated by understanding the uncertainties associated with the experimental results as well as the non-ideal scenarios that exist in reality.

From the perspective of the experiment, one of the major uncertainties involved deals with the assumption of the flow statistics being two dimensional. Based on the results of Eisma [14] and Tomas [15], shown in Figure 5.25, the flow around a fence does have significant instantaneous spanwise components despite the two-dimensional model. This is not totally unexpected due to the turbulent nature of the flow which is often three dimensional. On top of this, the ESP model as well as the line source not spanning the entire width of the water channel test section, raise the possibility of three dimensional flow characteristics. However, it is still possible that the mean flow is two-dimensional in nature. It is recommended that stereoscopic PIV be performed, in tandem with PLIF, to appreciate the three dimensional nature of the flow better.

The evaluation of efficiency is dependent on the velocities as well as the dye intensities. In some of the raw PIV images, filaments of the fluorescent dye were visible despite the presence of a color filter. These were observed mainly near the line source i.e. away from the efficiency evaluation domain. However, since conclusions about flow velocities and regimes have been based made on time averaged experiments, their effect is expected to be negligible.

In some cases, the laser sheet has a profile with local minimas. These are visible as stripes, for example in Figure 5.8. In addition, sometimes, the imprint of the porous ESP model is visible in the PLIF raw images. Both of these might result in an underestimation of the local dye intensity in front of the ESP entrance.

Even though the dye intensities provide an accurate estimate of the aerodynamic performance of the ESP, using concentrations would be more reliable. However, concentration measurements are ridden with their own set of uncertainties, as summarized by Crimaldi [80], including photobleaching

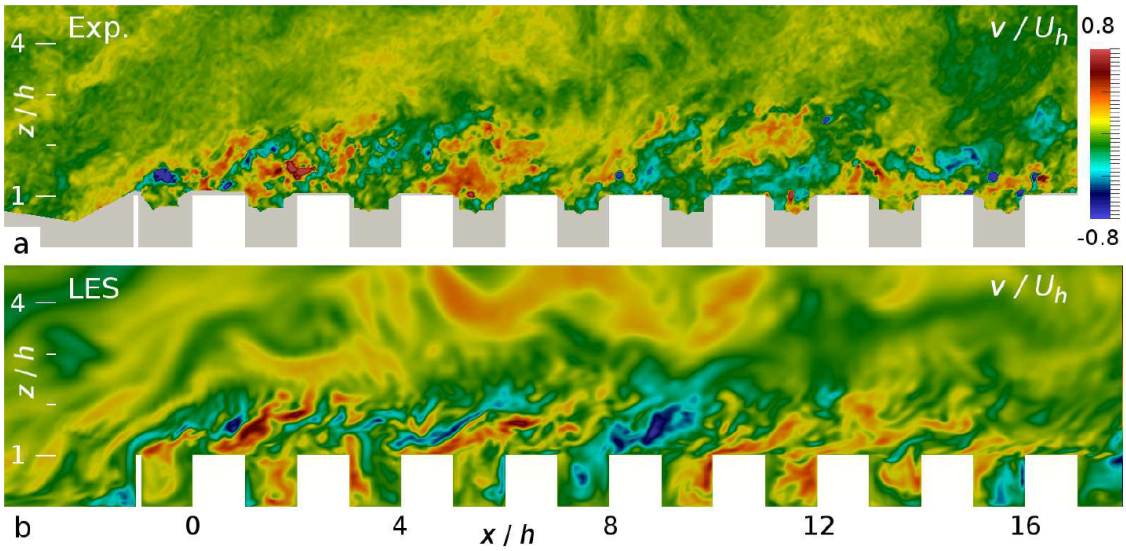

Figure 5.25: Instantaneous spanwise flow velocities around a fence. (a) Experiments (b) Large Eddy Simulations. Figure reproduced from Eisma [14] and Tomas [15].

effects and shot-to-shot laser power variation, both of which were investigated by Eisma [14]. Effects of secondary fluorescence and out-of-sheet dye were also investigated by Vanderwel and Tavoularis [81]. For this, a calibration procedure would need to be devised. The one implemented by Eisma [14] is recommended.

The nature of the advective components (for example, the time averaged line plots just in front and above the SB) and turbulent components (for example, the probability distribution functions) were looked at. However, further analysis from the turbulent perspective can still be performed, mainly to understand how the dye flows towards the ESP.

The scaled down experiments represented a very ideal case, with the flow approaching the SB along its normal. The reality, however, is far more chaotic than the current simplified model. This includes moving vehicles, heated surfaces, unsteady atmospheric conditions and so on. Some guesses on the effect of the above on the ESP aerodynamic performance are made based on the literature reported in Chapter 2.

Sunny conditions may correspond with the rush hours, especially during spring and summer. In such cases, an unstable ABL would be expected. This, along with the UFPs being entrained in warm exhaust gases, would increase the probability of the PM to spread out vertically, and might result in reduced particle capture, owing to the fixed ESP height. In comparison, during fall and winter, the rush hours are likelier to correspond to stable ABLs where the pollutants might not disperse as effectively in the vertical direction, increasing the ESP effectiveness. The current study was based on neutral ABLs which is observed during moderately windy and overcast conditions (on an average day in the Netherlands, three-fifths of the sky is clouded, as noted in Pradhan [95]). Furthermore, any oblique wind angle will only bring along a channeling effect and retain the PM on the highway, and is expected not to affect the aerodynamic efficiency estimation. Thus, the current flow configuration relative to the models, i.e. the crosswind flow configuration, represents the least desirable situation with the highest probability for the pollutants to escape the freeway.

Traffic induced turbulence is expected to play an increased role, especially under calm conditions (low local wind speeds), and cause increased dispersion of pollutants, thus, reducing the aerodynamic effectiveness of the ESP. The presence of vegetation around the SB can also assist in particle deposition, but their effect to the flow conditions is dependent on their placement and size, which would need to be investigated separately.

Installing an ESP in a region prone to high winds might not be recommended due to the reduced collection efficiencies. Under rainy conditions, the ESP will probably not be operated as noted by Alfonsi et al. [11], due to the risks associated with short-circuiting. The turbulent nature of the flow around the ESP, especially during windy conditions, should also deter insects and birds from approaching the

ESP, who can risk causing short-circuiting or getting electrocuted.

The model for the urban canyons, while extremely useful in understanding the flow regimes, does have some shortcomings in relation to its relevance to reality. For example, the cases where the 'reverse skimming flow' regime was observed, have seemingly rather disproportionate canyon aspect ratios (canyon width:height), where the sound barrier heights anomalously exceed the width of the highway. However, such cases may occur occasionally along depressed roadways or extremely high SBs (for example, 20 m high ones in Paris shown in Bendtsen [96]). The other extreme of the canyon aspect ratio might correspond to normally sized SBs located along broad highways.

In the current modeling, it is assumed that an urban area is located downstream of the downstream SB. In case an upstream SB were installed, common sense would lead to one guessing the presence of urban regions upstream of the upstream SB as well. Installing an expensive upstream SB without any urban settlement upstream of it would be implausible. While this has not been modeled, the upstream urban region too would play a highly influential role in determining the different flow regimes at the highway. The presence of a 'reverse skimming flow' regime is unlikely as the upstream SB is no longer the first element of roughness. Furthermore, for this case, if there are obstacles downstream of the downstream SB, it is possible that the 'reverse skimming flow' regime is not observed any further. However, such a hypothesis would need verification through future experiments.

In addition, if two SBs are present, for the sake of symmetry, ESPs would probably be installed on both. This was not possible in the current experiments since only a single ESP was manufactured and also due to lack of available physical space to suspend an ESP atop the upstream SB. The addition of an upstream SB too would affect the flow in a slightly unpredictable manner. Previously, it was seen that the addition of a downstream ESP could affect the flow regime via a step-up canyon effect. Having the upstream ESPs would recreate a symmetric canyon. However, the addition of the porous ESP would give rise not only to a shear layer but also to a 'bleed flow' through the ESP, both of which may play countering roles, especially for canyons displaying the 'reverse skimming flow' regime.

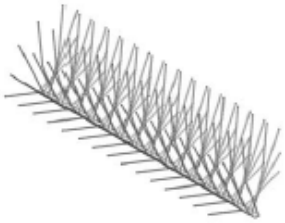

(a) An illustration of bird spikes recommended to be installed on top of the ESP. Figure reproduced from Alfonsi et al. [11].

(b) A curved sound barrier located at Dordrecht in 1999. Image reproduced from Mongeau [97].

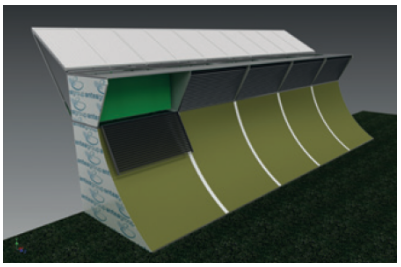

(c) An illustration of a sound barrier, ESP and solar panels on top. Figure reproduced from a magazine article written by the Antea group [98].

Figure 5.26: Subtle aspects that may affect local flows around the ESP.

Besides the above, in real application, other subtle features would also be present, whose effect is unclear. Some of these features are illustrated in Figure 5.26.

One recommendation put forth in Alfonsi et al. [11] and shown in Figure 5.26a, was the installation of bird spikes on top of the ESP to discourage the birds from coming near the ESP. These spikes are quite porous and have typical heights of about 10 cm. Thus, their influence on the flow at the ESP entrance is expected to be minimal.

SBs come in various shapes, colors and sizes. While the effect of size has been investigated and the effect of color is irrelevant, the SB shape could play a role in the pollutant dispersion. In the model, the SB was modeled by a simple L-shaped structure. In reality, SBs are shaped to maximize the acoustic efficiency. Bendtsen [96] provides a comprehensive overview of SBs used across Europe. Quite often, the SBs have a slight inclination or even a curvature, as illustrated in Figure 5.26b. It can be expected that these subtle changes in shape can affect the upstream separation bubble, and the subsequent pollutant dispersion events. Verification of this hypothesis is needed through additional experiments.

The Open Air Line ESP consumes low energy, about 20 W/m (a coffee maker in comparison requires over 800 W; of course the operation duration matters as well). The Antea group have proposed

powering the ESP through solar power, as illustrated in Figure 5.26c. If the solar panels are installed in the manner as illustrated (i.e. away from the ESP entrance and at an obtuse angle), their potential to obstruct flow around the ESP entrance would be reduced.

Another possible improvement is shaping the inlet of the ESP in a convergent manner which could give rise to a higher pressure drop at the inlet and enhance the aerodynamic performance of the ESP by reducing the hindrance to the incoming flow with PM.

The results obtained can be used as a starting point for the ESP installation for full-scale field experiments. The velocity characteristics (ratio between $\overline{u}$ and $\overline{u}_{max}$) can be used to approximate the incoming velocity (at least for an ESP oriented like in the experiments). As a reference for $\overline{u}_{max}$, the velocity at a height of 10 m (commonly used to characterize atmospheric flows) can be used. A guess for the optimal angular orientation can be obtained from the mean values of the flow angle at the ESP entrance. If the ESP were to be utilized at this angle, the velocity component normal to the ESP entrance can be re-estimated even though it is expected that tilting the ESP would affect the flow fields as well.

Identifying the model most relevant to the full-scale implementation needs to be done correctly as well. This aspect was already introduced in Section 3.2. For example, the model ABL and model ESP heights are fixed. This means that the shortest SB represents reality most accurately from the perspective of the ABL while the tallest SB is most representative of the reality from the viewpoint of the ESP. Deeper ABLs are expected when the upstream fetch of the model contains roughness elements (such as forests and urban areas, which have not been modeled) and shallower ABLs are expected if the flow enters from a smooth surface such as grasslands or the sea. In case the model chosen has an inappropriate ESP to SB height ratio, the aerodynamic efficiency can be modified proportionally.

As an example, if the ratio between $\overline{u}$ and $\overline{u}_{max}$ from the experiments are predicted as 0.5 and the incoming flow angle at α = 45°, the following steps can be followed. For field experiments, it is recommended that velocity measurements be made at the height of 10 m to obtain an estimate of $\overline{u}_{max}$, say 3 m/s. The expected incoming horizontal velocity for the ESP would then be about 1.5 m/s, with a flow angle of 45°, which results in a vertical velocity component of 1.5 m/s, yielding a total velocity magnitude of 2.1 m/s. If the ESP were tilted by an angle α = 45°, a factor of $\sec(\alpha) = \sqrt{2}$ would be required, and the incoming velocity for this case would become approximately 2.1 m/s. The above is a conservative estimate, as tilting the ESP to align with the incoming flow would alleviate the flow resistance and further increase the velocity magnitude. The obtained incoming speed, i.e. 2.1 m/s, can be further used to estimate the collection efficiency, say 0.8. The aerodynamic efficiency, say 0.3, would be known, which too can be multiplied by a factor of $\sec(\alpha) = \sqrt{2}$ to obtain an aerodynamic performance of 0.42. The product of these aerodynamic and collection efficiencies would result in a net ESP effectiveness of 0.336 or 33.6%.

When all is said and done, the exact numerical values of the aerodynamic efficiencies reported here must be taken with a grain of salt, for the many reasons discussed above. While there are far too many uncertainties surrounding the exactness of these values, especially in application to real life scenarios, the trends and regimes observed can still be accepted with a high level of confidence. As a next step, it would indeed be recommended to select a viable test location and have full-scale field measurements performed to evaluate the effectiveness of the ESP. A ballpark estimate for the amount of PM released near the highway, say over a period of 12 hours, can be made at first. The amount of PM deposited in the ESP during this period can be determined. The net efficiency, i.e. the ratio between the weight of the collected PM and the predicted weight of PM released, would become known. However, no clear demarcation between the collection efficiency and aerodynamic efficiency is known yet. If simultaneous velocity measurements near the ESP entrance are made, this can be used to make an approximation for the collection efficiency. An estimate for the aerodynamic efficiency can then be made from the ratio between the overall and collection efficiencies. Of course, investigating the aerodynamics through computational fluid dynamics, for further validation, is also a possibility. However, this will pose its own limitations and challenges.

5.5. Do aerodynamic efficiency maximizing events exist?

From the probability distribution functions presented in Section 5.4, the turbulent nature of the flow leading to the huge range of ESP aerodynamic efficiencies was evident. Naturally, it would be desirable to maximize the occurrence of events, if any, which maximize the aerodynamic efficiency of the ESP. The aim of the following brief exercise is to identify the presence of any such event. If one is identified, control mechanisms, passive or active, may be implemented to increase the probability of that event.

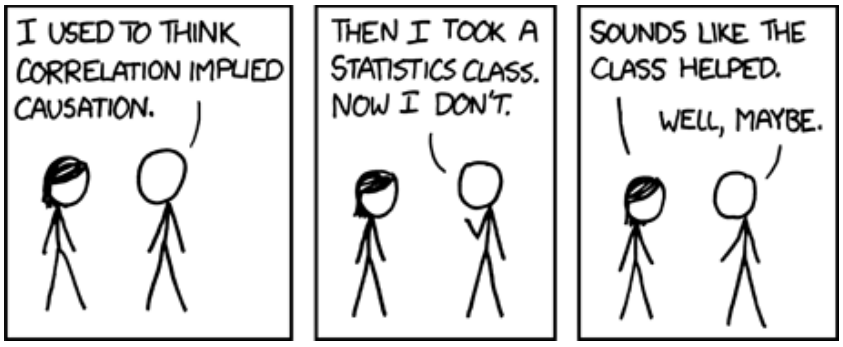

Figure 5.27: "Correlation doesn't imply causation, but it does waggle its eyebrows suggestively and gesture furtively while mouthing 'look over there'." Image and quote reproduced from xkcd comic 552 [99].

5.5.1. The proposed hypothesis

In order to verify/identify events that maximize the aerodynamic efficiency of the ESP, a hypothesis is formulated to see whether certain parameters are correlated with one another. This is done through joint probability distribution functions. However, a correlation only shows the likelihood of the joint occurrence of events and does not offer evidence of the cause and effect between parameters, as well noted by Pearson et al. [100] and also in the comic in Figure 5.27. If a correlation exists, cross correlations between the parameter pair can be used to verify the causality. However, since cross correlations require time-resolved measurements (not performed in the current experiments), this cannot be done in the current investigation.

The hypothesis assumed in this case is based on the findings of Pearson et al. [100] and Sherry et al. [101] for a forward facing step. Even though it has a geometry different from a fence, the region upstream is expected to have similar characteristics. It has been shown that a high velocity in the incoming boundary layer simultaneously suppresses the upstream separation bubble while increasing the flow velocity, at a lower angle, just above the step. If the above is valid for a fence, it should enhance the aerodynamic efficiency of the ESP. However, the aerodynamic efficiency is also dependent on the dye intensities. Analysis of passive scalar dispersion through coherent flow structures might provide hints on flow events which help with the higher dye intensities at the ESP entrance. In the current experiments, the top of the SB has a semipermeable ESP, which may prevent the above hypothesis from being perfectly valid in the current case.

5.5.2. Isolating the upstream separation bubble

Results from a PIV only experiment, i.e. no dye release from the line source, with 1000 images are considered first. This was done since the acquisition times in experiments with simultaneous PLIF measurements were much shorter, by a factor of five.

The first complexity involved here is the identification of the extremities of the upstream separation region, in order to determine its dimensions. It is not straightforward to identify these in case of instantaneous images as the streamlines are often complex and meandering. Estimation of these limits is done by considering regions with a negative velocity component (streamwise or wall-normal). For

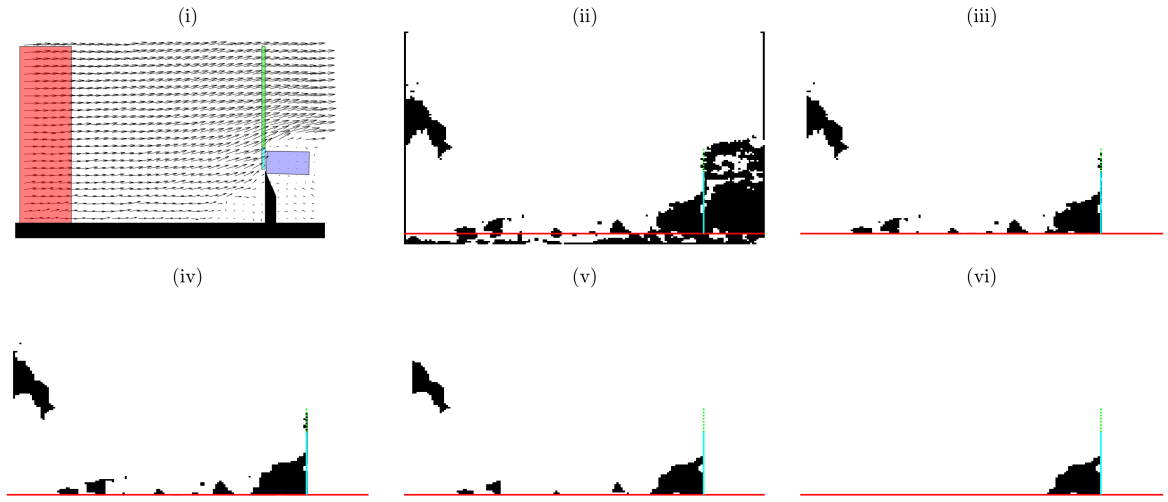

(a) Procedure followed to demarcate the upstream separation bubble. The red, green and cyan patches in (i) define the incoming boundary layer, outgoing boundary layer and ESP entrance regions used in the current analysis. Every fifth velocity vector is shown in (i). The red, cyan and dotted green lines from (ii)→(vi) represent the ground, sound barrier and ESP entrance respectively.

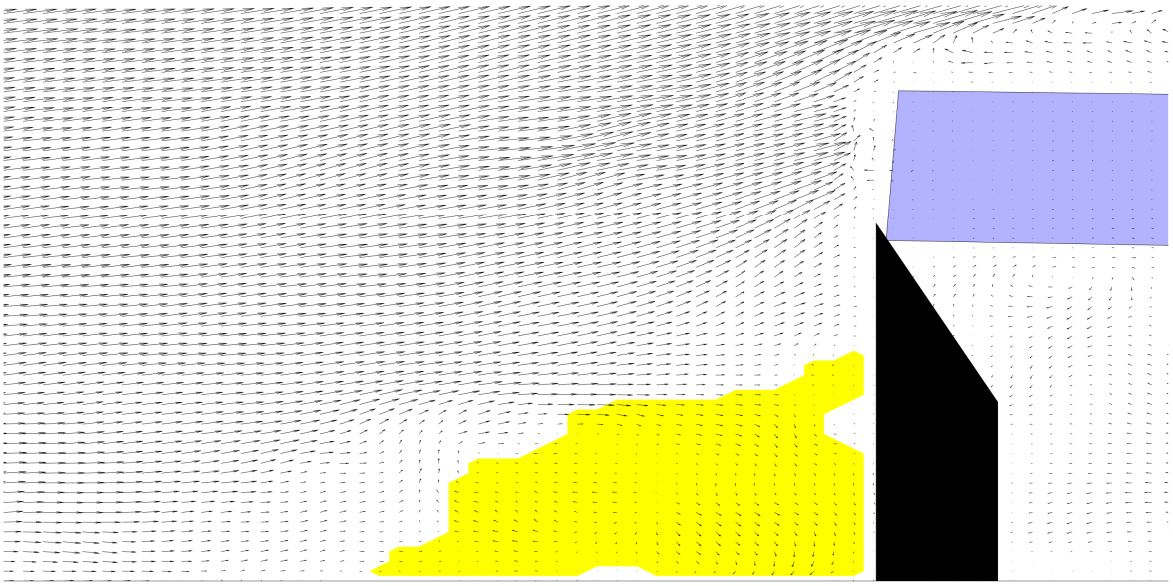

(b) Overlay of the upstream separation bubble on the velocity vectors.

Figure 5.28: Definition of the upstream separation bubble.

example, the height of the instantaneous separation bubble is the largest wall-normal coordinate just upstream of the SB, with a negative velocity component. Similarly, the length of the separation bubble is the magnitude of the lowest streamwise coordinate just above the ground with a negative velocity component. This definition is used and is illustrated in Figure 5.28.

Other possibilities include considering negative streamwise velocity components to obtain the length and negative wall-normal velocity components to obtain the height. This technique follows from the typical time averaged separation regions. Another possibility is to outline the separation region by defining any location with a negative streamwise velocity component belonging to the separation region, as used by Pearson et al. [100].

The procedure to demarcate the upstream separation bubble is as follows, illustrated in Figure 5.28a.

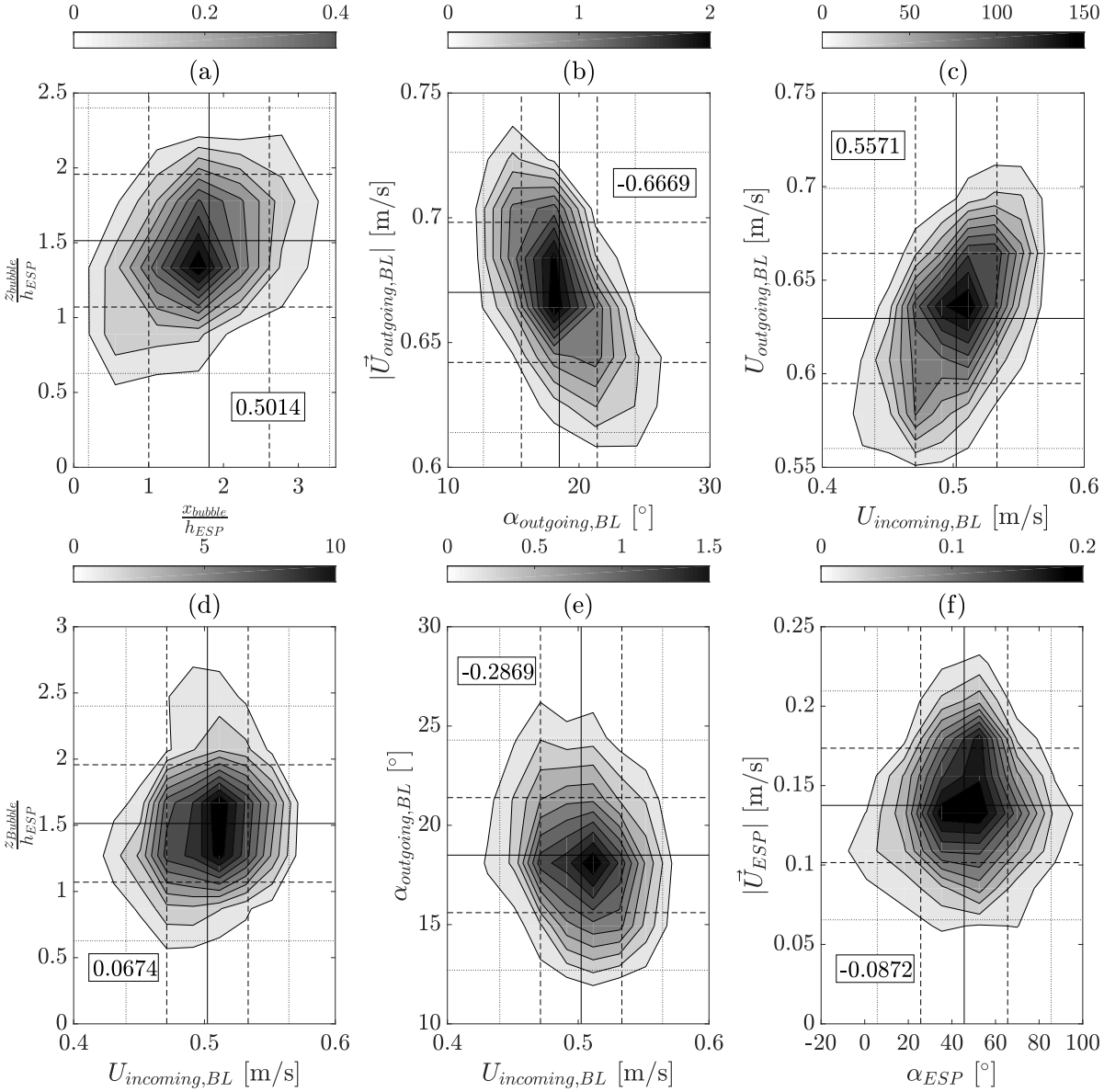

Figure 5.29: Joint probability density functions between: (a) Normalized separation bubble dimensions in streamwise and wall-normal directions (b) Velocity angle and velocity magnitude in the outgoing boundary layer region (c) Streamwise velocity in the incoming and outgoing boundary layer (d) Streamwise velocity in the incoming boundary and normalized separation bubble height (e) Streamwise velocity in the incoming boundary and velocity angle in the outgoing boundary layer region (f) Velocity angle and velocity magnitude at the ESP entrance. Parameters evaluated in the incoming boundary layer, outgoing boundary layer and ESP entrance are obtained by spatially averaging over their respective domains. Contour color scales are normalized such that the bounded volume is unity. Solid lines represent mean, dashed lines represent $\pm$1std and dotted lines represent $\pm$2std for the abscissa and ordinate. The numbers in the boxes are the correlation coefficients between the parameter pairs. $U_{incoming,BL}$ and $U_{outgoing,BL}$ are the horizontal components of the velocity in the incoming and outgoing boundary layer respectively. $|\vec{U}_{outgoing,BL}|$ and $\alpha_{outgoing,BL}$ are the flow speed and angle, respectively, in the outgoing boundary layer. Similarly, $|\vec{U}_{ESP}|$ and α_{ESP} are the flow speed and angle, respectively, at the ESP entrance.

Firstly, all the locations with a negative velocity component are identified (i→ii) and the velocities are stored in a binary format. Secondly, all locations below the ground, behind the SB and the edges of the dataset are 'cropped' (ii→iii). Thirdly, a 3×3 square element is used to perform a morphological close

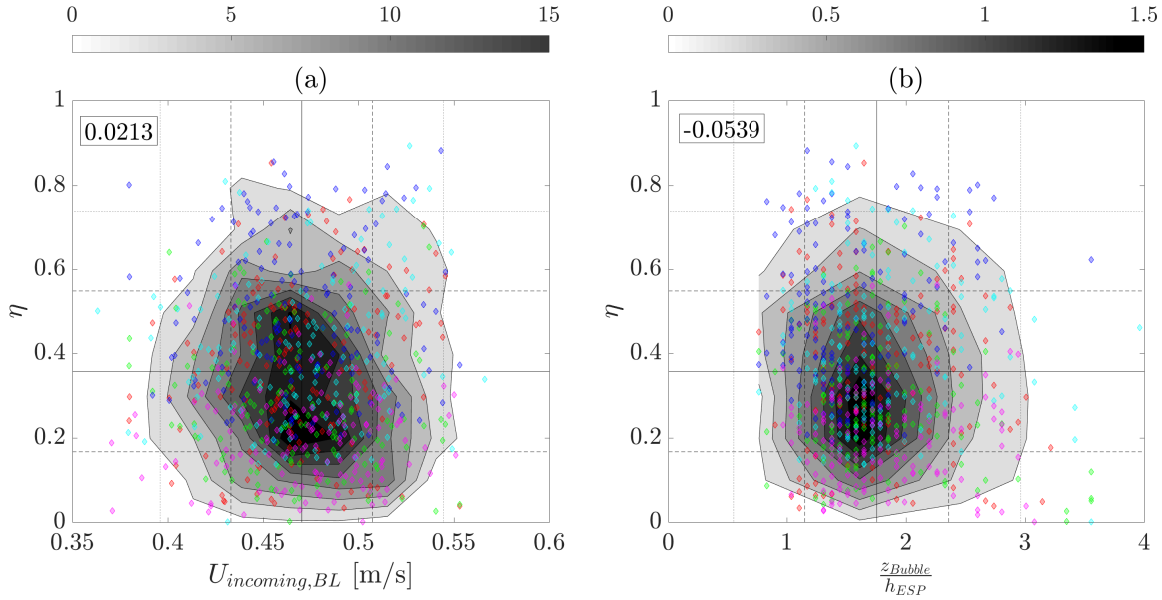

Figure 5.30: Joint probability density functions of the ESP aerodynamic efficiency and: (a) Velocity in the incoming boundary layer averaged over the wall-normal coordinates corresponding to the ESP location (b) Separation bubble height. Contour color scales are normalized such that the bounded volume is unity. Scatter plots for different runs of the experiments are overlaid in different colors. Runs 1 to 5 are indicated in red, green, blue, cyan and magenta. Solid lines represent mean, dashed lines represent ±1std and dotted lines represent ±2std for the abscissa and ordinate. The numbers in the boxes are the correlation coefficients between the parameter pairs.

operation on the binary array (iii→iv). This operation is intended to connect nearby regions with negative velocity. Fourthly, a filtering operation (minimum of north, east, west and south neighbors) is used to eliminate extremely thin regions with negative velocity, especially at the ESP entrance (iv→v). Fifthly and finally, the largest object attached to the ground and the SB, presumably the upstream separation bubble, is retained (v→vi). The extremities of this object are used to calculate the separation bubble dimensions.

5.5.3. (Dis)proving the hypothesis

As a first step, the trends in the flow were first compared with observations of Pearson et al. [100], which are illustrated in Figure 5.29. The plot in (a) demonstrates that the separation bubble expands and contracts simultaneously in both directions. The correlation in (b) indicates that the flow approaching the region above the ESP tends to be faster when the flow angle is more horizontal and slower at higher angles. The correlation in (c) suggests that a higher velocity in the incoming boundary layer leads to higher velocities in the flow leaving the region above the ESP. These trends are in line with the findings of Pearson et al. [100].

However, there was no appreciable effect of the mean incoming boundary layer velocity on the upstream separation bubble height, as indicated in (d). This result goes against the hypothesis proposed at the beginning of this section. The plot in (e) shows the weak negative correlation between the velocity in the incoming boundary layer and the flow angle in the outgoing boundary layer, which is in line with the proposed hypothesis. Unlike in the outgoing boundary layer, no appreciable correlation was found between the velocity magnitude and angle at the ESP entrance, as shown in (f), which is due to the semi-permeable structure of the ESP.

The velocity in the incoming boundary layer not affecting the upstream separation bubble size comes as a bit of a surprise. Other possible ways to look into this is by considering the wall shear stress or the displacement thickness of the incoming boundary layer profile, in place of the incoming velocity averaged over the wall-normal direction. The latter option could not be used in the current case as the height of the incoming boundary layer far exceeds the limits of the field of view. Another possibility

is that the current definition of the upstream separation bubble causes this discrepancy. Yet another reason is that the separation bubble dynamics is indeed independent of the energy in the incoming boundary layer.

As the second part of verifying the hypothesis, correlations were made between select parameters and the aerodynamic efficiency. These correlations are based on experiments where the dye was released from the line source. Since such experiments had a rather short ensemble of 150 images, the correlations were derived from the results of five such experiments and the results are illustrated in Figure 5.30. Both the results indicate the lack of any correlation between the parameters, which invalidate the assumed hypothesis. However, the correlations are subject to random errors introduced while repeating the experiments. The correlation coefficient of the individual runs in (a) and (b) are [0.15,-0.12,0,0.14,0] and [-0.08,-0.2,0.21,0.04,0.04] respectively. The large variation in these individual correlation coefficients indicate that the correlation coefficients might be susceptible to sensitive changes in the ESP positioning. The other reason for this large variation could also be due to the extremely short sample size of the individual ensembles.

Based on the investigation thus far, the answer to the question posed in the title of this section is still ‘maybe’. The hypothesis postulated at the beginning of the section was not proven. Further investigation, perhaps a different hypothesis, is still needed to answer the question.

6

A rESPirator to reduce widESPread trESPassing of particulate matter and increase lifESPans in rural-urban fringes

Scaled down experiments, using PIV and PLIF, to study the phenomenon of pollution dispersion from highways were performed and the major findings were shared in Section 5.4. These findings can act as a guideline for the installation of the 'Open Air Line ESP' (or any other similar air pollutant capturing/treatment device) along highways. The major conclusions of this project are summarized in Section 6.1, whereas a few recommendations for future work are put forth in Section 6.2.

6.1. Installation of the Open Air Line ESP by highways: aerodynamically feasible

The aerodynamics of pollutant dispersion from a highway towards a SB with an ESP atop was looked into. Clear, and sometimes nontrivial, trends were observed regarding the configurations under which the ESP installation might be most fruitful. A preliminary, but fruitless, effort to identify events that maximize the aerodynamic efficiency of the ESP was also made. Extrapolating from the results of the scaled down experiments, guidelines for the full-scale ESP installation to extract the maximum (aerodynamic) performance are summarized below:

- Installing an ESP is expected to be more advantageous on a shorter SB (64% efficiency) than on a taller one (27% efficiency), at least from an aerodynamic perspective. This is primarily due to the formation of a rather large upstream separation bubble in the latter case which leads to a larger vertical dispersion of the pollutants and increases the flow angle at the ESP entrance. Conversely, to improve pollutant capturing probability on taller SBs, relative to shorter SBs, a larger ESP would need to be installed, which would have its associated constraints in terms of material costs and energy requirements.
- Slightly lifting the ESP from the top of the SB is expected to improve the aerodynamic efficiency of the ESP, by about 9-11%. The gap between the SB and the ESP thus created, helps the flow attain a larger horizontal velocity component at the ESP entrance and enhances its aerodynamic performance. However, as the elevation is increased further, the size of the gap increases and an upsurge in the pollutant escaping, reducing its opportunity to reach the ESP entrance, is observed.
- Flow over 'highway canyons' formed by two isolated sound barriers (i.e. away from the influence of any other obstacles) displays complex regimes. Installing an ESP on the top of a SB in a canyon with a low aspect ratio (ratio between canyon width and height) is expected to be pointless due to the existence of the 'reverse skimming flow regime', where the backward flow through the ESP will cause the pollutant to escape over the ESP. In such cases, it is recommended that the ESPs

be installed at an elevation that surpasses the shear layer formed by the upstream SB (and a possible upstream ESP) to have a nonzero effectiveness (39% efficiency). On the other hand, installing an ESP in a canyon with an intermediate to low aspect ratio is expected to be more effective (efficiencies between 16-35%), especially in the intermediate ones.

In addition to the aerodynamic efficiencies of the ESP, the flow velocity characteristics, the magnitude of the ESP entrance aligned component (horizontal, in the current study) and the flow direction, expected at the inlet of the ESP have been reported as well. Guidelines to incorporate this information into understanding the overall ESP performance can be summarized as follows:

- The magnitude of the velocity component aligned to the entrance of the ESP can serve as an input to compute the collection efficiency of the ESP. It is expected that if the timescale in which a particle penetrates the entire width of the ESP is lesser than the timescale in which the particle can attain a charge and migrate to a collection plate, the collection efficiency is expected to reduce. Collection efficiency of the ESP is also one of the topics discussed by Alfonsi et al. [11].
- The flow angle can serve as an installation guideline for the ESP whereby tilting the ESP to orient it to coincide with the incoming flow velocity, is expected to reduce the flow resistance and enhance the number of particles entering the ESP. This should further enhance the aerodynamic efficiency of the ESP.
- Orienting the ESP entrance to align it with the incoming flow will also have a second, possibly negative, effect. The realigned ESP will now provide lesser resistance to the flow, causing increased incoming flow velocities and possibly reduced collection efficiencies.

The information provided in the report can serve as promising first order estimates for field tests or possibly, even, full-scale installations of the ESPs by (Dutch) highways. In short, the work presented in this thesis can be considered as a successful modeling of the pollution dispersion from the highway. The results from the models are extensible to real-scale installations, albeit with the caveat of neglecting existing effects of atmospheric thermal stratification, traffic-induced turbulence as well as spatial and temporal variation of wind characteristics.

6.2. Food for thought: Improving upon the current experiments

The major conclusions of this project were summarized previously in Section 6.1, which included initial guesses for optimizing the aerodynamic performance. The section here primarily deals with what further can be done in order to understand the aerodynamic performance of the ESP better or validate the findings reported in this document.

- Extensive pressure drop measurements can be made across the prototype ESP to understand the resistance it provides to the flow. In addition, these measurements should be made at different incoming velocities to establish the presence or absence of a Reynolds number independent flow regime. The results of these measurements will be useful in designing better scaled down ESP models. In addition, PIV measurements can be made around an ESP model, freely suspended in the flow, to understand the flow around an ESP in greater detail, with an emphasis on the influence of the Reynolds number.
- Even though some hypotheses on the individual effects of atmospheric thermal stratification, traffic induced turbulence and oblique wind flows were made in Section 5.4.5, validation would be required through scaled down experiments. For example, traffic induced turbulence can be modeled in accordance with the similarity criterion put forth by Plate [49]. Unstable ABLs can be simulated through heated ground plates and satisfying the Richardson number criterion. Oblique wind flows can be studied by rotating the turntable to the desired angle of attack. While the possibility to rotate the setup exists, it currently rotates in a manner that would not allow viewing the region upstream of the fence. Isolating each effect and studying them individually will give a clearer idea on what strongly influences the ESP performance.

- The quality of the current experiments can be improved by having stereoscopic PIV measurements instead of planar PIV. This would primarily aid in understanding the three dimensional nature of the flow and reassessing the determined efficiencies. On top of that, performing PLIF along with a calibration (i.e. to interpret the information using concentrations in place of dye intensities) would mark an improvement too, in terms of the accuracy of the measurements.
- Maintaining geometric scaling in the current experiment was not straightforward. For example, the tallest SB has the best geometric scaling with respect to the ESP model, whereas the shortest SB has the best geometric scaling with respect to the ABL. Of course, this is not ideal and can be taken care of by either simulating an extremely tall ABL (which is constrained by the height of the flow facility) or creating minuscule models (which pose manufacturing constraints, as well as demand higher spatial resolution from the measurement techniques, as noted by Eisma [14]). Successful implementation of either would allow for a better interpretation of results.
- As noted previously in Section 5.4.5, the case study of the isolated 'highway canyons' is not very realistic (i.e. symmetric placement of ESPs as well as presence of urban regions on either side of the SBs would be expected). These changes can have a drastic effect on the observations made, concerning the flow regimes. This too can be simulated by adding cubic/cuboid blocks into the flow.
- The interpretation of the observed ESP performance trends in the current work is mainly bound to understanding the mean flow characteristics. Pollution dispersion is largely governed by the turbulent structures and processes (for example, the compression/expansion of the upstream separation bubble or the shear layer flapping in case of a highway canyon) in the flow. If a strong positive/negative correlation between a certain event and high ESP performance exists, verifying the event as the cause (through time-resolved measurements) can be performed too. If verified, (practically feasible) control mechanisms for increasing/reducing, respectively, the probability of the aforementioned event can be thought of and implemented, first at a laboratory scale and then at full scale.
- There are several articles in literature, including those by Adrian et al. [102] and Depardon et al. [103], that look into extracting features from instantaneous flow fields. Future work can also include the identification of flow structures responsible for the dispersion of passive scalars.
- In addition to experiments, well-resolved numerical simulations can be applied to study this flow. Implementation of the porous ESP in the numerical model is expected to be a challenging task. However, if successfully implemented, certain parameters can be tweaked easily (for example, the ESP dimensions and characteristics) as compared to experiments.
- Since large-scale installations of the ESPs by the freeways is the ultimate objective, first tests using actual ESPs can be performed at a carefully selected location. It is recommended to have a measure of the wind speed and angle near the SB to get an idea of the mean flow characteristics. Even though the mass of PM collected by an ESP is measurable, it is difficult to predict the mass of PM released from the freeway. Nonetheless, a rough estimate of the overall ESP efficiency can be made with a ballpark estimate of the emitted PM. With the aforementioned mean wind characteristics measured, an estimate for the collection efficiency can be made. The aerodynamic efficiency can then be obtained using the above two efficiencies. The possibility to separate these two efficiencies (collection and aerodynamic) will allow for testing different ESP configurations at full-scale too, in order to fine tune and optimize the placement and orientation of the ESP.

Bibliography

[1] Lidia Morawska, Zoran Ristovski, E.R. Jayaratne, Diane U. Keogh, and Xuan Ling. Ambient nano and ultrafine particles from motor vehicle emissions: Characteristics, ambient processing and implications on human exposure. *Atmospheric Environment*, 42(35):8113–8138, 2008.

[2] World Health Organization. Health risks of particulate matter from long-range transboundary air pollution, 2006.

[3] M.P. Keuken, M. Moerman, M. Voogt, M. Blom, E.P. Weijers, T. Röckmann, and U. Dusek. Source contributions to $PM_{2.5}$ and PM_{10} at an urban background and a street location. *Atmospheric Environment*, 71:26–35, 2013.

[4] D. Hamers, K. Nabielek, M. Piek, and N. Sorel. Verstedelijking in de stadsrandzone. Een verkenning van de ruimtelijke opgave. *Den Haag, PBL Netherlands Environmental Assessment Agency*, 2009.

[5] Kersten Nabielek, Pia Kronberger-Nabielek, and David Hamers. The rural-urban fringe in the Netherlands: recent developments and future challenges. *Spool*, 1(1):101–120, 2013.

[6] World Health Organization. *Air quality guidelines: global update 2005: particulate matter, ozone, nitrogen dioxide, and sulfur dioxide*. World Health Organization, 2006.

[7] Review Scientific Board: International review of the Air Quality Innovation Programme (IPL), December 2009.

[8] J. Hooghwerff, C.C. Tollenaar, and W.J. van der Heijden. In-situ air quality measurements on existing and innovative noise barriers. In *Air Pollution XVIII*, pages 129–139. WIT Press Kos, Greece, 2010.

[9] R. Baldauf, E. Thoma, A. Khlystov, V. Isakov, G. Bowker, T. Long, and R. Snow. Impacts of noise barriers on near-road air quality. *Atmospheric Environment*, 42(32):7502–7507, 2008.

[10] Invloed schermen op de luchtkwaliteit - eindrapport onderzoek naar de werking van (geluids)schermen op de luchtkwaliteit langs snelwegen, December 2009.

[11] Matteo Alfonsi, Jerke Eisma, Özlem Gezici, Vivian Jacobs, Robert Knegjens, Sander Roobol, Smiet Chris, Martin van Son, and Jasper Tomas. The fine dust problem near urban highways - optimization of the electrostatic precipitator device. In *Proceedings Physics with Industry 2013*, pages 3–24.

[12] Antea Group Nederland. Open Air Line ESP [Video File], 2016. URL `https://www.youtube.com/watch?v=gLESqc-7toU`. [Online; accessed 29-November-2016].

[13] James H. Turner, Phil A. Lawless, Toshiaki Yamamoto, David W. Coy, Gary P. Greiner, John D. McKenna, and William M. Vatavuk. Sizing and Costing of Electrostatic Precipitators: Part II. Costing Considerations. *JAPCA*, 38(5):715–726, 1988.

[14] Jerke Eisma. *Pollutant dispersion in wall-bounded turbulent flows: An experimental assessment*. PhD thesis, Technische Universiteit Delft, 2017.

[15] Jasper Tomas. *Obstacle resolving Large-Eddy Simulation of disperion in urban environments: Effects of stability and roughness geometry*. PhD thesis, Technische Universiteit Delft, 2016.

[16] Toshiaki Yamamoto. Effects of turbulence and electrohydrodynamics on the performance of electrostatic precipitators. *Journal of Electrostatics*, 22(1):11–22, 1989.

[17] B.S. Choi and C.A.J. Fletcher. Turbulent particle dispersion in an electrostatic precipitator. *Applied Mathematical Modelling*, 22(12):1009–1021, 1998.

[18] Alfredo Soldati. On the effects of electrohydrodynamic flows and turbulence on aerosol transport and collection in wire-plate electrostatic precipitators. *Journal of aerosol science*, 31(3):293–305, 2000.

[19] Gregory A. Kallio and David E. Stock. Flow visualization inside a wire-plate electrostatic precipitator. *IEEE transactions on industry applications*, 26(3):503–514, 1990.

[20] Jerzy Mizeraczyk, Jaroslaw Dekowski, M. Kocik, T. Ohkubo, and S. Kanazawa. Laser flow visualization and velocity fields by particle image velocimetry in an electrostatic precipitator model. *Journal of visualization*, 6(2):125–133, 2003.

[21] Anna Niewulis, Janusz Podliński, Marek Kocik, Robert Barbucha, Jerzy Mizeraczyk, and A. Mizuno. EHD flow measured by 3D PIV in a narrow electrostatic precipitator with longitudinal-to-flow wire electrode and smooth or flocking grounded plane electrode. *Journal of Electrostatics*, 65(12):728–734, 2007.

[22] Brandn Gazzolo. Near field modeling of the effects of sound barriers on flow and dispersion, 2012.

[23] Roland Stull. The Atmospheric Boundary Layer. In John M. Wallace and Peter V. Hobbs, editors, *Atmospheric Science: An Introductory Survey*, chapter 9, pages 375–418. Elsevier, 2006.

[24] Roland Stull. Atmospheric Boundary Layer. In *Practical Meteorology: an algebra based survey of atmospheric science*, chapter 18, pages 687–722. BC Campus, 2016.

[25] Barbara Hennemuth and Andrea Lammert. Determination of the atmospheric boundary layer height from radiosonde and lidar backscatter. *Boundary-Layer Meteorology*, 120(1):181–200, 2006.

[26] Martin Piringer, Sylvain Joffre, Alexander Baklanov, Andreas Christen, Marco Deserti, Koen De Ridder, Stefan Emeis, Patrice Mestayer, Maria Tombrou, Douglas Middleton, Kathrin Baumann-Stanzer, Aggeliki Dandou, Ari Karppinen, and Jerzy Burzynski. The surface energy balance and the mixing height in urban areas—activities and recommendations of COST-Action 715. *Boundary-layer meteorology*, 124(1):3–24, 2007.

[27] Joost J.M. de Jong, Arjen C. de Vries, and Wim Klaasen. Influence of obstacles on the aerodynamic roughness of the Netherlands. *Boundary-Layer Meteorology*, 91(1):51–64, 1999.

[28] J.K. Raine and D.C. Stevenson. Wind protection by model fences in a simulated atmospheric boundary layer. *Journal of Wind Engineering and Industrial Aerodynamics*, 2(2):159–180, 1977.

[29] H.B. Kim and S.J. Lee. Time-resolved velocity field measurements of separated flow in front of a vertical fence. *Experiments in fluids*, 31(3):249–257, 2001.

[30] Henri A. Siller and Hans-Hermann Fernholz. Separation behaviour in front of a two-dimensional fence. *European Journal of Mechanics-B/Fluids*, 20(5):727–740, 2001.

[31] L.W. Sigurdson. The structure and control of a turbulent reattaching flow. *Journal of Fluid Mechanics*, 298:139–165, 1995.

[32] I.P. Castro. Relaxing wakes behind surface-mounted obstacles in rough wall boundary layers. *Journal of Fluid Mechanics*, 93(4):631–659, 1979.

[33] George E. Bowker, Richard Baldauf, Vlad Isakov, Andrey Khlystov, and William Petersen. The effects of roadside structures on the transport and dispersion of ultrafine particles from highways. *Atmospheric Environment*, 41(37):8128–8139, 2007.

[34] Nico Schulte, Michelle Snyder, Vlad Isakov, David Heist, and Akula Venkatram. Effects of solid barriers on dispersion of roadway emissions. *Atmospheric Environment*, 97:286–295, 2014.

[35] F. Durst, M. Founti, and Shinnosuke Obi. Experimental and computational investigation of the two-dimensional channel flow over two fences in tandem. *Journal of fluids engineering*, 110(1): 48–54, 1988.

[36] Tim R. Oke. Street design and urban canopy layer climate. *Energy and buildings*, 11(1):103–113, 1988.

[37] Walter F. Dabberdt, F.L. Ludwig, and Warren B. Johnson. Validation and applications of an urban diffusion model for vehicular pollutants. *Atmospheric Environment (1967)*, 7(6):603–618, 1973.

[38] Roland Stull. *Practical Meteorology: an algebra based survey of atmospheric science*. BC Campus, 2016.

[39] Adrie Jacobs. The flow around a thin closed fence. *Boundary-Layer Meteorology*, 28(3-4):317–328, 1984.

[40] Yasushi Ogawa and P.G. Diosey. Surface roughness and thermal stratification effects on the flow behind a two-dimensional fence—II. a wind tunnel study and similarity considerations. *Atmospheric Environment (1967)*, 14(11):1309–1320, 1980.

[41] D.A. Trifonopoulos and G.C. Bergeles. Stable stratification effects on the flow past surface obstructions: A numerical study. *International Journal of Heat and Fluid Flow*, 13(2):151–159, 1992.

[42] Christof Gromke and Bodo Ruck. Influence of trees on the dispersion of pollutants in an urban street canyon—experimental investigation of the flow and concentration field. *Atmospheric Environment*, 41(16):3287–3302, 2007.

[43] Sara Janhäll. Review on urban vegetation and particle air pollution–Deposition and dispersion. *Atmospheric Environment*, 105:130–137, 2015.

[44] D.K. Heist, S.G. Perry, and L.A. Brixey. A wind tunnel study of the effect of roadway configurations on the dispersion of traffic-related pollution. *Atmospheric Environment*, 43(32):5101–5111, 2009.

[45] Sam Pournazeri and Marko Princevac. Sound wall barriers: Near roadway dispersion under neutrally stratified boundary layer. *Transportation Research Part D: Transport and Environment*, 41:386–400, 2015.

[46] Jonathan T. Steffens, David K. Heist, Steven G. Perry, and K. Max Zhang. Modeling the effects of a solid barrier on pollutant dispersion under various atmospheric stability conditions. *Atmospheric Environment*, 69:76–85, 2013.

[47] Jonathan T. Steffens, David K. Heist, Steven G. Perry, Vlad Isakov, Richard W. Baldauf, and K. Max Zhang. Effects of roadway configurations on near-road air quality and the implications on roadway designs. *Atmospheric Environment*, 94:74–85, 2014.

[48] K. Ahmad, M. Khare, and K.K. Chaudhry. Wind tunnel simulation studies on dispersion at urban street canyons and intersections—a review. *Journal of Wind Engineering and Industrial Aerodynamics*, 93(9):697–717, 2005.

[49] E.J. Plate. Windkanalmodellierung von ausbreitungsvorgängen in stadtgebieten. *Kolloquiumsbericht Abgasbelastungen durch den Straßenverkehr*, pages 61–83, 1982.

[50] Robert E. Eskridge and S. Trivikrama Rao. Turbulent diffusion behind vehicles: experimentally determined turbulence mixing parameters. *Atmospheric Environment (1967)*, 20(5):851–860, 1986.

[51] N. Isyumov. Physical modeling of atmospheric dispersion in complex settings, wind climate in cities. *Proceedings of the NATO advance study institute at waldbrown, Germany*, 1993.

[52] N. Isyumov and S. Ramsay. Physical Modelling of Atmospheric Dispersion in Complex Settings. In *Wind Climate in Cities*, pages 131–152. Springer, 1995.

[53] P. Kastner-Klein, E. Fedorovich, and M.W. Rotach. A wind tunnel study of organised and turbulent air motions in urban street canyons. *Journal of Wind Engineering and Industrial Aerodynamics*, 89(9):849–861, 2001.

[54] P. Kastner-Klein, R. Berkowicz, and E.J. Plate. Modelling of vehicle-induced turbulence in air pollution studies for streets. *International Journal of Environment and Pollution*, 14(1-6):496–507, 2000.

[55] F. Scarano. Experimental Aerodynamics, February 2013.

[56] R.N. Meroney. Wind tunnel and numerical simulation of pollution dispersion: a hybrid approach. *Paper for Invited Lecture at the Croucher Advanced Study Institute, Hong Kong University of Science and Technology*, pages 6–10, 2004.

[57] J. Armitt and J. Counihan. The simulation of the atmospheric boundary layer in a wind tunnel. *Atmospheric Environment (1967)*, 2(1):49IN363–6271, 1968.

[58] J.C.R. Hunt and H. Fernholz. Wind-tunnel simulation of the atmospheric boundary layer: a report on Euromech 50. *Journal of Fluid Mechanics*, 70(03):543–559, 1975.

[59] William H. Snyder. Similarity criteria for the application of fluid models to the study of air pollution meteorology. *Boundary-Layer Meteorology*, 3(1):113–134, 1972.

[60] Albert A. Townsend. *The structure of turbulent shear flow*. Cambridge university press, 1980.

[61] G.K. Batchelor. The conditions for dynamical similarity of motions of a frictionless perfect-gas atmosphere. *Quarterly Journal of the Royal Meteorological Society*, 79(340):224–235, 1953.

[62] A.S. Monin and A.M.F. Obukhov. Basic laws of turbulent mixing in the surface layer of the atmosphere. *Contrib. Geophys. Inst. Acad. Sci. USSR*, 151(163):e187, 1954.

[63] Yoshihide Tominaga and Ted Stathopoulos. Ten questions concerning modeling of near-field pollutant dispersion in the built environment. *Building and Environment*, 105:390–402, 2016.

[64] Martin Jensen. The model-law for phenomena in natural wind. *Ingenioren*, 2(4):121–128, 1958.

[65] A.G. Sutton. *Atmospheric turbulence*. Methuen, 1955.

[66] Stefano Leonardi, Paolo Orlandi, and Robert A. Antonia. Properties of d-and k-type roughness in a turbulent channel flow. *Physics of fluids*, 19(12):125101, 2007.

[67] Antea Group Nederland. Open Air Line ESP, Technical drawing of the prototype, 2016.

[68] F. Davies, D.R. Middleton, and K.E. Bozier. Urban air pollution modelling and measurements of boundary layer height. *Atmospheric environment*, 41(19):4040–4049, 2007.

[69] K.A. Antonopoulos. Pressure drop during laminar oblique flow through in-line tube assemblies. *International journal of heat and mass transfer*, 30(4):673–681, 1987.

[70] P.E. Roach. The generation of nearly isotropic turbulence by means of grids. *International Journal of Heat and Fluid Flow*, 8(2):82–92, 1987.

[71] Neil E. Todreas and Mujid S. Kazimi. *Nuclear systems: thermal hydraulic fundamentals*, volume 1. CRC Press, 2012.

[72] A. Žukauskas. Heat transfer from tubes in crossflow. *Advances in heat transfer*, 8:93–160, 1972.

[73] Engineering Laboratory Design Inc. Water tunnel facility model 505 24". URL `http://www.eldinc.com/pages/Model50524`. [Online; accessed 16-March-2017].

[74] G.E. Elsinga and J. Westerweel. Tomographic-PIV measurement of the flow around a zigzag boundary layer trip. *Experiments in fluids*, 52(4):865–876, 2012.

[75] H.P.A.H. Irwin. The design of spires for wind simulation. *Journal of Wind Engineering and Industrial Aerodynamics*, 7(3):361–366, 1981.

[76] Rex Klopfenstein Jr. Air velocity and flow measurement using a Pitot tube. *ISA transactions*, 37 (4):257–263, 1998.

[77] Markus Raffel, Christian E. Willert, Steve T. Wereley, and Jürgen Kompenhans. *Particle Image Velocimetry: A Practical Guide*. Springer Science & Business Media, 2007.

[78] Ronald J. Adrian and Jerry Westerweel. *Particle Image Velocimetry*. Cambridge University Press, 2011.

[79] Francisco Pedocchi, J. Ezequiel Martin, and Marcelo H. García. Inexpensive fluorescent particles for large-scale experiments using particle image velocimetry. *Experiments in Fluids*, 45(1):183–186, 2008.

[80] J.P. Crimaldi. Planar laser induced fluorescence in aqueous flows. *Experiments in fluids*, 44(6): 851–863, 2008.

[81] Christina Vanderwel and Stavros Tavoularis. On the accuracy of PLIF measurements in slender plumes. *Experiments in fluids*, 55(8):1801, 2014.

[82] P.K. Kundu, I.M. Cohen, and D. Dowling. *Fluid Mechanics*. Academic Press, New York, NY, 2012.

[83] Yasuharu Nakamura and Yuji Ohya. The effects of turbulence on the mean flow past two-dimensional rectangular cylinders. *Journal of Fluid Mechanics*, 149:255–273, 1984.

[84] A. Sohankar. Flow over a bluff body from moderate to high Reynolds numbers using large eddy simulation. *Computers & fluids*, 35(10):1154–1168, 2006.

[85] E. Achenbach and E. Heinecke. On vortex shedding from smooth and rough cylinders in the range of Reynolds numbers 6×10^3 to 5×10^6. *Journal of fluid mechanics*, 109:239–251, 1981.

[86] T. Tamura, T. Miyagi, and T. Kitagishi. Numerical prediction of unsteady pressures on a square cylinder with various corner shapes. *Journal of Wind Engineering and Industrial Aerodynamics*, 74:531–542, 1998.

[87] Ahmad Sohankar, C. Norberg, and L. Davidson. Simulation of three-dimensional flow around a square cylinder at moderate Reynolds numbers. *Physics of fluids*, 11(2):288–306, 1999.

[88] Y. Tomonari. Aeroelastic galloping of square cylinders at low reynolds numbers (in Japanese). *Bulletin Nippon Bunri University*, 11, no. 1:161–167, 1982.

[89] Guido Buresti. Bluff-body aerodynamics. 2000.

[90] H.W. Teunissen. Characteristics of the mean wind and turbulence in the planetary boundary layer. Technical report, Toronto University Downsview (Ontario) Institute for Aerospace studies, 1970.

[91] P. Henrik Alfredsson and Ramis Örlü. The diagnostic plot—a litmus test for wall bounded turbulence data. *European Journal of Mechanics-B/Fluids*, 29(6):403–406, 2010.

[92] P. Lavoie, G. Avallone, F. De Gregorio, Giovanni Paolo Romano, and R.A. Antonia. Spatial resolution of PIV for the measurement of turbulence. *Experiments in Fluids*, 43(1):39–51, 2007.

[93] Christian Cierpka, Sven Scharnowski, and Christian J. Kähler. Parallax correction for precise near-wall flow investigations using particle imaging. *Applied optics*, 52(12):2923–2931, 2013.

[94] Enrico Paterna. *Wind Tunnel Investigation of Turbulent Flow in Urban Configurations: A Time-resolved PIV Analysis*. PhD thesis, ETH-Zürich, 2015.

[95] Rajendra Pradhan. 'Mooi weer, meneer': Why do the Dutch speak so often about the weather? *Etnofoor*, (1):3–14, 1989.

[96] Hans Bendtsen. Noise barrier design: Danish and some European examples. Technical report, 2009.

[97] Luc Mongeau. The effectiveness of noise barriers. 2003.

[98] Antea group. Open Air Line ESP gaat fijnstof te lijf. *Civiele Techniek*, (3), March 2016.

[99] URL `https://m.xkcd.com/552/`. [Online; accessed 26-July-2017].

[100] D.S. Pearson, P.J. Goulart, and B. Ganapathisubramani. Investigation of turbulent separation in a forward-facing step flow. In *Journal of Physics: Conference Series*, volume 318, page 022031. IOP Publishing, 2011.

[101] Michael John Sherry, David Lo Jacono, John Sheridan, Romain Mathis, and Ivan Marusic. Flow separation characterisation of a forward facing step immersed in a turbulent boundary layer. In *TSFP DIGITAL LIBRARY ONLINE*. Begel House Inc., 2009.

[102] R.J. Adrian, K.T. Christensen, and Z-C. Liu. Analysis and interpretation of instantaneous turbulent velocity fields. *Experiments in fluids*, 29(3):275–290, 2000.

[103] S. Depardon, J.J. Lasserre, L.E. Brizzi, and J. Borée. Instantaneous skin-friction pattern analysis using automated critical point detection on near-wall PIV data. *Measurement Science and Technology*, 17(7):1659, 2006.

[104] Oranjewoud. Protection Against Fine Dust: the Line ESP. URL `http://www.lorentzcenter.nl/lc/web/2013/575/Oranjewoud.pdf`. [Online; accessed 24-July-2017].

[105] P. Ackermans. Ultrafijnstof is voor 75 procent af te vangen. *Land+Water*, (5), May 2016.

[106] Antea Group Nederland. Revolutionary solution captures particulate matter. URL `http://www.anteagroup.nl/sites/default/files/infographic_open_air_line_esp_eng_-_def.pdf`. [Online; accessed 24-July-2017].

[107] Henri Deelstra. Valleys of the Future, November 2015. URL `https://www.kivi.nl/uploads/media/565493800e2e1/plenair-Deelstra.pdf`. [Online; accessed 24-July-2017].

[108] Csaba Horváth. Pre-measurement class I, July 2009.

[109] Ethirajan Rathakrishnan. *Instrumentation, measurements, and experiments in fluids*. CRC Press Boca Raton, FL, 2007.

[110] CETONI GmbH. neMESYS Manual - Summaries and directories, January 2014.

[111] William K. George. Lectures in Turbulence for the 21st Century. *Chalmers University of Technology*, 2013.

[112] James M. Wallace, Helmut Eckelmann, and Robert S. Brodkey. The wall region in turbulent shear flow. *Journal of Fluid Mechanics*, 54(1):39–48, 1972.

[113] James M. Wallace. Quadrant analysis in turbulence research: history and evolution. *Annual Review of Fluid Mechanics*, 48:131–158, 2016.

A

Appendix - More dirt on the Open Air Line ESP

The content in this appendix is a collection of information from publications on the 'Open Air Line ESP' by the Antea group. The reader can expect to get a broader overview of the product from this appendix. All the questions encompassing the overall performance of the ESP are given in a document by Oranjewoud (now the Antea group) [104].

The Antea group currently currently holds a Dutch patent for the PM eliminating ESP and are currently working on a worldwide patent, per a magazine article [105]. Several configurations of the internal structure of the ESP were tested out in collaboration with TU Eindhoven, before arriving at the most effective design. Another collaborator is TU Delft, which looks into the aerodynamics of the pollutant dispersion i.e. the subject of this thesis.

One major advantage of this device is its dependence on natural wind for capturing pollutants and a single ESP is capable of cleaning 2 m^3 of air per second. Per May 2016, the Antea group were exploring the possibility to test the ESP for about five months, along the A27 in Oosterhout. Each module consumes about 10 W of energy collected through solar cells and automatically shuts off during rain, contributing to its safety.

An infographic published by the Antea group [106], describing the purpose and functioning of the ESP is shown in Figure A.1. The interested reader may also find the infographic online, in case the text here is illegible. However, a short summary of the working mechanism is given below.

Tiny, invisible PM is often emitted by vehicular traffic on highways passing through densely populated urban regions. The PM is comprised of sand, sea salt, soot from diesel engines and dust particles due to braking, tire wear and the road surface. Often, the legal limits for PM in urban regions is breached and these pollutants can lead to asthma, lung cancer and respiratory diseases. The Antea group proposes the installation of the 'Open Air Line ESP' on top of the SBs, from where the majority of the fine particles escape the highway towards urban regions.

The turbulent flow on the freeway drives the PM towards the ESP. The ESP comprises of an external casing, power wires that generate electrostatic fields, and an internal mesh structure where the PM settle and clump together. Once the particles become heavier, by clumping together, they cease to belong to the most harmful category of $PM_{0.1}$ or less. The clumped particles are also regularly cleaned by wind and rain which fall to the ground level and are transported away in a controlled manner with the sewage flow.

This ESP is low-maintenance, safe and easy to install, while capable of being powered through solar energy (through attached solar panels). This ESP can be employed along freeways, in urban areas (for instance, the inlets of ventilation systems in hospitals) and also in tunnel mouths.

Shown in Figure A.2, is another illustration of the ESP installation. The ESPs are installed flush on top of the SB, with a facility to collect and drain PM washed away by rain, presumably to a gutter. This ensures that the problem is eliminated and not simply displaced. Shown also is what seems to be an earlier version of the ESP prototype, as the internal design differs significantly from that shown in the technical drawings provided by the Antea group [67].

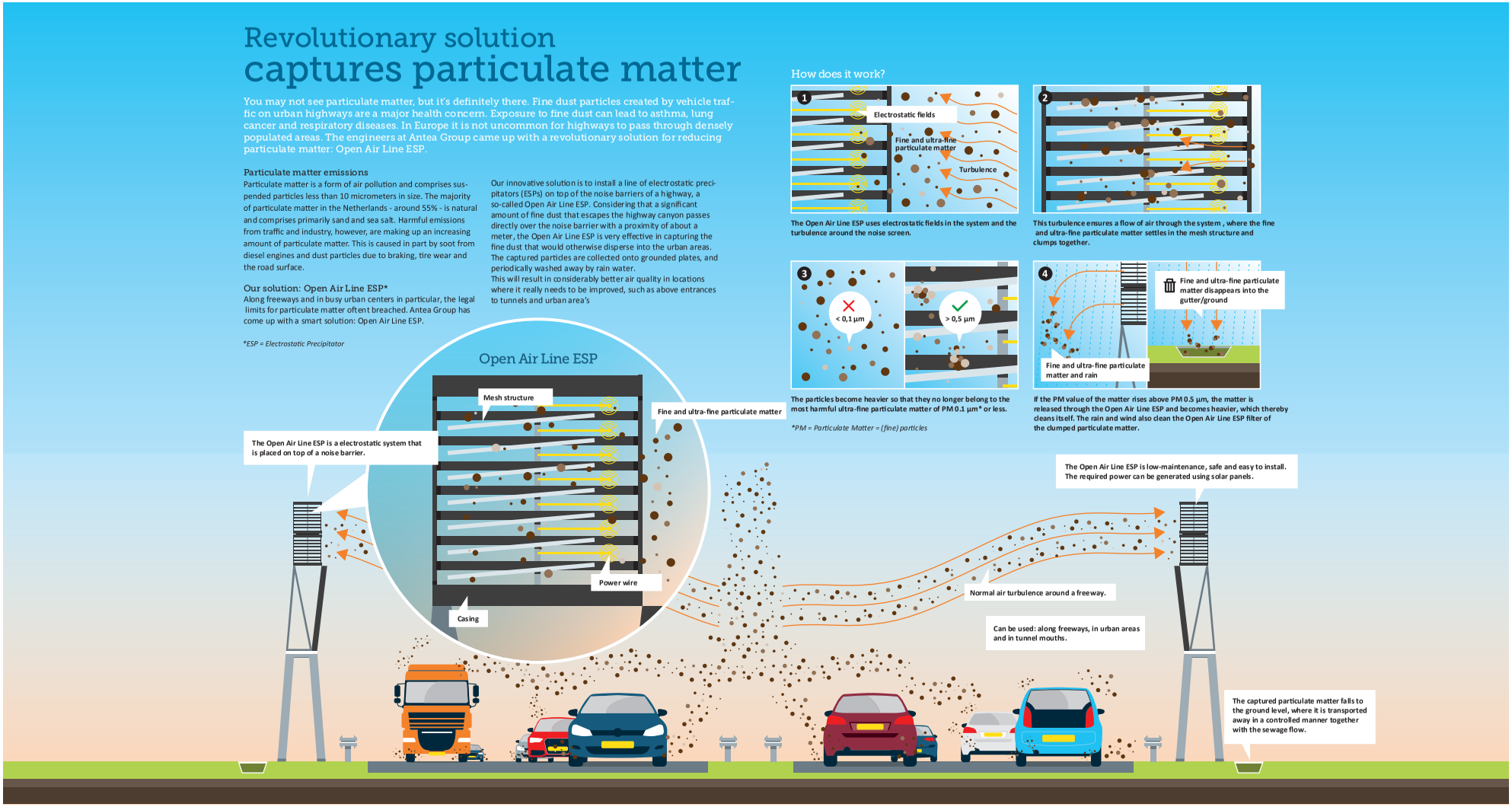

Figure A.1: An infographic on the purpose and functioning of the Open Air Line ESP. Image reproduced from a document of the Antea group [106].

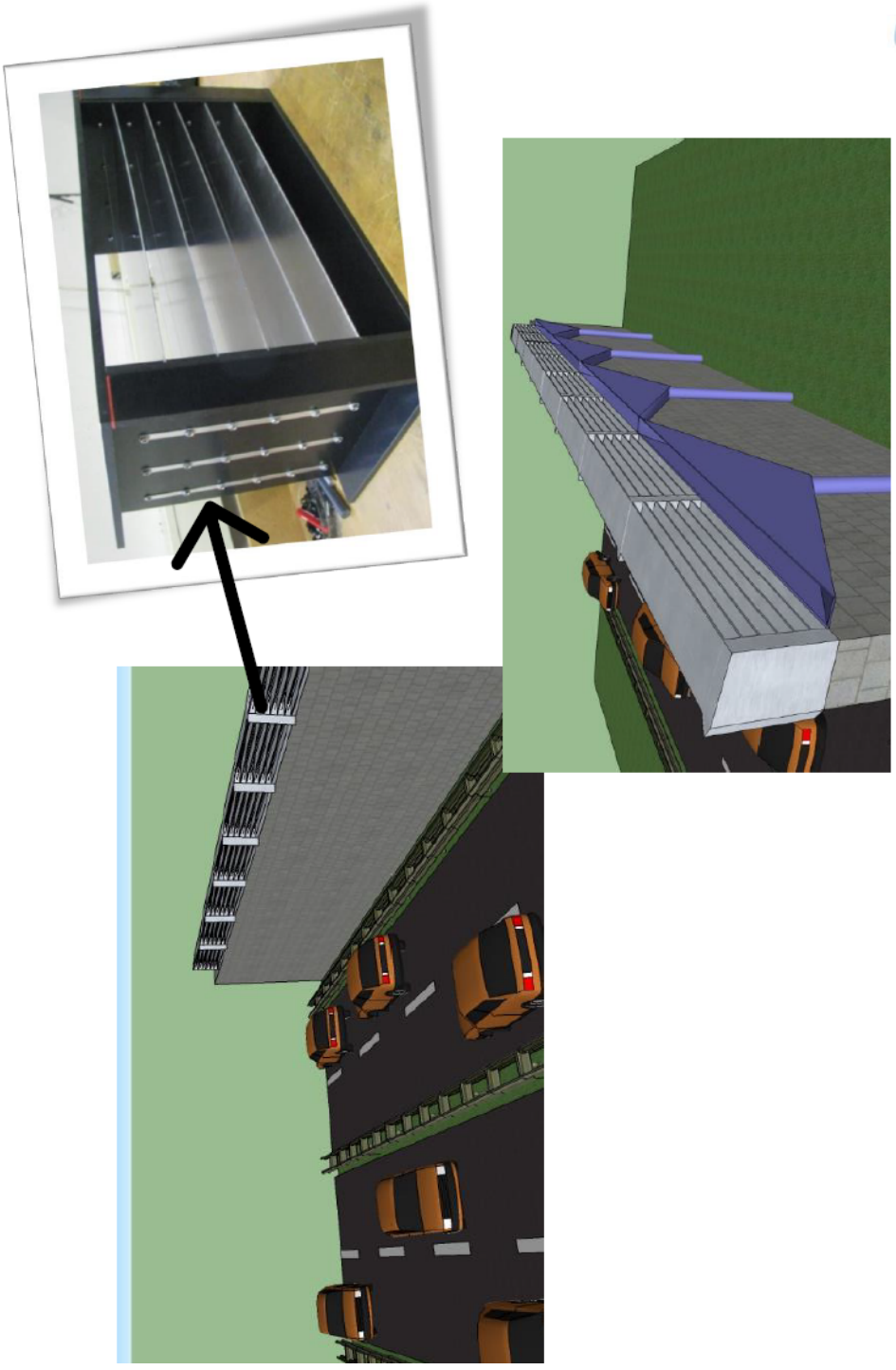

Figure A.2: Plan for ESP installations along highways. Image reproduced from Deelstra [107].

B

Appendix - Practical aspects of the current experimental setup

The information given in this appendix details the practical aspects of the different measurement techniques within the scope of the present experimental setup. Information on pitot-static tubes, planar PIV and PLIF is given in Appendix B.1, Appendix B.2 and Appendix B.3, respectively. The content here might be useful to any experimentalist who is just starting out.

B.1. Practical aspects of using the Pitot tube

In this section of the appendix, different practical aspects of using the pitot-static tube are dealt with. In Appendix B.1.1, the calibration of the pressure transducer is discussed. This is followed by subsequent discussions on the operation of the pitot tube and the traverse used for the pressure drop measurements in Appendix B.1.2 and Appendix B.1.3 respectively.

B.1.1. Calibration of the pressure transducer

Information received from the pressure transducer is in voltage difference across its ends. Physically, the pressure transducer senses the dynamic pressure. In order to relate these two quantities, the pressure transducer needs to be calibrated. A schematic of the calibration setup can be seen in Figure B.1.

Calibration is performed using a Van Essen Betz manometer shown in Figure B.2. The Betz manometer is pressurized using Nitrogen. The Betz Manometer works in a manner similar to a U-tube manometer, as noted by Rathakrishnan [109].

As shown in Figure B.3, the manometer is composed of a reservoir and a cylindrical column filled with distilled water. The column carries a float with a graduated scale on it. The scale is transparent and an enlarged image of the scale is projected onto the frosted glass. The scale on the system returns the height difference between the water column and the reservoir in millimeters and is accurate up to one tenth of a millimeter.

Applying excessive pressure may result in water squirting out of the top of the manometer. It should be ensured that there are no traces of water present in the tubing and that the pressure transducer setup is completely dry. The positive end of the transducer is connected to the positive end of the manometer and vice versa.

The regulating valve in Figure B.1 is initially shut off completely, and the pressure reading on the manometer is adjusted to zero. At the same time, the zero knob on the demodulator is fixed to have a low voltage difference reading of a value between 0 and 1 V. Following this, the regulating valve is opened till the maximum expected pressure, approximately 500 Pa (or 50 mm on the Manometer), is reached. Then, the span knob on the demodulator is adjusted to give a reading of 10 V on the voltmeter. This sets the voltage range.

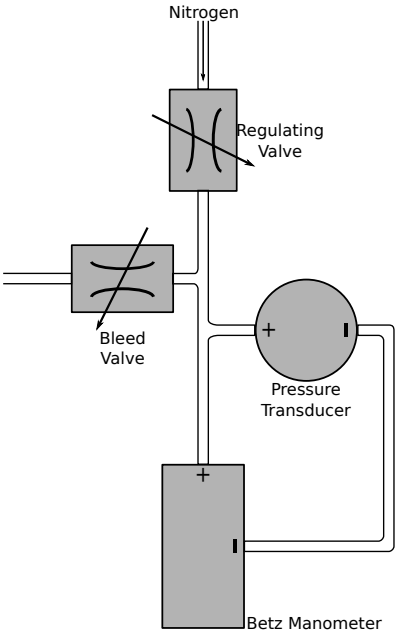

Figure B.1: Schematic of the setup used to calibrate the pressure transducer.

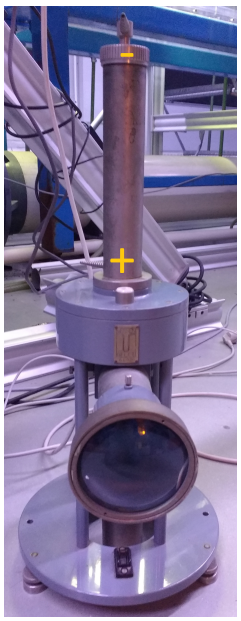

Figure B.2: The Betz Manometer used for calibrating the pressure transducer.

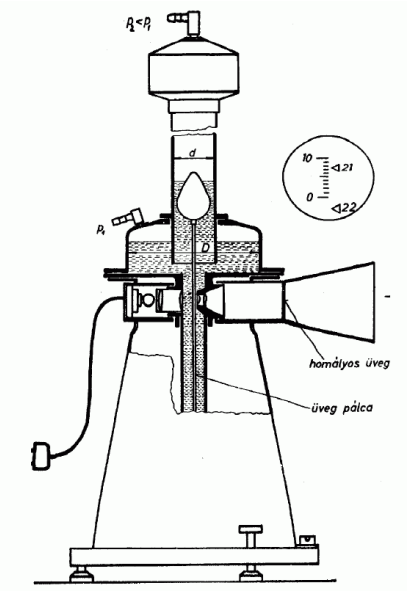

Figure B.3: Schematic of a Betz Manometer. Image reproduced from Horváth [108].

Next, to get the requisite data points, the bleed valve is opened regularly to reduce the system pressure in small steps (say 20-30 Pa or 2-3 mm on the manometer) till the zero is reached again. The voltage difference is noted at each of these different pressure differences. It is also advisable to keep a note of the values of zero and span on the demodulator. Finally, a linear fit is made through the logged data points to obtain the calibration curve. It is advisable to have at least 10 points for the linear fit. A sample fit is shown in Figure B.4 where the linear fit has a R^2 value of 0.9999.

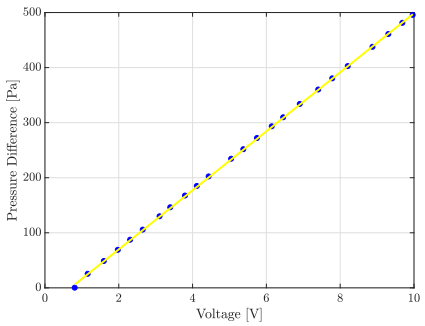

Figure B.4: Linear fit for the calibration of the pressure transducer.

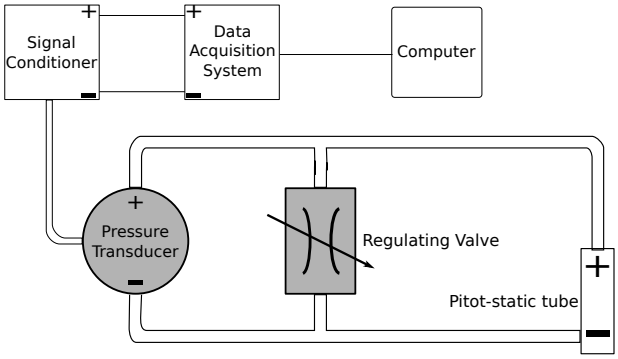

Figure B.5: Schematic of the pitot tube setup.

B.1.2. Operation of the Pitot tube

Once the calibration is complete, the pressure transducer is ready to be used in conjunction with the pitot-static tube, in a manner shown in Figure B.5. The next step involves introducing water into the tubing while avoiding air bubbles. Air bubbles, being compressible, may result in incorrect voltage measurements, if present in the system.

The first step involved in the air bubble removal is opening the regulating valve, which shorts the two ends across the differential pressure transducer. To get the water flowing, the end of the tube at one of the pressure ports is loosened and lowered below the water channel, resulting in a flow. The use of

transparent tubing helps identify the presence of air bubbles in the system. Once all the air is removed, the loosened end can be reattached back to the pitot tube, preferably underwater. The regulating valve must then be shut off. If residual air bubbles still exist in the system, they may be first gathered at the highest location (using buoyancy to advantage) by tapping the tubing around the bubbles. They can then be guided through the tubing by forming temporary, local maximas in the tubing, and released underwater.

B.1.3. Traverse for the Pressure drop measurements

Pitot tube measurements were required in the front as well as the rear of the model ESP. This necessitated a development of a traverse structure that easily facilitated a quick to and fro displacement of the pitot tube relative to the ESP. Two sets of such structures were constructed and implemented for the pressure drop measurements.

The first traverse structure can be seen in Figures B.6a and B.6b. It was compiled from an assortment of cylindrical rods and mechanical traverses. The structure provided flexibility in the placement of the pitot tube relative to the model ESP, but was not suited for precise placement, i.e. poor repeatability of experiments. In addition, it did not provide ample support to the pitot tube leading to vibrations of the pitot tube even at relatively low water tunnel speeds. As was discussed in Section 5.1, the velocity measurements from the pitot tube (especially behind the ESP) are extremely sensitive to their relative placement to the ESP. Thus, it would be desirable to have a structure where experiments could be considered repeatable.

The second traverse structure, seen in Figures B.6c and B.6d, provided several improvements over the first one, including increased stability as well as precision placement of the pitot tube relative to the ESP, allowing for repeatable measurements.

B.2. Practical aspects of performing a successful PIV experiment

As mentioned previously in Section 4.4.1, PIV is a relatively complicated experimental technique requiring experience and expertise from the experimentalist. Some tips learned on the job by the author are dealt with in the forthcoming subsections.

B.2.1. Starting up the laser

A laser requires the following for successful operation: (i) A set of mirrors (one 100% reflective and one 80% reflective) which form a cavity allowing for energy buildup until the Q-switch (an optical shutter) opens (ii) An energy source (a white mercury lamp in the current case) (iii) A crystal/gas to fluoresce (Nd:YAG crystal) in the current case. Energy is obtained through emission of photons.

The laser used for the current experiments can be seen in Figure 4.11a and Figure 4.11b. Before getting the laser into a running state, several connections, electrical and hydraulic, need to be performed.

(i) The power supply of the laser must be connected to the main electricity line.

(ii) Connections (electrical and hydraulic) must be made between the power supply and the laser head.

(iii) The outer casing of the laser head and the power supply must be installed, failing which the laser will not operate.

(iv) Electrical connections must be made between the programmable timing unit and the triggers in the laser (flash lamps and Q-switches).

(v) The interlock connection must be made. This is a precautionary safety mechanism that shuts down the laser if the door to the laboratory is opened accidentally/deliberately.

(a) The first pitot tube traverse structure composed of cylindrical rods and mechanical traverses.

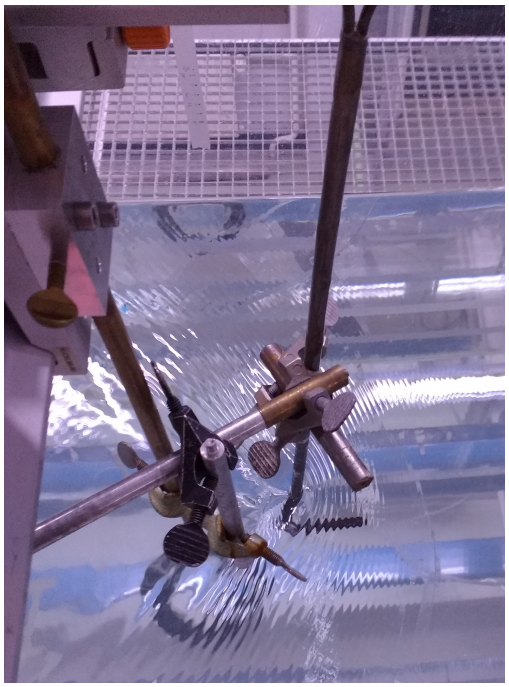

(b) The first pitot tube traverse structure in the water tunnel.

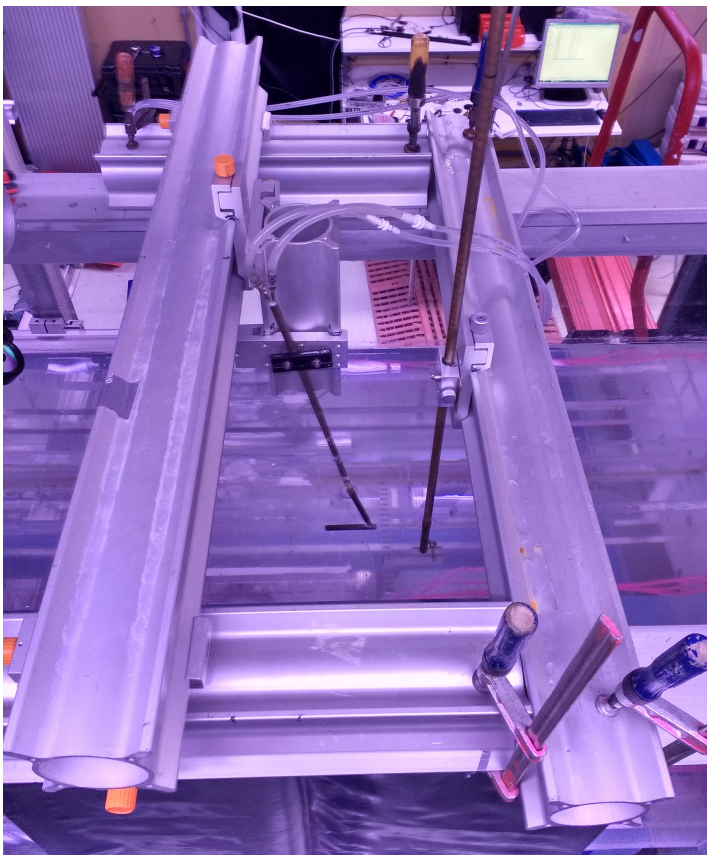

(c) The second pitot tube traverse with the pitot tube in front of the ESP.

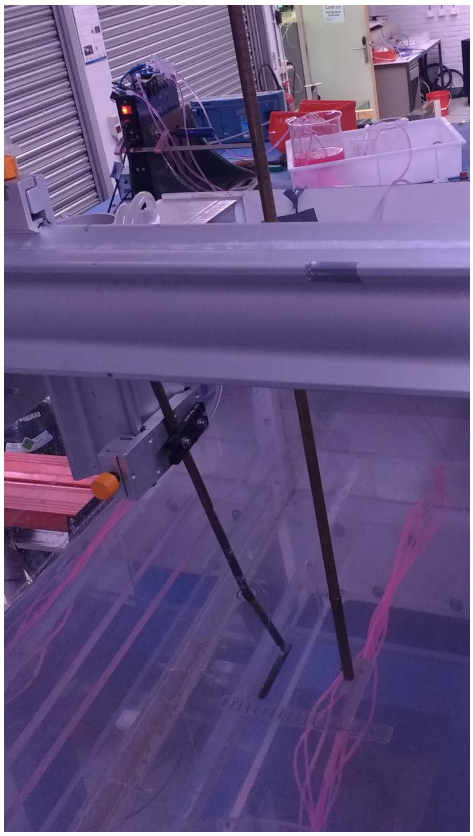

(d) The second pitot tube traverse with the pitot tube behind the ESP.

Figure B.6: The two constructions of traverses utilized for pressure drop measurements.

(vi) Hoses must be attached between the power supply and a (tap) water source as well as a sink, which too helps in heat exchanging.

(vii) Sufficient (demineralized/deionized) water must be present in the chamber that provides water for cooling the laser head. If not, the water must be pumped into the chamber and the chamber must be run for about 15 minutes to remove air.

(viii) Since the laser head is being controlled by the programmable timing unit, it must be set to be used in the external mode.

(ix) Before the beginning of an experiment, the laser heads must be operated at maximum power (via the hand-held controller) for about 15 minutes to warm up the machine and have it running in a stable state.

B.2.2. Setting the field of view

For a good quality PIV experiment, the cameras need to focus well at the region of interest. Typical images of the calibration target obtained after setting the field of view can be seen in Figure 4.11g and Figure 4.11h. The following steps are recommended in order to set the field of view.

(i) It should be ensured that the cameras are mounted on X95 rails in a manner that allows for flexible translation of the cameras in all three directions. The presence of Scheimpflug adapters provide additional degrees of freedom to focus into the field of view.

(ii) A calibration target must be inserted in the region of interest and it must stably stay in its position.

(iii) Starting up the camera requires a few minutes till it reaches the temperature at which the sensor operates is reached.

(iv) The field of view (in terms of physical length units) need to be determined beforehand. Then, using DaVis, the cameras must be adjusted so that the image covers the desired field of view. In case there are multiple cameras intended for the same field of view, it must be ensured that both focus at the same space.

(v) Once the field of view is set, the lenses of the cameras should be fine-tuned. This is done by zooming in on the markers (crosses/dots) in DaVis.

(vi) If the field of view is wide, imaging can be improved by either translating the camera away or using a lens with a lower focal length.

(vii) In order to improve the quality of the measurements, all surfaces of the water channel must be cleaned (especially from the seeding particles that adhere to the walls) and dark, non-reflective shades be installed in the background to reduced background light.

B.2.3. Performing calibration

Calibration too is an important step in the process of a successful PIV experiment. It correlates distances in the physical space with distances in the images. It should be noted that calibration is performed under natural light conditions. Care must be taken that the calibration target is removed before operating the water channel, or else it might be pushed into the downstream expansion.

(i) Calibration can be performed using either a stock calibration target or a custom-made one (in case the field of view has an irregular shape). In the current project, a custom-made target, used by Eisma [14], was utilized. For the boundary layer characterization, Type 31 was used.

(ii) In case a custom-made target is utilized, it must be added to DaVis along with the specifications (size of symbols and spacing between them).

(iii) Following the instructions on DaVis, the calibration is finished after a third order polynomial is fit through the detected markers. The standard deviation of the fitting error was reported at approximately 0.3 pixels in the current study.

(iv) Even if a single component of the apparatus (laser, optics or camera) is disturbed, the calibration procedure must be performed again.

(v) It is recommended that each all experiments performed following a new calibration be saved under a new project in DaVis. This reduces the probability of combining the raw images and calibration data incorrectly.

B.2.4. Aligning the laser sheet

One of the more complicated but important steps in a successful planar PIV experiment is the formation of a thin laser sheet in the region of interest. Section of the optics forming the laser sheet can be seen in Figure 4.11d and Figure 4.11j.

(i) Optics play a very important role in the laser sheet alignment procedure. It should be ensured that the X95 beams upon which the laser sheet forming optics are mounted, do not have any contact with the water tunnel. This is because the water tunnel vibrates during operation and can lead to significant fluctuations in the light sheet.

(ii) A calibration target needs to be placed in the region of interest. If possible, it is advisable to have a mechanism that allows the calibration grid to be placed firmly while also allowing for reproducibility.

(iii) The first step involves setting the laser at a low power output. The knobs for both the lasers on the hand-held controller are set to their minimums. The laser setting on DaVis must be set to the 'Adjust mode'.

(iv) Then the knob to control the straight beam is slowly rotated until a green beam is visible. At this point, the beam polarizer of the frequency doubler is rotated until the green beam reaches its minimum intensity. Rotating the polarizer changes the intensity of light able to reach the exit of the laser.

(v) From a safety perspective, it is recommended that the user not have a watch, jewelry or any reflective material on his/her hands. This could reflect the near infrared light into the users eyes and cause permanent damage. Near infrared light is undetectable to the human eye, making it even more lethal.

(vi) The laser power can also be reduced via DaVis which manipulates the phase between the trigger signals to the Q-switch and the flash lamps. However, this is not recommended.

(vii) An object with a transparent bottom must be held firmly on the free water surface and over the region of interest. This reduces the laser sheet distortion by waves and other disturbances.

(viii) Reflective mirrors are clamped onto the X95 structures in a manner that the final beam grazes and illuminates the front section of the calibration target. Ideally, all the mirrors must be mounted along the same axis. This beam should ideally be perpendicular to the streamwise direction and be striking the center of the region of interest, for example, as shown in Figure 4.11f. In specific cases, such as a large field of view or insufficient physical access, the beam can be introduced at an angle. However, this increases the chances for the formation of shadows behind objects.

(ix) The perpendicular beam can be manipulated by rotating the final mirror so that the back reflections coincides with the incoming beam.

(x) The next step involves adding a cylindrical lens in the optical path, just before the final reflecting mirror. This lens is responsible for creating the light sheet profile. It is advisable to mount the lens on a fine-tunable traverse. Rotating the cylindrical lens would rotate the laser sheet whereas translating it along its axis would translate the profile. While installing the lenses, one must be

careful about possible reflections from the running laser. Turning off the laser during these steps would be a recommended safety precaution.

(xi) The cylindrical lens is adjusted so that the laser sheet illuminates the desired field of view. Clearly visible reflections of the green laser at the top and bottom portions of the calibration target, are an indicator of good illumination.

(xii) The next step involves the addition of the spherical (plano-convex) lens which thins the light sheet. It is recommended to have the convex portion facing the incoming beam to avoid the convergence of back-reflections. The mirrors and cylindrical lens are slightly adjusted again.

(xiii) The straight laser beam is turned off and the zigzag one is used to verify if the laser sheet illuminates the field of view reasonably well.

B.2.5. Seeding the flow

Seeding the flow in the current setup (a recirculating water channel) is a simple process.

(i) Sphericell particles are mixed well in water to form a milky solution. The solution is simply poured into the operating water channel and after a couple of flow recirculation time periods, the particles are spread out homogeneously across the cross-section.

(ii) The solution is added until the flow is reasonably translucent. Adding too many particles might result in poor image quality since the particles in the far-field might not receive sufficient light.

(iii) An estimate of the amount of particles to be added can be obtained by correlating the desired seeding density in the images to the physical seeding density.

(iv) If the water tunnel has not been operated for a long period (for example overnight) and the particle density seems low, it is recommended that the surfaces of the perforated screens, honeycomb meshes are scrubbed/cleaned. This frees the particles adhered to these surfaces and increases the seeding density.

(v) DaVis provides a feature to display the image particle density. In the current experiments, a density of around 0.04 particles per pixel was maintained. This corresponds to having approximately 10 particles in an interrogation window of size 16×16 pixels.

B.2.6. Beam overlap

Beam overlap too is an important part of the PIV experiment. If the beam overlap in the region of interest is low, the two images might focus at different sets of particles. This would increase the possibility of spurious vectors in the results. This step is performed in a dark room, and safety goggles must be utilized.

(i) If the laser beam intensity output is still low (from the calibration), it must be raised until the particles become visible on DaVis (at a resolution of 2k/4k).

(ii) Taking a few quick images (at a very low time separation, say 10 µs, the overlap of the light sheet can be judged visually by comparing an image pair. Since the laser beam has a Gaussian profile, so does the laser sheet. Thus, any large discrepancies in the laser sheet overlap would be discernible at this stage.

(iii) In the above set of images, one can also zoom in and observe whether the same particles are being visualized. Since the time separation is really small, the consecutive images should focus on the same particles, if the beam overlap is good.

(iv) DaVis also provides a feature to measure and display the instantaneous beam overlap at a certain region in the image. Two screws for fine tuning one of the mirrors associated with the zigzag laser beam are available to improve the overlap. Rotating either would displace the laser sheet in a certain direction. This can be fine-tuned until a satisfactory beam overlap value is obtained (typically larger than 0.8). This relevant mirror is shown in Figure 4.11c.

(v) A few images can be captured (while maintaining a time separation of 10 µs), and the correlation map can be observed. It too gives an estimate of the particle overlap. A higher value indicates better overlap.

B.2.7. Assessing the quality of the data

Before drawing any conclusions from the PIV data, it is necessary to ensure that the quality of the data is good. There are a few ways to go about this.

(i) The first step is to have a close look at the raw data i.e. is the profile of the laser sheet similar in both the frames and if, upon zooming in, a clear displacement of particles is observable.

(ii) Following this, the data can be processed to obtain the vector fields. Having a quick glance searching for spurious vectors, it would be clear whether the results physical or not.

(iii) To check whether the time separation between the two frames is good, one can also have a look at the pixel displacement at random locations in the field of interest. If the pixel displacement is low (for example, 1-2 pixels), the signal to noise ratio would drop. A typical value for noise is estimated at 0.1 pixels.

(iv) Along the same lines, one can look at the statistics of the flow (i.e. mean and standard deviation of the displacement), preferably at a small region in the freestream flow. The mean resembles the signal whereas the standard deviation contains, both, noise as well as turbulence. So, judgments here should be done more carefully.

(v) Lastly, one can also have a look at the percentage of vectors which are first choice, second choice and so on. As a general rule of thumb, it is recommended that the flow field is comprised of at least 95% first choice vectors.

(vi) As a suggestion, it is recommended that the user evaluate a few images before actually acquiring the experimental data. By doing so, valuable time might be saved lest errors be present in the measurement.

B.3. Practical aspects of setting up the PLIF system

Due to an overlap in the apparatus involved in the PLIF setup with the PIV setup, the practical aspects for using the laser, setting the field of view and aligning the laser sheet for PLIF are similar to those discussed in Appendix B.2. The aspects unique to the PLIF system are the topic of discussion in the forthcoming subsections.

B.3.1. Line Source

The line source is one of the most important components in the scaled down model. Thus, it's proper installation and functioning, according to the following points, is of utmost importance.

(i) The line source is embedded into the turntable which in turn is fixed onto the false bottom. The line source is glued to a rectangular slot cut into the turntable, as shown in Figure 4.12c. The tubing from the line source is drawn out at the downstream exit of the water channel via underneath the false bottom. Then further connections to the syringe pump are made as shown in Figure 4.12f.

(ii) Assessing the uniformity of the dye release in the spanwise direction can be done by making spanwise concentration measurements at different streamwise locations downstream of the line source à la Eisma [14]. Such an assessment was not performed in the current study. Nonetheless, visual inspection of the dye release in the spanwise direction, as seen in Figure 4.12d, indicates that the dye release may be considered reasonably uniform, at least around the centerline of the water channel. The absence of dye near the side walls of the water channel can be attributed to the fact that the line source does not span the entire width of the channel.

B.3.2. Syringe pump

The flow of the fluorescent dye solution to the line source is controlled through the syringe pump shown in Figure 4.12e. The system has a base module which is then connected to further syringe pumps. While four pumps were present in the setup, only three were in an operating state. Each pump is equipped with a glass syringe of 50 ml capacity and is held firmly by a syringe holder. Each syringe can also operate with a maximum flowrate of 4.5 ml/s. The direction of the flow to and from the pump can be controlled by a 3/2-way solenoid valve. The valve has three ports. One of them is used to connect to the syringe, whereas the other two are utilized as inlet and outlet. The valve has an internal switch which allows flow either from the inlet or the outlet. The syringe pump was set up and utilized per the following points:

(i) Nut fittings (with a 1/16" hole) are present at open end of the syringe as well as the three ports of the solenoid valve. Conventionally, these nuts are meant to be utilized in tandem with 1/16" outer diameter tubing. However, in the current case, tubes with outer diameter 1/4" are simply glued to these nuts as they allow for lower pressure drops and a smoother flow to and from the syringe pump. To modify the fluidic connections to the solenoid valve, the user would have to unscrew the valve, allowing for easy access.

(ii) Connections between the syringe pump and line source pass through a couple of multiple port manifolds. Using manifolds is recommended as they allow selective use of the syringes and can assist in troubleshooting. Several components from the Luer valve assortment kit supplied by World Precision Instruments are utilized in establishing all the fluidic connections.

(iii) In the initial phases of the experiments, it is highly likely that air would enter the syringe pumps via the tubing, which is undesirable. If not accounted for, this air is ejected as air bubbles from the line source, while also disturbing the release fluorescent dye. For this reason, the syringe pumps are held upright like in Figure 4.12e. Before the commencement of experiments, the tubing is flushed off all the air by directing the flow to the dye dump, shown in Figure 4.12f, instead of the line source. In this upright configuration of the syringe pump, the lighter air is closer to the open end of the syringe, and is driven out into the dye dump first. Nonetheless, air may creep in between experiments and care must be taken that the open end of the tubing placed in the dye reservoir is completely submerged within the dye solution.

(iv) The motion of the syringes are controlled by a freeware, called the Nemesys user interface. Details on using the software are given by the manufacturers [110]. Ideally, having four working syringes would enable having a continuous flow towards the line source allowing longer measurement periods. However, with three syringes, there are limitations. One of them being that a perfectly uniform outflow of dye is not possible, since one syringe would need to operate at double the flow rate of the remaining two. The maximum working flow rate is also limited since at high flow rates, air may also enter the system. Finally, for the experiments, each of the three syringes operates at an outflow rate of 1.5 ml/s, thus giving approximately 30 seconds of dye release (approximately 150 images at 5 Hz).

B.3.3. Assessing the quality of the data

Just like with the PIV images, before processing the experimental data, it must be ensured that the PLIF images are of reasonably good quality. The quality of the images can be assessed by comparing the contrast between the signal (intensity signal of the fluorescent dye) and the noise (intensity signal of the fluorescent dye in the background). The experiments were performed with a $f_\#$ of 5.6. The results obtained would have been better if the camera had been operated at its lowest $f_\#$ value of 2.8. A lower $f_\#$ allows for a higher intake of fluorescent light.

The amount of background fluorescence increases progressively as more experiments are performed. In such a case, the laser sheet will be visible in orange through the laser safety goggles. The effect of the noise is reduced by subtracting background images. If the dye intensity is deemed too low (i.e. the boundaries of the dye is not clearly discernible), it can be improved by either increasing the concentration of the fluorescent dye in the reservoir or increasing the outflow rate from the line source.

C

Appendix - Effect of averaging lengths on the boundary layer profiles

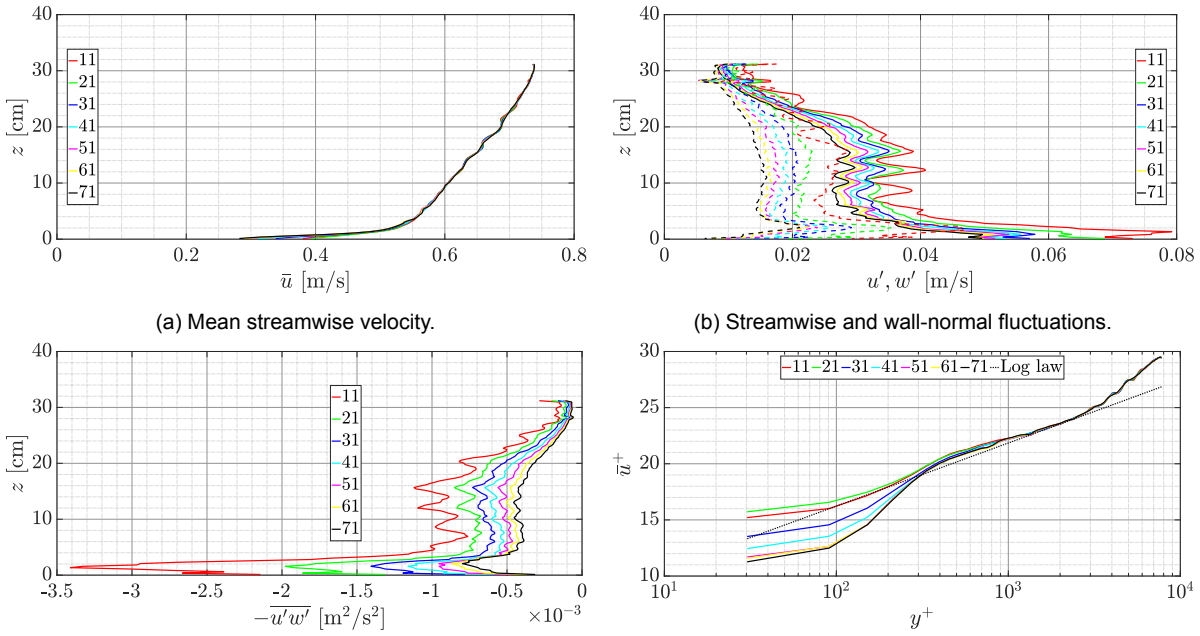

(a) Mean streamwise velocity.

(b) Streamwise and wall-normal fluctuations.

(c) Reynolds stress.

(d) Log-law fit.

Figure C.1: Effect of the number of streamwise pixels used for boundary layer characterization on different properties. The numbers in the legend represent the number of streamwise data points used for averaging. Separation between two data points is approximately 2.4 mm. The streamwise and wall-normal fluctuations in (b) are denoted by the solid and dashed lines respectively.

The boundary layer characteristics in Figure 5.5 were evaluated by averaging over a certain streamwise length, the effect of which is demonstrated in Figure C.1. The statistics are based on data from 1000 image pairs. Difference between two consecutive data points correspond to approximately 2.4 mm. The range over which the effect of averaging was tested, thus, ranges from 2.4 cm to 16.8 cm (shorter than the boundary layer thicknesses). Longer averaging lengths could not be investigated due to the limitation posed by the (lack of) goodness of the laser sheet intensity profile.

Using a longer averaging length leads to fewer fluctuations in the wall-normal direction profiles of the mean velocity, velocity fluctuations, as well as the Reynolds stress, as demonstrated in Figures C.1a to C.1c. Furthermore, the magnitudes of the fluctuations and subsequently, the Reynolds stress, are reduced as longer streamwise lengths are employed. This is mostly due to the decrease in the standard

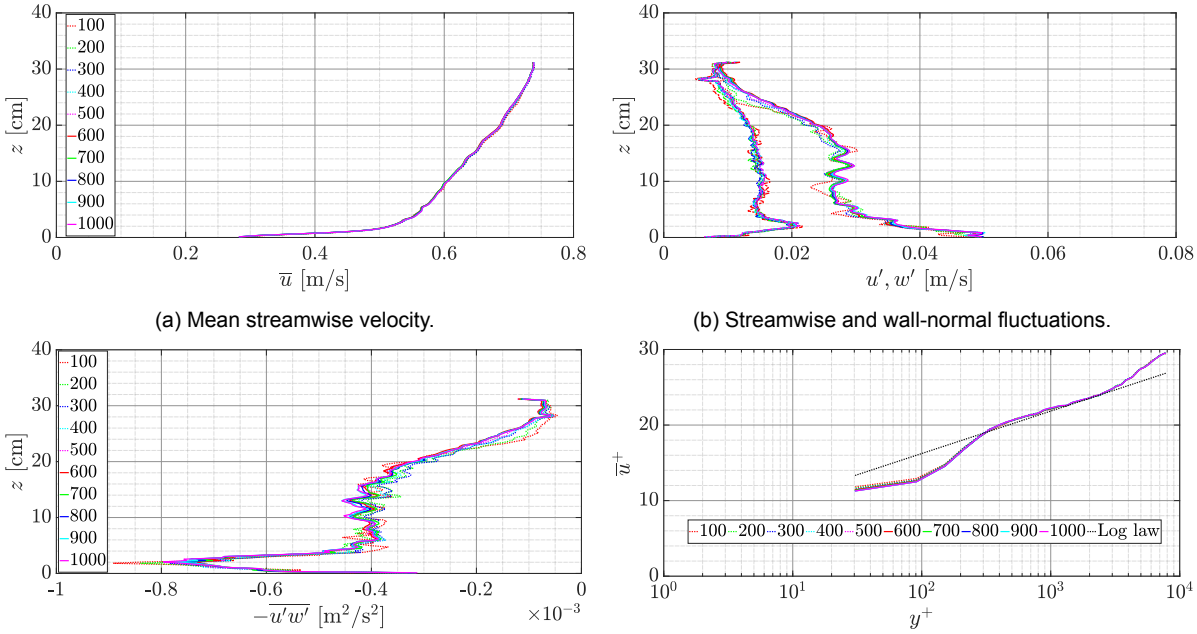

(a) Mean streamwise velocity.

(b) Streamwise and wall-normal fluctuations.

(c) Reynolds stress.

(d) Log-law fit.

Figure C.2: Effect of the measurement time used for boundary layer characterization on different properties. The numbers in the legend represent the number of images used for averaging. Separation between two images is approximately 0.2 s. The streamwise fluctuations in (b) are represented by the same convention in (a), while the wall-normal fluctuations are denoted by dashed and dash-dot (in place of solid and dotted lines respectively).

deviation upon increasing the number of measurement points. While the mean velocity too changes with the averaging length, its effect on the root mean squared velocities is not expected to be as high. Upon comparing the plots in the inner scaling form in Figure C.1d, a good overlap between the different profiles (ignoring the wiggles) is present above z^+ of 1000. None of the plots fit perfectly with the linear log-law curve, bar the region between z^+ of 1000 and 3000, which might indicate the presence of an imperfect approaching neutral ABL.

A similar convergence study on the effect of the number of image pairs is shown in Figure C.2. As expected, a larger number of images improves the convergence.

D

Appendix - Parameters affecting aerodynamic efficiency evaluation

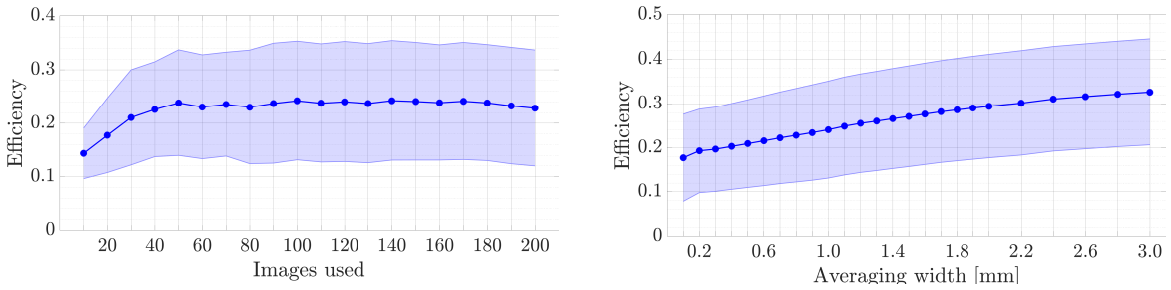

(a) Number of images used.

(b) Width of rectangular windows.

Figure D.1: Effect of spatial and temporal averaging on the aerodynamic efficiency determination of the ESP. The width of rectangular windows in (b) refers to the width of region A shown in Figure 5.10. The symbols represent the means while the shaded areas represent the standard deviations.

The effect of three parameters on the efficiency evaluation, defined previously in Figure 5.10, were looked into. The three were: number of frames used for averaging; width of the spatial averaging rectangular area (regions A and B defined in Figure 5.10) and; exclusion of the region in front of the outer casing of the ESP (i.e. compressing region A from Figure 5.10 in the wall-normal direction). The influence of the former two are illustrated in Figure D.1.

From Figure D.1a, it is observed that beyond 50 images, the mean value of the efficiency (evaluated for 'Run 1' of a 5 cm high SB) is steady and so is the standard deviation. The latter point implies that the error on the mean decreases with increasing number of images used. However, beyond the point of 160 images, the mean value shows a slight decline. This is attributed to the fact that the line source emits dye for about 30 seconds (corresponding to 150 images at 5 Hz). Fixing the fourth syringe of the syringe pump (as described in Appendix B.3.2) can allow for longer averaging times and thus, providing more reliable statistics.

From Figure D.1b, it is evident that increasing the width of the efficiency evaluation domain (also evaluated for 'Run 1' of a 5 cm high SB) increases the measured efficiency. Since the interest is mainly in an instantaneous efficiency, a thinner domain is preferable. However, having an infinitesimal width of the section might also result in higher instances of dye absence (owing to intermittency) leading to reduced efficiencies. An alternative selection would be of all the pixels where the instantaneous velocity vector would indicate that the dye would go over the SB before the next image is captured. However, this would be a tedious process and not very accurate either, since the turbulent nature of the flow would render the predicted dye motion useless. Finally, a width of 1.5 mm is chosen for the efficiency evaluation domain.

Lastly, the exclusion of the region in front of the external casing of the model ESP from the efficiency

evaluation domain can result in a decrease of the aerodynamic efficiency by a factor of two. This is attributed to the thickness of the plexiglass casing which accounts for nearly half of the ESP height. However, from the design of the ESP prototype, it is known that the external casing of the ESP is not as thick as the entrance of the ESP. Thus, for the current aerodynamic efficiency evaluations, the area in front of the ESP entrance is also considered.

E

Appendix - Repeatability of the experiments

The repeatability of the experiments was also looked into by performing five runs of experiments for flow over a SB with an ESP atop. The SB heights considered were 5 cm and 3 cm (h_{SB} = 4.27h_{ESP} and h_{SB} = 2.56h_{ESP} respectively). The contour plots of the mean dye intensities along with the mean velocity fields are shown in Figure E.1 and Figure E.3 respectively. While these plots make it seem that the experiments are quite repeatable, the plots in Figure E.2 and Figure E.4 as well as the results in Table F.2 and Table F.3 indicate otherwise. The differences in these plots between different runs is caused due to the inaccuracy associated with the placement of the ESP in the flow. These inaccuracies in the ESP placement are visible in the imprints of the ESP in the blue boxes in all the cases shown in Figure E.1 and Figure E.3. This indicates that the accuracy of the reported aerodynamic efficiencies in this report are extremely sensitive to the exact placement of the ESP on the flow. For future experiments, it is recommended that the traverse associated with the model ESP have a more precise mechanism to suspend the ESP into the flow.

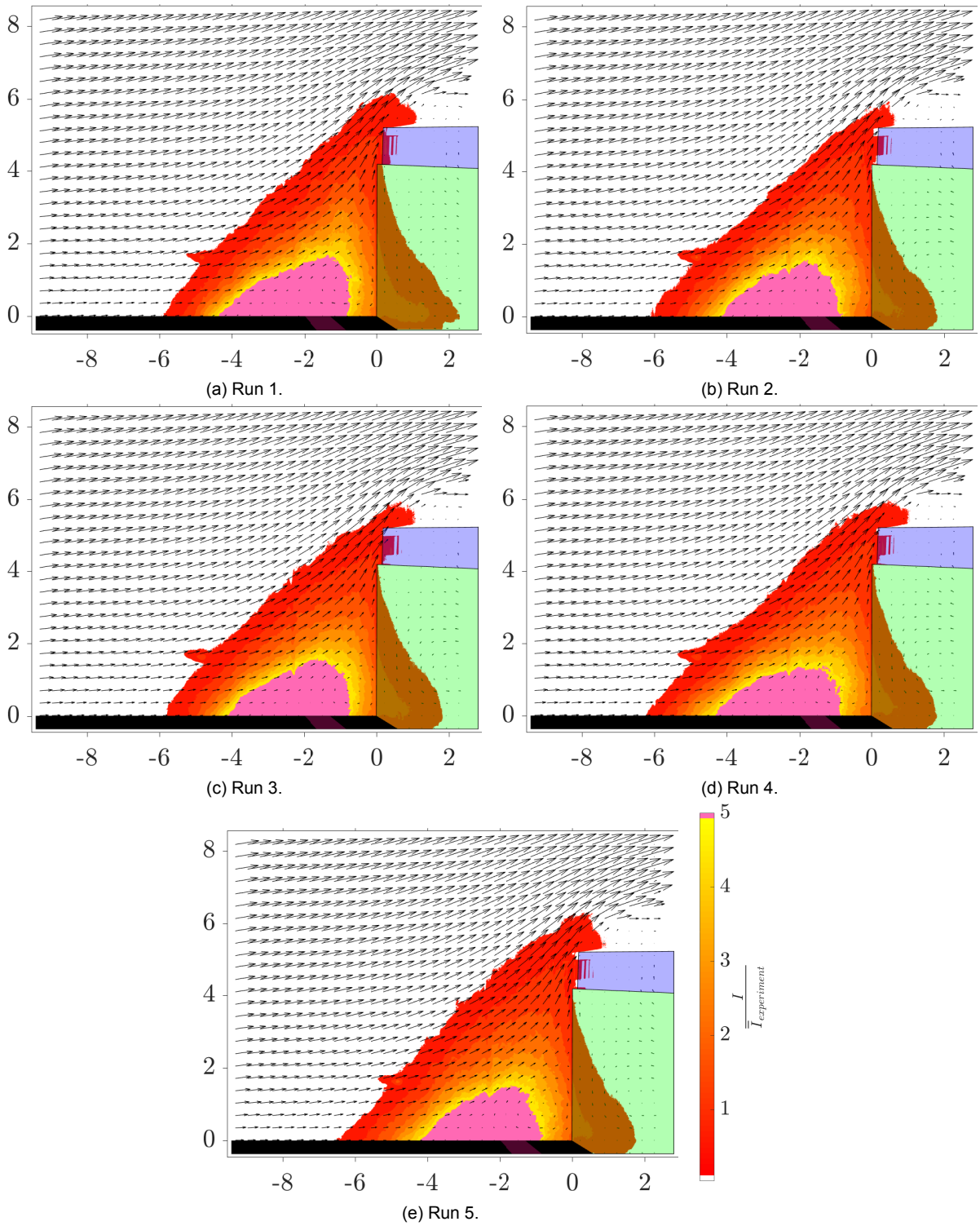

(a) Run 1.

(b) Run 2.

(c) Run 3.

(d) Run 4.

(e) Run 5.

Figure E.1: Pollution dispersion for five runs of a 5 cm high SB and an ESP atop (h_{SB} = 4.27h_{ESP}). Contours of the mean dye intensity and mean velocity vectors are shown. Every fifth vector, in each direction, is displayed. The x and y axes in these plots represent $\frac{x}{h_{ESP}}$ and $\frac{z}{h_{ESP}}$ respectively.

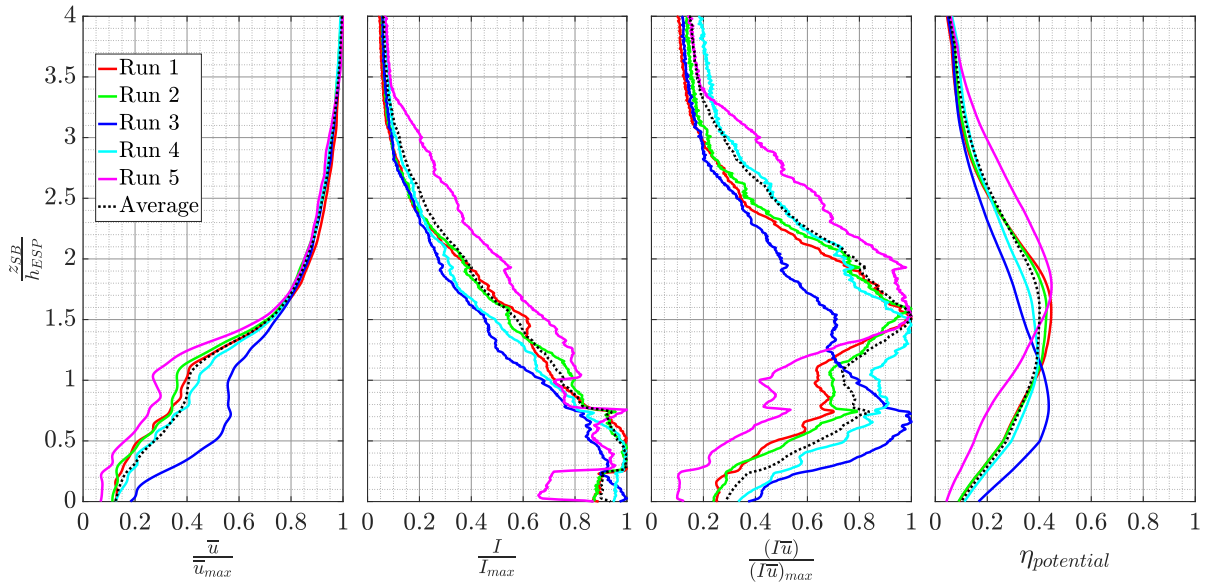

(a) Profiles of various normalized quantities.

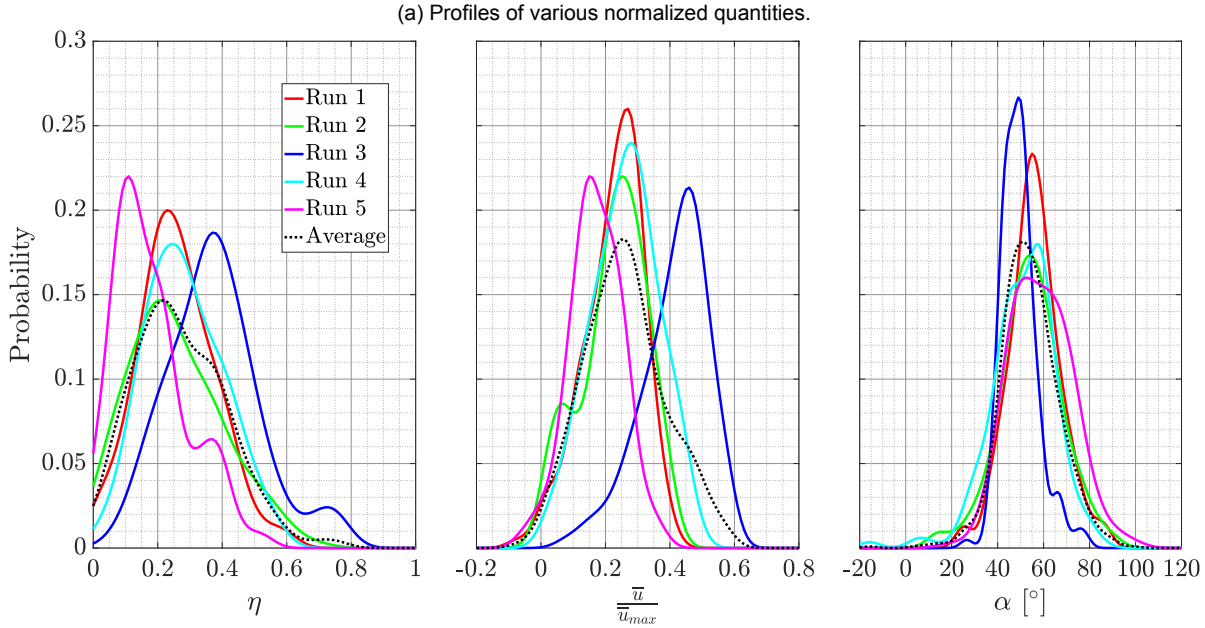

(b) Probability Distribution Functions of various quantities in front of the entrance of the ESP.

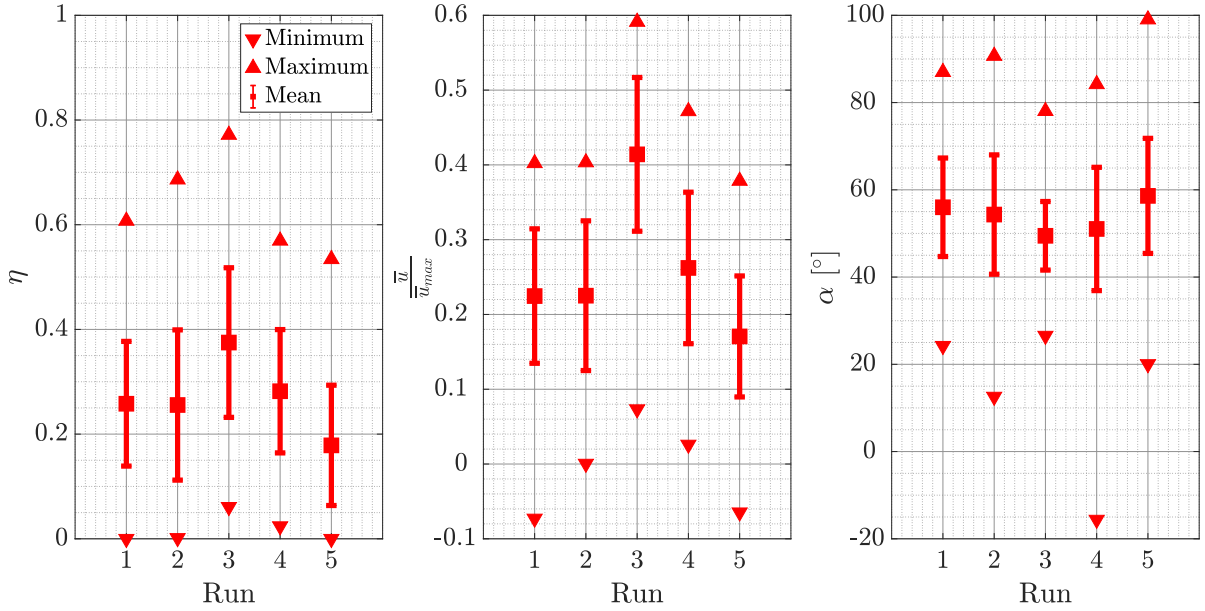

(c) Statistics on the inflow characteristics and performance of the ESP.

Figure E.2: Pollution dispersion characteristics just in front and above the sound barrier for different runs with a 5 cm high SB and an ESP atop (h_{SB} = 4.27h_{ESP}).

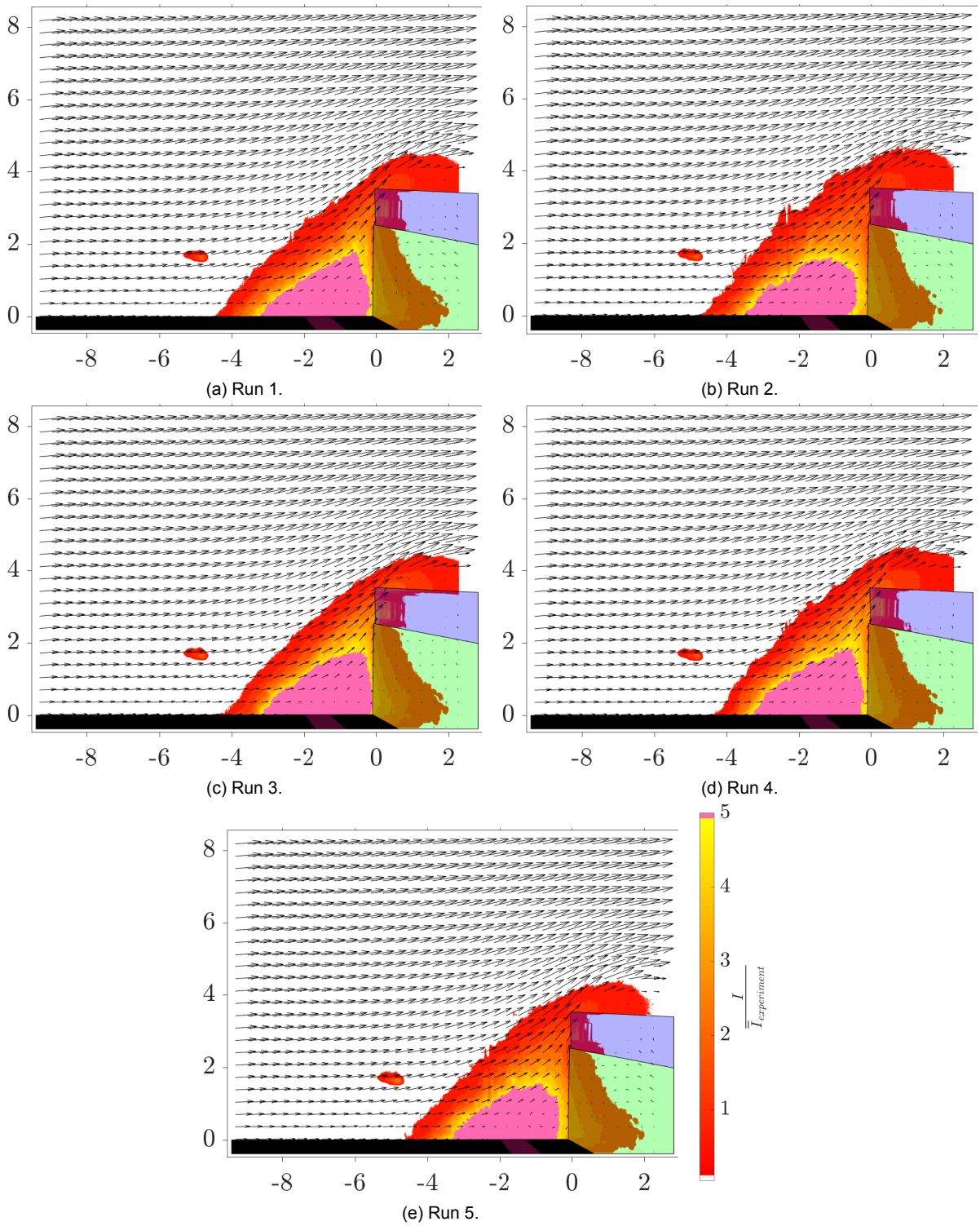

(a) Run 1.

(b) Run 2.

(c) Run 3.

(d) Run 4.

(e) Run 5.

Figure E.3: Pollution dispersion for five runs of a 3 cm high SB and an ESP atop (h_{SB} = 2.56h_{ESP}). Contours of the mean dye intensity and mean velocity vectors are shown. Every fifth vector, in each direction, is displayed. The x and y axes in these plots represent $\frac{x}{h_{ESP}}$ and $\frac{z}{h_{ESP}}$ respectively.

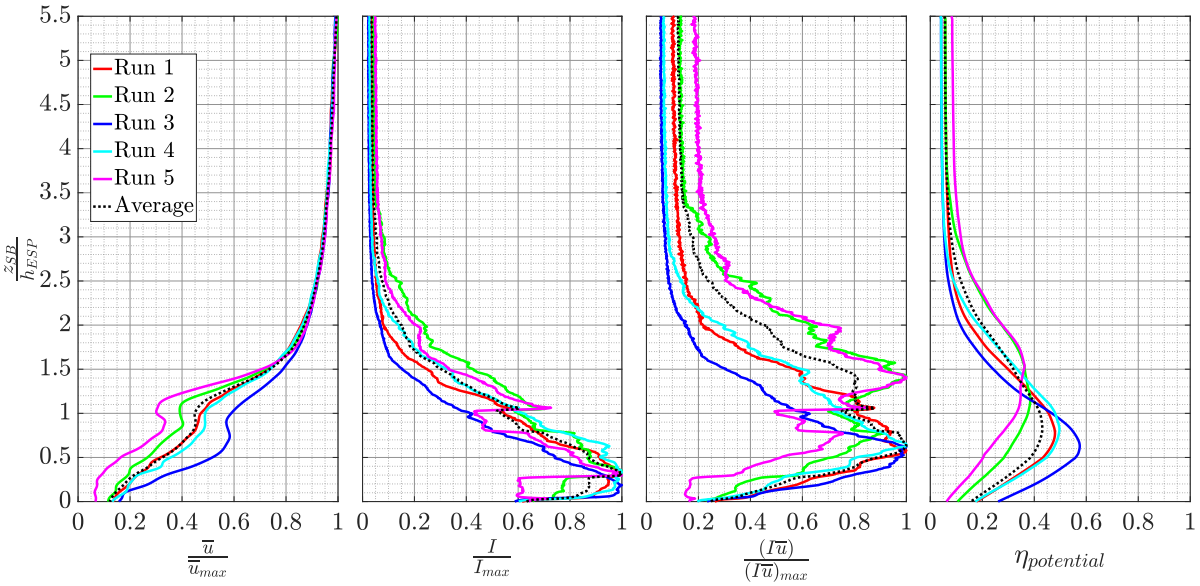

(a) Profiles of various normalized quantities.

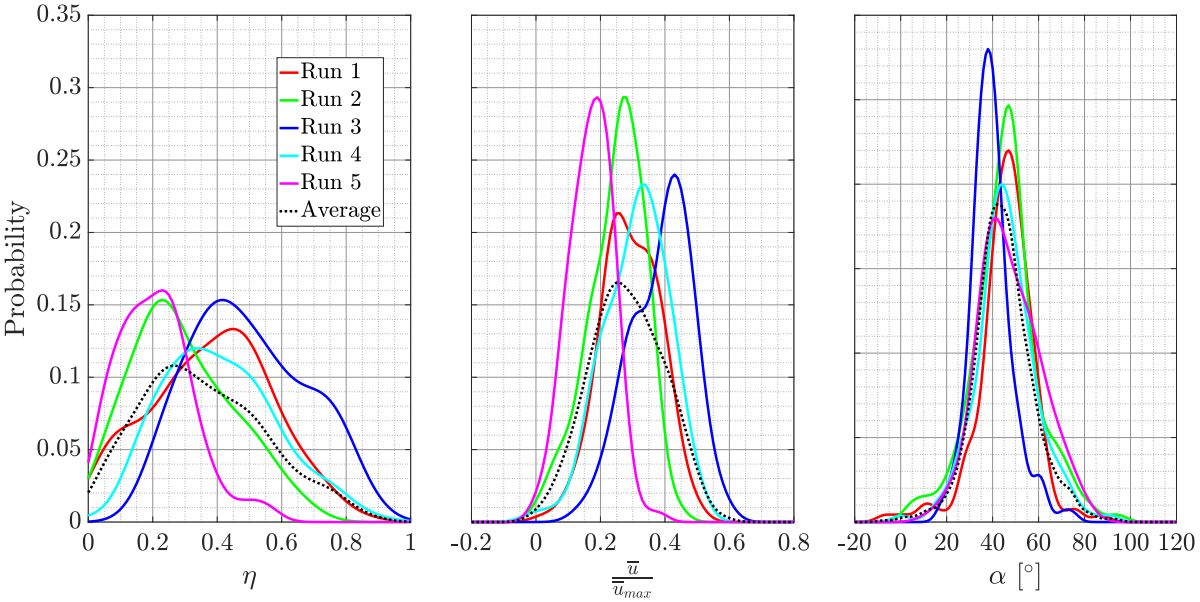

(b) Probability Distribution Functions of various quantities in front of the entrance of the ESP.

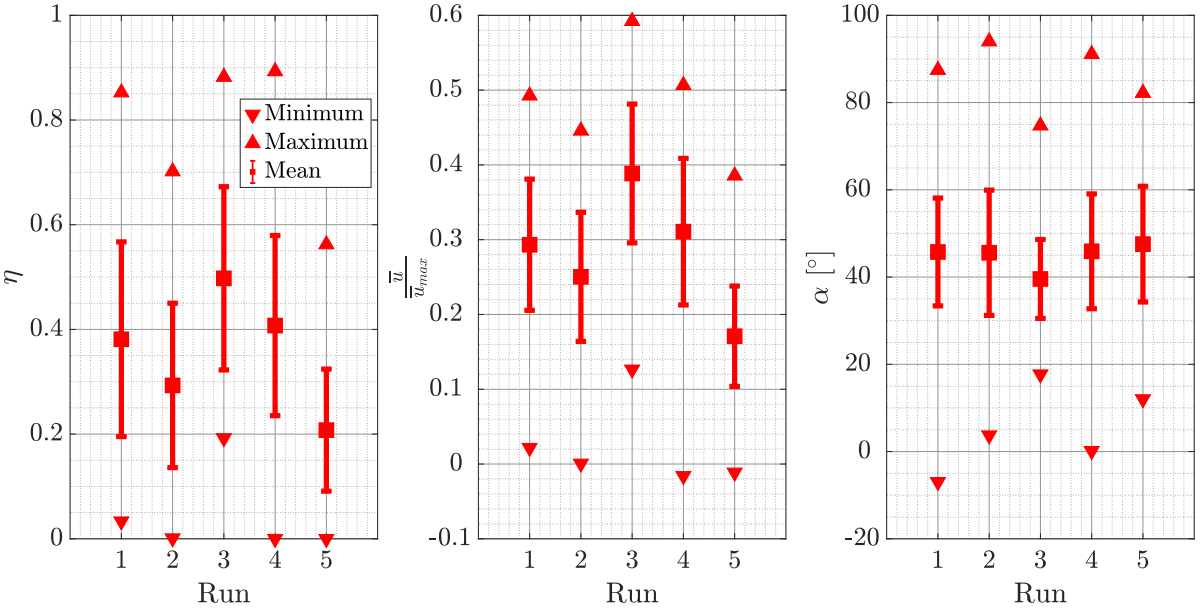

(c) Statistics on the inflow characteristics and performance of the ESP.

Figure E.4: Pollution dispersion characteristics just in front and above the sound barrier for different runs with a 3 cm high SB and an ESP atop (h_{SB} = 2.56h_{ESP}).

F

Appendix - Results tabulated

Some of the major results presented previously in line plots are summarized here in a tabulated form. The velocities used for velocity normalization for each case in Tables F.2 to F.8 are summarized in Table F.1.

Table F.1: Values of $\overline{u}_{max}$ used for velocity normalization in the following tables.

Table	a	b	c	d	e
Table F.2	0.6645	0.6597	0.6674	0.6662	0.6714
Table F.3	0.6517	0.6549	0.6625	0.6571	0.6620
Table F.4	0.6380	0.6551	0.6517	0.6535	0.6666
Table F.5	0.6307	0.6494	0.6576	0.6538	0.6658
Table F.6	0.6658	0.6921	0.6998	0.7083	0.6941
Table F.7	0.6576	0.6605	0.6697	0.6655	0.6696
Table F.8	0.6647	0.7029	0.7297	0.7712	0.7978

Table F.2: ESP performance and ESP entrance flow statistics for different runs on a 5 cm high SB (h_{SB} = 4.27h_{ESP}). Corresponding line plots can be found in Figure E.2c.

Quantity	Case	Run	Mean	Standard Deviation	Minimum	Maximum
η	a	1	0.2580	0.1191	0	0.6074
	b	2	0.2556	0.1435	0.0016	0.6862
	c	3	0.3749	0.1429	0.0610	0.7716
	d	4	0.2819	0.1178	0.0241	0.5694
	e	5	0.1785	0.1149	0	0.5341
$\frac{\overline{u}}{\overline{u}_{max}}$	a	1	0.2246	0.0899	-0.0729	0.4022
	b	2	0.2251	0.1001	0.0005	0.4030
	c	3	0.4141	0.1028	0.0733	0.5912
	d	4	0.2622	0.1013	0.0260	0.4717
	e	5	0.1706	0.0809	-0.0646	0.3786
α [°]	a	1	56.00	11.29	24.24	86.99
	b	2	54.33	13.68	12.59	90.69
	c	3	49.46	7.86	26.56	78.04
	d	4	51.03	14.13	-15.61	84.20
	e	5	58.61	13.19	20.06	99.04

Table F.3: ESP performance and ESP entrance flow statistics for different runs on a 3 cm high SB (h_{SB} = 2.56h_{ESP}). Corresponding line plots can be found in Figure E.4c.

Quantity	Case	Run	Mean	Standard Deviation	Minimum	Maximum
η	a	1	0.3812	0.1860	0.0334	0.8525
	b	2	0.2930	0.1570	0.0011	0.7017
	c	3	0.4976	0.1750	0.1924	0.8823
	d	4	0.4073	0.1721	0	0.8929
	e	5	0.2076	0.1166	0	0.5623
$\frac{\overline{u}}{\overline{u}_{max}}$	a	1	0.2932	0.0877	0.0217	0.4926
	b	2	0.2503	0.0863	0.0007	0.4457
	c	3	0.3885	0.0928	0.1265	0.5922
	d	4	0.3107	0.0980	-0.0159	0.5066
	e	5	0.1709	0.0671	-0.0113	0.3856
α [°]	a	1	45.75	12.36	-6.95	87.46
	b	2	45.57	14.36	3.73	94.00
	c	3	39.56	9.05	17.71	74.72
	d	4	45.90	13.16	0.16	91.09
	e	5	47.55	13.26	12.02	82.19

Table F.4: Performance and entrance flow statistics for a hypothetical ESP placed on fences of different heights. Corresponding line plots can be found in Figure 5.15c.

Quantity	Case	$\frac{h_{SB}}{h_{ESP}}$	Mean	Standard Deviation	Minimum	Maximum
η	a	0.85	0.5686	0.2283	0.0801	0.9678
	b	1.71	0.5482	0.2202	0.1017	0.9596
	c	2.56	0.4642	0.1560	0.1242	0.8420
	d	2.99	0.5008	0.2014	0.0494	0.8849
	e	4.27	0.4148	0.1156	0.1740	0.7030
$\frac{\overline{u}}{\overline{u}_{max}}$	a	0.85	0.5107	0.1182	0.1735	0.7452
	b	1.71	0.4741	0.1086	0.1051	0.7502
	c	2.56	0.4780	0.1063	0.1525	0.6962
	d	2.99	0.5035	0.1322	0.0169	0.7861
	e	4.27	0.5351	0.1119	0.1424	0.7985
α [°]	a	0.85	25.13	5.81	12.97	46.33
	b	1.71	37.67	7.27	21.50	65.54
	c	2.56	42.03	9.01	-8.47	72.61
	d	2.99	45.63	10.63	9.21	86.68
	e	4.27	48.39	7.38	28.16	75.77

Table F.5: Performance and entrance flow statistics for an ESP placed on fences of different heights. Corresponding line plots can be found in Figure 5.17c.

Quantity	Case	$\frac{h_{SB}}{h_{ESP}}$	Mean	Standard Deviation	Minimum	Maximum
η	a	0.85	0.6403	0.2038	0.1148	0.9477
	b	1.71	0.5441	0.2075	0.0244	0.9235
	c	2.56	0.3573	0.1631	0	0.8929
	d	2.99	0.3648	0.1673	0.0179	0.8068
	e	4.27	0.2698	0.1283	0	0.7716
$\frac{\overline{u}}{\overline{u}_{max}}$	a	0.85	0.3771	0.0953	0.0846	0.5752
	b	1.71	0.4237	0.1176	0.0059	0.7042
	c	2.56	0.2827	0.0870	-0.0159	0.5922
	d	2.99	0.2881	0.0912	0.0102	0.4952
	e	4.27	0.2593	0.0954	-0.0729	0.5912
α [°]	a	0.85	31.25	9.75	-4.85	67.94
	b	1.71	38.15	10.31	15.87	92.01
	c	2.56	44.87	12.57	-6.95	94.00
	d	2.99	45.71	11.30	15.56	81.83
	e	4.27	53.89	12.25	-15.61	99.04

Table F.6: Performance and entrance flow statistics for an ESP suspended at different vertical displacements above a 5 cm high SB (h_{SB} = 4.27h_{ESP}). Corresponding line plots can be found in Figure 5.19c.

Quantity	Case	$\frac{h_{Shift}}{h_{ESP}}$	Mean	Standard Deviation	Minimum	Maximum
η	a	0	0.2698	0.1283	0	0.7716
	b	0.43	0.3535	0.1186	0.1243	0.7424
	c	0.77	0.3141	0.0869	0.1484	0.5943
	d	1.28	0.2336	0.0667	0.0540	0.5241
	e	1.71	0.1902	0.0744	0.0398	0.4610
$\frac{\overline{u}}{\overline{u}_{max}}$	a	0	0.2593	0.0954	-0.0729	0.5912
	b	0.43	0.4833	0.1164	0.1188	0.7179
	c	0.77	0.5255	0.1339	0.0529	0.7341
	d	1.28	0.5892	0.0754	0.2103	0.7852
	e	1.71	0.6463	0.0785	0.3254	0.7932
α [°]	a	0	53.89	12.25	-15.61	99.04
	b	0.43	44.47	7.60	31.04	81.27
	c	0.77	41.74	8.48	22.34	77.40
	d	1.28	37.30	5.02	23.50	50.01
	e	1.71	35.42	6.17	21.19	58.03

Table F.7: Performance and entrance flow statistics for an ESP suspended at different vertical displacements above a 3 cm high SB (h_{SB} = 2.56h_{ESP}). Corresponding line plots can be found in Figure 5.21c.

Quantity	Case	$\frac{h_{Shift}}{h_{ESP}}$	Mean	Standard Deviation	Minimum	Maximum
η	a	0	0.3573	0.1631	0	0.8929
	b	0.43	0.4660	0.1565	0.0159	0.8304
	c	0.86	0.2511	0.1093	0.0882	0.6532
	d	1.28	0.1614	0.0752	0.0355	0.4452
	e	1.62	0.1272	0.0518	0.0284	0.4163
$\frac{\overline{u}}{\overline{u}_{max}}$	a	0	0.2827	0.0870	-0.0159	0.5922
	b	0.43	0.5394	0.1227	0.0080	0.7162
	c	0.86	0.6418	0.0827	0.4139	0.8117
	d	1.28	0.6425	0.0940	0.1607	0.8146
	e	1.65	0.6729	0.0781	0.3526	0.8343
α [°]	a	0	44.87	12.57	-6.95	94.00
	b	0.43	36.99	9.44	25.09	88.59
	c	0.86	30.50	5.49	16.19	48.24
	d	1.28	30.89	7.45	14.72	76.29
	e	1.62	27.47	5.59	17.05	49.22

Table F.8: Performance and entrance flow statistics for an ESP located above the downstream SB in different canyon configurations. 'R' in the list refers to the case where the ESP is raised. Corresponding line plots can be found in Figure 5.24c.

Quantity	Case	$\frac{h_{SB}}{h_{ESP}}$	$\frac{w_{canyon}}{h_{canyon}}$	Mean	Standard Deviation	Minimum	Maximum
η	a	0.85	4.2	0.1583	0.1485	0	0.7631
	b	1.71	2.1	0.3491	0.2140	0	0.8394
	c	2.56	1.4	0.0127	0.0443	0	0.2835
	d	4.27	0.84	0.0038	0.0170	0	0.1707
	e	4.27R	0.84	0.3905	0.1932	0	0.8448
$\frac{\overline{u}}{\overline{u}_{max}}$	a	0.85	4.2	0.0469	0.0400	-0.0404	0.1510
	b	1.71	2.1	0.1278	0.0792	-0.0717	0.3218
	c	2.56	1.4	-0.0794	0.0842	-0.2526	0.2051
	d	4.27	0.84	-0.0547	0.0394	-0.1470	0.0482
	e	4.27R	0.84	0.2512	0.1566	-0.0601	0.6715
α [°]	a	0.85	4.2	-18.26	27.45	-86.13	58.95
	b	1.71	2.1	-48.32	18.82	-96.66	11.11
	c	2.56	1.4	-18.22	81.57	-145.15	146.79
	d	4.27	0.84	14.27	68.25	-128.87	130.46
	e	4.27R	0.84	6.13	27.44	-49.14	98.19

G

Appendix - Flow statistics around a sound barrier with an ESP on top

Contour plots of certain flow statistics and probabilities of events for flow around a 3 cm high SB and an ESP atop (h_{SB} = 2.56h_{ESP}) are presented in this appendix. This corresponds to 'Run 1' illustrated in Figure E.3a. The information here can be used for validation of results obtained through computational techniques. A brief introduction to various flow analyses techniques is given by Paterna [94].

Any turbulent flow may be decomposed into a mean and a fluctuating part, in what is known as the Reynolds decomposition. The mean, for both the streamwise and wall-normal velocity components, is estimated through a time average of 1000 images, and are illustrated in Figure G.1a and Figure G.1b respectively. An estimate of the size of the region with reverse flow around the SB can be made through these plots.

Similarly, an estimate of the turbulent fluctuations at a given location is derived from the standard deviation of the velocity components. The contour plots for the standard deviation of the streamwise and wall-normal fluctuations are shown in Figure G.1c and Figure G.1d respectively. The highest intensity of fluctuations are present in and around the SB, and especially in the shear layer emanating from the upstream corner of the ESP.

The turbulent fluctuations exert a stress on the mean flow. The normal stresses can also be interpreted as turbulent kinetic energies, for example, as illustrated in Figure G.1e. An example of shear stresses is given in Figure G.1f. The highest magnitude of shear stresses are found in the aforementioned shear layer which follows from the presence of high root mean square velocity magnitudes.

Some higher order statistics are plotted in Figure G.2. George [111] also provides an introduction to these dimensionless quantities. These higher order moments mainly assist in getting a better understanding of the probability distribution functions of turbulent quantities.

Skewness, the third order moment, is a measure of the distribution of realizations with respect to the mean, i.e. positive skewness implies a higher presence of positive fluctuations and vice versa. The skewness of select turbulent quantities are shown in Figure G.2a and Figure G.2b respectively. A Gaussian distribution has a skewness of zero.

Kurtosis or flatness, the fourth order moment, gives an indication of the tails of a probability distribution function, i.e. a higher kurtosis implies a higher probability of excursions from the mean. Flatness can also be construed as a measure of intermittency, as a higher intermittency implies the higher probability of occurrence of extreme events. A Gaussian distribution has a flatness of three. The flatness of select turbulent quantities are shown in Figure G.2c and Figure G.2d respectively. It seems that the shear layer around the ESP is more prone to extreme events than the other regions of the flow, which can contribute to the aforementioned high shear stresses.

The contour plots shown seem to be spotty and noisy. It is unclear whether this is physical or if the size of the sampling data set was insufficient. It is likely that the accurate determination of higher order statistics requires a larger data size.

Quadrant analysis is a technique that has been used for analyzing turbulent shear flows and was introduced by Wallace et al. [112] and reviewed more recently by Wallace [113]. This technique is mainly is used to understand the source of turbulent shear stresses.

Each velocity component has a fluctuating component in a turbulent flow. If the streamwise and wall-normal fluctuating components are denoted by u and w respectively, four categories of events can identified: Q_1 $(+u,+w)$, Q_2 $(-u,+w)$, Q_3 $(-u,-w)$ and Q_4 $(+u,-w)$.

Q_2 and Q_4 contribute the most to the Reynolds shear stresses and correspond to ejections and sweeps respectively. Ejections are those events where low-speed fluid close to the wall is pumped away into a region away from the wall. This fluid is then replaced by a high speed-fluid moving towards the wall, in what is known as a sweep event. Q_1 and Q_3 events are known as outward and inward interactions respectively.

Contour plots of the probability of occurrence of these events are shown in Figure G.3. Regions close to the SB, especially in the shear layer, seem to be more prone to the ejections and sweeps, which might contribute significantly to the higher magnitudes of turbulent shear stresses.

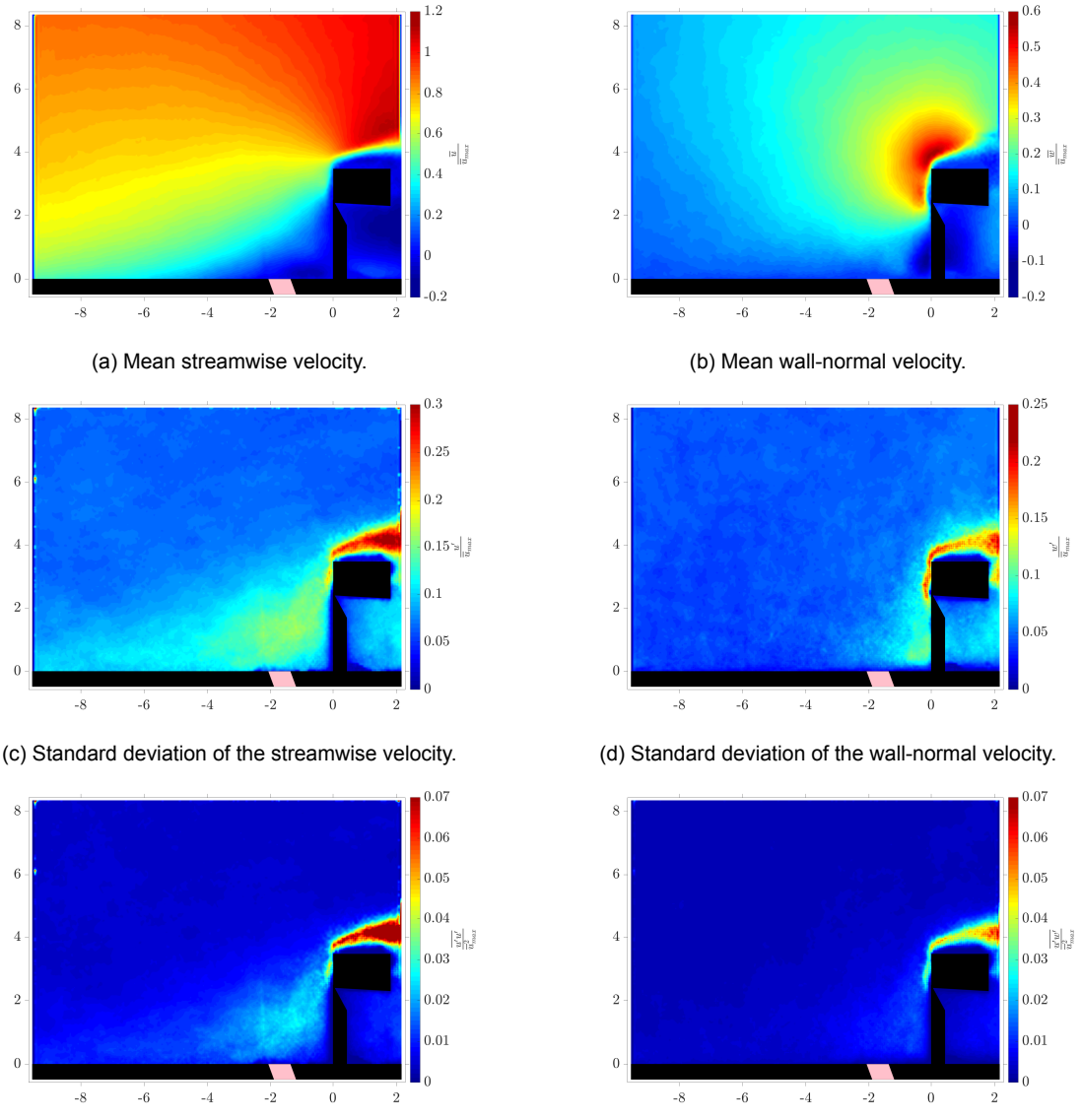

(a) Mean streamwise velocity.

(b) Mean wall-normal velocity.

(c) Standard deviation of the streamwise velocity.

(d) Standard deviation of the wall-normal velocity.

(e) Streamwise turbulent kinetic energy.

(f) Streamwise-Wall-normal Reynolds shear stress.

Figure G.1: Contour plots of lower order statistics.

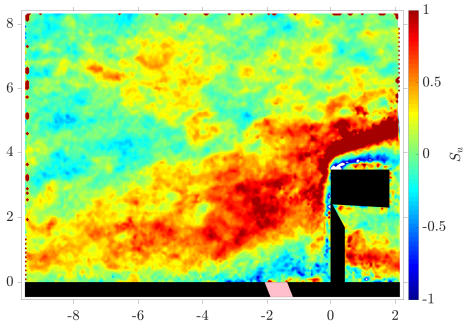

(a) Skewness of streamwise velocity fluctuations.

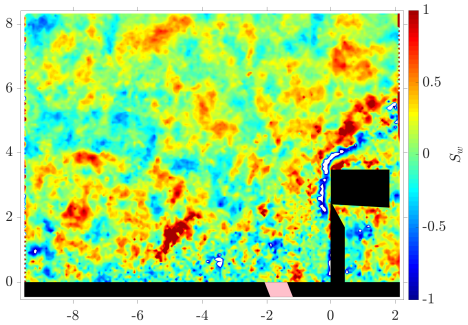

(b) Skewness of wall-normal velocity fluctuations.

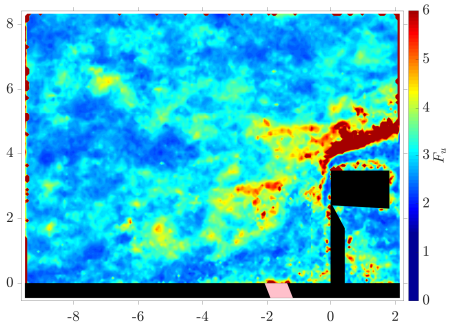

(c) Flatness of streamwise velocity fluctuations.

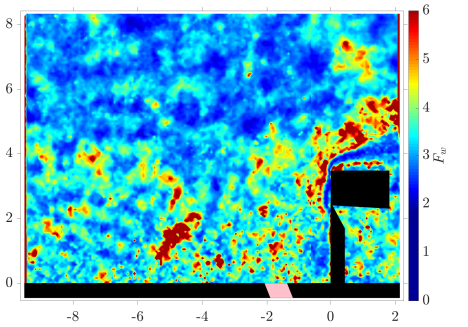

(d) Flatness of wall-normal velocity fluctuations.

Figure G.2: Contour plots of higher order statistics.

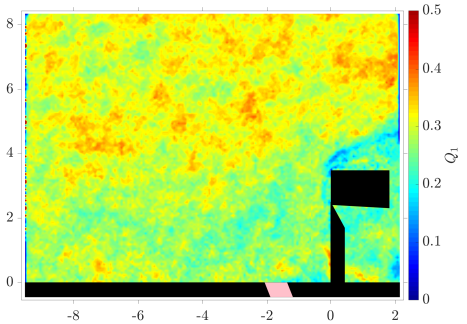

(a) Q1 events or outward interactions.

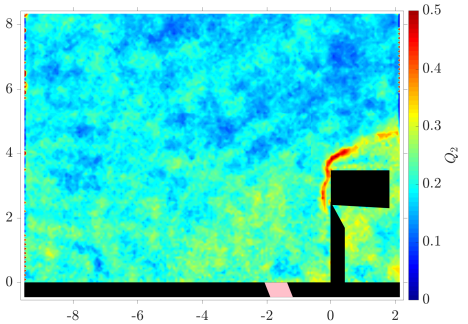

(b) Q2 events or ejections.

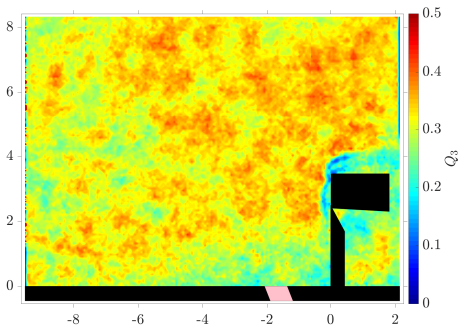

(c) Q3 events or inward interactions.

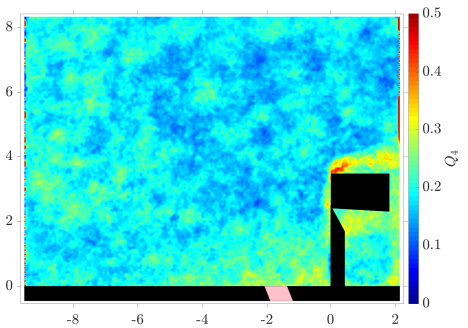

(d) Q4 events or sweeps.

Figure G.3: Probabilities of event occurrence corresponding to different quadrants.